The University of Nottingham

Numerical and Experimental Investigation of Novel Materials for Laser and Amplifier Operations

By

OLADEJI Ayodele

B.Sc.(Hons.) MSc.

Thesis submitted to the University of Nottingham
for the degree of Doctor of Philosophy

June, 2015

Abstract

One of the most exciting areas of research in optics is rare-earth doped glasses and fibres with capacity for near-infrared to mid-infrared operations. In particular, there is great interest in optimising parameters like ion concentration, fibre length/geometry, and pump conditions for applications in photoluminescence, amplification and lasing. Round trip investigation from material fabrication, experimental setup and actual device can be laborious, expensive and come with some uncertainties. Some of these uncertainties are *accurate identification of ion-ion interactions, impact of such interactions on device performance, correct extraction of phenomenological material properties and the prediction of combination of properties with numerical methods* . In this thesis, the spectroscopic behaviour of rare-earth doped materials are theoretically studied via numerical simulations and experimentally verified. The models developed are applicable to steady-state and transient behaviour of rare-earths under different excitation conditions. For the simulation, a couple of spectroscopic parameters are needed which have to be obtained in advance from bulk glasses. Parameters like radiative and non-radiative lifetimes are calculated by complementing theoretical analysis with a few experimental measurements.

The first part of the research concentrates on the study of ion-ion interactions in different concentrations of erbium doped sol-gel SiO_2 prepared by the sol-gel method. The work includes continuous-wave (CW) and pulsed excitation spectroscopic measurement on the glasses that provide data for the model. These measurements together with the rate-equation modelling are used to obtain a physical understanding of the processes responsible for the fluorescence features observed. A particle swarm optimisation technique was used to predict the values of the ion-ion interactions. The behaviour of the 488 nm and 800 nm excitations were consistent with the predictions of the model. Indeed, the agreement between the calculated photoluminescence and the measured emission indicates that the six important processes that influence the ion-ion interactions in the bulk material have been correctly identified and included. With this model of photoluminescence at hand, it was possible to extend it to laser or amplifier configurations.

Subsequently, erbium doped ZBLAN glass fibre with lower phonon energy were explored for lasing in the mid-infrared for application to 2.73 μm high-power delivery for tissue surgery. Accurate laser characteristics were predicted for two different designs, including the ultimate thermal designs. Optimum boundary conditions of mirror end-facet reflectivity, fibre length and effects of modelling parameters were addressed. The study is complimented with experimental data of double-clad fibre and the results reported were a clear documentation of the design of erbium doped ZBLAN fiber laser.

Finally, the potential of Pr^{3+} doped chalcogenide (GeAs(Ga/In)Se) glass for photoluminescence and lasing at 4.73 μm is studied. This is to answer the research question - *Can we extract the spectroscopic parameters and also model the superior property of these novel glasses?*. The laboratory facilities and availability of experimental data were decisive in the choice of praseodymium ions as well as inclusion of Gallium or Indium for this part of the research. The superior characteristics of Indium over Gallium for photoluminescence and consequently device characteristics were studied with the aid of a rate equation model. The phenomenon of photon reabsorption in the chalcogenide fibres were also simulated and verified with experiment. The work has produced a comprehensive numerical model for the simulation of photoluminescence in Pr^{3+}doped selenide based chalcogenide glass and fibre from NIR to mid-IR especially in the Gallium and Indium based analogues.

Acknowledgements

It is a great honour to have had the opportunity to experience first hand the depth of experimental and theoretical knowledge from many talented people during the course of this PhD. This experience will stay with me for the rest of my career. The wonderful time could not have been possible without the support of all the people I worked with at the University of Nottingham.

I am extremely grateful to my primary supervisor; Dr Slawomir Sujecki for his insights and guidance on directing my thesis research and as a personal role model for hard-working and effective communication. I also appreciate my second supervisor: Dr Andy Phillips whose knack for asking the right questions, helped in channelling my research. I also appreciate my internal moderator; Dr Malcolm Woolfson and my external examiner Ryszard Dr Piramidowicz for the viva examination and their thoroughness in producing the final version of this thesis.

I am indebted to the Novel Glasses research group headed by Professor Angela Seddon for many useful discussions about the Chalcogenide glass preparation, experimental setup and modelling. I appreciate the efforts of Professor Trevor Benson, David Furniss, Tang, Hesham, Lukasz.

No amount of thanks would be enough to give to the past and present members of the George Green Institute of Electromagnetic Research (GGIEMR); Xuesong Meng(Vicky), Sendy, Ahmed, Dan, Bukky, Hayan, Harshana, Priye and others, for all the great evenings, lunch times, movies and random office rants. I also recognise the suppport of friends in the Electrical Systems and Optics Group: Rohan, Abisayo, Tosin, Afam, Hasula and others too numerous to mention. My experience at UoN would not have been the same without the wonderful support from Tutors of Southwell and Newark hall especially the deputy warden (Grazziela Figueredo) who took out time to read and correct this thesis. I also appreciate the wonderful support of my choir and local family at God's Vineyard Church

List of Publications

This section presents a list of publications formed as part of the research work for this thesis.

[1] **A. Oladeji**, P. L. Arnold, M. I. Ali, S. Sujecki, A. Phillips, I. V. Sazanovich, and J. A. Weinstein, "Numerical and experimental investigation of NIR-to-visible energy up-conversion in Er^{3+}-doped sol-gel SiO_2 powders", *Journal of Materials Chemistry C*, vol. 1, no. 48, pp. 8075 - 8085, 2013.

[2] **A. Oladeji**, P. L. Arnold, M. I. Ali, A. Phillips, I. V. Sazanovich, J. A. Weinstein, and S. Sujecki, "Numerical and experimental investigation of NIR-infrared-visible luminescence in erbium doped sol-gel SiO_2", in *Transparent Optical Networks (ICTON), 2013 15th International Conference on*, pp. 1 - 4, 2013.

[3] **A. Oladeji**, P. L. Arnold, M. I. Ali, A. Phillips, I. V. Sazanovich, J. A.Weinstein, and S. Sujecki, "Numerical and experimental investigation of upconversion in Er^{3+} doped sol-gel SiO_2", *in Numerical Simulation of Optoelectronic Devices (NUSOD), 11th International Conference*, pp. 99 - 100, 2011.

[4] **A. Oladeji**, L. Sojka, Z. Tang, D. Furniss, A. Phillips, A. Seddon, T. Benson, and S. Sujecki, "Numerical investigation of mid-infrared emission from Pr^{3+} doped GeAsGaSe Fibre", *Optical and Quantum Electronics*, vol. 46, no. 4, pp. 593 - 602, 2014.

[5] L. Sojka, Z. Tang, D. Furniss, H. Sakr, **A. Oladeji**, E. Beres-Pawlik, H. Dantanarayana, E. Faber, A. Seddon, T. Benson, and S. Sujecki, "Broadband,

mid-infrared emission from Pr^{3+} doped GeAsGaSe chalcogenide fibre, optically clad", *Optical Materials*, vol. 36, pp. 1076 - 1082, Apr. 2014.

[6] S. Sujecki, **A. Oladeji**, L. Sojka, A. Phillips, A.B. Seddon, T.M. Benson, H. Sakr, Z. Tang, D. Furniss, K. Scholle, S. Lamrini, and P. Furberg," Modelling and Design of MIR Chalcogenide Glass Fibre Lasers (invited)" *Numerical Simulation of Optoelectronic Devices (NUSOD), 2014 14th International Conference on. IEEE*, 2014.

[7] S. Sujecki, **A. Oladeji**, A. Phillips, A. Seddon, T. Benson, H. Sakr, Z. Tang, E. Barney, D. Furniss, L. Sojka, E. Beres-Pawlik, K. Scholle, S. Lamrini, and P. Furberg, "Theoretical study of population inversion in active doped MIR chalcogenide glass fibre lasers" *Optical and Quantum Electronics*, pp. 1 - 7, 2014.

[8] **A. Oladeji**, S. Sujecki, , A. Phillips, K. Scholle, S. Lamrini, P. Furberg, A. Seddon, and T. Benson, "Design of erbium doped double-clad ZBLAN fibre laser", *Sixth International Conference on Optical, Optoelectronic and Photonic Materials and Applications*, 2014

[9] S. Lamrini, K. Scholle, M. Schafer, J. Ward , M. Francis , M. Farries , S. Sujecki , T. Benson, A. Seddon , **A. Oladeji** , B. Napier, and P. Fuhrberg, "Design of erbium doped double-clad ZBLAN fibre laser", *Conference on Lasers and Electro-Optics Europe and European Quantum Electronics Conference*, 2015

Contents

List of Figures

List of Tables

List of Acronyms

ChGs   Chalcogenide glasses

RE   Rare Earth

J-O   Judd-Ofelt

PL   Photoluminescence

IR   InfraRed

NIR   Near-InfraRed

MIR   Mid-InfraRed

MPR   Multiphonon Rate

PSO   Particle Swarm Optimisation

ppmw   parts per million weight

ETU   Energy Transfer Upconversion

ESA   Excited State Absorption

LASER   Light Amplification by Stimulated Emission of Radiation

CR   Cross Relaxation

ZBLAN $ZrF_4 - BaF_2 - LaF_3 - AlF_3 - NaF$

PXRD   Powder X-Ray Diffraction

PDFA   Praseodymium Doped Fibre Amplifier

ODCF   Octagonal Double Clad Fibre

Chapter 1

Introduction

Some naturally occurring elements , if incorporated in a properly engineered device, have been known to amplify specific properties of light in different materials. These elements belong to a category of elements referred to as Lanthanides in the periodic table [1.1]. An understanding of their underlying properties in host materials at the atomic levels produces valuable information in developing suitable mathematical expressions to describe their physical interaction with light.

The increase in computational power over the years, enables researchers to create models that are capable of transforming the necessary characteristics of the real world and provide insights into the development of devices. Although, both experimental and numerical investigations complement each other in optimising materials for specific applications, the use of considerably modelling assists in the determination of real world experiments.

This thesis investigates erbium and praseodymium ions as candidates for the investigation of photoluminescence, amplification and lasing in novel glasses to optimise characteristics such as doping concentration, size/length/ geometry using the method of rate equations. We attempt to answer research questions like - What are the interactions leading to photoluminescence and can we successfully reproduce them through numerical models? We also try to fill the gaps in literature especially relating to the multiphonon properties

of Indium and Gallium samples in selenide based chalcogenide glasses.

In this chapter therefore, the research is introduced by examining the motivation in section 1.1. In section 1.2, the author highlights how the research contributes to the body of knowledge and section 1.3 summaries the structure of the thesis with a summary of the chapters.

◌◌◌◌◌
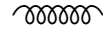
1.1 Motivation

Rare-earth ions such as Erbium(Er^{3+}), Ytterbium(Yb^{3+}), Neodymium(Nd^{3+}), thulium (Tm^{3+}), Holium (Ho^{3+}) and Praseodymium (Pr^{3+}) have long been used in optical applications close to the near infrared spectra range. One of the pioneering works on a working optical fiber laser and amplifier was demonstrated in the early 60s with Nd^{3+}-doped glass rod [1.2,1.3]. This has also inspired the development of the first thin-film waveguide glass amplifier [1.4] and the first integrated optical glass laser [1.5].

Since then, the solubility of other rare-earths in different glass matrices has been widely explored. The interest in 1550 nm band for optical communication systems shifted research towards Er^{3+}doped glasses in the late 1980s [1.6]. The first successful erbium doped fiber amplifier was developed in the early 90s [1.7]. The transparency and low loss value of silica (0.2dB/km) in the 1.3 μm - 1.55 μm telecoms window is credited for this success [1.7]. Silica glass fabrication is an established technology and the incorporation of rare-earths has produced a few interesting applications: Er^{3+}doped fiber amplifier [1.8] , Er^{3+} [1.9] / Yb^{3+} [1.10] / Tm^{3+} [1.11] / Ho^{3+} [1.12,1.13] lasers. The preparation technique employed is known to influence the incorporation of rare-earths into the glass hosts and consequently the suitability for particular applications. Sol-gel technique is attractive because of the flexibility and choice of host constituents the process offers. Despite the high chemical durability and superior chemical resistance silica glasses offer, in-depth luminescence and upconversion studies are limited to only a few transitions owing to their higher phonon energies [1.14]. Erbium doped $CdS - SiO_2$ glasses prepared by the sol–gel

route produced intense green and red upconversion fluorescence bands around 533, 549 and 622 nm under 800 nm pumping [1.15]. Energy transfer upconversion (ETU), excitated state absorption (ESA) and cross relaxation (CR) were identified as the mechanisms leading to the measured photoluminescence [1.15]. The study was however limited to a single sample doped with 0.01M of Er^{3+} under one excitation. Though the study reveals the potential of the glass for the $^4S_{3/2}/^2H_{11/2}$ lasing transitions, quantitative values of the stated mechanisms were not measured or calculated to justify the assumption under a different pump excitation. Erbium-doped tin dioxide (SnO_2:Er^{3+}) was also obtained by the sol-gel method, with apectroscopic properties analysed using the JuddOfelt (JO) theory [1.16]. The potential for laser and amplifier operation was explored at 798 nm with very high emission cross section ($1.31 \times 10^{-20} cm^2$) measured at 1.54 μm compared to other systems. This study also identfied a few ETU and CR processes to explain the efficient up-conversion and infrared luminescence measured. Like the previous author, the exact magnitude of the photoluminescence cannot be reproduced numerically at other wavelengths because of unavailable upconversion values. Similar observations and conclusions were drawn by another research into sol-gel derived Er^{3+}:$Al_2O_3 - SiO_2$ planar waveguides with broadband peak at 1531nm [1.17]. Like the previous authors, their work did not produce spectroscopic parameters of upconversion to describe the sample prepared. However in another study involving erbium doped $SiO_2 - TiO_2$ sol-gel powder [1.18], the authors verified the upconversion mechanisms leading to photoluminescence in 3 different samples with excitations at 1532 nm, 979 nm and 490 nm. Upconversion parameters that characterise the sample was not measured or calculated and therefore the potential of this material for other applications could not be explored further by a numerical model. Compared to other authors, however, a study into erbium-doped sol-gel waveguide amplifiers [1.19], produced a comprehensive model of rate equations and estimated upconversion parameters. This study used the method of lines to predict the propagation of pump and signal fields. The authors acknowledged that the analysis produced would be complete with the inclusion of other quenching mechanisms such contributions from OH impurities.

In the light of some of these reviewed works, this research will first consider an erbium doped silica sample prepared by the sol-gel route with different concentrations and pump conditions. We will also attempt to produce accurate values of upconversion parameters unique to the sample for reproducible photoluminescence at different wavelengths. This fills the gaps where there was need for rigorous experimental studies and measurements [1.20]

With advancement in the preparation of high-purity materials, there is renewed interest in applications beyond the visible wavelength where silica is found to be opaque. One solution to improve transparencies up to the infrared region is to lower the phonon-energy of the host material, the most common example being the heavy-metal fluoride glasses [1.21]. The interest in 2.7 μm emission for laser surgery is because it coincides with the highest absorption peak of water around 2.7 μm .

Indeed a few studies have produced 158 mW at 2.7 μm [1.22], 1W at 3 μm [1.23] in ZBLAN host. Also the thermal capacities [1.24] and the experimental setup demonstrating cooling requirements [1.25] in the same glass hosts have been investigated. A few studies have also examined how the laser pump configuration impacts the output performance or efficiency of the laser [1.26,1.27]. Efficiencies as high as 13% for pump powers at 975 nm and laser power at 2.8 μm have been reported with an output power of 24 W [1.25] and 4.6 W [1.28]. A few of the studies relied on cascade lasing while others have utilised upconversion process to prevent population bottleneck by radiative decay. Despite the potential for high power delivery by using multicore ZBLAN fibers to obtain 100 W output at 2.7 μm in the future [1.29], the performance in a real system is limited by the thermal loading on the fibre laser. It is therefore important to provide a comprehensive insight into the optimum operation condition of the ZBLAN laser setup for parameters like length, doping concentration, mirror reflectivities and thermal limit given the possibility to engineer the fibre geometry for tailored pump absorptions.

There are other rare-earth ions like Pr^{3+}, Tm^{3+} and Dy^{3+} with rich spectral spread and a wide bandwidth in the mid-infrared region. Specifically Pr^{3+} is being investigated in compounds made up of Ge, Ga, As with a S and Se network former. This specific glass

composition, referred to as chalcogenide glass has the advantage of low loss, high linear and non-linear refractive index, making it attractive to numerous applications involving chemical sensing, medical endoscopy [1.30,1.31] supercontinuum generation and optical switching applications [1.32,1.33]. The maximum phonon energy in chalcogenide hosts is low compared to silica ($1100cm^{-1}$, [1.7]) and therefore enhances rich spectral of broad-band mid-IR emissions when doped with praseodymium. A few studies have examined the mid-IR properties of different compositions of chalcogenide glasses [1.34–1.36]. To the best of our knowledge, there is no literature on the spectroscopic properties of selenide based chalcogenide where Indium was substituted for Gallium. Also few of the studies have been complemented with numerical studies that is capable of explaining the ionic distribution of all the excited states of Praseodymium or the phenomenological parameters of multiphonon relaxations.

The objective of this study is to establish knowledge and understanding of the interactions that lead to the processes of photoluminescence, amplification and lasing and how these interactions can be optimised for operations from NIR to mid-IR.

1.2 Thesis Contribution

There are several contributions that can be credited to this thesis. Firstly, we developed a rate equations' based model to study photoluminescence spectra and decay rates in 1%, 4% and 10 % erbium doped SiO_2 samples prepared by the sol-gel method. Using this model and particle swarm algorithm, we identified five dominant ion-ion interactions comprising of 4 upconversion processes and 1 cross relaxation process which are key to understanding the experimentally observed photoluminescence spectra and recorded photoluminescence decay traces.

Secondly, we developed a computer model of an erbium doped ZBLAN fibre laser operating at 2.7 μm that includes the radiative upconversion processes. The model has the ability to predict the temperature distribution within the fibre. The heat sources include the effect of direct multiphonon transitions and phonon assisted upconversion processes.

To the best knowledge of the author, such model has not been reported previously in the available literature. The developed model was used to design ZBLAN fibre lasers for operation in the mid-infrared wavelength range.

Thirdly, the photoluminescence simulation of praseodymium doped chalcogenide glass with Gallium and Indium network formers were performed. For this purpose, rate equation models were developed. Using the developed models, the author explained the superior characteristics of photoluminescence in Indium based glass when compared with Gallium one. To the best of the author's knowledge, this is phenomenon has not been explained by other authors. Further the model was used to extract the phenomenological parameters α and β describing multiphonon decay in the chalcogenide glass samples that contain gallium. From these results, we calculated the corresponding quantum efficiencies. Unlike the results presented by other authors, the results obtained by the author are consistent with the ones reported in the available literature for Silicate, Tellurite and ZBLAN glasses.

1.3 Survey of the thesis

This thesis consists of eight chapters.

Chapter 1 presents a review of the background of optical materials and their applications. Time and steady state numerical simulation techniques are used to model these materials to investigate photoluminescence, amplification and lasing. These simulations have assisted us to investigate how changes in material properties impact spectroscopic properties for different applications.

To this end, Chapter 2 of this thesis examines rare-earth elements with emphasis on light-matter interactions based on energy levels and phonon-energy in glass hosts. The non-radiative decay processes of excited state manifolds are discussed. The chapter concludes with particular attention to two lanthanide ions namely erbium and praseodymium which are the focus of the rest of this thesis . From their electronic configurations, existing and potential applications are identified.

Chapter 3 then examines the sol-gel route and melt and quench method which are the

experimental techniques explored in our research. From the techniques highlighted, some parameters important for modelling like lifetime calculations are discussed based on the theories of energy-gap law and Judd-Ofelt. The chapter concludes with a discussion on the limitations of applying Judd-Ofelt to praseodymium and introduces a modified technique for overcoming these limitations, subsequently, the relationship between cross-sections is realised with the McCumber method.

Once the required modelling parameters are established, the numerical modelling techniques centred on 1D rate equation methods are presented in Chapter 4. The peculiar behaviour of this modelling technique with regards to its tendency to drift into stiffness is discussed. In the same chapter, some solutions to overcome these limitations from within the numerical technique are also discussed. An evolutionary algorithm that provides a good estimate of ion-ion interaction in doped materials is also presented. The rate equation technique is then extended to two-dimensions to investigate light propagation in a lasing medium. The chapter concludes with a few techniques for modelling mode profiles and thermal performance of a fiber laser.

Chapter 5 investigates the Erbium (Er^{3+}) doped Silica prepared with the sol-gel technique. The potential of improving the lifetime and quantum efficiency of fluorescence with the addition of a network modifying element (Al_2O_3) is investigated. Three samples with different erbium concentrations are considered with one used as the control sample. The primary interest is to study the influence of the Er^{3+} concentration on the luminescent properties of the sol-gel. The techniques earlier established in chapter 4 are applied to study the origins of energy transfer ion-ion interactions. The measurement of luminescence intensities from excited state manifolds as a function of pump power allowed the modelling of the population evolution of the system. The chapter concludes with a comprehensive model including a set of up-conversion parameters whose values are predicted with the aid of the particle swarm algorithm (PSO).

Having tested the numerical techniques presented in chapter 4 with success with application to bulk material modelling in Chapter 5 , Chapter 6 extends the application of the rate equation to low-phonon Praseodymium doped chalcogenide glass. The

fluorescence intensities predictions are consistent with the explanation that multi-phonon decay rates at localised sites throughout the glass network are at least of the order of the radiative transitions. Quantum efficiencies in the mid-infrared transitions are compared in two major samples: one with Gallium (Ga) and Selenium (Se), Arsenic (As), Germanium (Ge) network formers and the other with Indium (In) replacing Ga.

In Chapter 7 , the laser simulation of an octagonal double clad fiber is discussed as an application of rare earth spectroscopy. We show the influence of multiphonon emission on the lasing capability of two different fiber geometries in cascade lasing configuration. Furthemore, these outcomes were used to make predictions about the optimum operation of the laser. The model is further extended to include thermal calculations and the impact on the efficiency of the laser.

In the final chapter of this thesis - Chapter 8, the main conclusions of this work are presented. Further findings of this research and recommendations for future work are also discussed.

References

[1.1] D. Atwood, *The Rare Earth Elements: Fundamentals and Applications.* EIC Books, Wiley, 2013.

[1.2] E. Snitzer, "Optical maser action of Nd^{3+} in a barium crown glass," *Physical Review Letters*, vol. 7, no. 12, p. 444, 1961.

[1.3] C. J. Koester and E. Snitzer, "Amplification in a fiber laser," *Applied Optics*, vol. 3, no. 10, pp. 1182–1186, 1964.

[1.4] H. Yajima, S. Kawase, and Y. Sekimoto, "Amplification at 1.06 μm using a Nd : glass thin–film waveguide," *Applied Physics Letters*, vol. 21, no. 9, pp. 407–409, 1972.

[1.5] M. Saruwatari and T. Izawa, "Nd-glass laser with three-dimensional optical waveguide," *Applied Physics Letters*, vol. 24, no. 12, pp. 603–605, 1974.

[1.6] M. Digonnet, *Rare-Earth-Doped Fiber Lasers and Amplifiers, Revised and Expanded.* Optical Science and Engineering, Taylor & Francis, 2001.

[1.7] P. C. Becker, J. R. Simpson, and N. Olsson, *Erbim-doped fiber amplifiers fundamentals and technology.* San Diego: Academic Press., 1999.

[1.8] E. Desurvire, J. R. Simpson, and P. C. Becker, "High-gain erbium-doped traveling-wave fiber amplifier," *Opt. Lett.*, vol. 12, pp. 888–890, Nov 1987.

[1.9] R. Mears, L. Reekie, S. Poole, and D. Payne, "Low-threshold tunable CW and Q-switched fibre laser operating at 1.55 μm ," *Electronics Letters*, vol. 22, pp. 159–160, January 1986.

[1.10] H. Pask, R. Carman, D. Hanna, A. Tropper, C. Mackechnie, P. Barber, and J. Dawes, "Ytterbium-doped silica fiber lasers: versatile sources for the 1-1.2 μm region," *IEEE Journal of Selected Topics in Quantum Electronics*, vol. 1, pp. 2–13, Apr 1995.

[1.11] S. Mehrabani and A. M. Armani, "Blue upconversion laser based on thulium-doped silica microcavity," *Opt. Lett.*, vol. 38, pp. 4346–4349, Nov 2013.

[1.12] D. Hanna, R. Percival, R. Smart, J. Townsend, and A. Tropper, "Continuous-wave oscillation of holmium-doped silica fibre laser," *Electronics Letters*, vol. 25, no. 9, pp. 593–594, 1989.

[1.13] S. D. Jackson, A. Sabella, A. Hemming, S. Bennetts, and D. G. Lancaster, "High-power 83 W holmium-doped silica fiber laser operating with high beam quality," *Opt. Lett.*, vol. 32, pp. 241–243, Feb 2007.

[1.14] V. R. Kumar, M. R. Reddy, and N. Veeraiah, "Effect of DC Field and X-Ray Irradiation on Dielectric Properties of $ZnF_2 - PbO - TeO_2$ Glasses," *Physica Status Solidi (a)*, vol. 147, no. 2, pp. 601–610, 1995.

[1.15] P. Dutta, "Efficient green fluorescence and upconversion emissions from Er^{3+} ions in CdS sol-gel silica glass," *Optoelectronics And Advanced Materials - Rapid Communications*, vol. 6, pp. 427–433, March-April 2012.

[1.16] C. Bouzidi, A. Moadhen, H. Elhouichet, and M. Oueslati, "Er^{3+}-doped sol-gel SnO_2 for optical laser and amplifier applications," *Applied Physics B*, vol. 90, no. 3-4, pp. 465–469, 2008.

[1.17] M. Benatsou, B. Capoen, M. Bouazaoui, W. Tchana, and J. Vilcot, "Preparation and characterization of sol-gel derived Er^{3+}: $Al_2O_3 - SiO_2$ planar waveguides," *Applied Physics Letters*, vol. 71, no. 4, pp. 428–430, 1997.

[1.18] J. Castañeda, M. Meneses-Nava, O. Barbosa-Garcıa, E. De la Rosa-Cruz, and J. Mosiño, "The red emission in two and three steps up-conversion process in a doped erbium $SiO_2 - TiO_2$ sol–gel powder," *J. Lumin.*, vol. 102, pp. 504–509, 2003.

[1.19] A. Laliotis, E. M. Yeatman, M. M. Ahmad, and W. Huang, "Molecular homogeneity in erbium-doped sol-gel waveguide amplifiers," *IEEE Journal of Quantum Electronics*, vol. 40, no. 6, pp. 805–814, 2004.

[1.20] V. Bogdanov, *Energy exchange processes in erbium-doped fluoride glasses*. PhD thesis, Optical Technology Research Laboratory, School of Communications and Informatics, Victoria University, 1999.

[1.21] R. Caspary, *Applied Rare Earth Spectroscopy for Fiber Laser Optimization*. Berichte Aus der Lasertechnik Series, Shaker Verlag GmbH, 2002.

[1.22] M. Pollnau, C. Ghisler, G. Bunea, M. Bunea, W. A. Luethy, and H. P. Weber, "Erbium 3-μm fiber laser in the power range for surgery," in *Biomedical Optoelectronics in Clinical Chemistry and Biotechnology*, vol. 2629, pp. 234–244, 1996.

[1.23] M. Pollnau, "The route toward a diode-pumped 1-W erbium 3-μm fiber laser," *IEEE Journal of Quantum Electronics*, vol. 33, no. 11, pp. 1982–1990, 1997.

[1.24] M. Pollnau, "Analysis of heat generation and thermal lensing in erbium 3 μm lasers," *IEEE Journal of Quantum Electronics*, vol. 39, pp. 350–357, 2003.

[1.25] S. Tokita, M. Murakami, S. Shimizu, M. Hashida, and S. Sakabe, "Liquid-cooled 24 W mid-infrared Er: ZBLAN fiber laser," *Optics letters*, vol. 34, no. 20, pp. 3062–3064, 2009.

[1.26] T.-Y. Tsai, Y.-C. Fang, H.-X. Tsao, S.-T. Lin, and C. Hu, "Passively cascade-pulsed erbium ZBLAN all-fiber laser," *Optics Express*, vol. 20, no. 12, pp. 12787–12792, 2012.

[1.27] C. Ghisler, M. Pollnau, G. Bunea, M. Bunea, W. Lüthy, and H. Weber, "Up-conversion cascade laser at 1.7 μm with simultaneous 2.7 μm lasing in erbium zblan fibre," *Electronics Letters*, vol. 31, no. 5, pp. 373–374, 1995.

[1.28] S. Jackson, "High-power erbium cascade fibre laser," *Electronics Letters*, vol. 45, no. 16, pp. 830–832, 2009.

[1.29] X. Zhu and N. Peyghambarian, "High-power ZBLAN glass fiber lasers: review and prospect," *Advances in OptoElectronics*, vol. 2010, 2010.

[1.30] A. B. Seddon, "A Prospective for New Mid-Infrared Medical Endoscopy Using Chalcogenide Glasses," *International Journal of Applied Glass Science*, vol. 2, pp. 177–191, Sept. 2011.

[1.31] A. B. Seddon, "Mid-infrared (IR)–A hot topic: The potential for using mid-IR light for non-invasive early detection of skin cancer in vivo," *Physica Status Solidi (b)*, vol. 250, no. 5, pp. 1020–1027, 2013.

[1.32] A. Zakery and S. R. Elliott, "Optical properties and applications of chalcogenide glasses: a review," *Journal of Non-Crystalline Solids*, vol. 330, no. 1, pp. 1–12, 2003.

[1.33] A. Seddon, "Chalcogenide glasses: a review of their preparation, properties and applications," *Journal of Non-Crystalline Solids*, vol. 184, pp. 44–50, 1995.

[1.34] L. Shaw, B. Harbison, B. Cole, J. Sanghera, and I. Aggarwal, "Spectroscopy of the IR transitions in Pr^{3+} doped heavy metal selenide glasses," *Optics Express*, vol. 1, no. 4, pp. 87–96, 1997.

[1.35] L. Shaw, B. Cole, P. Thielen, J. Sanghera, and I. Aggarwal, "Mid-wave IR and long-wave IR laser potential of rare-earth doped chalcogenide glass fiber," *IEEE Journal of Quantum Electronics*, vol. 37, no. 9, pp. 1127–1137, 2001.

[1.36] J. K. Kim, B. Kyou Jin, W. J. Chung, B. J. Park, J. Heo, and Y. G. Choi, "Influence of the Ga addition on optical properties of Pr in Ge–Sb–Se glasses," *Journal of Physics and Chemistry of Solids*, vol. 72, no. 11, pp. 1386–1389, 2011.

Chapter 2

Lanthanides and glass materials

In order to model and predict the behaviour of lanthanides as driving elements for photoluminescence, gain medium and device characteristics, the first step is to understand their spectroscopic properties. This chapter contains the background information, concepts and important principles that guide the physical phenomena developed in all other parts of this work. The chapter starts with a review of the fundamental properties of the trivalent ions at the atomic level in section 2.1. Section 2.2 describes the interaction of light with matter with special emphasis on absorption, stimulated emission and spontaneous emission processes. Section 2.3 describes the kind of interactions that exists between ions as a function of doping concentration. Section 2.4 discusses the energy-levels of erbium and praseodymium. Section 2.5 describes the importance of phonon energies in glass hosts for the realisation of specific device charatcteristics. Section 2.6 discusses the state of research into erbium and praseodymium doped glasses. Section 2.7 summaries the chapter and highlights a few applications of interests based on ion-host material compatibility.

ᴔᴔᴔᴔᴔᴔ
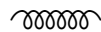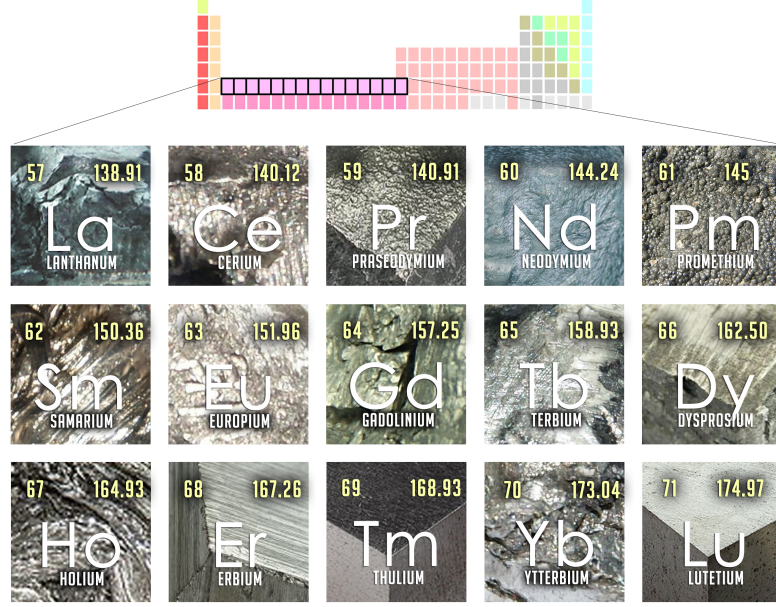
2.1 General Characteristics of rare-earths

Rare earth elements belong to the group of 15 elements, known chemically as Lanthanides, occupying atomic number 57 (Lanthanum) to 71 (Lutetium) in the periodic table. Figure 2.1 shows the rare-earth elements. The pull-out part of figure 2.1 shows each of the rare-earth elements in different metal forms including their atomic number, weight and chemical symbol. They are naturally found in a variety of minerals, however, the major commercial sources are xenotime, monazite and bastnaesite [2.1].The elements in this group are most stable in their triply ionised form. Though similar by chemical properties, their spectroscopic properties are a major distinguishing feature. All rare-earth ions have the same $5s^2 5p^6 6s^2$ outer shell and have an electronic structure that is identical to that of Xenon ($[\text{Xe}]4f^{1}26s^2$) in addition to a few 4f electrons. The 5s and 5p electrons shield the 4f electrons resulting in sharp optical transitions, which are not affected by the environment of the host material. The 4f states have transition probabilities that are sensitive to the ions around the rare-earth. The spectroscopic properties and consequently the design of materials and devices are dependent on the interaction between several f-f transitions and the host ions. Apart from Praseodymium (Pr^{3+}, green), Neodymium (Nd^{3+}, violet) and Erbium (Er^{3+}, rose), other lanthanide trivalent ions appear colourless in an aqueous solution [2.1].

2.2 Light-Matter Interactions

In thermodynamic equilibrium, the atoms making up a material are in a rest state at the ground state until an excitation is impacted. To describe the interaction of electromagnetic wave with matter, Einstein identified three processes: absorption(B_{12}), stimulated emission(B_{21}) and spontaneous emission (A_{21}). The three processes in an optical medium are related by equation 2.1 [2.2]. In thermal equilibrium, equation 2.1 can then be rearranged in the form of equation 2.2.

Figure 2.1: Rare-earth elements of the periodic table

$$\frac{dn_1}{dt} = -n_1 B_{12}\rho(\nu) + n_2 B_{21}\rho(\nu) + n_2 A_{21} \tag{2.1}$$

$$\frac{n_1}{n_2} = \frac{B_{21}\rho(\nu) + A_{21}}{B_{12}\rho(\nu)} \tag{2.2}$$

Where n_1 and n_2 are the number of atoms per unit volume in each state 1 and 2 respectively. $n_1 + n_2 = N$ is the total number of ions in the system. This conforms to the principle of mass conservation, which assumes that the number of atoms distributed among the two levels is constant. $\rho(\nu)$ is the spectral energy density of the radiation field at frequency ν. Planck's constant retains the standard notation h throughout this study. The processes are explained in terms of a simple atomic level system involving 2 energy levels shown in figure 2.2. E_1 is the energy of the lower level 1 and E_2 is the energy of the upper level 2 such that $E_1 < E_2$.

- **Absorption process**: In the absorption process, an electron absorbs a photon and the excitation produced by the kinetic energy of the incident photon (h) translates it from an initial level E_1 to a final level E_2. In the figure 2.2, $E_2 - E_1 = h\nu$, is
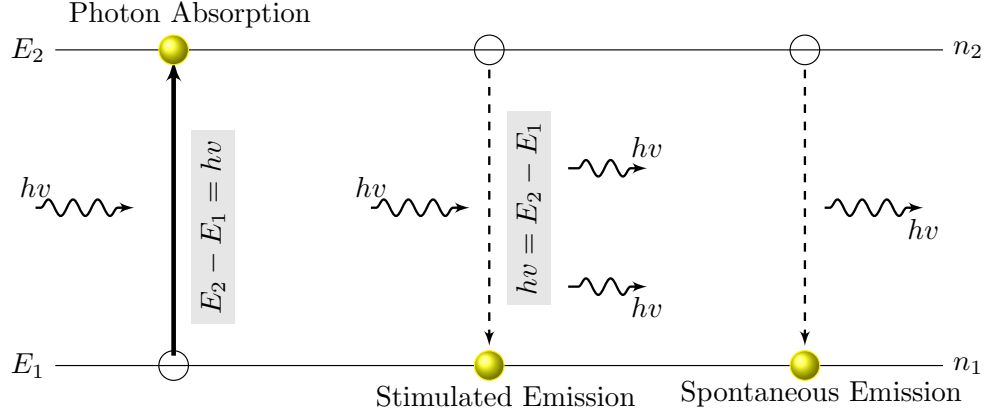
Figure 2.2: Interaction of radiation with matter through the processes of absorption, stimulated emission and spontaneous decay.

the energy-gap separating the two levels and also matches the resonant energy of the incident photon. The absorption process occurs with a probability described by Equation 2.3. Absorption processes are further categorised as ground state absorption (GSA) and excited state absorption (ESA). GSA is from the ground state to an upper state while ESA requires that an ion in an excited state(at least level 2) gets promoted to an even higher state(at least level 3). It is important to state that ESA only applies to a system that has more than 2 energy levels.

$$W_{12}^a = B_{12}\rho(\nu) \tag{2.3}$$

where B_{12} is the Einstein coefficient with dimensions $cm^3(J.s)^{-1}$ and $\rho(\nu)$ is the spectral energy density of the incident radiation in $Js^{-1}cm^{-3}$. The superscript 'a' stands for absorption and the subscript '12' indicates that the direction of the observation is from level 1 to level 2.

- **Stimulated emission**: This process is usually initiated when an incident photon travelling through an active medium causes an electron in an excited state to relax to a lower energy and emit another photon with identical frequency (ν), phase (ϕ), polarization and wavelength (λ) to the incident one. This process is important

for signal gain in a fibre amplifier or lasing medium. A beam of coherent light is formed through this process when multiple photons acquire the same wavelength and oscillate in phase with one another. The probability of a stimulated emission is described by equation 2.4

$$W_{21}^{se} = B_{21}\rho(\nu) \tag{2.4}$$

Where B_{21} is the Einstein coefficient with dimensions $cm^3(J.s)^{-1}$ and $\rho(\nu)$ is the spectral energy density of the incident radiation in $Js^{-1}cm^3$. The superscript 'se' stands for stimulated emission and the subscript '21' indicates that the direction of the observation is from level 2 to level 1.

- **Spontaneous emission:** A third process which does not rely on an external excitation occurs when an electron in an excited state relaxes to a lower energy state and emits a photon of light with random phase, polarization and direction. This process is radiative because of the photon emitted. Beyond a 2-level system, the photon given off by the spontaneous emission can interact with excited electrons to cause stimulated emissions at wavelengths that are not desired. When the de-excitation does not result in the emission of a photon, but rather in the vibration of the host matrix, it is referred to as non-radiative emission. The whole process reduces the gain of a system and adds noise to the output signal in an amplifier or laser. The probability of a spontaneous emission is defined by the Einstein coefficient A_{21}. The inverse of this coefficient is an important parameter known as the metastable level lifetime ($\tau = \frac{1}{A_{21}}$). Maximum possible lifetimes are usually desired to retain ions at energy-levels so that population inversion which is a major determinant for amplification and lasing can be easily achieved.

It is not possible to obtain population inversion in a 2-level system. In thermal equilibrium ($n_1 + n_2 = n$), the atoms are continously excited from the ground state to the excited state by optical absorption which will attain equilibrium through competing processes of

spontaneous and stimulated emission. The probability for absorption and spontaneous emission is exactly the same and occur at equal rates as shown by Einstein and expressed by Einstein A and B coefficients [2.3]. At best, the population of the states $n_1 = n_2 = \frac{n_1}{2}$ is achieved, producing optical transparency but no net optical gain. Whereas for population inversion, it is required that at least $n_2 \geq 2n_1$.

De-excitation of atoms from energy levels is usually attributed to stimulated or spontaneous emission processes. Depending on the application, both processes can either be beneficial to a system or impede performance.

2.3 Ion-ion Interactions

As the concentration of lathanide ions increase, the separation between neighbouring ions reduces, thereby increasing the probability of ion-ion interactions. The probability of energy-transfer by ion-ion interaction can be expressed as follows [2.4]

$$P_{ET} = C_{i-i} exp \left(-\frac{2R}{L} \right) \tag{2.5}$$

where R is the distance between donor-acceptor pair, C_{i-i} is the ion-ion interaction constant and L is the effective Bohr radius. The equation shows that the rate of energy-transfer between ions depends on the inter-ionic distance. The increase in the ionic distance(reduced concentration) will reduce the energy-migration among the lanthanide ions. This has been verified by theoretical and experimental investigation [2.5,2.6]. Also the non-radiative energy transfer processes due to dipole-dipole interaction is expressed as [2.7,2.8]:

$$W(D_0^1 \rightarrow A_1^0)_{ij} = \frac{1}{\tau_{D_0^1}} \frac{R_{06}(D_0^1 \rightarrow A_1^0)^6}{R_{D_i A_j}^6} \tag{2.6}$$

where $R_{0S}(D_0^1 \rightarrow A_1^0)$ defines the Forster distance. τ_{FS}^{IS} is the radiative lifetime of a donor relaxing radiatively from the initial state *IS* to a final state *FS*. $R_{D_i A_j}$ is the interionic distance between the jth donor and the ith acceptor. In a crystalline host, D

and A are uniformly distributed and therefore $R_{D_i A_j}$ is a discrete random variable that depends on the dopant concentration as well as the crystalline phase of the material [2.9].

This process involves transitions between energy-levels through energy exchange between ions and does not lead to the generation of photons. The interactions are categorised as energy migration, upconversion and cross-relaxation processes.
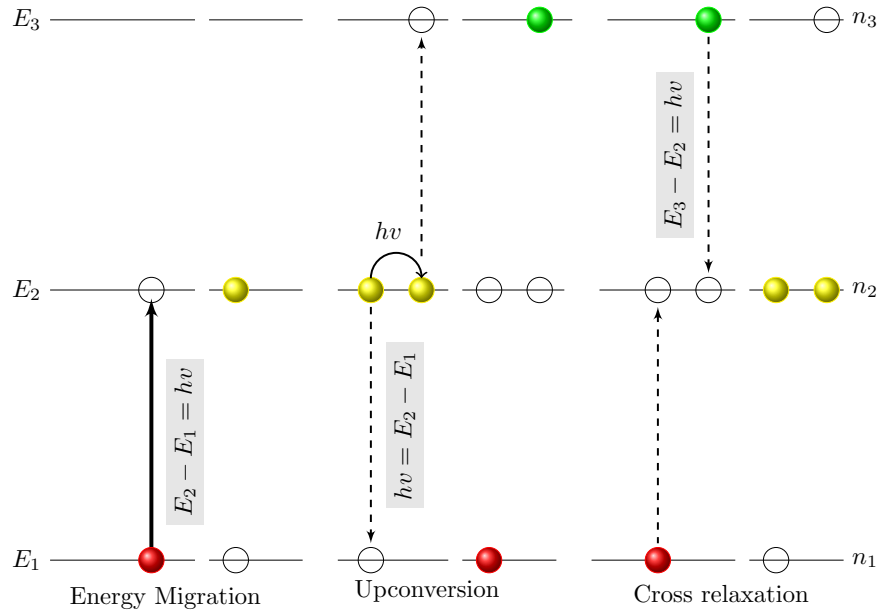
Figure 2.3: A schematic diagram of the energy migration, upconversion and cross-relaxation processes

Figure 2.3 shows the ion-ion interactions common in highly doped lathanide materials. The processes of energy migration, upconversion and cross relaxation (see figure 2.3) are all non-radiative as they only absorb energies and at best use phonons vibrations to compensate for energy-mismatch between transitions. In some contexts however, energy transfer can be said to be radiative, because real photons are emitted by the sensitizer ion and are then absorbed by any activator ion within a photon travel distance [2.10]. Since the emitted photon is absorbed, the process is acceptably non-radiative

Ions at the ground state are colour coded 'red' while ions at excited states 2 and 3 are colour coded 'yellow' and 'green', respectively. In the figure, E_i and n_i represent the energy and total ion density of level i. In the energy migration process, energy is

transferred from one lanthanide ion whose higher state coincides with the lower state of another ion. The process is employed in co-doped materials to transfer pump photons to ions that do not interact with the incident light. This can help to counter de-excitation processes that deplete the ion population by non-radiative transition. This scheme has been successfully used to improve optical device characteristics [2.11,2.12].

Upconversion is a non-linear optical effect that can be used to convert low energy incident radiation (e.g infrared light) into higher energy emitted radiation (e.g visible light), first discovered in the 1960's [2.13–2.15]. In the upconversion process, one of the yellow coded ions in the excited state 2 transfers its energy ($h\upsilon$) to the other ion. This energy transfer process causes the first ion (often referred to as the donor) to relax to level 1 while the other ion (the acceptor that acquires the transferred energy) is promoted to level 2. For this process to be efficient, the energy gap between levels 1 and 2 must match those of levels 2 and 3. The upconversion process can be useful in the construction of upconversion lasers [2.16,2.17] because it increases the population of higher levels without relying on direct excitation. It also influences the thermal performance of a fibre laser if it couples with multiphonon relaxation processes [2.18,2.19].

Cross relaxation process on the other hand is the inverse process of upconversion. The final state of the ions involved is an intermediate level between the initial state of both ions. The process is endothermic and can therefore be useful in cooling down a fibre laser [2.18]. Cross-relaxation is also known as self-quenching, a process which occurs between two identical ions. When the first ion initially in an excited state exchanges its energy with a second ion which is initially in the ground state, resulting in both ions simultaneously changing to excited states which are in intermediate positions between the two initial states. The energy dropped by the first ion is equal to the energy acquired by the second ion thereby conserving energy in the process. The energy rate equation describing cross-relaxation between the ground state(1) and an excited state (3) with an

intermediate state(2) would have the following form

$$
\begin{aligned}
\frac{dn_1}{dt} &= -cN_1N_3 \\
\frac{dn_2}{dt} &= 2cN_1N_3 \\
\frac{dn_3}{dt} &= -cN_1N_3
\end{aligned}
\tag{2.7}
$$

where c is the cross-relaxation rate for this ion, N_1, N_2, N_3 are the population densities of ions that are in the ground state(1), the intermediate state(2) and the upper excited state(3) respectively.

The cross-relaxation rate is influenced by the physical properties of the molecule and the sample. The CR processes influences the radiative lifetime [2.20] of the excited state by reducing the number of ions at the upper level that can migrate by spontaneous emission probability. Depending on the particular level involved however, the cross-relaxation process can add or remove population from the level and hence can enhance or limit the performance of any practical device.

2.4 Energy Levels of a few rare-earths

Through quantum mechanics, it is known that electrons orbit the nucleus of an atom in states with specific energies. Electrons orbiting an atomic nucleus therefore possess a discrete set of possible energy levels. The energy levels are the solution to the time-independent Schrödinger equation which are beyond the scope of this work. The details of this can be found in literature [2.21,2.22]. Following the Russell-Saunders notation, the energy states of rare-earths are labelled as $^{2S+1}L_J$, where S is the total spin of the electrons, L is the orbital angular momentum, and J is the total angular momentum of the state. The incorporation of rare-earths into a host material leaves the position of the energy levels unchanged. However the electric interactions between the ions and host atoms cause stark-splitting of the levels into a manifold of finely spaced levels. The splitting pattern determines a few spectroscopic properties like the absorption

and emission bands. Erbium and praseodymium ions are two ions with characteristics that are important to the overall objectives of this work. The interband-transitions in erbium span 400 - 3000 nm and are useful for applications from the visible to mid-IR. The interband-transitions in praseodymium span the visible to the mid-IR wavelengths and in a suitable glass host, opens up a wide range of applications like optical fiber amplifier, coloured lasers, gas sensing, just to mention a few [2.23–2.25]

2.4.1 Erbium

Erbium (Er^{3+}) has an atomic number of 68, lying in the eleventh position in the lanthanide group, between Holmium and Thulium [2.26]. In the triply ionized state, Er^{3+} has 11 electrons in its 4f shell based on [Kr] $4d^{10}4f^{11}5s^25p^6$ electronic configuration. Figure 2.4 shows the energy level diagram of the Er^{3+} ion. Energy level values shown are wavenumbers in cm^{-1}. When doped into silica glass, a number of transitions in Er^{3+} become dominated by multi-phonon decay because the small gap between the energy-levels is easily bridged by one or more photons with phonon energies $\approx 1100 cm^{-1}$ [2.27].

To explore the Er^{3+} ion further, the characteristics of each excited manifold are reviewed as follows.

- $^4I_{13/2}$ **manifold**: This manifold is the first excited state (state $|1\rangle$) of Er^{3+} and is located ≈ 6550 cm^{-1} above the ground state. The $^4I_{13/2} \rightarrow {}^4I_{15/2}$ transition produces an emission band spanning 1400 nm - 1625 nm, coinciding with the low loss region referred to as the 3rd telecommunication window. This manifold can be pumped directly around 1480 nm or excited through the decay of higher energy manifolds such as $^4I_{11/2}$, $^4I_{9/2}$. $^4I_{11/2}$ is the most efficient because it has a lower multiphonon rate to the next lower level compared to the $^4I_{9/2}$ and therefore more ions are retained at $^4I_{11/2}$. In silica glass host, the decay from this level is dominated by radiative transition because of the wide-energy gap that can only be bridged by about 7 phonons. This level has been successfully employed in a three-transition cascade erbium laser at 1.6 μm [2.28]. Luminescence quantum efficiencies are close to 100%

$^4G_{11/2}$ ——————————————— n_9, $26385 cm^{-1}$

$^2G_{9/2}$ ——————————————— n_8, $24570 cm^{-1}$

$^4F_{3/2}$ ═══════════════════════ $22573 cm^{-1}$
$^4F_{5/2}$ ——————————————— n_7, $22172 cm^{-1}$

$^4F_{7/2}$ ——————————————— n_6, $20492 cm^{-1}$

$^2H_{11/2}$ ——————————————— $19157 cm^{-1}$
$^4S_{3/2}$ ——————————————— n_5, $18416 cm^{-1}$

$^4F_{9/2}$ ——————————————— n_4, $15243 cm^{-1}$

$^4I_{9/2}$ ——————————————— n_3, $12437 cm^{-1}$

$^4I_{11/2}$ ——————————————— n_2, $10183 cm^{-1}$

$^4I_{13/2}$ ——————————————— n_1, $6535 cm^{-1}$

$^4I_{15/2}$ ——————————————— n_0, $0 cm^{-1}$
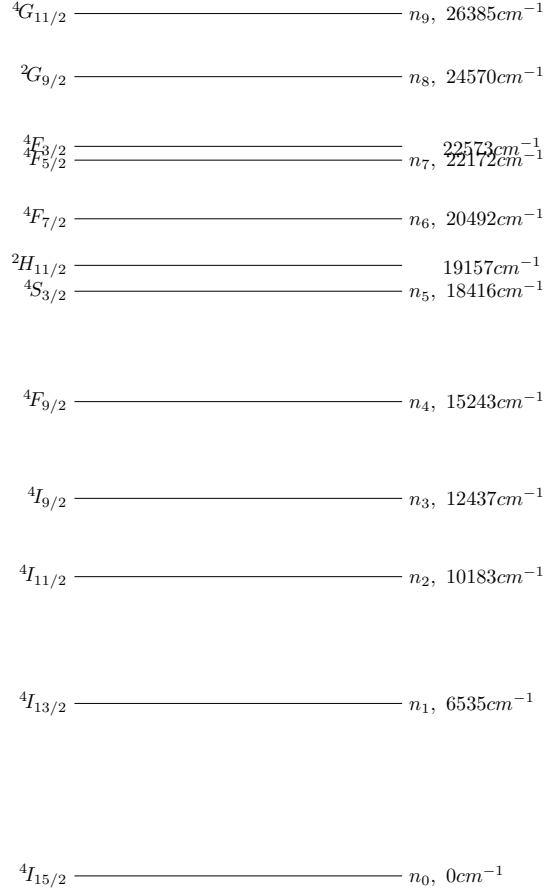
Figure 2.4: Energy level diagram of Er^{3+} ion

and lifetime values of 14 ms in Silica host [2.27], 8.9 ms in ZBLAN host [2.28] and 6 ms in sol-gel Silica glass host [2.29] have been reported.

- $^4I_{11/2}$ **manifold**: This manifold (state $|2\rangle$) is located ≈ 10200 cm^{-1} from the ground state and ≈ 3700 cm^{-1} above the $^4I_{13/2}$ manifold. There are commercially available high-powered laser sources of 980 nm wavelength coinciding with the excitation wavelength of this level. The $^4I_{11/2} \rightarrow {}^4I_{13/2}$ transition produces an emission with a wavelength of ≈ 2700 nm, close to the absorption of water and therefore attractive to medical applications. This manifold can also be populated through the decay of higher energy manifolds such as $^4I_{9/2}$ and above, whose ions originate from processes of excited state absorption (ESA) or energy transfer ion-ion interactions. The gap between this level ($^4I_{11/2}$) and the next lower level ($^4I_{13/2}$) is

large compared to the highest phonon energy in many glass hosts(see later in table 2.1). Therefore, the process of multiphonon emissions is reduced, making it attractive for the accumulation of ions at the $^4I_{11/2}$ level. Processes like up-conversion and excited state absorption occur very often in erbium-doped materials pumped with 980 nm lasers. In a recent work [2.30], erbium doped $Ga_{10}Ge_{25}S_{65}$ excited at 980 nm produced luminescence intensities with observations of two-laser photons (ESA to $^2H_{11/2}$) and up-conversion photon emissions. In some other studies conducted by Cherif *et al* [2.31–2.34] involving erbium doped materials with 980 nm excitation, the processes that led to the luminescence measured are consistent, namely excited state absorption and/or energy-transfer up-conversion to higher states followed by spontaneous and multiphonon decay.

- $^4I_{9/2}$ **manifold**: This is the third excited state (state $|3\rangle$) of Er^{3+} and is located ≈ 12500 cm^{-1} above the ground state. The transition from this state to the immediate lower state corresponds to ≈ 4.35 μm with potential applications in mid-infrared spectroscopy. This is however unrealisable in a practical device because the energy-gap (≈ 2300 cm^{-1}) between $^4I_{9/2}$ and $^4I_{11/2}$ is easily bridged by 2 phonons in silica host for example. This reduces the availability of ions in the $^4I_{11/2}$ manifold and consequently the probability of the mid-infrared transition. The scarcity of ions at this level also reduces the probability of further excitations like ion-ion interactions or excited state absorption directly from this level except through secondary photon absorption from $^4I_{11/2}$ and/or $^4I_{13/2}$, which was preceeded by multiphonon decay [2.35–2.37].

- $^4F_{9/2}$ **manifold**: This manifold (state $|4\rangle$) of Er^{3+} corresponds to the 656nm emission wavelength and is detected as red emission in luminescence studies. The large gap between this state and that of $^4I_{9/2}$makes it immune to multiphonon decay in many applications and therefore the quantum efficiency of the emission approaches 100%.

- $^4S_{3/2}/^2H_{11/2}$ **manifold**: These two levels (states $|5\rangle$ and $|6\rangle$) of Er^{3+} correspond

to the 532 nm and 514 nm emission wavelength respectively and are detected as the green emission in luminescence studies. The energy gap between the two levels ($\Delta E_{56} \approx 660 cm^{-1}$) is smaller than the highest phonon energy in a few hosts like silica ($\approx 1100 cm^{-1}$) and therefore it allows for thermal population of the $^2H_{11/2}$ level [2.38,2.39]. The temperature-dependent radiative decay of $^4S_{3/2}$ is stated in Equation 2.8 [2.39]

$$\frac{1}{\tau_r} = \frac{\sum_j A(^4S_{3/2} \to j) + 3e^{-\frac{\Delta E_{56}}{K_B T}} \sum_j A(^2H_{11/2} \to j)}{1 + 3e^{-\frac{\Delta E_{56}}{K_B T}}} \qquad (2.8)$$

- $^4F_{7/2}$ **manifold**: The $^4F_{7/2} \to {}^4I_{15/2}$ corresponds to the 488 nm resonant pumping band. Emission from this state is detected as the blue luminescence in photoluminescence measurements. The gap between this level and $^2H_{11/2}$ is ≈ 1330 cm^{-1} and is strongly quenched by multiphonon decay in a high-phonon glass like silica. Due to this effect, emission from this level is usually very weak in studies involving erbium.

Apart from the manifolds stated, sometimes the inclusion of higher energy levels with comparatively smaller populations provides a good indicator of the processes coupling these levels with lower levels.

2.4.2 Praseodymium

Praseodymium is the third element in the lanthanide group and has two electrons in its 4f shell in its triply ionised state (Pr^{3+}). Physically, it is soft, has a silvery metal look with low toxicity. The praseodymium ion has one of the richest energy level structures for mid-infrared to far-infrared transitions. The energy level diagram for a free Pr^{3+} ion is shown in Figure 2.5. The first 5 energy levels of Pr^{3+} can fit within the first energy level of Er^{3+}. In a low phonon energy host, the large energy gap between the excited states of Pr^{3+} reduces the dominant relaxation mechanism to radiative transitions.
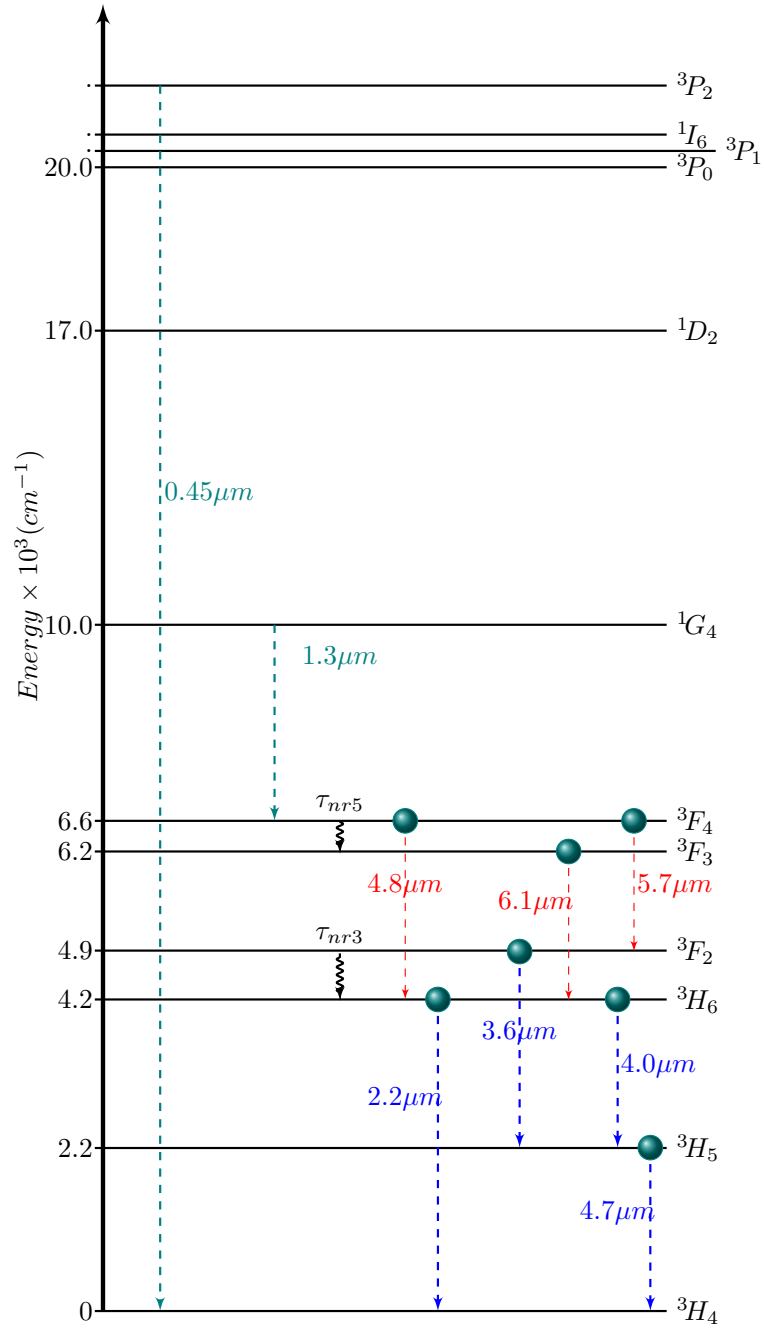
Figure 2.5: Energy level diagram of Pr^{3+} ion

- $^3H_5$ **manifold**: This manifold is the first excited state (state $|1\rangle$) of Pr^{3+} and is located $\approx$2100 cm^{-1}above the ground state. The $^3H_5\to {}^3H_4$ transition is of interest to many mid-infrared applications as it produces a broadband emission band spanning 3500 nm $-$ 6000 nm, with an approximate FWHM of 70nm [2.40]. The absorption spectrum of a few gases are found in this emission region: CO_2(4.2 μm), HSe(4.75 μm), HGe(5.0 μm) [2.41]. The radiative lifetime from this state($^3H_5\to {}^3H_4$) in chalcogenide glass host with Se former is 11.3 ms [2.42]. The stark splitting results in broad absorption and emission spectra [2.40] with possibility of broadband lasing in the range 3.5 – 6.0 μm

- $^3H_6/^3F_2$ **manifold**: These two manifolds are the second and third excited states of Pr^{3+}, emitting wavelengths in the range 2.0 - 2.5 μm . The energy gap between both levels is estimated to be of the order of ≈ 550 cm^{-1} which is less than the highest phonon energy in most oxide hosts (see later in table 2.1). The peaks of both manifolds are often indistinguishable in absorption measurements and the tail of the measurement is often deconvolved into a single Gaussian curve and assigned as the contribution of $^3H_6$ alone to the overlapping transition.

- $^3F_3$ **manifold**: This is the fifth excited state (state $|5\rangle$) located 6250 cm^{-1} above the ground state and therefore in resonance with the 1.55 μm pump.

- $^3F_4$ **manifold**: The energy level of this state is 6750 cm^{-1}. In most high phonon energy glasses, ions at this level experience rapid multiphonon relaxation to the next lower level $^3F_3$.

- $^1G_4$ **manifold**: This level has a wavelength of $\approx$ 1000 nm. The transition $^1G_4\to {}^3H_5$is 1.3 μm and has been previously studied for telecommunication applications and the development of praseodymium doped fibre amplifiers [2.43,2.44]

2.5 Phonon Energies and glass hosts

The quantized thermal energy or vibration mode occurring in a crystal lattice is known as a phonon. An ion excited to a higher state can relax to the immediate lower state in a similar manner to the spontaneous emission process described in section 2.2. Unlike the emission process however, the the energy difference between the two states is transferred to one or more phonons which is reflected as heat in the host glass. This leakage process affects the efficiency of luminescence as it competes for the availability of ions that emit photons based on the energy difference between the two states. Therefore to achieve better efficiencies, the relaxation processes caused by phonon decay have to be minimized. For this reason, energy-gaps in excess of 1500 cm^{-1} between excited states are useful in rare-earth ions. Alternatively, if the highest phonon-energy $h\nu_{max}$ is tuned such that the number of phonons required to bridge the energy gap is high, then the multiphonon-relaxation rate (MPR) reduces. The theory of lattice vibration and multiphonon transition has been well established. Raman spectroscopy is a standardised technique for determining the vibrational characteristics of a glass host. Figure 2.6 shows the Raman spectra of a few selected glasses [2.45].
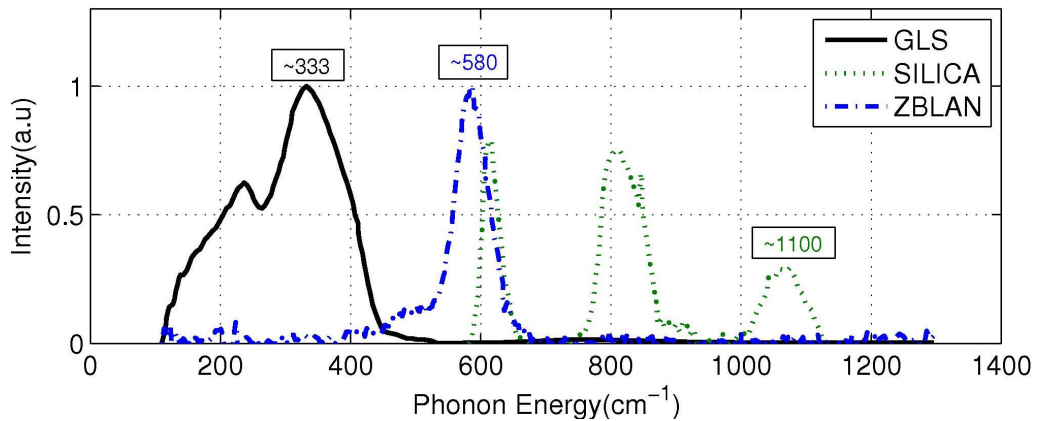
Figure 2.6: Raman Spectra of GLS, Silica and ZBLAN [2.45]

Table 2.1 shows a few typical phonon-energy in some glass hosts for both oxides and non-oxide glasses. Compared to oxides hosts, non-oxides hosts are characterised by having more metastable states and experiencing transparencies beyond 2 μm wavelength.

Table 2.1: Typical vibrational energies of a few glass hosts [2.27]

	Glasses	Phonon Energy(cm^{-1})
Non-oxides	Selenide/Telluride	230
	Selenide	300
	Sulfides	350
	Flourides	500
Oxides	Telurite	700
	Germanate	900
	Silicate	1100
	Phosphate	1200
	Borate	1400

The search for new glass compositions with heavier glass ions and weaker bond strengths led to the development of various glass hosts for rare-earth doped devices. Some of the glass hosts that have been the focus of intense research efforts include silica, fluoride, oxide and more recently, chalcogenide glasses [2.23,2.24,2.40,2.41,2.46–2.50]. To characterise the quantum efficiency of a glass host, it is important to quantify the multiphonon emission rates inherent in measured photoluminescence. The total lifetime τ_i of an excited state i is made up of both radiative and non-radiative transition probabilities between levels i to j as stated in Equation 2.9

$$\tau_i = \sum_j \left(\frac{1}{\tau_{rij}} + \frac{1}{\tau_{nrij}} \right) + w_x \tag{2.9}$$

where τ_r is the fluorescence lifetime, τ_{nr} is the nonradiative decay as a result of the interaction between the ions and the lattice vibrations of the host material and W_x accounts for nonradiative decay from other processes such as energy transfer up-conversion and cross relaxation. In low dopant concentrations, the MPR can be described by an exponential energy-gap law, which increases exponentially as energy gap decreases [2.27], as shown in equation 2.10 below

$$W_{nr} = Ce^{-\alpha\Delta E} \left[n(T) + 1 \right]^p \tag{2.10}$$

Where the phenomenological parameters C and α are the experimentally determined

host-dependent constants which depend on the strength of the ion-lattice coupling and are independent of the particular rare-earth ion. $h\nu$ is the phonon energy, and p is the number of phonons required to bridge the gap (ΔE) between two levels. $n(T)$ is the Bose-Einstein number [2.27], which relates the phonon population to a function of temperature as stated in equation 2.11 below:

$$n(T) = \left(e^{\frac{h\nu}{KT}} - 1\right)^{-1} \tag{2.11}$$

Some examples of these parameters are stated in Table 2.2 for different glasses. Figure 2.7 shows the trend for different glasses

Table 2.2: Nonradiative phenomenological transition parameters for different glasses [2.27]

Host glass	Phonon energy	$C(s^{-1})$	α (10^{-3}cm)
ZBLAN	500	1.99×10^5	2.1
Germanate	900	3.4×10^{12}	4.9
Silicate	1100	1.4×10^{12}	4.7
Phosphate	1200	5.4×10^{12}	4.7
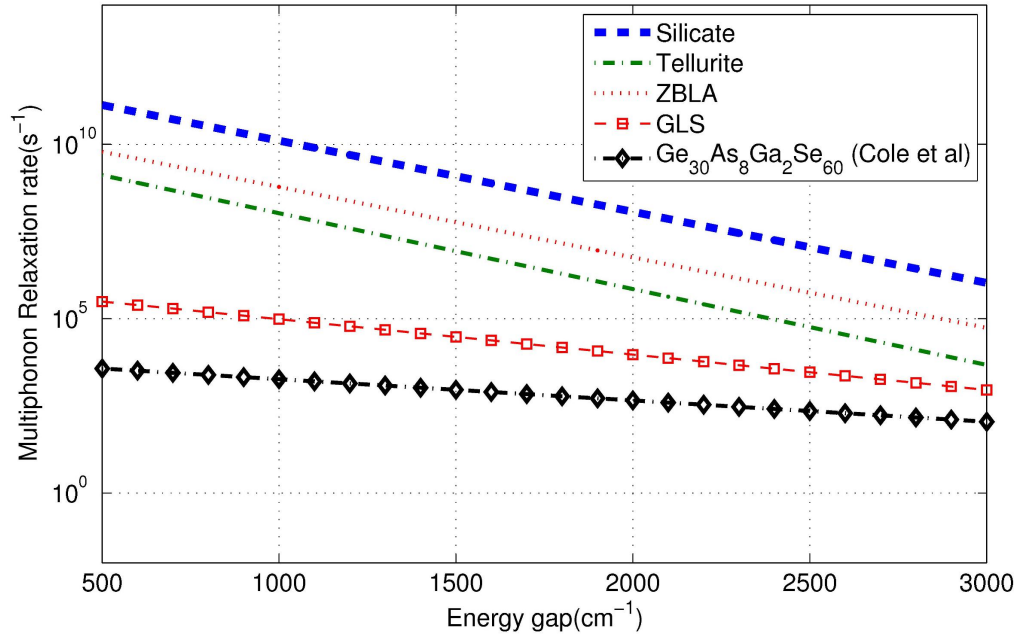
Figure 2.7: Measured and calculated multiphonon-relaxation rates as a function of the energy gap between energy levels for different glasses: Silicate, tellurite, ZBLA, GLS [2.51], $Ge_{30}As_8Ga_2Se_{60}$ [2.52]

.

2.6 The State of the Art with Erbium/Praseodymium doped materials

In this section, we review some of the literature concerned with the preparation route of doped glasses, tuning the characteristics of host materials and rare-earth element and how a trade-off between the vibrational energy and energy-gaps have helped in the realisation of devices for specific applications.

2.6.1 Erbium doped bulk materials and devices

The first successful erbium-doped fiber was developed in late 1980s and has proved to be attractive to an array of applications like broadband optical sources, tunable lasers and optical amplifiers [2.27]. The first successful erbium doped amplifier (EDFA) which influenced the optical communication industry was designed in the early 1990s. This is because the spectral region of maximum transparency and minimum dispersion coincides with the same window of radiative transition ($^4I_{13/2} \rightarrow {}^4I_{15/2}$) wavelength of erbium. With EDFAs, the signal in an optical network are able to travel over long distances directly in the optical domain [2.53]. With the success of the optical fiber amplifier, the erbim-doped fiber lasers have shown tremendous progress in recent years due to the good beam quality, wide tunable wavelength and lower cost [2.54]. As photoluminescence of the rare-earth ion in a host glass is a precursor to both amplification and lasing, research efforts in this direction will be examined next.

An important property for amplication is the concentration of the active ion. The maximum gain achievable is closely tied to the product of the emission cross section(σ_{em}) and the active Er^{3+} concentration. Typical values for σ_{em} are $10^{-21} - 10^{-20} cm^2$ and for concentrations are 10^{19} - 10^{20} cm^{-3} [2.55]. Silica glass is the most widely explored hosts for the erbium ion as the composition lends itself to continuous tuning and the addition of network modifiers. The spectral properties of different host glasses with Er^{3+} are presented and discussed.

Detailed study of Er^{3+} green luminescence arising from energy-transfer processes was

carried out in crystals [2.56]. The quadratic concentration dependence of the decay from the thermal levels ($^4S_{3/2}$, $^2H_{11/2}$) was due to three-ion processes originating from $^4S_{3/2}$, $^2H_{11/2}$, $^4I_{15/2}$ and terminating on the ground state $^4I_{15/2}$, $^4I_{13/2}$ and $^4I_{11/2}$ respectively. Some other authors have also reported green up-conversion and up-conversion lasing in other crystals like $LiYF_4$ [2.57,2.58], $GdAlO_3$ [2.59] and $kGd(WO_4)_2$ [2.60]. Luminescence tuning has been studied in nanocrystalline erbium doped zirconium oxide. The authors observed green(545nm) and red(680 nm) emission bands with 489 nm and 962 nm excitation [2.61]. The red band was however nearly quenched at 489 nm as opposed to the observation at 962 nm, an indication of strength of the underlying cross-relaxation process.

Erbium ions have also been successfully doped into chalcogenide glasses As_2S_3 and $As_{24}S_{38}Se_{38}$, producing strong emissions at 1.54 μm [2.62]. The authors [2.62] noted that high refractive index of the host glass led to cross sections which are two times higher than the doped silica counterpart. The difference in the lifetime properties (2.3 ms as against 10 ms at $^4I_{13/2}$) and (0.25 ms at $^4I_{11/2}$) makes it possible to engineer this glass composition for applications in the field of integrated optics. Another low phonon energy (≈ 370 cm^{-1}) glass composition Er^{3+} : $Ga_{10}Ge_{25}S_{65}$ with wide transparency window from the infrared to the blue/green region was investigated for stokes and anti-stokes luminescence [2.30]. The pulsed excitation wavelengths of 980 nm and 532 nm used [2.30] were similar to those of CW excitation by other authors [2.61]. Though the energy pathways suggested were different from those earlier suggested [2.61], the variations between red and green luminescence intensity for the excitation wavelengths are similar.

The ceramic glasses of Al_2O_3 and Y_2O_3 have high refractive index and also show similar crystal structure to the Er_2O_3 (source of Er^{3+} ions) and therefore a high solubility of Er^{3+} ions. The smallest amplifier with a glass hosts was made using Al_2O_3 channel waveguide with pump operation 10 mW and a gain of 2.3 dB [2.63]. The gain limiting factor was found to be cooperative upconversion between $^4I_{13/2}$ and $^4I_{11/2}$ of the orders of $10^{-15}cm^3/s$. Another author [2.64] also demonstrated efficient dopant distribution from erbium-doped Al_2O_3 thin films. Very intense photoluminescence was measured at 1.5

μm and a lifetime of 4.4ms The addition of Al_2O_3 was observed to alter the thermal and structural properties of erbium doped glasses [2.65]. The authors [2.65] noted that concentrations greater than 10 mol% of Al_2O_3 increased the compactness of the glass. These findings have been confirmed by other authors [2.66] who also observed that the increase in concentration of Al_2O_3 up to 6.0 mol% in a Tm^{3+} and Er^{3+} codoped calcium fluoro phosphorous silicate glass system led to considerable increase in the intensity of the emission bands.

In a study involving both theoretical and experimental investigation of erbium doped heavy-metal fluoride glass [2.67], the authors noted that energy-transfer rates and concentrations can be tuned for efficient optical system. In fact, the system which had a combination of Er^{3+} and Tm^{3+} showed potential to improve lasing transition at 2.7 μm between $^4I_{11/2}$ and $^4I_{13/2}$ provided a fast channel is created to drain $^4I_{13/2}$. This fast channel has been exploited by processes of energy transfer upconversions, cross-relaxations or cascade lasing schemes to prevent self-termination of the lasing level. The luminescence properties of YLF crystal doped with 15 mol % of Er^{3+} showed great potential for efficient generation of radiation near 2.75 μm [2.68]. With a primary excitation of the $^4I_{11/2}$ by cw pump at 972nm, the pathways of energy-transfer processes originating from a $^4I_{13/2}$ and $^4I_{11/2}$ were found to be enough to create the possibility of laser action at the CW regime [2.68]. The gain profile is however confined to concentrations between 9 and 15 mol % with a pump rate of 300 s^{-1} [2.68].

Compared to some of the glasses previously discussed, heavy metal oxide glasses and tellurite glasses have potential to be better hosts because of their resistance to devitrification, and a characteristic high refractive index [2.69]. As a result of this Er^{3+} doped $Na_2O-Nb_2O_5-TeO_2$(NNT) glasses was fabricated and characterized by a group at the University of Arizona [2.69]. They observed intense green upconversion luminescence under 975 nm diode laser and 798nm laser excitation. The maximum emission cross section is $1.02 \times 10^{-20} cm^2$ at 1.533 μm (30% more than those of silicate and phosphate glasses) [2.69]. Similar to the findings from the studies that used 489nm [2.61] and 532nm [2.30] excitation, weak red upconversion luminescence was observed under 798nm excitation in

their experiment [2.30]. This is because of the wide gap between the $^4S_{3/2}$ and $^4F_{9/2}$ levels which potentially reduces the number of ions that relaxes to $^4F_{9/2}$ by multiphonon emission. Other energy pathway processes were also not efficient in promoting/relaxing ions to the $^4F_{9/2}$ energy level. The stability of the glass [2.69] especially with the addition of Na_2O makes the glasses suitable for the fabrication of optical waveguide devices by ion-exchanged process. Another waveguide amplifier was fabricated using ion-exchanged Er^{3+} and Yb^{3+} processes [2.70]. The efficiency of the energy transfer processes between Yb^{3+} and Er^{3+} helped to realise a low cost and high performing integrated amplifier.

The intense and broad green upconversion fluorescence of the doped glasses discussed previously can be used in colour display, infrared sensor and underwater communication. Despite extensive study of the green luminescence of erbium in different glass hosts, there are varying opinions in literature on the actual pathways responsible for the measurement observed. An attempt was made in Er^{3+} doped ZBAN(ZrF_4-BaF_2-AlF-NaF) glasses over a wide range of Er^{3+} concentrations(0.2 - 18 mol%) using 2 pulsed excitations at 800 nm and 520 nm [2.71] . The predictions of the model developed however led to the identification of both two and three-ion interactions which like previous authors [2.56], complicates the analysis further. From the works reviewed, it can be concluded that tuning the concentration of the rare-earth ion with respect to the host glass material property is responsible for the intensity of the emissions under different excitation conditions. The phonon energy of the glass hosts also influences the radiative quantum efficiency of the emissions. This has been tabulated in a previous work on Er^{3+} in various glasses [2.72], where lifetimes values between 2.59 ms (Zinc Tellurite) and 14.10 ms (B-Ge-Na, Silicate) were recorded. This is particularly evident when we compare the properties of high phonon energy glasses(silica) to low phonon energy glasses(heavy-flouride and chalcogenide glasses). A selected summary of emissions at wavelength from visible to mid-infrared is shown in Table 2.3. The table includes the host glass composition, pump wavelength, emission transitions and applications.

Host glass composition	Conc $\times 10^{26}$ ions/m^3	Pumpλ(nm)	Emissionλ(nm)	Application	Reference
Er^{3+}/Yb^{3+}: Phosphate	$N_{Er} = 2.6$, $N_{Yb} = 12$	980	1535	Compact fiber amplifier	[2.73]
Er^{3+}/Ce^{3+}: Telluride	N_{Er} =0.81125 , N_{Ce}= 1.8225	980	1550	Fiber amplifier	[2.74]
Er^{3+}:19ZnO-80TeO$_2$-Er_2O_3	-	632.8	1535	Fibre and waveguide	[2.75]
Er^{3+}/Yb^{3+}: Phosphate, Silicate	1.2 - 4.2	980	1535	Waveguide amplifier	[2.70]
Er^{3+}: ZBLAN	0.16 (1000 ppm)	987.33	3000	Double clad fiber laser	[2.58]
Er^{3+}: ZBLAN	-	980	546	EDFA	[2.76]
Er^{3+}:Na$_2$O-Nb$_2$O$_5$-TeO$_2$	1.57	975, 798	1530, 546	Waveguide device	[2.77]
$Er^{3+} : CaZrO_3/CaSZ$	1, 2 mol %	787, 800	500 - 700	Bulk glass	[2.78]
Er^{3+}/Yb^{3+}: Borate-Silicate	N_{Er} =0.5mol% , N_{Yb}=0-6mol%	980	1400 - 1700	Bulk glass	[2.79]
Er^{3+}: $Ga_{10}Ge_{25}S_{65}$	-	980, 532	488, 1530	Bulk glass	[2.30]

2.6.2 Praseodymium doped bulk materials and devices

Praseodymium is considered as one of the richest sources of near-infrared to long wavelength rare-earth ions. Its energy spectrum contains an exceptional large number of metastable multiplets from which laser action has been demonstrated from visible to near infra-red [2.80]. In this section, the historical progress and the properties of praseodymium in different glass hosts are briefly described. Some of the advances towards the realisation of efficient mid-infrared sources are addressed. Finally, constraints on the existing state of the art are analyzed and discussed. Praseoydmium is showing promise of generating long wavelength photoluminescence and ultimately lasing in the $4.4 - 7.5$ μm window.

One of the earliest research using praseodymium is the coherent emission of strong infrared fluorescence at 1.047 μm in calcium tungstate [2.81]. Since then, stimulated emission and laser action of Pr^{3+} has been studied in a variety of glass hosts like Pr^{3+}:$YA1O_3$ [2.82] where laser transition at 746.9 nm with a maximum slope efficiency of 24.6%, a maximum output power of 49.6 mW, and a laser threshold of 25 mW was recorded. The lasing and amplification characteristics of praseodymium doped silica based fibers have been studied previously [2.83]. However, compared to Er^{3+}, Yb^{3+} and Tm^{3+} doped silica fibers, Pr^{3+} have so far been less efficient [2.83]. Laser action was achieved at both 1080 nm (2 %) and 888 nm (0.7 %) with 488 nm and 590 nm pumping [2.83]. In the second telecoms window(1300 nm), a gain of 10.5 dB was achieved in a Pr^{3+}-doped single-mode fluorozirconate fibre [2.84]. The authors noted that with a composition of 560 ppmW, Pr^{3+} and pump wavelength of 1.007 μm, there was a linear relationship between the gain and launched pump power with a slope efficiency of 0.019 dB/mW [2.84]. In 1992, a glass composition which had been known for several decades (Gallium Lanthanum Sulphide) was studied as a host material for praseodymium to investigate its potential for 1.3 μm fiber amplification [2.85]. Compared to previous authors [2.84], a yield of 30dB at 1.3 μm was measured [2.85].

The size of the energy gap of the metastable states in Pr^{3+} impacts the quantum efficiency of the radiative transitions. The rapid multiphonon transitions present in glass

hosts like silica and fluoride glass competes with the spontaneous emission processes thereby reducing photoluminescence. Because of this, intense research effort is drawn towards engineering low phonon glasses for realisation of the full potential of the Pr^{3+} interband transitions especially in the MidIR ($^3H_5 \rightarrow {}^3H_4$, $^3F_2$ / $^3H_6 \rightarrow {}^3H_5$). One of the earlier works in this direction was the fabrication of a 1.3 μm fiber amplifier using an Arsenic-Sulphide chalcogenide glass host [2.86]. As at the time of the publication, As-S chalcogenide glass was the most thermally stable Pr^{3+} doped chalcogenide glass reported. With a doping concentration of 500ppm, a gain coefficient of $1.05 \times 10^{-20} cm^2$ was predicted. The peak wavelength at 1340 nm was close to those of La-Ga-S and Ge-Ga-S glass systems [2.86] which also exhibit good RE solubility but a strong tendency to crystallize. In 1996, a group of authors [2.87] reported a Pr-doped Ga-La-S multi-mode fiber which had an attenuation loss of 5 dB/m. However, the research did not demonstrate any amplification characteristics in those glasses. A few years earlier, Ga-Na-S(GNS) was reported to be thermally stable and allowed the incorporation of a high concentration of rare-earth ions [2.88]. Following the published results [2.88], optical amplification with a gain coefficient of 0.81 dB/mW was then reported at 1.31 μm in a Ga-Na-S(GNS) system [Hiromasa,2000]. This was the highest gain coefficient with a net gain of 32dB for a pump power of 90mW in a single-mode chalcogenide fiber. Another study however reported that florescence quenching was the main problem in designing an efficient Pr^{3+} doped amplifier at 1.3 μm [2.89]. The results showed that Pr^{3+} doping levels below 800 ppm are insignificant, while the optimum doping level in a practical device is $\approx$ 1000 ppm [2.89]. To extend the wavelength further to a region (1610 $-$ 1650 nm) where the existing erbium-doped fiber amplifiers cannot provide an optical gain, the sensitizing effect of Er^{3+} was adopted [2.90]. The authors significantly enhanced the emission intensity by adopting a non-radiative energy transfer, Er^{3+} :$^4I_{13/2} \rightarrow Pr^{3+}$: ($^3F_3, ^3F_4$). The moderate lifetime measured ($\approx 215 \pm 5$ μs) and the high stimulated emission cross section ($\approx 3 \pm 1$) x $10^{-20} cm^2$ made the glass a suitable candidate for 1.6 μm band fiber-optic amplifier [2.90]. Another related work utilised the same energy transfer process between Er^{3+} and Pr^{3+} in chalcogenide glasses for dual-wavelength fiber-optic amplifiers [2.91]. Ge-As-Ga-S glass

was codoped with Er^{3+} and Pr^{3+} and synthesized for fiber-optic amplification in the 1.3 μm and 1.5 μm telecommunication windows. The energy transfer Er^{3+} :$^4I_{11/2} \rightarrow$ Pr^{3+}:$^1G_4$ enhanced the efficiency of 1.3 μm while Er^{3+} :$^4I_{13/2} \rightarrow Pr^{3+}$:$^3F_{4,3}$ enhanced the 1.5 μm band producing signal gains of 30 and 40 dB respectively [2.91].

The spectroscopic properties of chalcogenide has been widely reviewed in literature [2.24,2.25] and substituting with different network formers, sulphides, selenides and tellurides, the transmission wavelengths of Pr^{3+} in chalcogenide glasses can be extended into the far-IR. The $3 - 25$ μm region of interest covers the absorption bands of a few liquids, solids and gases. Also, hyride and hydroxide impurities absorb in the mid-IR, a region dominated by weak absorption tail and extrinsic absorption [2.24]. The longer wavelengths $(8 - 12$ μm) also experience oxide contamination problem [2.92] which limits the transmission wavelengths to $\approx 6\mu$m [2.93]. Recent research effort is therefore focused on producing low-phonon, high purity glasses for transmission in the mid-IR. Shaw et al. [2.41] demonstrated MIR fluorescence up to 5.5 μm in 0.2wt % Pr^{3+} doped Ba-In-Ge-Ga-Se bulk glass samples pumped at 1.064 μm with a continuous wave (CW) Nd: YAG laser. In the 3.4-5.5 range, Park et al [2.94], measured broad MIR fluorescence for a series of Pr^{3+} doped GeGaSbSe bulk glasses and in 0.02 mol %, Pr^{3+}-doped GeGaSbSe fiber. Similarly the work of Charpentier et al [2.95] reported broad MIR spectra spanning $3.5 - 5.5$ wavelength in $Ga_5Ge_{20}Sb_{10}Se_{65}$ fiber doped with 500 ppmW and 1000 ppmw Pr^{3+} ions and pumped with a homemade Tm:YAG laser. The PL behaviour measured by all these authors [2.41,2.94,2.95] was based on glasses with gallium added to the glass network. The addition of gallium was motivated by the findings of Aitken et al. [Aitken, 1999] who found that Ga co-doping improved the solubility of the RE ion. New direction is steering towards replacing Gallium with other similar elements especially those in the same group on the periodic table. One of the most successful attempt was replacing Gallium with Indium , with superior photoluminescence measured in the former compared to the latter [2.48,2.96,2.97]. in both bulk and fiber glass. Table 2.4 summarises some of the advances made with emission wavelengths beyond 3.5 μm.

Table 2.4: Characteristics of Pr^{3+} doped chalcogenide glasses with emission beyond 3.5 μm

Dopant	Host glass	Pump wavelength λ (μm)	Emission λ (μm)	Transition	Reference
Pr^{3+}	$Ga_5Ge_{25}Sb_{10}Se_{60}$	2.0	4.8	$^3H_6$ $^3H_5+$ $^3H_5$ $^3H_4$	[2.98]
Pr^{3+}	$Ge_{30}Ga_2As_6S_{62}$	1.1	4.7	$^3H_5 \rightarrow {}^3H_4$	[2.42]
Pr^{3+}	$Ge_{28}Ga_5As_{12}S5_5$	1.1	4.7	$^3H_5 \rightarrow {}^3H_4$	[2.42]
Pr^{3+}	GeGaAsSe	2.0	4.8	$^3H_5 \rightarrow {}^3H_4$	[2.50]
Pr^{3+}	GeGaAsSe	2.0	4.0	$^3H_6 \rightarrow {}^3H_5$	[2.50]
Pr^{3+}	$Ga_5Ge_{20}Sb_{10}S_{65}$	2.0	4.8	$^3H_6 \rightarrow {}^3H_5+{}^3H_5 \rightarrow {}^3H_4$	[2.95]
Pr^{3+}	$Ge_{16.5}Ga_{0.5}As_{18.5}S_{64.5}$	1.55	4.8	$^3H_6 \rightarrow {}^3H_5+{}^3H_5 \rightarrow {}^3H_4$	[2.99]
Pr^{3+}	GeAsGaSe	1.55	4.8	$^3H_6 \rightarrow {}^3H_5+{}^3H_5 \rightarrow {}^3H_4$	[2.40]
Pr^{3+}	GeAsGaSe	1.55/1.94	4.8	$^3H_6 \rightarrow {}^3H_5+{}^3H_5 \rightarrow {}^3H_4$	[2.40]
Pr^{3+}	$Ge_{30}Ga_2Sb_8Se_{60}$	1.48/2.05	4.8	$^3H_6 \rightarrow {}^3H_5+{}^3H_5 \rightarrow {}^3H_4$	[2.94]

2.7   Summary

This section reviewed the characteristics of erbium and praseodymium as optically active ions in glass hosts. The energy levels and corresponding transitions of each of the ions were discussed for applications from visible to mid-IR. A few applications were discussed, which were limited by the maximum phonon energies of the glass hosts and the transition energies of the doping ion. The review shows that the transitions in erbium ion finds applications in high-phonon (> 500 cm^{-1}) glasses while praseodymium ion is best suited for low-phonon (< 500 cm^{-1}) glasses. Rapid research into new materials can be limited by available experimental techniques or resources. Chapter 3, covers some of the experimental procedures to prepare and characterise erbium and praseodymium doped glasses. The techniques will also highlight how the host materials are varied to tune the phonon-energies for specific applications.

References

[2.1] Webelements, "Periodic Table of the Elements by WebElements," 2014.

[2.2] E. U. Condon and G. H. Shortley, *The Theory of Atomic Spectra*. Cambridge Univ.Pr.209, Cambridge University Press, 1951.

[2.3] R. C. Hilborn, "Einstein coefficients, cross sections, f values, dipole moments, and all that," *American Journal of Physics*, vol. 50, no. 11, pp. 982–986, 1982.

[2.4] J. Wang, R. Deng, M. A. MacDonald, B. Chen, J. Yuan, F. Wang, D. Chi, T. S. A. Hor, P. Zhang, G. Liu, *et al.*, "Enhancing multiphoton upconversion through energy clustering at sublattice level," *Nature materials*, vol. 13, no. 2, pp. 157–162, 2014.

[2.5] O. Malta, "Mechanisms of non-radiative energy transfer involving lanthanide ions revisited," *Journal of non-crystalline solids*, vol. 354, no. 42, pp. 4770–4776, 2008.

[2.6] M. L. Debasu, D. Ananias, J. Rocha, O. L. Malta, and L. D. Carlos, "Energy-transfer from Gd^{3+} to Tb^{3+} in (Gd, Yb, Tb) PO 4 nanocrystals," *Physical Chemistry Chemical Physics*, vol. 15, no. 37, pp. 15565–15571, 2013.

[2.7] J. Vega-Durán, L. Diaz-Torres, M. Meneses-Nava, J. Maldonado-Rivera, and O. Barbosa-Garcia, "Optimal co-doping concentrations and dynamics of energy transfer processes for Tm^{3+}-Tb^{3+} and Tm^{3+}-Eu^{3+} in $LiYF_4$ crystal hosts," *Journal of Physics D: Applied Physics*, vol. 34, no. 21, p. 3203, 2001.

[2.8] L. A. Diaz-Torres, O. Barbosa-Garcia, C. W. Struck, and R. A. McFarlane, "Analysis of experimental Nd^{3+} emission transients with fast sub-microsecond decay component and a subsequent non-exponential long-term decay with Monte-Carlo simulations," *Journal of Luminescence*, vol. 78, no. 1, pp. 69 – 86, 1998.

[2.9] L. Diaz-Torres, O. Meza, D. Solis, P. Salas, and E. D. la Rosa, "Visible upconversion emission and non-radiative direct Yb^{3+} to Er^{3+} energy transfer processes in nanocrystalline ZrO_2:Yb^{3+},Er^{3+}," *Optics and Lasers in Engineering*, vol. 49, no. 6, pp. 703 – 708, 2011. Research in Optics and Photonics at CIO, Mexico.

[2.10] F. Auzel, "Upconversion and Anti-Stokes Processes with f and d Ions in Solids," *Chem. Rev.*, vol. 104, no. 1, pp. 139–174, 2004. PMID: 14719973.

[2.11] Y. G. Choi, K. H. Kim, S. H. Park, and J. Heo, "Comparative study of energy transfers from Er^{3+} to Ce^{3+} in tellurite and sulfide glasses under 980 nm excitation," *Journal of Applied Physics*, vol. 88, no. 7, pp. 3832–3839, 2000.

[2.12] Y. Tsang, B. Richards, D. Binks, J. Lousteau, and A. Jha, "Tm^{3+} / Ho^{3+} codoped tellurite fiber laser," *Optics letters*, vol. 33, no. 11, pp. 1282–1284, 2008.

[2.13] F. Auzel, "Compteur quantique par transfert d'energie entre deux ions de terres reres dans un tungstate mixte et dans un verre," *C. R. Acad. Sci. Paris B*, vol. 262, pp. 1016–1019, 1966.

[2.14] F. Auzel, "Compteur quantique par transfert d'energie entre de Yb^{3+} a Tm^{3+} dans un tungstate mixte et dans verre germanate," *C. R. Acad. Sci. Paris B*, vol. 263, pp. 819–821, 1966.

[2.15] V. V. Ovsyankin and P. P. Feofilov, "Mechanism of summation of electronic excitations in activated crystals," *JETP Lett*, vol. 3, pp. 322–323, 1966.

[2.16] A. Silversmith, W. Lenth, and R. Macfarlane, "Green infrared-pumped erbium upconversion laser," *Applied Physics Letters*, vol. 51, no. 24, pp. 1977–1979, 1987.

[2.17] R. Paschotta, P. R. Barber, A. C. Tropper, and D. C. Hanna, "Characterization and modeling of thulium:ZBLAN blue upconversion fiber lasers," *Journal of the Optical Society of America B*, vol. 14, pp. 1213–1218, May 1997.

[2.18] M. Pollnau, "Analysis of heat generation and thermal lensing in erbium 3 μm lasers," *IEEE Journal of Quantum Electronics*, vol. 39, pp. 350–357, 2003.

[2.19] O. Hadeler, *Distributed feedback fibre laser strain and temperature sensors.* PhD thesis, University of Southampton, 2002.

[2.20] H. Ebendorff-Heidepriem and D. Ehrt, "Optical spectroscopy of rare earth ions in glasses," *Glass Science and Technology-Glastechnische Berichte*, vol. 71, no. 10, pp. 289–299, 1998.

[2.21] R. Caspary, *Applied Rare Earth Spectroscopy for Fiber Laser Optimization.* Berichte Aus der Lasertechnik Series, Shaker Verlag GmbH, 2002.

[2.22] P. Jander, *An Investigation of Novel Materials for Active Optical Devices.* Phd thesis, University of Southampton, 2002.

[2.23] A. B. Seddon, "A Prospective for New Mid-Infrared Medical Endoscopy Using Chalcogenide Glasses," *International Journal of Applied Glass Science*, vol. 2, pp. 177–191, Sept. 2011.

[2.24] A. Seddon, "Chalcogenide glasses: a review of their preparation, properties and applications," *Journal of Non-Crystalline Solids*, vol. 184, pp. 44–50, 1995.

[2.25] A. Zakery and S. R. Elliott, "Optical properties and applications of chalcogenide glasses: a review," *Journal of Non-Crystalline Solids*, vol. 330, no. 1, pp. 1–12, 2003.

[2.26] D. Atwood, *The Rare Earth Elements: Fundamentals and Applications.* EIC Books, Wiley, 2013.

[2.27] P. C. Becker, J. R. Simpson, and N. Olsson, *Erbim-doped fiber amplifiers fundamentals and technology.* San Diego: Academic Press., 1999.

[2.28] M. Pollnau, C. Ghisler, W. Lüthy, H. Weber, J. Schneider, and U. Unrau, "Three-transition cascade erbium laser at 1.7, 2.7, and 1.6 μm," *Optics letters*, vol. 22, no. 9, pp. 612–614, 1997.

[2.29] Y. Li, L. Liu, Z. He, H. Tang, S. Xiao, L. Xu, and W. Wang, "Improvement of fluorescence lifetime from Er^{3+}-doped sol-gel silica glass by dehydration in CCl_4," *Journal of sol-gel science and technology*, vol. 30, no. 1, pp. 29–33, 2004.

[2.30] M. L. Frej, E. Valdez, C. B. de Araujo, Y. Ledemi, and Y. Messaddeq, "Stokes and anti-Stokes luminescence of Er^{3+}doped $Ga_{10}Ge_{25}S_{65}$ glass excited at 980 and 532 nm," *Journal of Applied Physics*, vol. 108, no. 9, p. 093514, 2010.

[2.31] A. Cherif, A. Kanoun, and N. Jaba, "Red up-conversion dynamics in Er^{3+}-doped $Te_2 - ZnO$ glasses," *Optica Applicata*, vol. 40, no. 1, 2010.

[2.32] J. M. Ward, D. G. OShea, B. J. Shortt, and S. N. Chormaic, "Optical bistability in Er-Yb codoped phosphate glass microspheres at room temperature," *Journal of Applied Physics*, vol. 102, no. 2, p. 023104, 2007.

[2.33] K. Kadono, T. Yazawa, S. Jiang, J. Porque, B.-C. Hwang, and N. Peyghambarian, "Rate equation analysis and energy transfer of Er^{3+}-doped $Ga_2S_3 - GeS_2 - La_2S_3$ glasses," *Journal of Non-Crystalline Solids*, vol. 331, pp. 79–90, Dec. 2003.

[2.34] F. Vetrone, J.-C. Boyer, J. a. Capobianco, A. Speghini, and M. Bettinelli, "980 nm excited upconversion in an Er-doped $ZnO - TeO_2$ glass," *Applied Physics Letters*, vol. 80, no. 10, p. 1752, 2002.

[2.35] Z. . A. Pan, a. Ueda, R. Mu, and S. H. Morgan, "Upconversion luminescence in Er^{3+}-doped germanate-oxyfluoride and tellurium-germanate-oxyfluoride transparent glass-ceramics," *Journal of Luminescence*, vol. 126, pp. 251–256, Sept. 2007.

[2.36] L. Li, Z. Zhou, H. Tian, D. Gong, Z. Yang, and Y. Yang, "Spectroscopic and upconversion properties of erbium-doped potassium lithium tantalate niobate crystals under 800 nm femtosecond laser excitation," *Journal of Applied Physics*, vol. 108, no. 4, p. 043520, 2010.

[2.37] S. Xiao, X. Yang, Z. Liu, and X. H. Yan, "Up-conversion in Er^{3+}:Y_2O_3 Nanocrystals Pumped at 808nm," *Journal of Applied Physics*, vol. 96, no. 3, p. 1360, 2004.

[2.38] J. T. Seo, A. J. Steckl, and B. R. Birkhahn, "Green Luminescence and Excited State Thermalization in Er-Doped Gallium Nitride," *Journal of the Korean Physical Society*, vol. 49, no. 3, pp. 943–946, 2006.

[2.39] C. Da Silva, M. De Araujo, E. Gouveia, and A. Gouveia-Neto, "Thermal effect on multiphonon-assisted anti-Stokes excited upconversion fluorescence emission in Yb^{3+}-sensitized Er^{3+}-doped optical fiber," *Applied Physics B*, vol. 70, no. 2, pp. 185–188, 2000.

[2.40] L. Sójka, Z. Tang, D. Furniss, H. Sakr, A. Oladeji, E. Bereś-Pawlik, H. Dantanarayana, E. Faber, A. Seddon, T. Benson, and S. Sujecki, "Broadband, mid-infrared emission from Pr^{3+}doped GeAsGaSe chalcogenide fiber, optically clad," *Optical Materials*, vol. 36, pp. 1076–1082, Apr. 2014.

[2.41] L. Shaw, B. Harbison, B. Cole, J. Sanghera, and I. Aggarwal, "Spectroscopy of the IR transitions in Pr^{3+}doped heavy metal selenide glasses.," *Optics express*, vol. 1, pp. 87–96, Aug. 1997.

[2.42] Y. S. Han and J. Heo, "Midinfrared emission properties of Pr^{3+}-doped chalcogenide glasses at cryogenic temperature," *Journal of Applied Physics*, vol. 93, no. 11, pp. 8970–8974, 2003.

[2.43] C. Berkdemir and S. Ozsoy, "Modelling consideration of praseodymium-doped fiber amplifiers for 1.3 μm wavelength applications ," *Optics Communications*, vol. 26, no. 1, pp. 102 – 106, 2007.

[2.44] V. Morin and E. Taufflieb, "High output-power praseodymium-doped fiber amplifier single-pumped at 1030 nm: analysis and results," *Selected Topics in Quantum Electronics, IEEE Journal of*, vol. 3, no. 4, pp. 1112–1118, 1997.

[2.45] T. Schweizer, *Rare-Earth-Doped Gallium Lanthanum Sulphide Glasses for Mid-Infrared Fibre Lasers*. PhD thesis, Optoelectronics Research Centre, University of Southampton and Institut fur Laser-Physik, Universitat Hamburg, 1998.

[2.46] Z. Tang, N. C. Neate, D. Furniss, S. Sujecki, T. M. Benson, and A. B. Seddon, "Crystallization behavior of Dy^{3+}-doped selenide glasses," in *Journal of Non-Crystalline Solids*, vol. 357, pp. 2453–2462, 2011.

[2.47] A. B. Seddon, "Mid-infrared (IR)–A hot topic: The potential for using mid-IR light for non-invasive early detection of skin cancer in vivo," *Physica Status Solidi (b)*, vol. 250, no. 5, pp. 1020–1027, 2013.

[2.48] H. Sakr, D. Furniss, Z. Tang, L. Sojka, N. A. Moneim, E. Barney, S. Sujecki, T. M. Benson, and A. B. Seddon, "Superior photoluminescence (PL) of Pr^{3+}-In, compared to Pr^{3+}-Ga, selenide-chalcogenide bulk glasses and PL of optically-clad fiber," *Opt. Express*, vol. 22, pp. 21236–21252, Sep 2014.

[2.49] J. Sanghera and I. Aggarwal, "Active and passive chalcogenide glass optical fibers for IR applications: a review," *Journal of non-crystalline solids*, vol. 256, pp. 6–16, 1999.

[2.50] L. Shaw, B. Cole, P. Thielen, J. Sanghera, and I. Aggarwal, "Mid-wave IR and long-wave IR laser potential of rare-earth doped chalcogenide glass fiber," *IEEE Journal of Quantum Electronics*, vol. 37, no. 9, pp. 1127–1137, 2001.

[2.51] R. Reisfeld, "Glass lasers and solar applications," *Ettore Majorana Int Sci Ser Phys Sci*, vol. 30, pp. 343–396, 1987.

[2.52] Y. G. Choi, B. J. Park, K. H. Kim, and J. Heo, "Cross relaxations between and multiphonon relaxation of near-infrared excited states of Pr^{3+} ions in selenide glasses," *Chemical physics letters*, vol. 368, no. 5, pp. 625–629, 2003.

[2.53] R. Mears, L. Reekie, S. Poole, and D. Payne, "Low-threshold tunable CW and Q-switched fibre laser operating at 1.55 μm ," *Electronics Letters*, vol. 22, pp. 159–160, January 1986.

[2.54] M. Melo, O. Frazao, A. Teixeira, L. Gomes, J. F. Da Rocha, and H. Salgado, "Tunable l-band erbium-doped fibre ring laser by means of induced cavity loss using a fibre taper," *Applied Physics B*, vol. 77, no. 1, pp. 139–142, 2003.

[2.55] P. Kik and A. Polman, "Erbium-doped optical-waveguide amplifiers on silicon," *MRS bulletin*, vol. 23, no. 04, pp. 48–54, 1998.

[2.56] I. Ursu, A. Lupei, S. Georgescu, V. Lupei, A. Prokhorov, V. Zhekov, T. Murina, and M. Studenikin, "Energy transfer characteristics of the $^4S_{3/2}$ level of Er^{3+} in Yag," *Optics Communications*, vol. 72, no. 3-4, pp. 209 – 213, 1989.

[2.57] F. Tong, W. Risk, R. Macfarlane, and W. Lenth, "551 nm diode-laser-pumped upconversion laser," *Electronics Letters*, vol. 25, pp. 1389–1391, Sept 1989.

[2.58] M. Pollnau, W. Luthy, and H. P. Weber, "Population mechanisms of the green Er^{3+}:$LiYF_4$ laser," *Journal of Applied Physics*, vol. 77, no. 12, pp. 6128–6134, 1995.

[2.59] A. Brenier, A. Jurdyc, H. Verweij, M. Cohen-Adad, and G. Boulon, "Up-conversion dynamics in $GdAlO_3$:Er^{3+} single crystal fibre," *Optical Materials*, vol. 5, no. 4, pp. 233 – 238, 1996.

[2.60] M. Rico, M. Pujol, F. Daz, and C. Zaldo, "Green up-conversion of Er^{3+} in $KGd(WO_4)_2$ crystals. Effects of sample orientation and erbium concentration," *Applied Physics B*, vol. 72, no. 2, pp. 157–162, 2001.

[2.61] E. De la Rosa-Cruz, L. Dıaz-Torres, R. Rodrıguez-Rojas, M. Meneses-Nava, O. Barbosa-Garcıa, and P. Salas, "Luminescence and visible upconversion in nanocrystalline zro2: Er3+," *Applied physics letters*, vol. 83, no. 24, pp. 4903–4905, 2003.

[2.62] J. Fick, E. Knystautas, A. Villeneuve, F. Schiettekatte, S. Roorda, and K. Richardson, "High photoluminescence in erbium-doped chalcogenide thin films," *Journal of non-crystalline solids*, vol. 272, no. 2, pp. 200–208, 2000.

[2.63] A. Polman, "Exciting erbium-doped planar optical amplifier materials," in *Symposium on Integrated Optoelectronics*, pp. 2–13, International Society for Optics and Photonics, 2000.

[2.64] R. Serna and C. N. Afonso, "In situ growth of optically active erbium doped Al_2O_3 thin films by pulsed laser deposition," *Applied physics letters*, vol. 69, no. 11, pp. 1541–1543, 1996.

[2.65] A. B. Corradi, V. Cannillo, M. Montorsi, and C. Siligardi, "Influence of Al_2O_3 addition on thermal and structural properties of erbium doped glasses," *Journal of materials science*, vol. 41, no. 10, pp. 2811–2819, 2006.

[2.66] Y. Gandhi, M. R. Rao, C. S. Rao, I. Kityk, and N. Veeraiah, "Role of Al_2O_3 in upconversion and NIR emission in Tm^{3+} and Er^{3+} codoped calcium fluoro phosphorous silicate glass system," *Journal of Luminescence*, vol. 131, no. 7, pp. 1443–1452, 2011.

[2.67] C. Chen, J. Adam, R. Petrin, D. Yeh, and W. Sibley, "Concentration-dependent energy-transfer processes in Er^{3+}-and Tm^{3+}-doped heavy-metal fluoride glass," *Optics letters*, vol. 14, no. 9, pp. 432–434, 1989.

[2.68] L. Gomes, A. F. H. Librantz, F. H. Jagosich, W. A. L. Alves, I. M. Ranieri, and S. L. Baldochi, "Energy transfer rates and population inversion of $^4I_{11/2}$ excited state of Er^{3+} investigated by means of numerical solutions of the rate equations system in Er:$LiYF_4$ crystal," *Journal of Applied Physics*, vol. 106, no. 10, pp. –, 2009.

[2.69] H. Lin, S. Jiang, J. Wu, F. Song, N. Peyghambarian, and E. Pun, "Er^{3+} doped $Na_2O - Nb_2O_5 - TeO_2$ glasses for optical waveguide laser and amplifier," *Journal of Physics D: Applied Physics*, vol. 36, no. 7, p. 812, 2003.

[2.70] V. Donzella, V. Toccafondo, S. Faralli, F. Di Pasquale, C. Cassagnettes, D. Barbier, and H. H. Figueroa, "Ion-exchanged Er^{3+}/Yb^{3+} co-doped waveguide amplifiers longitudinally pumped by broad area lasers," *Optics express*, vol. 18, no. 12, pp. 12690–12701, 2010.

[2.71] V. Bogdanov, D. Booth, and W. Gibbs, "Energy transfer processes and the green fluorescence in heavily doped Er^{3+}: fluoride glasses," *J. Non-Cryst. Solids*, vol. 321, no. 1, pp. 20–28, 2003.

[2.72] B. Chen, G. Righini, M. Bettinelli, and A. Speghini, "A comparison between different methods of calculating the radiative lifetime of the $^4I_{13/2}$ level of Er^{3+} in various glasses ," *Journal of Non-Crystalline Solids*, vol. 322, no. 1-3, pp. 319 – 323, 2003. Proceedings of the 4th Franco-Italian Symposium on SiO2 and Advanced Dielectrics.

[2.73] Z. Cheng, F. Song, C. Zou, R. Su, X. Yu, W. Zang, J. Tian, and S. Jiang, "Numerical investigation of gain characteristics of Er^{3+}/Yb^{3+} co-doped fiber amplifiers," *Optical and quantum electronics*, vol. 40, no. 13, pp. 1021–1031, 2008.

[2.74] Z. Chen, K. Zhou, and C. Jiang, "Optimization of pump efficiency of $Er^{3+} - Ce^{3+}$ doped telluride fiber amplifier," *Appl. Opt.*, vol. 49, pp. 2845–2849, May 2010.

[2.75] R. Rolli, K. Gatterer, M. Wachtler, M. Bettinelli, A. Speghini, and D. Ajo, "Optical spectroscopy of lanthanide ions in ZnO–TeO_2 glasses," *Spectrochimica Acta Part A: Molecular and Biomolecular Spectroscopy*, vol. 57, no. 10, pp. 2009–2017, 2001.

[2.76] D. Péan, P. Urquhart, and J.-C. Favreau, "Green upconversion erbium-doped fibre amplifiers pumped into $^4I_{11/2}$: a numerical simulation," *Optics communications*, vol. 107, no. 5, pp. 489–498, 1994.

[2.77] H. Lin, S. Jiang, J. Wu, F. Song, N. Peyghambarian, and E. Pun, "Er^{3+} doped Na_2O–Nb_2O_5–TeO_2 glasses for optical waveguide laser and amplifier," *Journal of Physics D: Applied Physics*, vol. 36, no. 7, p. 812, 2003.

[2.78] R. Balda, S. Garca-Revilla, J. Fernndez, V. Seznec, V. Nazabal, X. Zhang, J. Adam, M. Allix, and G. Matzen, "Upconversion luminescence of transparent Er^{3+}-doped chalcohalide glass–ceramics," *Opt. Mater.*, vol. 31, no. 5, pp. 760 – 764, 2009.

[2.79] L. Shan-Feng, M. Zhuang, P. Yang, and Z. Qing-Yu, "Optical properties and cooperative luminescence of Yb-doped borate-silicate glasses," *ACTA PHYSICA SINICA*, vol. 55, no. 8, pp. 4315–4320, 2006.

[2.80] L. Esterowitz, R. Allen, M. Kruer, F. Bartoli, and L. Goldberg, "Blue light emission by a Pr:$LiYF_4$-laser operated at room temperature," tech. rep., DTIC Document, 1977.

[2.81] A. Yariv, S. P. S. Porto, and K. Nassau, "Optical maser emission from trivalent praseodymium in calcium tungstate," *Journal of Applied Physics*, vol. 33, no. 8, pp. 2519–2521, 1962.

[2.82] T. Danger, A. Bleckmann, and G. Huber, "Stimulated emission and laser action of Pr^{3+}-doped $YA1O_3$," *Applied Physics B*, vol. 58, no. 5, pp. 413–420, 1994.

[2.83] P. J. Suni, D. C. Hanna, R. Percival, I. R. Perry, R. G. Smart, J. E. Townsend, and A. C. Tropper, "Lasing characteristics of ytterbium, thulium and other rare-earth doped silica based fibers," in *OE/FIBERS'89*, pp. 244–260, International Society for Optics and Photonics, 1990.

[2.84] S. Carter, D. Szebesta, S. Davey, R. Wyatt, M. Brierley, and P. France, "Amplification at 1.3 μm in a Pr^{3+}-doped single-mode fluorozirconate fibre," *Electronics Letters*, vol. 27, pp. 628–629, April 1991.

[2.85] P. Becker, M. Broer, V. Lambrecht, A. Bruce, and G. Nykolak, "Pr^{3+}:La-Ga-S glass: A promising material for 1.3 μm fibre amplificationc," in *in: Technical Digest of Topical Meeting on Optical Amplifiers and their Applications (Optical Society of America, Washington DC), post-deadline papers PDP5*, 1992.

[2.86] Y. Ohishi, A. Mori, T. Kanamori, K. Fujiura, and S. Sudo, "Fabrication of praseodymium-doped arsenic sulfide chalcogenide fiber for 1.3μm fiber amplifiers," *Applied Physics Letters*, vol. 65, no. 1, pp. 13–15, 1994.

[2.87] D. Hewak, R. Moore, T. Schweizer, J. Wang, B. Samson, W. Brocklesby, D. Payne, and E. Tarbox, "Gallium lanthanum sulphide optical fibre for active and passive applications," *In, 10th International Symposium on Non-Oxide Glasses, Corning, US*, 1996.

[2.88] M. Palazzi, "Study of the system $Ga_2S3 - Na_2S$-existence of a glass-former region," *Comptes Rendus de l'academie des sciences seriee II*, vol. 299, no. 9, pp. 529–532, 1984.

[2.89] M. Naftaly, A. Jha, and W. G. Jordan, "1.3 μm fluorescence quenching in pr-doped glasses," *Journal of Applied Physics*, vol. 84, no. 4, pp. 1800–1804, 1998.

[2.90] Y. G. Choi, K. H. Kim, B. J. Park, and J. Heo, "1.6 μm emission from Pr^{3+}:$(^3F_3, ^3F_4) \rightarrow {}^3H_4$ transition in $Pr^{3+}-$ and Pr^{3+}/Er^{3+}-doped selenide glasses," *Applied Physics Letters*, vol. 78, no. 9, p. 1249, 2001.

[2.91] S. H. Park, D. C. Lee, J. Heo, and D. W. Shin, "Energy transfer between Er^{3+} and Pr^{3+} in chalcogenide glasses for dual-wavelength fiber-optic amplifiers," *Journal of applied physics*, vol. 91, no. 11, pp. 9072–9077, 2002.

[2.92] C. Moynihan, P. Macedo, M. Maklad, R. Mohr, and R. Howard, "Intrinsic and impurity infrared absorption in As_2Se_3 glass," *Journal of Non-Crystalline Solids*, vol. 17, no. 3, pp. 369 – 385, 1975.

[2.93] N. J. Pitt, "Loss mechanisms in chalcogenide glass optical fibres," *Proc. SPIE*, vol. 0799, pp. 25–32, 1987.

[2.94] B. J. Park, H. S. Seo, J. T. Ahn, Y. G. Choi, D. Y. Jeon, and W. J. Chung, "Mid-infrared (3.5 – 5.5 μm) spectroscopic properties of Pr^{3+}-doped Ge–Ga–Sb–Se glasses and optical fibers," *Journal of Luminescence*, vol. 128, pp. 1617–1622, Oct. 2008.

[2.95] F. Charpentier, F. Starecki, J.-L. Doualan, P. Jovari, P. Camy, J. Troles, S. Belin, B. Bureau, and V. Nazabal, "Mid-IR luminescence of Dy^{3+} and Pr^{3+} doped $Ga_5Ge_{20}Sb_{10}S(Se)_{65}$ bulk glasses and fibers," *Materials Letters*, vol. 101, pp. 21–24, 2013.

[2.96] H. Sakr, Z. Tang, D. Furniss, L. Sojka, N. Moneim, E. Barney, S. Sujecki, T. Benson, and A. Seddon, "Towards mid-infrared fiber-lasers: rare earth ion doped, indium-containing, selenide bulk glasses and fiber," in *SPIE BiOS*, pp. 89380V–89380V, International Society for Optics and Photonics, 2014.

[2.97] D. Furniss, H. Sakr, Z. Tang, L. Sojka, S. Sujecki, E. Barney, T. Benson, and A. Seddon, "Development of praseodymium-doped, selenide chalcogenide glass, step-index fibre towards mid-infrared fibre lasers," in *Transparent Optical Networks (ICTON), 2014 16th International Conference on*, pp. 1–4, IEEE, 2014.

[2.98] S. Cui, R. Chahal, C. Boussard-Plédel, V. Nazabal, J.-L. Doualan, J. Troles, J. Lucas, and B. Bureau, "From selenium-to tellurium-based glass optical fibers for infrared spectroscopies," *Molecules*, vol. 18, no. 5, pp. 5373–5388, 2013.

[2.99] B. Cole, L. Shaw, P. Pureza, R. Mossadegh, J. Sanghera, and I. Aggarwal, "Rare-earth doped selenide glasses and fibers for active applications in the near and mid-ir," *Journal of non-crystalline solids*, vol. 256, pp. 253–259, 1999.

Chapter 3

Measurements and Experimental Techniques

In this chapter, we present the experimental and measurement techniques for the bulk and fibre glasses studied in chapters 5, 6 and 7. The praseodymium doped chalcogenide bulk and fibre samples (Pr^{3+}:$Ge_xAs_y(Ga_z/In_z)Se_i$) [3.1] were fabricated by the Novel Photonics Glasses Group led by Prof. Angela Seddon, at the University of Nottingham, together with all the spectroscopic characterisation. The author was involved in the polishing of the samples for absorption and photoluminescence measurements. The Erbium-doped sol-gel SiO_2 powders were made by the Research group led by Prof. Polly Arnold, school of Chemistry of the University of Edinburgh. In addition, the power dependence studies and Photoluminescence measurements of the sol-gel samples were done by the Research group led by Dr Julia Weinstein, school of Chemistry of the University of Sheffield. The Erbium doped double clad fibres were commercially available and were sourced from FiberLabs Inc. It is not known how they were fabricated. This multi-composite optical glass fibre ($\alpha_{loss} < 50$ dB/km) composition consists of ZrF_4-BaF_2-LaF_3-AlF_3-NaF commonly referred to as ZBLAN. The results from measurement were used to formulate the theoretical models discussed in chapters 5, 6 and 7

This chapter is arranged as follows: In Section 3.1, we present the

sample preparation techniques for bulk (sol-gel and melt and quench) and fibre samples (melt and quench). Section 3.2 deals with the spectroscopic characterisation techniques to describe the properties of the glass samples based on absorption and photoluminescence measurements. Section 3.4 introduces the Judd-Ofelt analysis which describes the samples by a set of phenomenological parameters based on absorption measurements in the previous section. Section 3.5 introduces the McCumber's reciprocity theory as a reliable technique that produces emission cross-section measurements from absorption measurements of section 3.2.1. Section 3.6 summaries the chapter by comparing a few relevant properties of all the glass materials and indicating the best to be used in our experiments.

〰〰〰〰〰

3.1 Sample preparation

This section provides the experimental process for preparing the rare-earth doped glasses. Experimental procedures will be described as follows: silica glass prepared by the sol-gel method, chalcogenide glass prepared by melting, quenching and annealing.

3.1.1 Erbium doped bulk glass

The sol-gel technique produces vitreous materials under low temperature, incorporating high level of rare earths with good homogeneity [3.2]. A major significant advantage of the sol-gel process over other glass fabrication techniques is the ease with which bulk materials can be made. The flexibility of the method has gained a high research interest with the development of interesting and novel synthetic methods that were difficult to achieve in the past. The sol-gel technique has been successfully applied to the fabrication of Er^{3+}-doped waveguides, exhibiting excellent passive performance [3.3]. The traditional concept of the sol-gel preparation is based on hydrolysis and the use of condensation of metal alkoxides, although different modifications have been developed [3.4].

To prepare the sol-gel samples used in this research, TEOS (tetra-ethoxysilane, $Si(OC_2H_5)_4$, Sigma Aldrich, 98%) was used as a source of SiO_2. Erbium triflate $Er(OTf)_3$ was employed as a source of Er^{3+} ions, which was prepared by a method previously by Abbasi *et al.* [3.5]. In a typical procedure, TEOS was first pre-hydrolysed by refluxing a mixture of $TEOS : C_2H_5OH : H_2O$ and 0. 1M HCl in the molar ratio of 1:2:4:0.025, respectively. This produced a transparent sol which was divided equally into 3 vials. The compositions with different erbium concentrations were then prepared by adding appropriate amounts of $Er(OTf)_3.9H_2O$ and $Al(NO_3)_3.9H_2O$ already dissolved in ethanol. The sols were then allowed to age at room temperature for two weeks in order for gelation to take place. The wet gels obtained were therefore dried at 80 ^oC for 48 hours to obtain the xerogel. Finally, erbium doped oxide materials were obtained by heating the xerogel samples up to 1000^oC with a heating rate of 1^oC/min and a dwell time of 2 hours. The erbium powders were obtained from unique compositions of $SiO_2 : Er_2O_3 = 99:1$, $SiO_2 : Er_2O_3 = 96:4$, $SiO_2 : Al_2O_3 : Er_2O_3 = 75:15:10$ described samples A, B and C respectively. The sol-gel process is described by the process diagram in Figure 3.1

3.1.2 Praseodymium doped fibre samples

Gallium, arsenic and germanium sulfides have been subject of intense research effort [3.6–3.10] as candidates for chalcogenide glass fibres . However the poor rare-earth solubility and coincidence of crystallization with fiber-drawing temperature in arsenictrisulfide [3.9] glasses made it necessary to seek alternative compositions for the chalcogenide glass fibre.

For this research, the network modifiers germanium (Ge; 5N purity, Cerac), arsenic (As; 7N purity and heated under vacuum, Furakawa Denshi), Indium(In 6N5 purity, Alfa Aesar) and selenium (Se; 5N purity and heat treated under vacuum; Materio) were used to produce chalcogenide glass samples in an effort to modify the local environment of the Pr^{3+} ions (Pr foil, 3N purity Alfa Aesar) [3.11]. A silica glass ampoule was first air-baked, then vacuum baked, followed by batching of the network modifiers inside a MBraun nitrogen glove box with a rating of < 0.1 ppmW of water and Oxygen. This is because chalcogenide glass has high vapour presure and the melts have high viscosity and
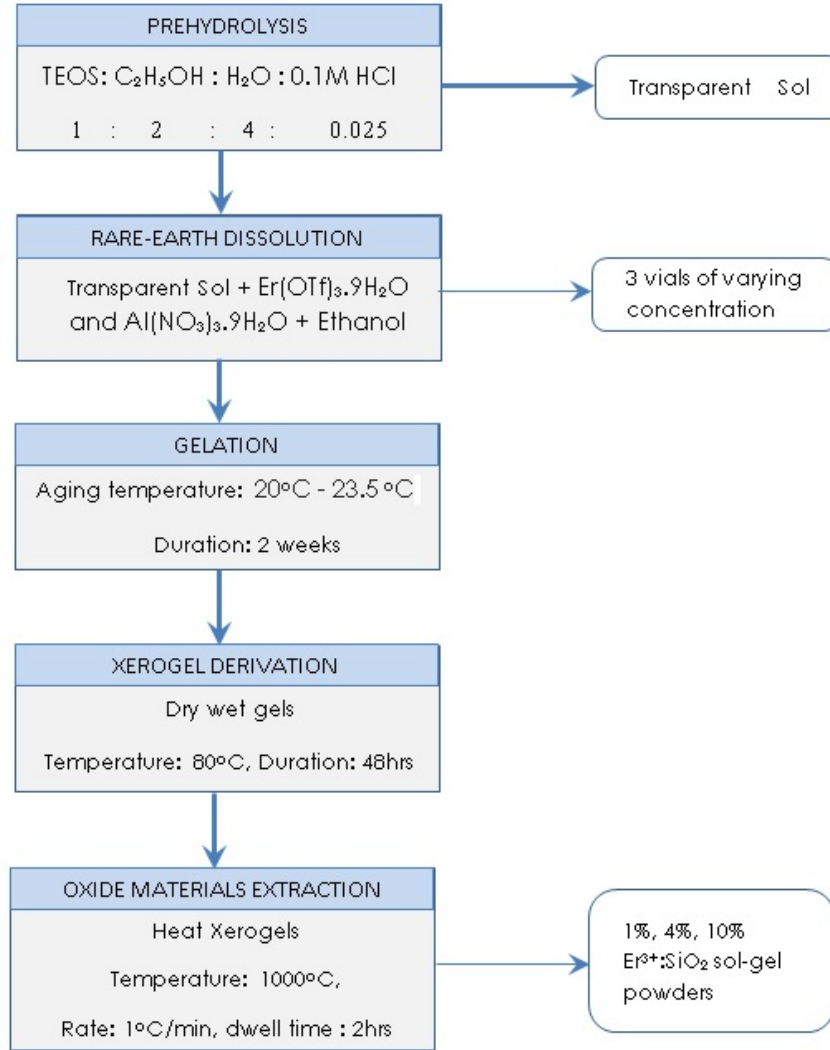
Figure 3.1: Sol-gel preparation procedure for bulk $Er : SiO_2$ samples

is susceptible to oxidation and hydrolysis [3.12] The ampoule was sealed under vacuum to a pressure of 10^{-3} Pa, and then transferred to a melting/rocking furnace heated to 850 ^oC for 12 - 14 hours. The chalcogenide glasses produced were quenched in position and then annealed near the glass-transition temperature. Annealing was followed by cutting and polishing of the fibre glass to a 1 μm finish. Once the preform has been made, it is drawn into a fibre using a drawing tower inside a class 10,000 cleanroom. The process produced a 250 μm diameter uncoated chalcogenide glass fibre with a core-clad ratio of approximately 80% [3.11,3.13]. The same process was repeated with the substitution of Indium for

Gallium, producing 500 and 1000 ppmW of glass samples (Pr^{3+}:$Ge_xAs_y(Ga/In)_zSe_i$). The full details of this proprietary glass, the composition and atomic parameters *x, y, z* and *i* can be found in the phD thesis of Zhuoqi Tang [3.1]. For the rest of this thesis, the indium and gallium based glasses will be jointly referred to as Pr^{3+}:GeAs(Ga/In)Se and individually as Pr^{3+}:GeAsInSe and Pr^{3+}:GeAsGaSe, respectively.

3.2 Spectroscopic Measurements

This section focusses on the optical characterization techniques used to assess the properties of the bulk and fibre glasses produced by the techniques discussed in the previous section. Absorption measurements were made to gain insight into the characteristics of the rare-earth ion in the host glass environment.

3.2.1 Fourier Transform Infrared Measurements

The Fourier transform infrared spectroscopy measurement uses the full spectrum of a white light source to study the absorption property of a doped glass sample. In a typical setup, the intensity of the light from the sample is first recorded based on the position of an oscillating mirror and then Fourier transformed to obtain the spectrum. The absorption spectra of praseodymium doped glass samples presented in this work were measured with a Bruker IFS 66/S Fourier transform Infrared Spectrometer for the range $0.6-10$ μm with a resolution of *1 nm*. Initially, the characteristic spectrum of the whole setup without the sample was made and recorded for pre-correction reference and accuracy. Subsequently, the sample - a 10 mm diameter glass disk cut to 3 mm thickness and polished to 1 μm finish was placed. The measurement was repeated and marked $I(\lambda)$ after correcting for the background reference. The Spectrometer measured the decrease of the incident optical intensity of the beam travelling through the glass sample as a function of wavelength. Figure 3.2 illustrates the decrease in optical intensity through a bulk glass sample as typically used in the experimental setup.

The incident optical intensity is labelled I_0 and the transmitted intensity is labelled
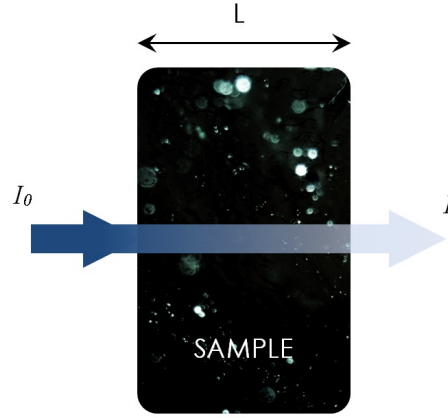
Figure 3.2: Decrease of optical intensity incident on a sample for the measurement of transmittance

I_T so that transmittance can be defined by Equation 3.1.

$$T(\lambda) = \frac{I(\lambda)}{I_O(\lambda)} \tag{3.1}$$

λ is the wavelength. The incident and transmitted intensities are related through the Lambert-Beers law stated in Equation 3.2.

$$I(\lambda) = I_0(\lambda)e^{-\alpha(\lambda)L} \tag{3.2}$$

Where $\alpha(\lambda)$ and L are the absorption coefficient and thickness of the sample respectively. Combining equations 1.1 and 1.2, the absorption coefficient can be expressed as Equation 3.3

$$\alpha(\lambda) = -\frac{Log_e(T(\lambda)}{L} \tag{3.3}$$

In the bulk samples, the absolute values of the absorption cross sections (σ_{abs}) were determined from the concentration of the doping ions (N_d) and the absorption coefficient using Equation 3.4 below:

$$\sigma_{abs} = \frac{\alpha(\lambda)}{N_d} \tag{3.4}$$

Figure 3.3 shows the absorption data measured from 500 ppm Pr^{3+}-doped Chalcogenide glass sample. In Figure 3.3, the scattering background was removed by subtracting a baseline function from the measurement. Baseline correction separates the properties of the glass host from those of the rare earth dopants [3.14]. The baseline function used was derived from an adaptive iteratively reweighted Penalised Least squares method [3.15–3.17].
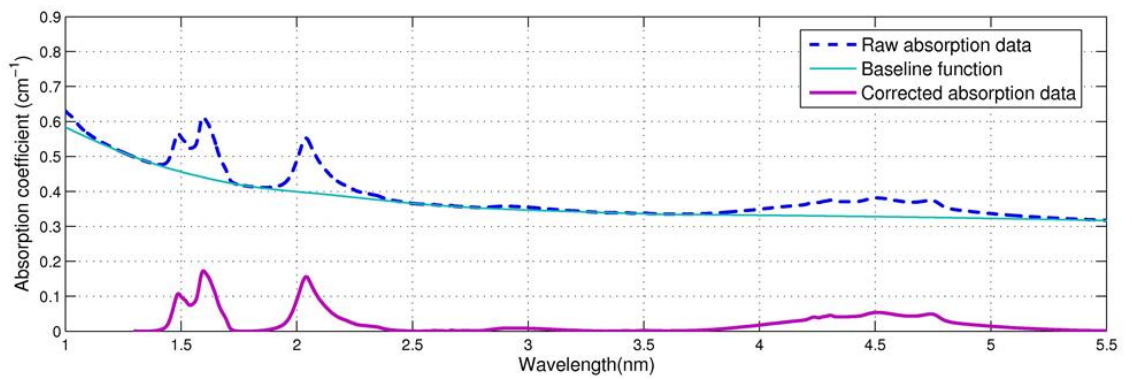
Figure 3.3: Baseline correction of the absorption coefficient of a Pr^{3+}-doped Chalcogenide glass obtained by the FTIR method (Based on measurements results provided by the Novel Glasses Group [3.1,3.11,3.13])

The onward processing of the absorption data for the extraction of spectroscopic properties, such as radiative lifetimes and emission cross sections are discussed in the subsequent sections.

3.2.2 Photoluminescence (PL) Measurements

Photoluminescence measures spontaneous emission through the process of radiative decay between excited states. The emissions from different excited states of the erbium and praseodymium ions have already been discussed in section 2.4. Therefore, this section discusses photoluminescence spectroscopy based on underlying principles and instrumentation. Photoluminescence measurement is important to characterise the efficiency of the emitting levels of the rare-earth ion. This provides useful information about the tuning characteristics that may be required to engineer the material for specific applications. The general setup for photoluminescence comprises of illumination of the

glass sample with photons of certain energy dependent on the excitation wavelength of a laser beam followed by a subsequent detection of photons of a particular spectral range coming out of the sample. The shape of photoluminescence spectra as a function of wavelength can be traced to the atomic bonding between the rare-earth ion and the host material. The next sections discusses the experimental setup for photoluminescence in erbium doped bulk glasses with silica glass hosts. It is then followed by the setup for photoluminescence in praseodymium doped bulk and fibre glass.

3.2.2.1 Erbium doped bulk Glasses

The CW-PL setup used in the experiment for $Er^{3+}:SiO_2$ sol-gel is made up of an Ar-ion laser with fixed excitation energy (excitation power up to 70mW) at 488nm wavelength. The laser beam was directed to the sample powders contained in a quartz cell of 1mm path length. The luminescence emitted by the sample were recorded on a home built system comprising a Coherent Innova 300 CW Ar ion laser as the excitation source and a Bentham TMC600 spectrograph coupled with an Andor iDus DU440A CCD camera in the detection part. The emission spectra were corrected for the overall spectral response of spectrograph and CCD detection system using the instrument response of the setup. The wavelength calibration was performed using a Ne pen-type calibration lamp. Figure 3.4 shows a simplified setup for the photoluminescence measurements.

The same detection system was used for emission spectral measurements with 800 nm excitation, where the output of a home-made Ti:Sapphire tunable laser was used as an excitation source. The energy of nanosecond laser pulsed excitation delivered to the sample was up to 20 mJ at 800 nm at 10 Hz repetition rate. The Ti:Sapphire laser was pumped with the second harmonic (532 nm) of a Q-switched Nd:YAG laser LS-2137U (LOTIS TII).

For the time-resolved emission measurements, the second harmonic (532 nm, 7 ns pulse width, 10 Hz repetition rate) of the Q-switched Nd:YAG laser LS-2137U (LOTIS TII) was used as the excitation source. The excitation energy delivered to the sample was up to 4 mJ per pulse, and was focused into 0.5×1 mm spot on the sample. The emission from
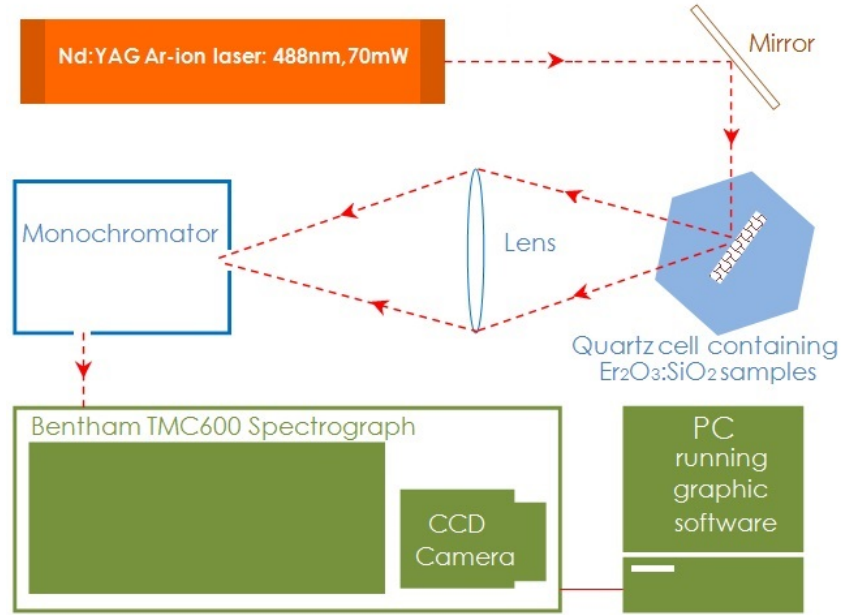
Figure 3.4: Experimental setup for photoluminescence measurements of Er^{3+}:SiO_2 sol-gel(Based on the setup described to the Author)

the sample was collected through a wide-angle lens and detected by a SPEX MiniMate monochromator equipped with a home-built detector unit, based on FEU-118 PMT. The detector current output was coupled into a Tektronix TDS 3032B digital oscilloscope and subsequently the collected data was transferred to a computer. The instrumental response function is estimated as ca. 32 ns FWHM. The same detection configuration was used for the time-resolved emission measurements with 800 nm excitation. The excitation source used was a fundamental output of home-made Ti:Sapphire tunable laser (10 Hz repetition rate, 25 ns pulsewidth). The experiments were performed at the excitation energies 2 mJ per pulse and 15 mJ per pulse; the excitation was slightly defocused to a spot size of 1.5 × 1.5 mm on the sample to counterbalance the inhomogeneity of the powder. The instrumental response function is estimated as ca. 29 ns FWHM. The analysis of the time-resolved data to obtain decay lifetimes was performed using Igor Pro software (WaveMetrics, Inc.) [3.18]. The decay kinetics were fitted to an exponential decay law using a least-squares algorithm built into Igor Pro. Figure 3.5 shows the emission up to the visible wavelength in an erbium doped sample of SiO_2 sol-gel under 488nm excitation.

Figure 3.6 shows the decay measurement for 532 nm pulsed excitation
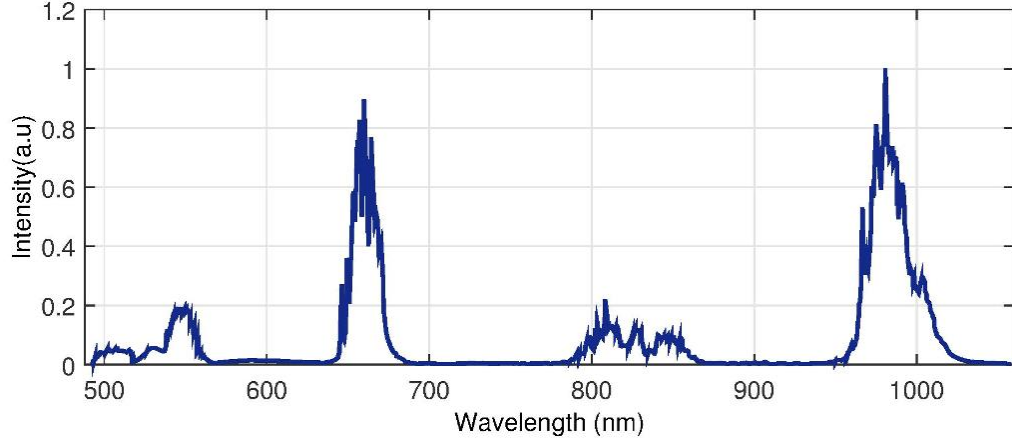
Figure 3.5: Emission spectra of the $Er^{3+}:SiO_2$ sol-gel sample with maximum peak normalised under 488 nm, cw Ar ion laser excitation
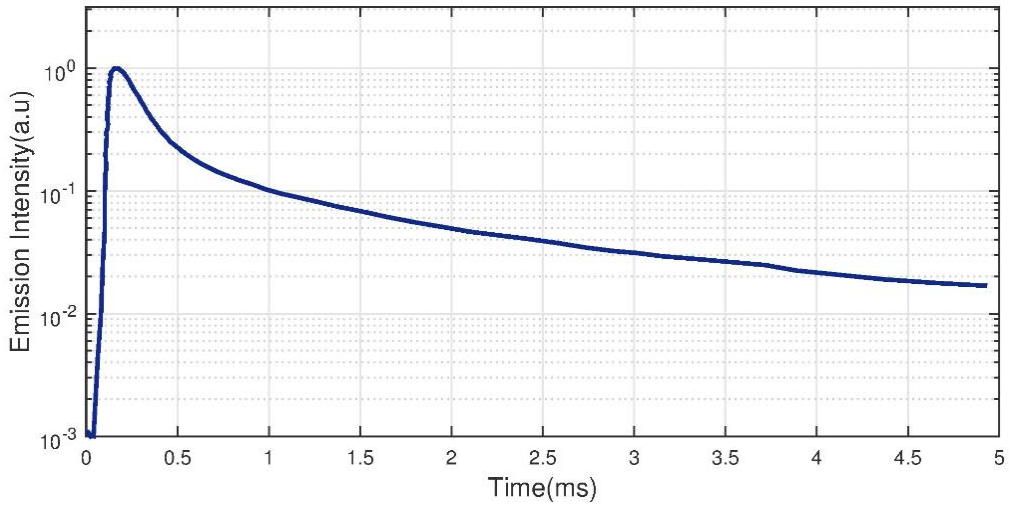
Figure 3.6: Emission decay of the $^4F_{9/2}$ excited state recorded at 660 nm following excitation of a 10 mol% Er^{3+} doped sol-gel sample with 7ns, 532 nm laser pulse.

3.2.2.2   Praseodymium doped Fibre and glass samples

Room temperature fluorescence spectra were obtained in the mid-IR by pumping the step-index Pr^{3+}fibre at 1550 nm with a 100 mW fibre-coupled, single-mode laser diode (FPL 1009S Thorlabs [3.19]) or at 1940 nm with a multimode laser diode with 500 mW (BA-1940-E0500-MMF200 M2K). The 1550 nm laser diode current was controlled using

a LDC205C (Thorlabs) laser driver in the range $0-500$ mA while the 1940 nm laser diode was controlled using a LDC240C(Thorlabs) laser driver in the range $0-4000$ mA; the temperature of both lasers was controlled by a CAB420-15 (Thorlabs) Peltier cooler driver. A 120 mm length of Pr^{3+}-doped fibre was used for the fluorescence emission measurements. Light from the laser diodes was introduced into the fibre using bulk optics. The fibre sample was mounted on a Melles Griot xyz translation stage to enable efficiency collection of the fluorescent emission signal. The launching equipment consisted of a fibre collimator (f = 11 mm and NA = 0.25) and a microscope objective with magnification $\times$ 10 and NA = 0.2. The fluorescence was collected using a ZnSe lens and focused on the entrance slit of a monochromator. The fluorescence signal was modulated by a chopper (Scitec Instruments [3.20]), since laser pump chopping gives poor lock-in due to the different lifetimes of the emission levels. The chopping frequency was in the range of 70 Hz. The emission from the chalcogenide glass fibre was passed through a motorized Spex MiniMate monochromator with diffraction-grating blazed at 6l m (51034 JobianYvon). The detection system consisted of a lock-in amplifier (EG&G Brookdeal 9503-SC), room temperature MCT detector (Vigo System PVI-6), preamplifier for the detector (Judson PA-6) and data acquisition card (NI USB-6008 National Instruments). The monochromator and data acquisition system were controlled by means of software in LabView. Emission spectra were collected over the range of wavelengths ca. 3 6.5 μm , at 300 K. For the bulk glass measurements the sample was cut and polished to a 1lm finish, into the form of a cuboid, with an end face 5 mm $\times$ 5 mm into which the pump laser was focused. In addition, side length was 10 mm, from which the emission was collected. This allowed the laser to be focused to within 0.5 mm of the collection face and collected from within 2 mm of the launch face, so that the reabsorption of the emission could be minimised. Fluorescence decay was measured using the on-and-off modulation of the pump laser at 1550 nm wavelength and at 8 and 10 Hz frequency. In order to try to minimize re-absorption of the emitted light, a short fibre length of 35 mm was employed. Figure 3.7 shows Mid-IR emission for 500 ppm Pr^{3+}doped GeAsGaSe bulk sample.

The mid-IR lifetime decay (reported later in Section 6.5.2) was detected using an InSb
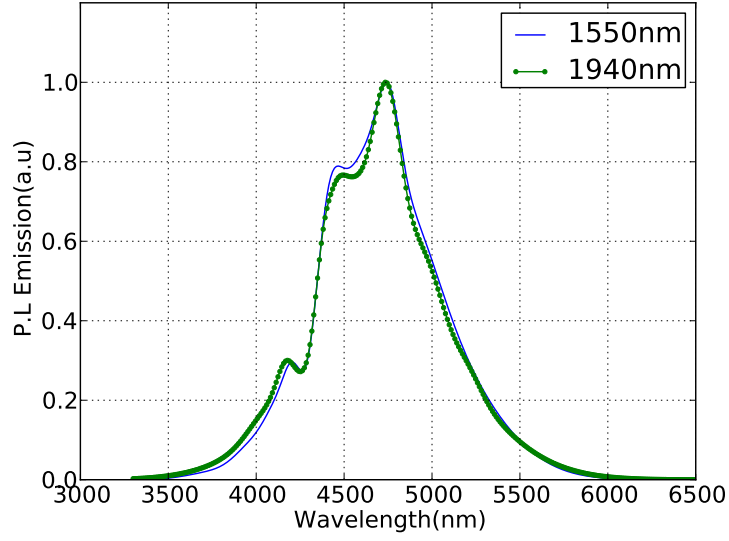
Figure 3.7: Measured mid-IR emission spectrum of 500 ppm Pr^{3+}: GeAsGaSe bulk glass using a lock-in and MCT detector (room temperature) with preamplifier and 1550 nm, 1940nm CW [3.13].

IR detector (Judson J10D-M204B-R01M-60WL-D413/6 cooled to 77 K) in conjunction with a fast preamplifier, of response time of 100 ns. It was analysed using a digital 1 GHz oscilloscope (DPO4102B Tektronix). The decay waveforms were averaged 512 times, which is high enough to significantly reduce the noise in the measurement . A set of long pass filters (2 μm and 4 μm) was used to block pump power and isolate the emission. All the fluorescence decay characteristics were measured at 300 K.

The photoluminescence measured from the glass samples is a convolution of the true photoluminescence from the excited level and the instrument response function of the laser diode used. The actual emission g(t) then has the following [3.21]:

$$h(t) = \int_0^t g(t - \tau) f(\tau) d(\tau) \tag{3.5}$$

The task is to determine g(t) when f(t) and h(t) are known, where h(t) is the measured intensity profile of the emission and f(t) is the instrument response function(IRF). The IRF is typically close to a Gaussian function. The de-convolution of Equation 3.5 produces the desired photoluminescence decay. Decay curves are corrected for the IRF before using it in numerical analysis.

3.3 Refractive Index and Loss Measurements

Spectral dependence of the refractive index for 500 ppm Pr^{3+}:GeAsGaSe fibre glasses were determined by ellispometric technique spanning the spectra region 1 - 20 μm .

Figure 3.8 shows the variation of refractive index with wavelength for 500 ppm Pr^{3+}:GeAsGaSe [3.1]. From the measured refractive index, a simple Sellmeier model equation [3.22] with a least square fit [3.23] was used to interpolate the data points, producing dimensionless coefficients B_1, C_1, B_2, C_2, B_3 and C_3 as stated in equation 3.6. δ_{rms} is the rms deviation of the fit from the measurement. Table 3.1 shows the Sellmeier coefficients for the core and clad refractive index in the 1 - 5 μm wavelength range. The measurement in both the core and clad showed that the influence of Pr^{3+}-doping is marginal.
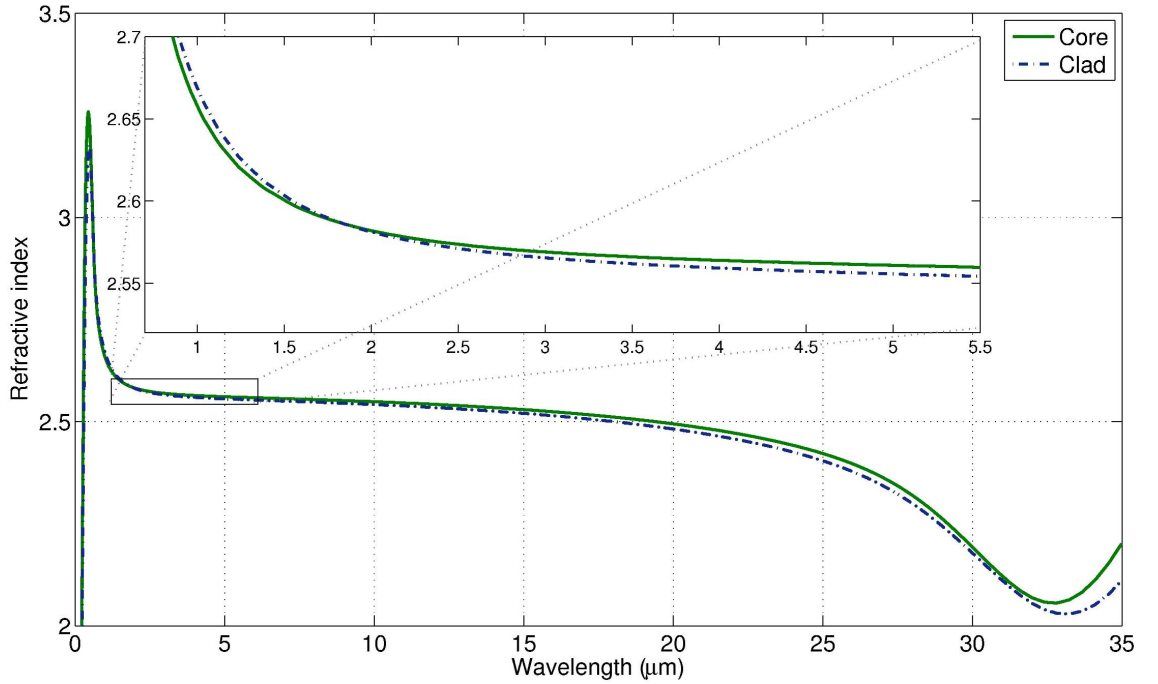
Figure 3.8: Measured refractive index of 500 ppmw Pr^{3+}-doped GeAsGaSe (clad., 1 at. % difference in composition). Inset shows refractive index variation in the wavelength range of interest (1 - 5 μm).

$$n(\lambda) = \sqrt{\left(1 + \frac{B_1\lambda^2}{\lambda^2 - C_1} + \frac{B_2\lambda^2}{\lambda^2 - C_2} + \frac{B_3\lambda^2}{\lambda^2 - C_3}\right)} \qquad (3.6)$$

Table 3.1: Table of Sellmeier coefficients for 500 ppm Pr^{3+}:GeGaAsSe glass

	B_1	C_1	B_2	C_2	B_3	C_3	δ_{rms}
Core	2.6310e-2	-6.4665e-1	1.5344	6.5473e-2	7.8540e7	6.3162e11	8.7912e-7
Clad	3.8325e-2	6.8579e-2	1.5164	6.8579e-2	5.903e-2	4.8426e2	1.4849e-6

As at the time of this research, the refractive index for the indium based chalcogenide glass sample had not been measured. However, from the literature it was observed that substituting indium for gallium [3.24] increased the refractive index by $\approx$5.5%. In this work, therefore, a correction factor based on this percentage was used to predict the refractive index of the indium based glasses.

Figure 3.9 shows the loss spectra of optically clad Indium and Gallium-based fibers measured using the cutback technique. InGaAs and InSb cooled detectors were used in the measurement. Pr^{3+}:GeAsInSe fiber shows typical lowest loss of 5.58 dB/m at 2.75 μm , while Pr^{3+}:GeAsGaSe fiber shows 2.8 dB/m at 6.65 μm [3.11].
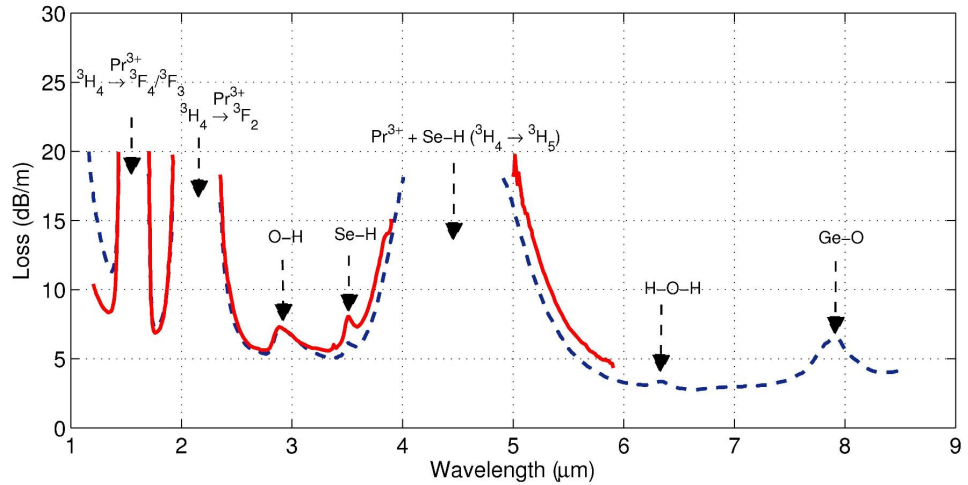
Figure 3.9: Loss spectra of optically clad In- fiber(Red) and Ga- fiber(Blue dash) measured using the cutback technique [3.11]

3.4 Judd-Ofelt Analysis of Lanthanides in Glass Hosts

In rare-earths, the $4f^N$ electronic configurations have the same parities and therefore, electric dipole transitions between them are not allowed. By adding a crystal field however, the $4f^N$ configuration can be adjusted such that it begins to interact with others with

opposite parity, for example with $4f^N5d$. Based on this premise, Judd and Ofelt [3.25,3.26] deduced an expression which has gained widespread popularity for the calculation of the band intensities of rare-earth ions using the oscillator strength of electric dipole transitions. Their theory described the line strength of an ion in a host material based on the absorption measurements described in Section 3.2.1. Since absorption spectra measurements are easier to make compared to emission spectra, this approach became widely accepted to predict the spectroscopic properties of rare-earth doped materials. The Judd-Ofelt theory makes the following assumptions [3.27]:

- The excited configuration $4f^{N-1}5d$ above $4f^N$ possesses average energy.

- The average energy difference (4f-5d) is the same as the difference between the average energy of $4f^{N-1}5d$ and the energy of both initial and final states of $4f^N$.

- The host material is optically isotropic.

- All the stark levels have equal distribution of atoms.

The Judd-Ofelt procedure is widely accepted (with over 5570 citations by 2014) and has been used to produce radiative lifetimes and spontaneous emission probabilities of rare-earth transitions in many glass hosts [3.27–3.31]. The Judd-Ofelt parameters are phenomenological parameters (Ω_t,t=2,4,6) obtained from fits to experimental line-strength (S_{ED}) data. The electric-dipole oscillator strength (f_{ED}) relates to the electric dipole line strength (S_{ED}) and the magnetic dipole line strength (S_{MD}) from an initial level J to a level J', described by equation 3.7 below:

$$f_{jj'}^{ed} = \frac{8\pi^3 e^2}{3hc} \frac{N\lambda}{(2J+1)n^2} \left[\frac{n(\lambda)[n(\lambda)^2+2]^2}{9} S_{jj'}^{ed} + n^3 S_{jj'}^{md} \right] \tag{3.7}$$

where n is the wavelength-dependent refractive index of the glass material. The parameters *N, h, e* and *c* are the number of active ions per unit volume, Planck's constant, electronic charge and speed of light, respectively. The Judd-Ofelt parameters (Ω_t,t = 2,4,6) are

related to the line strength of the electric dipole transition, defined by Equation 3.8 below:

$$S_{ED}(J, J') = e^2 \sum_{t=2,4,6} \Omega_t \left\langle \Psi \left\| U^t \right\| \Psi' \right\rangle^2 \tag{3.8}$$

where Ψ and Ψ' denote the initial *[S,L]J* and final *[S,L]J* states respectively. Ω_t is the host-dependent Judd-Ofelt intensity parameter. $\left\langle - \left\| U^t \right\| - \right\rangle^2$ is the host-independent doubly reduced matrix elements. The table of reduced elements published by Nielson [3.32] in 1963 is popularly referred to in the literature. This study has however used a more recent version of the table of elements produced by Caspary [3.14] as years of research have produced more accurate and reliable techniques.

S_{MD} magnetic dipole line strength was calculated from intermediate coupled wave functions in Equation 3.9. S_{MD} is often ignored in Judd-Ofelt calculations as its contribution to the calculated experimental oscillator strength is negligible.

$$S_{MD}(J, J') = \frac{n}{2mc} \left\langle f^n[SL]J \left\| U^t \right\| f^n[S'L']J' \right\rangle^2 \tag{3.9}$$

The experimental oscillator strengths ($f_{jj'}^{ed}$) in Equation 3.7 are found by integrating the measured absorption coefficient for each of the transitions using Equation 3.10 below:

$$f_{jj'}^{ed} = \int_{band} (2.303k(\lambda)d\lambda) \tag{3.10}$$

where $k(\lambda)$ is the absorption coefficient measured in Section 3.2.1.

The absorption spectral provides the transition peak spectral area for the left hand side of equation 3.8. With the constants of the equation expressed in Gaussian units (Cg.s), the electric dipole line strength can be extracted. By least square approximation, $S_{ED}(J, J')$ is then fit to values of host-independent reduced matrix elements (M) to determine the Judd-Ofelt parameters Ω_2, Ω_4, Ω_6. In the case of the least squares method, the minimisation yields an explicit expression as described by Equation 3.11:

$$\Omega_{ie2,4,6} = (M^T M)^{-1} M^T S_{ED} \tag{3.11}$$

The parameter Ω_2 is sensitive to the covalent bonding between the rare-earth ions and the ligands anions [3.33], which is an indication of the asymmetry of the local environment of the rare-earth sites. Ω_4 and Ω_6 reflect the bulk properties of the host such as rigidity and viscosity. The ratio Ω_4/Ω_6 is the spectroscopic quality parameter used to predict the strength of the stimulated emission of the first transition (for example, $^3H_5 \rightarrow {}^3H_4$: ≈ 4.73 μm in Pr^{3+}: Chalcogenide).

The accuracy of the Judd-Ofelt procedure is weighted by the root-mean-square deviation δ_{rms} in equation 3.12, which is an indication of the goodness of fit between the measured (f_{meas}) and the theoretical (f_{cal}) oscillator strengths for all available transitions.

$$\delta_{rms} = \sqrt{\frac{\sum_{i=1}^{N_p}(f_{cal} - f_{meas})^2}{N_p - N_t}} \tag{3.12}$$

Where N_p is the number of spectral bands measured and N_t is the taken as 3 since there are only 3 Judd-Ofelt parameters to account for. Using the J-O parameters obtained from the fit, the line strength S_{ed} corresponding to the transitions between manifolds J(initial) and J'(final) can be calculated. The radiative transition probability A is given by the expression in Equation 3.13 below:

$$A(J, J') = \frac{64\pi^2 e^2 \upsilon^3}{3h(2J'+1)}\left[\frac{n(n^2+2)^2}{9}S_{ed} + n_d{}^3 S_{md}\right] \tag{3.13}$$

Here *2J' + 1* is the degeneracy/multiplicity of the upper state and n_d is the wave number of the fluorescence peak. The radiative lifetime τ of the excited state is the sum of all the transition probabilities, as defined in Equation 3.14. The fluorescence quantum efficiency is the ratio of the measured lifetime τ_m from experimental decay curves and the lifetime τ_r obtained by Judd-Ofelt analysis ($\eta = \frac{\tau_m}{\tau_r}$).

$$\tau_r = \frac{1}{\sum A(J, J')} \tag{3.14}$$

The branching ratios or spontaneous emission probabilities are expressed in Equation 3.15

$$\beta = \frac{A(J, J')}{\sum A(J, J')} \tag{3.15}$$

Algorithm 3.1 shows the general procedure for the Judd-Ofelt analysis. The Judd-Ofelt procedure is applied to Er^{3+}-doped sol-gel glass, Pr^{3+}-doped chalcogenide glass and Er^{3+} doped ZBLAN glass in Chapters 5, 6 and 7.

Algorithm 3.1: Judd Ofelt Algorithm

Data: $\sigma_{abs}(\lambda) = (A_a, \lambda)$ such that A_a - absorption coefficients (cm^{-1})
$\qquad\quad$ λ is wavelength (nm)
Result: $\Omega_t = (\Omega_2, \Omega_4, \Omega_6)$ Judd-Ofelt parameters
$\qquad\quad$ $\tau_{ri} = (\beta_{ij}, \Omega_t, A_{ed})$
begin
$\quad$ $N_b \longleftarrow DetectNumberOfBandsMeasured(\lambda)$
$\quad$ $RF_b \longleftarrow StoreRefractiveIndex(\lambda_i(i = 1..N_b))$
$\quad$ $BaseTag \longleftarrow 2J + 1$ such that J is the ground state stark Level split
$\quad$ $c \longleftarrow 2.99792 \times 10^{10}(cm/2)$
$\quad$ $h \longleftarrow 6.626 \times 10^{e-27}(erg.s)$
$\quad$ $hbar \longleftarrow 1.05457266 \times 10^{-27}(erg.s)$
$\quad$ $e \longleftarrow 4.8032 \times 10^{-10}(esu(statC))$
$\quad$ $k \longleftarrow 1.381 \times 10^{-16}(erg/L)$
$\quad$ $me \longleftarrow 9.1093897 \times 10^{-28}(g)$
$\quad$ **for** $x \in N_b$ **do**
$\quad\quad$ $A_\lambda(x) \longleftarrow IntegrateBand(x)(nmcm^{-1})$
$\quad\quad$ $Se(x) \longleftarrow A_\lambda(x) \times 10.41 \times RF_b(x) \times (3/(RF_b(x)^2 + 2))^2 \times BaseTag/\lambda(x)$
$\quad\quad$ /* Table of reduced elements $\qquad\qquad\qquad\qquad\qquad\qquad\qquad\qquad$ */
$\quad\quad$ $M_i(x) \longleftarrow RM_i(U_2, U_4, U_6)$; such that i=1,2,3
$\quad$ /* Least Squares fit to obtain Judd-Ofelt Parameters $\qquad\qquad\qquad$ */
$\quad$ $\Omega_t \longleftarrow inverse(M^T \times M) \times M^T \times Se^T$
$\quad$ /* Theoretical/Calculated Line Strengths (ST) $\qquad\qquad\qquad\qquad$ */
$\quad$ **for** $x, j \in N_b, 3$ **do**
$\quad\quad$ $St(x) \longleftarrow St(x) + M_x(j) \times Omega(j)$
$\quad$ /* δ_{rms} for each transition $\qquad\qquad\qquad\qquad\qquad\qquad\qquad\qquad\quad$ */
$\quad$ $error \longleftarrow sqrt(sum(abs(Se - St)^2)/(N_b - 3))$
$\quad$ $OriTag \longleftarrow 2J_p + 1$ such that J_p is the stark Level split of all the bands
Function $TransitionValues(\Omega_t, N_b, J_p)$ **is**
$\quad$ β
end

3.4.1 Modified Judd-Ofelt analysis

Judd-Ofelt calculations for the praseodymium ions have not been as successful as in other rare-earth ions because of the small difference in the average energies between $4f^n$ and $4f^{n-1}5d$ configurations in Pr^{3+} ions compared to other rare-earths [3.34]. As a result, the Judd-Ofelt theory breaks down, producing negative values of the phenomenological paramters Ω_t. Several alternatives have been suggested to solve this problem; some authors modified the theory to account for the *4f5d* energy [3.35], Quimby and Miniscalco introduced fluorescence branching ratios [3.36] by making additional fluorescence measurements and fewer ground state absorption measurements, while Goldner and Auzel used the normalized least squares fitting technique to scale the measurements according to individual errors [3.37] . In this work we have adopted boltzmann's statistics to separate the overlapping transitions and then use the loss measurements to compensate for the impurities in the mid-IR measurement. The result is a stable positive set of values of Judd-Ofelt parameters which is then used for the calculation of branching ratios and radiative lifetimes.

3.4.2 Limitations and Inaccuracies of J-O calculations

To separate the property of the bulk glass from that of the rare-earth ion in the samples, base-line correction is performed on absorption data prior to Judd-Ofelt calculation. The calculated areas spanning the bands of the individual transitions are therefore dependent on the baseline function used. Many authors produce Judd-Ofelt fits based on the averages of several baseline functions [3.13,3.14] to minimise the error introduced by poor choices of the fit functions. Another source of error is the number of transitions from the absorption measurement used in the fitting procedure [3.38]. Inspite of this, there are still many other sources of error introduced by the Judd-Ofelt procedure and, in general, the accuracies are often quoted to have an error margin of about $\pm 20\%$. The Judd-Ofelt theory is limited to providing transition intensities or integrated cross sections. However, it does not provide spectral shape. Therefore in the next section, we provide a discussion on how to determine

spectral distributions of emission spectra.

3.5   McCumber's Method of Reciprocity

The McCumbers method relates the absorption to the emission cross sections by employing Equation 3.16 [3.39]. The theory assumes that within each manifold, thermal distribution is established faster than the lifetime of the manifold. The McCumber's method provides the spectral information of one of the cross sections when the other is known from measurements, assuming narrow bandwidth of the individual Stark levels compared to $k_B T$.

$$\sigma_{abs}(v) = \sigma_{ems}(v)e^{\left(\frac{hv - \Delta E}{k_B T}\right)} \tag{3.16}$$

where ΔE is the temperature-dependent excitation energy, which relates to the population of the lower n_1 and upper n_2 states defined by Equation 3.17

$$\frac{n_2}{n_1} = e^{\left(\frac{-\Delta E}{k_B T}\right)} \tag{3.17}$$

where k_B is the Boltzmanns constant and T is the absolute temperature. Using Stark level assignments, Equation 3.17 can be rewritten as Equation 3.18

$$\frac{n_2}{n_1} = \frac{\sum_{s=0}^{c_1-1} e^{\left(-\frac{E_{1s}}{k_B T}\right)}}{\sum_{s=0}^{c_2-1} e^{\left(-\frac{E_{2s}}{k_B T}\right)}} \tag{3.18}$$

where c_s is the number of stark levels in multiplet s. By kramers degeneracy, $c_s = J_s + \frac{1}{2}$ for odd number of f-electrons and $c_s = 2J_s + 1$ for even number of f-electrons. J_s is the quantum number of multiplet s. $c_s = 7$ in the first excited state ($^4I_{13/2}$) of erbium, while $c_s = 11$ in the first excited state of praseodymium ($^3H_5$). The positions of the Stark levels of rare-earths are not known. Therefore a modified McCumber theory [3.40], is defined in equations 3.19 and 3.20 below which assumed equidistant spacing to describe E_{1s} and E_{2s}:

(a) Stark Manifolds

(b) Application to the $^3H_5$ absorption spectra of Pr^{3+}
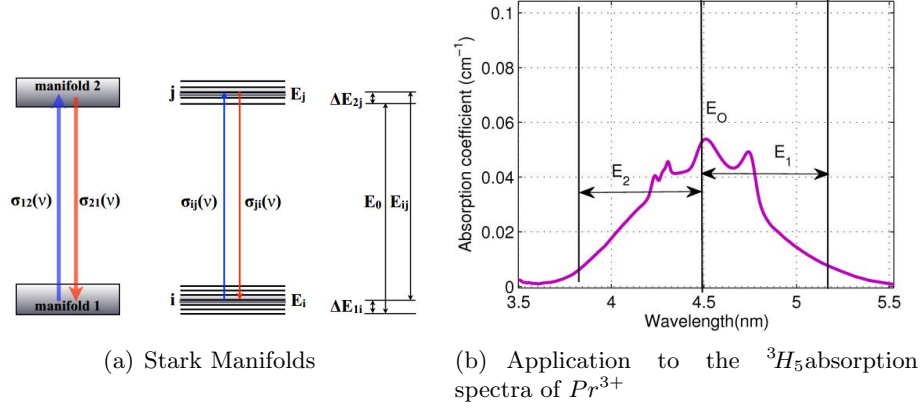
Figure 3.10: Modified McCumber description using optical transitions and absorption spectra

$$E_{1s} = \frac{s\Delta E_1}{c_1 - 1} \tag{3.19}$$

$$E_{2s} = \frac{s\Delta E_2}{c_2 - 1} + E_0 \tag{3.20}$$

The difference between the highest and lowest stark levels of multiplet i is represented by ΔE_i and the difference between the lowest stark levels of multiplets 1 and 2 is ΔE_0. Figure 3.10 shows the optical transitions between the stark manifolds. ΔE_1 is obtained from the 5% position at the high wavelength side of the emission spectrum (if measured) otherwise the absorption spectrum is used. ΔE_2 is calculated from the 5% position at the low wavelength side of the absorption spectrum. Algorithm 3.2 shows the implementation of the McCumber analysis. The modified McCumber technique is applied in chapters 5, 6, 7 and 8 to obtain the emission cross sections from absorption measurements.

3.6 Summary and discussion

This Chapter described the preparation techniques of rare-earth doped glasses, measurement of spectroscopic properties. It also presents the extraction of phenomenological parameters describing each glass for numerical simulations discussed in the rest of this thesis. From each of the measurements discussed, a set of spectroscopic

---

Algorithm 3.2: Modified McCumber Algorithm

Data: $\sigma_{abs}(\lambda) = (A_a, \lambda)$ such that A_a is an array of measured absorption cross sections and λ is an array of wavelength data.

Result: $\sigma_{ems}(\lambda) = (A_e, \lambda)$ such that A_e is an array of calculated emission cross sections interval order.

begin

   $T \longleftarrow 293$

   $h \longleftarrow 6.6262 \times 10^{-34}$

   $c \longleftarrow 2.99792458 \times 10^{8}$

   $k \longleftarrow 1.3807 \times 10^{-23}$

   $kT \longleftarrow (k \times T)/(h \times c \times 100)$

   if j_1 *is even* **then** $c_1 \longleftarrow 2j_1 + 1$ **else** $c_1 \longleftarrow j_1 + 0.5$

   if j_2 *is even* **then** $c_2 \longleftarrow 2j_2 + 1$ **else** $c_2 \longleftarrow j_2 + 0.5$

   $A_e \longleftarrow$ McCumberRec(A_a,C_1,C_2,λ)

Function *McCumberRec(A_a,C_1,C_2,λ)* **is**

   $E_0 \longleftarrow 1/(\lambda[getIndex(max(A_e))])$

   $E_1 \longleftarrow 1/max(\lambda[getAllIndex(A >= 0.05max(A_e))])$

   $E_2 \longleftarrow 1/min(\lambda[getAllIndex(A >= 0.05max(A_e))])$

   $dE_1 \longleftarrow E_0 - E_1$

   $dE_2 \longleftarrow E_2 - E_0$

   for $x \in c_1 - 1$ **do**

     $sum1 \longleftarrow sum(exp(-s/(x-1) \times dE_1/kT));$

   end

   for $y \in c_2 - 1$ **do**

     $sum2 \longleftarrow sum(exp(-s/(y-1) \times dE_2/kT));$

   end

   /* Convert wavelength to wavenumber in cm^{-1} */

   $LamdaCm \longleftarrow 1/\lambda$

   return $A_a * (sum1/sum2) * exp(E_0/kT) * exp(-LamdaCm/kT)$

end

---

derivations were made and the importance of the parameters to the properties being considered were highlighted. The Judd-Ofelt analysis for the extraction of radiative lifetimes and branching ratios from absorption measurements is described by a simple algorithm. The McCumber analysis was discussed to extract emission cross section from the measurement of absorption cross sections. The limitations of the methods were discussed and the required modifications for the applications in this study were highlighted.

References

[3.1] T. Zhuoqi, *Rare earth ion doped selenide-based chalcogenide glasses and fibres towards mid-infrared fibre lasers.* Phd thesis, University of Nottingham, 2012.

[3.2] L. L. Hench and J. K. West, "The sol-gel process," *Chemical Reviews*, vol. 90, no. 1, pp. 33–72, 1990.

[3.3] R. R. Thomson, *Active optical waveguides for lightwave applications.* Phd thesis, Heriot-Watt University, 2006.

[3.4] S. Bhandarkar, "Sol-Gel Processing for Optical Communication Technology," *Journal of The American Ceramic Society*, vol. 87, no. 7, pp. 1180–1199, 2004.

[3.5] A. Abbasi, P. Lindqvist-Reis, L. Eriksson, D. Sandström, S. Lidin, I. Persson, and M. Sandström, "Highly hydrated cations: deficiency, mobility, and coordination of water in crystalline nonahydrated scandium (III), yttrium (III), and lanthanoid (III) trifluoromethanesulfonates," *Chem. Eur. J.*, vol. 11, no. 14, pp. 4065–4077, 2005.

[3.6] R. Quimby, B. Aitken, M. Newhouse, and K. Gahagan, "Self-calibrating quantum efficiency measurement technique and application to Pr^{3+}-doped sulfide glass," *Optics letters*, vol. 20, no. 19, pp. 2021–2023, 1995.

[3.7] K. Wei, D. Machewirth, J. Wenzel, E. Snitzer, and G. Sigel, "Spectroscopy of Dy^{3+} in Ge–Ga–S glass and its suitability for 1.3-μm fiber-optical amplifier applications," *Optics letters*, vol. 19, no. 12, pp. 904–906, 1994.

[3.8] D. Simons, A. J. Faber, and H. De Waal, "GeS_x glass for Pr^{3+} -doped fiber amplifiers at 1.3 μm," *Journal of non-crystalline solids*, vol. 185, no. 3, pp. 283–288, 1995.

[3.9] Y. Ohishi, A. Mori, T. Kanamori, K. Fujiura, and S. Sudo, "Fabrication of praseodymium-doped arsenic sulfide chalcogenide fiber for 1.3μm fiber amplifiers," *Applied Physics Letters*, vol. 65, no. 1, pp. 13–15, 1994.

[3.10] D. Marchese and A. Jha, "The structural aspects of the solubility of Pr^{3+} ions in GeS_2-based glasses," *Journal of Non-Crystalline Solids*, vol. 213–214, no. 0, pp. 381 – 387, 1997.

[3.11] H. Sakr, D. Furniss, Z. Tang, L. Sojka, N. A. Moneim, E. Barney, S. Sujecki, T. M. Benson, and A. B. Seddon, "Superior photoluminescence (PL) of Pr^{3+}-In, compared to Pr^{3+}-Ga, selenide-chalcogenide bulk glasses and PL of optically-clad fiber," *Opt. Express*, vol. 22, pp. 21236–21252, Sep 2014.

[3.12] A. Seddon, "Chalcogenide glasses: a review of their preparation, properties and applications," *Journal of Non-Crystalline Solids*, vol. 184, pp. 44–50, 1995.

[3.13] L. Sójka, Z. Tang, D. Furniss, H. Sakr, A. Oladeji, E. Bereś-Pawlik, H. Dantanarayana, E. Faber, A. Seddon, T. Benson, and S. Sujecki, "Broadband, mid-infrared emission from Pr^{3+}doped GeAsGaSe chalcogenide fiber, optically clad," *Optical Materials*, vol. 36, pp. 1076–1082, Apr. 2014.

[3.14] R. Caspary, *Applied Rare Earth Spectroscopy for Fiber Laser Optimization*. Berichte Aus der Lasertechnik Series, Shaker Verlag GmbH, 2002.

[3.15] P. H. C. Eilers, "A perfect smoother.," *Analytical chemistry*, vol. 75, pp. 3631–3636, 2003.

[3.16] P. H. C. Eilers and H. F. M. Boelens, "Baseline Correction with Asymmetric Least Squares Smoothing," *Life Sciences*, pp. 1–26, 2005.

[3.17] F. Gan, G. Ruan, and J. Mo, "Baseline correction by improved iterative polynomial fitting with automatic threshold," *Chemometrics and Intelligent Laboratory Systems*, vol. 82, pp. 59–65, 2006.

[3.18] Wavemetrics.com, "Wavemetrics - scientific graphing, data analysis, curve fitting and image processing software," 2014. Available online at `wwww.wavemetrics.com` [Accessed: 01 March 2014].

[3.19] Thorlabs.de, "Thorlabs, inc. - your source for fiber optics, laser diodes, optical instrumentation, polarization measurement and control," 2014. Available online at `www.thorlabs.de` [Accessed: 01 March 2014].

[3.20] Scitec.uk.com, "Scitec instruments ltd," 2014. Available online at `www.scitec.uk.com` [Accessed: 01 March 2014].

[3.21] A. E. McKinnon, A. G. Szabo, and D. R. Miller, "The deconvolution of photoluminescence data," *The Journal of Physical Chemistry*, vol. 81, no. 16, pp. 1564–1570, 1977.

[3.22] G. Ghosh, *Handbook of Thermo-optic Coefficients of Optical Materials with Applications*. No. v. 4 in Handbook of Optical Constants of Solids Series, Academic Press, 1998.

[3.23] Zunzun.com, "Online Curve Fitting and Surface Fitting at ZunZun.com," 2014. Available online at `www.zunzun.com` [Accessed: 11 March 2013].

[3.24] M. N. Polyanskiy, "Refractive index database," 2014.

[3.25] B. Judd, "Optical Absorption Intensities of Rare-Earth Ions," *Physical Review*, vol. 127, pp. 750 –, 1962.

[3.26] G. S. Ofelt, "Intensities of Crystal Spectra of Rare-Earth Ions," *The Journal of Chemical Physics*, vol. 37, no. 3, pp. 511–520, 1962.

[3.27] B. M. Walsh, *Judd-Ofelt theory: principles and practices*. Springer, 2006.

[3.28] J. H. Choi, F. G. Shi, A. A. Margaryan, and A. Margaryan, "Spectral properties of Nd^{3+}ion in new fluorophosphates glasses: Judd-Ofelt intensity parameters," in *High-Power Lasers and Applications*, pp. 121–127, International Society for Optics and Photonics, 2003.

[3.29] W. Luo, J. Liao, and X. Chen, "Determination of Judd–Ofelt intensity parameters from the excitation spectra for rare-earth doped luminescent materials," *Physical Chemistry Chemical Physics*, vol. 12, no. 13, pp. 3276–3282, 2010.

[3.30] X. Shiqing, Y. Zhongmin, D. Shixun, Z. Junjie, H. Lili, and J. Zhonghong, "Spectroscopic Properties and Judd-Ofelt Theory Analysis of Er^{3+}-Doped Heavy Metal Oxyfluoride Silicate Glass," *J. Rare Earths*, vol. 22, no. 3, pp. 375–380, 2004.

[3.31] Z. Duan, J. Zhang, and L. Hu, "Spectroscopic properties and Judd-Ofelt theory analysis of Dy^{3+}doped oxyfluoride silicate glass," *Journal of Applied Physics*, vol. 101, pp. 043110–043110–6, Feb 2007.

[3.32] C. W. Nielson and G. F. Koster, *Spectroscopic Coefficients for the Pn, Dn, and Fn.* MIT Press, 1963.

[3.33] R. Reisfeld and C. K. Jrgensen, "Chapter 58 Excited state phenomena in vitreous materials ," in *Handbook on the Physics and Chemistry of Rare Earths* (J. Karl A. Gschneidner and L. Eyring, eds.), vol. 9 of *Handbook on the Physics and Chemistry of Rare Earths*, pp. 1 – 90, Elsevier, 1987.

[3.34] R. D. Peacock, "The intensities of lanthanide f-f transitions," *Structure and Bonding*, vol. 22, pp. 83–122, 1975.

[3.35] A. A. Kornienko, E. B. Dunina, and A. A. Kaminskii, "Dependence of the line strength of ff transitions on the manifold energy," *physica status solidi (b)*, vol. 157, no. 1, pp. 261–266, 1990.

[3.36] R. S. Quimby and W. J. Miniscalco, "Modified Judd–Ofelt technique and application to optical transitions in Pr^{3+}–doped glass," *Journal of Applied Physics*, vol. 75, no. 1, pp. 613–615, 1994.

[3.37] P. Goldner and F. Auzel, "Application of standard and modified Judd–Ofelt theories to a praseodymium–doped fluorozirconate glass," *Journal of Applied Physics*, vol. 79, no. 10, pp. 7972–7977, 1996.

[3.38] P. Goldner, "Accuracy of the Judd–Ofelt theory," *Molecular Physics*, vol. 101, no. 7, pp. 903–908, 2003.

[3.39] D. E. McCumber, "Theory of phonon-terminated optical masers," *Physical review*, vol. 134, no. 2A, p. A299, 1964.

[3.40] W. J. Miniscalco and R. S. Quimby, "General procedure for the analysis of Er^{3+} cross sections," *Opt. Lett.*, vol. 16, no. 4, pp. 258–260, 1991.

Chapter 4

Numerical Modelling Techniques

In the previous chapter, the experiment, measurement and the techniques for the extraction of spectroscopic parameters that form the defining characteristics of a bulk material, optical amplifier and lasers were presented. The spectroscopic parameters like absorption/emission cross section, radiative and non-radiative lifetimes can all be used to predict the behaviour of a glass material in a device context. Producing design and analysis tools reduces the time between rapid device optimisation and actual manufacture besides guiding investment in personnel and experimental techniques. In the optical terrain, modelling is not a difficult issue given the simplicity of optical fibre geometry [4.1]. Optical fibres are characterised by low level of rare-earth doping because of the length of the gain medium and consequently the population density of the system can be easily modelled using linear terms alone. Approximate analytical methods have also been used to solve the propagation equations along the length of a fibre [4.2–4.5]. The modelling of an active device becomes challenging for short interaction lengths with particularly high doping concentrations. This is because the population density equation becomes nonlinear with the introduction of second-order processes like cross-relaxation and energy-transfer up-conversion (see section 2.3). Different numerical methods which lend themselves to computational analysis exist to solve this problem [4.6–4.10]. The need to

optimise computational time makes it less efficient to adopt some of techniques previously proposed.

This chapter aims at developing a simplified model using the method of rate-equations for the optimisation of erbium and praseodymium doped bulk materials, lasers and amplifiers. Photoluminescence is a precursor to amplification and consequently lasing and therefore, the modelling of photoluminescence forms the first part of our discussion. The subject is presented as follows: Section 4.1 introduces the derivation of the rate equations describing the interaction between rare-earth ions after a pump excitation and the energy-levels based on the spectroscopic properties of lifetime, absorption and emission parameters. This section also highlights how increase in concentration and lifetimes results in stiff rate equations and the methods adopted to solve them. Section 4.2 introduces an evolutionary algorithm used to obtain the parameters that relate to ion-ion interactions difficult to measure experimentally. Having laid the foundation for a simplified model in a bulk material, the rate equation model is combined in a couple-solution technique with the power propagation equation in Section 4.3 to describe and formulate the population inversion/lasing between excited levels along the length of a fibre. This is followed Section 4.4 which discusses the modelling of amplified spontaneous emission (ASE) in a fibre laser. Section 4.5 presents the derivation of a thermal model to describe the optimum operation of a fibre. Finally the summary of this chapter is presented in section 4.6.

༄༅༅༅༅༅
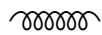
4.1   Rate Equation Formulation

Similar to Newton's first law of motion, the rare-earth ions in a doped material remain in the rest state until an external excitation is exerted in the form of heat, vibration energy

or energy from a pump photon. Ions are excited from a rest state known as ground state at a rate (R_p) proportional to the strength of the excitation pump flux. If the ions acquire enough energy to overcome the potential difference associated with the energy gap to the next level $(E_2 - E_1)$, then the ions will be absorbed by the energy level 2. At this level, the ions either absorb another photon to promote them to higher states or loose the state-energy and relax back to Level 1. Figure 4.1 shows the processes that lead to excitation and decay in a system made up of 2 energy levels.
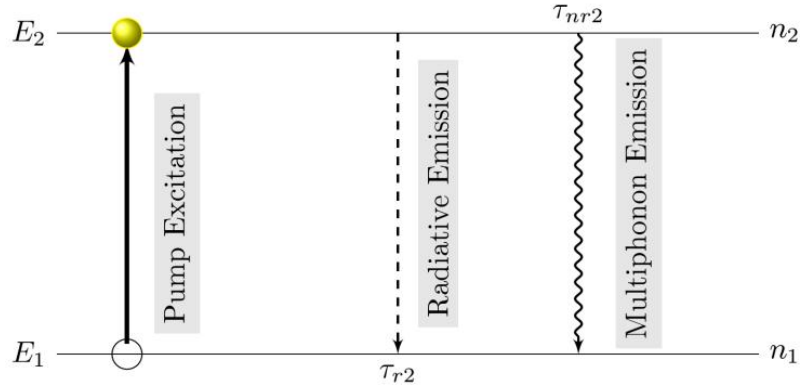
Figure 4.1: Excitation and decay processes for a simple 2-level system

Based on Figure 4.1, the rate of decay from any level i is a function of the contribution or depletion through pump excitation, multiphonon decay and spontaneous emission processes. This is mathematically described in rate equations 4.1 for the population densities of the two states:

$$
\begin{aligned}
\frac{dn_1}{dt} &= -n_1 R_{p12} + n_2 R_{p21} + \frac{n_2}{\tau_{r2}} + \frac{n_2}{\tau_{nr2}} \\
\frac{dn_2}{dt} &= n_1 R_{p12} - n_2 R_{p21} - \frac{n_2}{\tau_{r2}} - \frac{n_2}{\tau_{nr2}}
\end{aligned}
\tag{4.1}
$$

Where the term $n_1 R_p$ is the pump excitation term, $n_2 R_p$ is the stimulated emission of the pump. $\frac{n_2}{\tau_{r2}}$ is the radiative or spontaneous emission term and $\frac{n_2}{\tau_{nr2}}$ is the non-radiative or multiphonon emission term. τ_{r2} is the radiative lifetime and τ_{nr2} is the non-radiative lifetime.

The two rate equations describing the 2 energy levels are linearly dependent as one

equation is determined from the other. This 2-dimensional linear system of rate equations has rank of 1. Therefore to produce a system with full rank, with solutions at steady-state, one of the equations is replaced by the conservation of mass equation. This states that the total occupation number is the total number of ions in the system which forms the distribution to all excited states as stated in equation 4.2

$$n_1 + n_2 = N_d \tag{4.2}$$

Solving the equation 4.1 with the condition $n_1(t) = N_d$ (for initial rest state, here N_d is a constant that represents the total ion concentration of the system), produces an initial value problem. The temporal evolution of the population densities of the 2-level system represented by n_1, n_2 in equation 4.1 can be calculated by integration of the rate equations. The photoluminescence arising between two energy-levels i and j in steady state can be expressed as equation 4.3

$$PL_{ij} = \frac{hc\beta_{ij}n_i}{\lambda_{ij}\tau_{ri}} \tag{4.3}$$

where n_i is the population density per unit volume in the ith state, λ_{ij} is the transition wavelength, β_{ij} is the spontaneous emission probability between the two levels, τ_{ri} the radiative lifetime of level i. h is Plank's constant, c is the speed of light. It is clear from equation 4.3 that the photoluminescence intensity can be increased by increasing the doping concentration and/or decreasing the radiative lifetime.

In low concentration samples, the solution of the rate equation is straight forward. In steady state, the equations for a 2-level system can be reduced to a set of algebraic equations, represented in the following matrix form:

$$\begin{bmatrix} R_{p12} & -(R_{p21} + \frac{1}{\tau_{r2}} + \frac{1}{\tau_{nr2}}) \\ 1 & 1 \end{bmatrix} \times \begin{bmatrix} n_1 \\ n_2 \end{bmatrix} = \begin{bmatrix} 0 \\ N_d \end{bmatrix} \tag{4.4}$$

The self consistent solution of the level populations is then given by

$$n_1 = \frac{N_d\left(\tau_{nr2} + \tau_{r2} + R_{p21}\tau_{nr2}\tau_{r2}\right)}{\tau_{nr2} + \tau_{r2} + R_{p12}\tau_{nr2}\tau_{r2} + R_{p21}\tau_{nr2}\tau_{r2}} \tag{4.5}$$

$$n_2 = N_d - n_1 \tag{4.6}$$

In a high concentration sample on the other-hand, the gaps between ions reduces causing them to interact with each other. Two ions in level 2 can interact by energy-transfer upconversion whereby one ion loses its excitation energy and relaxes to level 1 while the other gets promoted to a higher level 3. Also the ion in level 3 can relax to an intermediate level 2, producing an excitation energy that promotes another ion in level 1 to the intermediate Level 2. This interaction introduces non-linear terms to the rate equations in a form xN_iN_j. Where x is the number of ions involved in the interaction between levels i and j, N_i and N_j are the ion population values of levels i and j respectively.

The resulting complex rate equation especially in a multi-level system can only be solved with time-domain techniques. In different hosts also, the values of lifetimes (τ_r and τ_{nr}) may vary widely resulting in unusual condition number of the coefficient matrix. The faster processes are usually associated with τ_{nr} especially for host materials having high phonon energy and small energy gap between band transitions. Because of the relative magnitude of τ_{nr} (< 1 μs) with respect to τ_r (> 1ms) in some host materials, numerical solution would require a fairly small temporal step size for stability. This also implies that the slower processes of radiative transition forces the computation to be performed over a longer time period. Generally, this characteristic equation with different time scales often referred to as "stiff-system", requires many numerical steps for accurate results. This kind of problem is not unique and is often found in nature, control systems, chemical processes and electrical systems

A standard technique best suited for this kind of problem is the Runge-kutta method. In this work we have adopted hybrid techniques to speed up computation. Energy-levels that possess very fast multiphonon-decays (< 1 μs)are combined with the level below

them($^4F_{7/2}$, $^2H_{11/2}$ and $^4S_{3/2}$ in erbium) while Boltzmann's distribution is used to calculate the population distribution. This approximation significantly reduces computational time in steady-state analysis when pumped with continous wave pump. In pulsed excitation where the evolution at small time scales are required, we have adopted an implicit technique that automatically switches between the Adams-Bashforth-Moulton and the 4th order Runge-Kutta ODE solvers.

4.2   Particle Swarm Optimisation Technique

Second-order parameters that feature as ion-ion interactions in high concentration samples are difficult to measure experimentally. One of the methods previously adopted to study upconversion include the threshold technique [4.11]. The experimental procedure involves the measurement of threshold values of the infrared and upconversion powers to evaluate and quantify the efficiency of the upconversion process. Another method is the Action spectrum experiment [4.12] which has been used to measure upconversion efficiency under sun-like excitation. Both methods [4.11,4.12] are both rigorous in principle and difficult in practice and not suitable for repeated measurements on a wide variety of rare-earth doped samples with varying levels of pump excitation and ion-concentrations.

In an effort to predict the values of the non-linear coefficients responsible for up-conversion, an evolutionary algorithm is applied to the non-linear rate equations in steady-state. The evolutionary algorithm of choice is the Particle Swarm Algorithm. Particle swarm optimization (PSO) is an artificial intelligence(AI) technique that is able to find approximate solutions to difficult numerical problems especially ones with many search space and many local minima [4.13]. The stochastic nature of the algorithm makes it highly efficient in optimizing a large set of parameters with operations in discontinuous solutions domains. Previously genetic algorithm (GA) was applied to multistage erbium doped fibre amplifiers(EDFA), optimising such properties like pumping scheme and pump-power allocation [4.14]. Also GA was applied to EDFA for obtaining maximum gains and bandwidths, optimising three parameters: fibre length, pumping

wavelength and signal power [4.15]. However, in another related work on EDFA, a design approach using particle swarm optimisation algorithm was adopted [4.16]. The authors [4.16] optimised six parameters including pump wavelength, input signal power, numerical aperture, doped core radius, ion concentration and fibre length. Benchmarking the PSO [4.16] technique with the GA [4.14,4.15] approach, it was shown that there was significant computational cost for the optimization in using genetic algorithm compared to particle swarm optimization technique. Since most typical systems by the rate equation technique are multi-level in nature and there's significant computation already, the natural option was to use PSO. To the best of the author's knowledge, this is the first time PSO is being used to extract upconversion parameters in an erbium based host using two different wavelengths as presented in chapter 5. In this section, we will proceed with laying out the basics of PSO as applied to this research.

The solution to a problem in PSO is called a particle. At every point in time, the particle i has a position in the search space represented by the equation 4.7

$$Particle_i^t = \left[C_{i,1}^t, C_{i,2}^t, C_{i,3}^t, ... \right] \tag{4.7}$$

Every particle has a *Velocity* property at a time t in the search space. The particles are able to adjust their flight trajectories using the information from the velocity property based on the equation 4.8

$$\vartheta_{ip}(k+1) = \omega\vartheta_{ip}(k) + C_1 r_1 (X_{ip} - \chi_{ip}) + C_2 r_2 (X_{gp} - \chi_{ip}) \tag{4.8}$$

where $p = 1, 2, ..10$ based on a population size 10, ϑ_{ip} is the velocity of the particle, χ_{ip} is the position of the particle (this stores the values of the second order coefficient at a point in space) and ω is the static inertia weight chosen from the interval [0,1]. This controls how the past velocity of the particle affects the current one thus influencing the exploration capability of the algorithm in both local and global space. $C_1, C_2 \epsilon \Re$ constants influencing the local and global best solutions respectively, C_1 is the cognitive acceleration coefficient, C_2 is the social acceleration coefficient. r_1, r_2 are pseudo-random numbers selected from

a uniform distribution U(0,1). X_{ip} is the personal best of particle i, also referred to as the best position vector encountered by the particle i. $X_{gp}$is the global best position of the entire swarm, also referred to as the best position encountered by the entire swarm of particles.

Equation 4.8 indicates that the new velocity of the ith particle is a function of three terms: the particle's previous velocity, the distance between the particle's best previous and current position and finally the distance between the swarms' best experience (the position of the best particle in the swarm) and i^{th} particle's current position.

Every particle also has a *Position* property in the search space. This property shows how close a particle is to the solution by measuring its performance with a predefined fitness function. The position property is iteratively manipulated according to the result from the velocity check of equation 4.8 by

$$\chi_{ip}(current) = \chi_{ip}(previous) + \vartheta_{ip}(updatedvelocity) \tag{4.9}$$

With an initial set of randomly generated parameters (ion-ion interactions), the algorithm follows the path with the fintess function and calculates the error at each point up to a predefined tolerance value. To define the fitness function, we integrated the area under the photoluminescence bands and stored them as a vector A. The rate equation photoluminescence calculated for all the energy levels using equation 4.3 was stored as a vector B. The fitness function is the standard deviation between A and B. The algorithm stops after a maximum number of iterations or when the fitness function returns a value below a threshold. The particles in this algorithm are the ion-ion interactions of upconversions and cross-relaxations. Figure 4.2 shows the implementation of the particle swarm technique with the rate equations in a flow diagram.

4.3 Laser propagation formulation

In the last section, the rate equation formulation describing the evolution of ions among the energy levels of a pumped material has been presented together with the solution

Figure 4.2: Particle Swarm Algorithm

techniques for optimising the parameters describing non-linear systems. This is then taken forward in application to the modelling of gain in a laser system and the conditions that lead to population inversion.

Following an excitation, the ions making up a material gets distributed to energy

levels by the processes of absorption, spontaneous emission, stimulated emission and multiphonon decay. Redistribution of atomic energy levels is essential for the onset of laser action. At equilibrium temperature, more atoms reside in low energy states than in higher ones. Following an excitation, the continuous process of absorption and emission is statistically constant. However a population inversion will take place when more atoms exist in the higher energy states than in the lower ones. The energy difference between these two energy levels corresponds to the energy of the photons of the lasing wavelength.

Based on this description, two broad categories of laser systems are possible: three-level lasers and four-level lasers. Figure 4.3 and Figure 4.4 show the laser systems
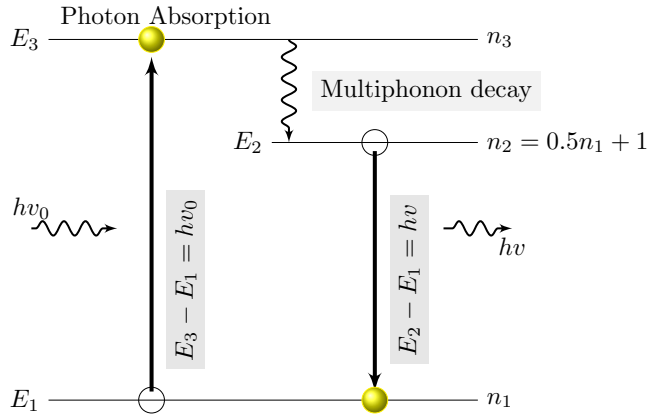
Figure 4.3: Three Level Laser System

A three level system has the advantage that there is a single transition ($E_3 \rightarrow E_2$) which does not contribute to the laser output as opposed to two transitions ($E_4 \rightarrow E_3$, $E_2 \rightarrow E_1$) in a four level system. In a 3-level system, the laser transition ends on the ground state. Population inversion only occur when half of the ions are pumped into the upper laser level and therefore, the laser medium must be very strongly pumped. On the other hand, a lower threshold pump power is required in a four-level system [4.17,4.18] where the lower laser level is above the ground state and multiphonon decay helps to quickly depopulate it. Because of this, four-level laser system is more efficient than its three-level counterpart and most practical lasers are based on the four-level system. A four-level system also requires just one electron to achieve population inversion while a three-level system requires at
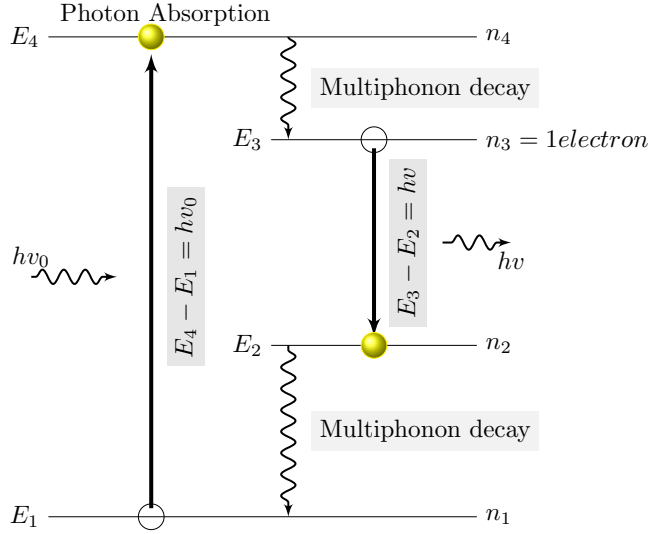
Figure 4.4: Four Level Laser System

least one electron more than half the population of the ground state to achieve population inversion. A four-level system usually has a near-empty lower laser level and population inversion is easily achieved as soon as n_3 level starts getting populated. The quantum efficiency of a three-level laser $(\frac{E_3 - E_1}{E_p - E_1})$ is greater than those of a four-level laser $(\frac{E_3 - E_2}{E_p - E_1})$. Fluorescence occurs between the upper and lower lasing levels with a total time of τ, made up of radiative τ_r and non-radiative τ_{nr} transitions.

The solution technique to this rate equation follows the same format as those in previous sections. The atomic gain of this system is proportional to the amount of population inversion Np achieved within the system given by equation 4.10

$$N_p = n_2 - n_1 \tag{4.10}$$

To deduce the evolution of N_p, it is generally assumed that the relaxation time of the lasing transition lifetime τ_2 is slower than that of the pumped level τ_3.

4.3.1 Gain Modelling

In this section we derive the gain parameter and consequently the propagation equations that define the fibre amplifier and laser. Consider a small segment of the fibre with length Δz, a cross-sectional area A, and N_i representing the atoms in a 2-level system. The lower-level experiences an effective area determined by its cross section σ_{12} for power absorption. The upper-level has an effective area determined by its emission cross section σ_{21}. The total absorbing volume by effective cross section is then $N_1\sigma_{12}A\Delta z$ at the lower level. The total emitting volume by effective cross section is $N_2\sigma_{21}A\Delta z$ at the upper level. Therefore the fraction of the net power incident on the cross sectional Area(A) relates to the effective emission and absorption by equation 4.12. The negative sign in equation 4.13 indicates the net decay with distance for the power P travelling through the medium, where g_{opt} is the optical gain of the atomic levels 1 and 2.

$$\left(\frac{\Delta P_{abs}}{P}\right) A = (N_1\sigma_{12}A\Delta z - N_2\sigma_{21}A\Delta z) \tag{4.11}$$

$$\left(\frac{\Delta P_{abs}}{P}\right) A = (N_1\sigma_{12} - N_2\sigma_{21})A\Delta z \tag{4.12}$$

$$\frac{dP}{dz} = \lim_{\Delta z \to 0} \left(\frac{\Delta P_{abs}}{\Delta z}\right) = -(N_1\sigma_{12} - N_2\sigma_{21})P = -g_{opt}P \tag{4.13}$$

Propagation through the fibre introduces a gain g_{opt} as a result of the cross sections and a loss α due to the material property of the fibre. Given this background, we can apply the same analysis to a 3-level system in cascade lasing configuration. Compared to lasing at a single wavelength, the cascade lasing technique offers the opportunity of efficiently depopulating Level 2. This process helps to achieve population inversion more reliably with reduced heat generation than relying on phonon-assisted transition. Cascade lasing has been demonstrated to produce 5 times higher signal output at a comparably shorter length compared with the traditional single laser wavelength scheme [4.19].
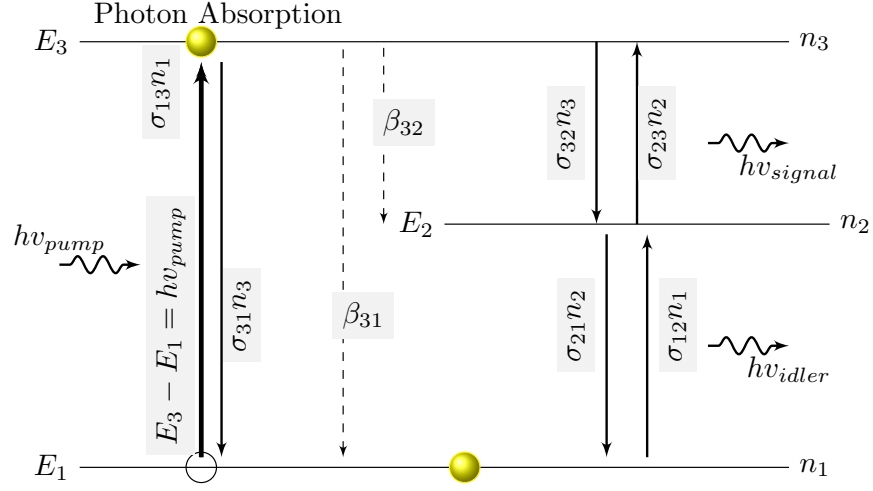
Figure 4.5: Cascade scheme with simultaneous lasing at λ_{signal} and λ_{idler}

Equation 4.14 is the rate equation for a 3-level system in cascade lasing scheme

$$
\begin{aligned}
\dot{n_1}(z) &= \underbrace{-n_1\sigma_{13}R_p}_{pump\ absorption\ term} +n_3\sigma_{31}R_p + \frac{n_1}{\tau_{r1}} + \frac{n_2}{\tau_{nr2}} + \frac{\beta_{31}n_3}{\tau_{r3}} + (n_2\sigma_{21} - n_1\sigma_{12})R_{id} \\
\dot{n_2}(z) &= \frac{-n_2}{\tau_{r2}} - \frac{n_2}{\tau_{nr2}} + \frac{\beta_{32}n_3}{\tau_{r3}} + \frac{n_3}{\tau_{nr3}} - \underbrace{(n_2\sigma_{21} - n_1\sigma_{12})R_{id}}_{Idler\ lasing\ term} + (n_3\sigma_{32} - n_2\sigma_{23})R_s \\
\dot{n_3}(z) &= \frac{-n_3}{\tau_{r3}} - \frac{n_3}{\tau_{nr3}} + n_1\sigma_{13}R_p - \underbrace{n_3\sigma_{31}R_p}_{pump\ stimulated\ emission\ term} - \underbrace{(n_3\sigma_{32} - n_2\sigma_{23})R_s}_{Signal\ lasing\ term}
\end{aligned}
$$

$$(4.14)$$

$$
\dot{n_1}(z) + \dot{n_2}(z) + \dot{n_3}(z) = N_d \tag{4.15}
$$

where $R_w = \frac{P_w}{h v_w A_{core}}$ is the photon flux rate and the subscript 'w' is 'p' for the pump, 'id' for the idler and 's' for signal while P_w denotes the power, h is the Planck's constant, A_{core} is the area of the fibre core. σ_{ij}, σ_{ji} $(i < j)$ are absorption and emission cross sections respectively for the transition. β_{ij} is the branching ratio or spontaneous emission probability from level i to j. Complementing with equation 4.15 transforms the rate equations into a system with full rank.

The spatial evolution of the powers for the pump, signal and idler given a cascade

lasing configuration are therefore given by the following ordinary differential equations

$$\frac{dP_p^\pm (\lambda_p)}{dz} = \pm \Gamma_p (\lambda_p) P_p^\pm (\lambda_p) (\sigma_{13} N_1 - \sigma_{31} N_3) \pm \alpha(\lambda_p) P_p^\pm(\lambda_p) \qquad (4.16)$$

$$\frac{dP_{s1}^\pm (\lambda_{s1})}{dz} = \pm \Gamma_{s1} (\lambda_{s1}) P_{s1}^\pm (\lambda_{s1}) (\sigma_{23} N_2 - \sigma_{32} N_3) \pm \alpha(\lambda_{s1}) P_{s1}^\pm(\lambda_{s1}) \qquad (4.17)$$

$$\frac{dP_{s2}^\pm (\lambda_{s2})}{dz} = \pm \Gamma_{s2} (\lambda_{s2}) P_{s2}^\pm (\lambda_{s2}) (\sigma_{12} N_1 - \sigma_{21} N_2) \pm \alpha(\lambda_{s2}) P_{s2}^\pm(\lambda_{s2}) \qquad (4.18)$$

Each of the equations id made up of both amplification and background loss terms, and represents both the forward and backward propagation for the respective wavelengths. The symbol '$\pm$' represents the direction of the travelling waves. The total power at any point z along the fibre is the sum of the waves travelling in both directions given by equations 4.19, 4.20 and 4.21.

$$P_p(\lambda_p) = P_p^+(\lambda_p) + P_p^-(\lambda_p) \qquad (4.19)$$

$$P_s(\lambda_s) = P_s^+(\lambda_s) + P_p^-(\lambda_p) \qquad (4.20)$$

$$P_{id}(\lambda_{id}) = P_{id}^+(\lambda_{id}) + P_{id}^-(\lambda_{id}) \qquad (4.21)$$

Γ is the overlap factor which defines the fraction of the power 'seen' by the doped core. Γ can be expressed as equation 4.22 [4.20]

$$\Gamma = 1 - e^{\left(-\frac{2b^2}{W_0^2}\right)} \qquad (4.22)$$

$$W_0 = a \left(0.761 + \frac{1.237}{V^{1.5}} + \frac{1.429}{V^6}\right) \qquad (4.23)$$

Where W_0 is the mode field radius given by equation 4.23, a is the diameter of the fibre core, b is the dopant radius of the core. For uniform doping concentration, b is assumed to be $a/2$. V is the normalized frequency. Equation 4.14 can be solved at steady-state for ion evolution at a small segment Δz of the fibre. Combining this solution with propagation across the entire fibre length results in the integration of 4.16 , 4.17, 4.18. At both fibre ends, i.e. $z = 0 \ or \ L$, the mirrors reflects the co- and counter-propagating photon fluxes

into each other. If we denote the reflectivity of input and output mirror by $R_{in}(\upsilon)$ and $R_{out}(\upsilon)$ respectively, we get the boundary conditions:

$$
\begin{aligned}
\phi^+(\upsilon,0) &= R_{in}(\upsilon)\phi^-(\upsilon,0) + T_{in}(\upsilon)\phi_p(\upsilon) \\
\phi^-(\upsilon,l) &= R_{out}(\upsilon)\phi^+(\upsilon,l) \\
\phi^+(\varphi,0) &= R_{in}(\varphi)\phi^-(\varphi,0) \\
\phi^-(\varphi,l) &= R_{out}(\varphi)\phi^+(\varphi,l) \\
\phi^+(\psi,0) &= R_{in}(\psi)\phi^-(\psi,0) \\
\phi^-(\psi,l) &= R_{out}(\psi)\phi^+(\psi,l)
\end{aligned}
\tag{4.24}
$$

The next section deals with the solution of the propagation equations.

4.3.2 Steady State Lasing Algorithm

Steady-state analysis of semiconductor lasers use algorithms that are based on the fixed point iteration method. The fixed point iteration methods of separate solution method (SSM) and coupled solution methods (CSM) are in use in numerical simulation of optical devices. Studies on both have found the latter to be more stable than the former [4.21]. The rate and gain equations that describe fibre lasers and amplifier operations in the previous sections are coupled differential equations whose solution technique is analogous to the coupled solution method. Though other techniques like the relaxation method (RM) and the shooting method with newton Raphson method (SM-NRM) have recently been implemented with improved efficiencies [4.22], the simplicity of the CSM algorithm makes it an attractive choice. Figure 4.6 shows the algorithm listing for the coupled solution method.

The calculation procedure solves the set of rate and propagation equations along the fibre of length L which is divided into m segments along the longitudinal axis which then yields a spatial resolution of $dz = \frac{L}{m}$ (see figure 4.7). The population density of each segment is unique and the pump and signal photon fluxes are calculated at the ends of

procedure ONESTEPSEGMENT$(z, P_s^\pm, P_p^\pm)$

$[n_0, n_1, n_2] \leftarrow \frac{dn}{dt} = 0$

do $\begin{cases} \textbf{comment: } \text{Optical gain Equations} \\ \frac{dP_p^+}{dz} \leftarrow -\Gamma_p P_p^+ (\sigma_{02} n_0 - \sigma_{20} n_2) - \alpha P_p^+ \\ \frac{dP_p^-}{dz} \leftarrow \Gamma_p P_p^- (\sigma_{02} n_0 - \sigma_{20} n_2) + \alpha P_p^- \\ \frac{dP_s^+}{dz} \leftarrow -\Gamma_s P_s^+ (\sigma_{12} n_1 - \sigma_{21} n_2) - \alpha P_s^+ \\ \frac{dP_s^-}{dz} \leftarrow \Gamma_s P_s^- (\sigma_{12} n_1 - \sigma_{21} n_2) + \alpha P_s^- \end{cases}$

return $(\frac{dP_p^\pm}{dz}, \frac{dP_2^\pm}{dz})$

main

$P_p^+ \leftarrow Pump\ Power\ at\ L = 0\ (left\ facet)$

while $error \geq tolerance$

do $\begin{cases} start \leftarrow \phi(i, L) \\ \textbf{comment: } \text{forward integration} \\ \phi(i, L) \leftarrow \textbf{output }(0, \text{ONESTEPSEGMENT}(L, P^\pm)) \\ \textbf{comment: } \text{Reflectivities right facet} \\ \begin{cases} \phi^-(\upsilon, l) \leftarrow R_{out}(\upsilon)\phi^+(\upsilon, l) \\ \phi^-(\varphi, l) \leftarrow R_{out}(\varphi)\phi^+(\varphi, l) \\ \phi^-(\psi, l) \leftarrow R_{out}(\psi)\phi^+(\psi, l) \end{cases} \\ \textbf{comment: } \text{Backward integration} \\ \phi(i, L) \leftarrow \textbf{output }(L, \text{ONESTEPSEGMENT}(0, P^\pm)) \\ \textbf{comment: } \text{Reflectivities left facet} \\ \begin{cases} \phi^+(\upsilon, 0) \leftarrow R_{in}(\upsilon)\phi^-(\upsilon, 0) \\ \phi^+(\varphi, 0) \leftarrow R_{in}(\varphi)\phi^-(\varphi, 0) \\ \phi^+(\psi, 0) \leftarrow R_{in}(\psi)\phi^-(\psi, 0) \end{cases} \\ error \leftarrow start - \phi(i, L) \end{cases}$

$P_{s1}(out) \leftarrow (1 - R_{out}(\upsilon))\phi^+(\upsilon, l)$

$P_{s2}(out) \leftarrow (1 - R_{out}(\varphi))\phi^+(\varphi, l)$

Figure 4.6: Laser modelling with coupled solution method

the segments.

The propagation equation described in equations 4.16,4.17 and 4.18 are solved for the forward propagation for powers at the end (right facet, z=L) of the fibre. In the next step, the reflectivities of the terminating mirrors are used to calculate the backward propagation powers (towards the left facet) and the initial values of pump $P_p^+(0) = P_{pump}$ and signal powers $P_{s1}^+ = 0, P_{s2}^+ = 0$. The total power at any point along the fibre is the sum of both forward and backward propagating power. The power values at all discrete z positions of the fibre are stored in arrays which makes it easy for computation using MATLAB. This
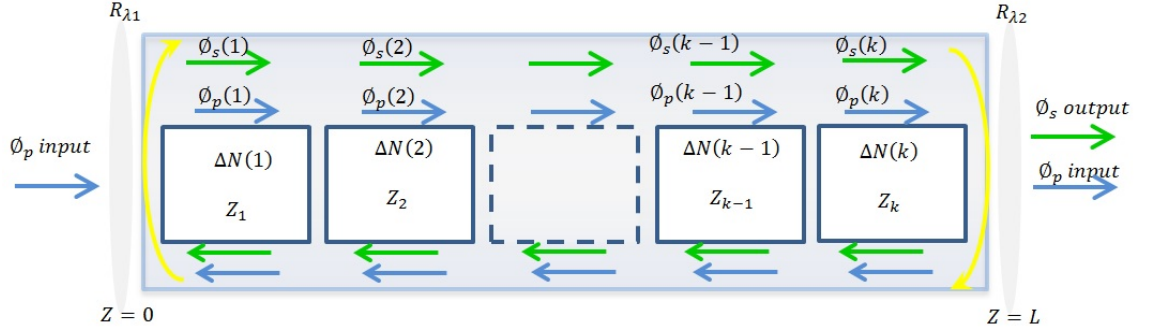
Figure 4.7: Schematic representation of the longitudinal discretisation in fibre laser cavity

process is repeated until subsequent calculations produce converging powers values.

4.4   Modelling Amplified Spontaneous Emission

In practice, higher concentration of rare-earth doping leads to short interaction length for the complete absorption of the pump photon whereas lower concentration requires longer fibre length. This is to account for the optimum number of ions per unit volume for the excitation photons. With longer fibre length however, amplification in the gain medium is accompanied by the process of amplified spontaneous emission. This phenomenon can be detrimental to the operation of an optical fibre amplifier [4.1] and consequently lasing operation. The equations 4.16, 4.17 and 4.18 describing the evolution of the pump and signal power are complemented with equation 4.25 that accounts for the power build-up from the process of amplified spontaneous emission.

$$
\begin{aligned}
\frac{dP_{ase}^{\pm}(\lambda_k)}{dz} &= \pm\Gamma_{ase}(\lambda_k)\,P_{ase}^{\pm}(\lambda_k)\,(\sigma_{abs}N_2 - \sigma_{ems}N_1) \mp \alpha(\lambda_k)P_{ase}^{\pm}(\lambda_k) \quad (4.25)\\
&\pm \left(\frac{2hc^2\Delta\lambda}{\lambda_k^3}\right) M\Gamma_{ase}(\lambda_k)\,\sigma_{ems}N_2
\end{aligned}
$$

The additional term $P_0 = \frac{2hc^2}{\lambda^3}$ [4.1,4.20,4.23] accounts for the contribution of spontaneous emission to the power density of a single mode (ASE). The factor '2' stands for the number of polarizations that can be propagated per mode. Where M is the effective

number of modes, c is the speed of light in the free space. The ASE spectrum is usually divided into slots of width $\Delta\lambda$ with typical values 1 nm – 4 nm and λ_k is the wavelength of the kth slot. The ASE slots are assumed to be coupled into the fundamental mode of the gain medium. If the ASE region under consideration is from λ_a to λ_b, with a resolution of $\Delta\lambda$, we have $Eq_{ase} = \frac{\lambda_b - \lambda_a}{\Delta\lambda}$ equations for each of forward ASE(+) and backward ASE(-). Therefore, the propagation equations combined with 4.16, 4.17 and 4.18 form a system of $2(Eq_{ase} + 3)$ coupled differential equations, which are solved iteratively by numerical integration along the length of the fibre. The ASE in the forwards and backwards directions are generated within the fibre itself and therefore the initial ASE powers are zero. The boundary conditions with the addition of the ASE are stated in equation 4.26

$$P_{ASE}^{+}(z = 0) = 0 \tag{4.26}$$

$$P_{ASE}^{-}(z = L) = 0 \tag{4.27}$$

With the introduction of ASE, the signal absorption $(W_{23} = \phi_{23}R_s)$ and emission terms $(W_{32} = \phi_{32}R_s)$rate in equation 4.14 is modified to produce equation 4.28

$$W_{23} = \Gamma_s \left(\frac{\sigma_{23}P_s(z)}{A_c hc} \right) \tag{4.28}$$

4.5 Thermal Model Formulation

The operation of efficient high-power fibre lasers is limited by heating effects in the laser active media under a pump excitation. Although most optical glass materials have a high transition temperature (T_g) up to a few hundred $^o C$, without cooling, excess heat can fracture the core. Two major sources of heat have been identified; Pump controlled quantum defect (PCQD) and Inherent relaxation losses (IRL). In this section, we developed equations that define each of the losses and then produce a model to describe the heat loss in a double-clad fibre laser.

4.5.1 Pump Controlled Quantum Defect

The energy of a pump photon is usually higher than those of the signal photon except in upconversion lasers. Since this energy difference is not turned into photons, the resulting quantum defect is passed off as heat at the lasing wavelength. The quantum defect can be controlled by tuning the pump ($\omega_p = \dfrac{c}{\lambda_p}$) and signal ($\omega_s = \dfrac{c}{\lambda_s}$) emission frequencies. Equation 4.29 states the quantum defect in a gain medium.

$$q = h(\omega_p - \omega_s) = h v_p \left(1 - \frac{\lambda_p}{\lambda_s} \right) \tag{4.29}$$

It is often defined as a percentage η, referring to the parentheses in equation 4.29. The heat produced in a short length Δz is given by

$$Q_{PCQD}(z) = \eta \alpha_{abs}(z) I_p(z) \Delta z \tag{4.30}$$

$$\alpha_{abs} = \Gamma_p \alpha_{GSA} n_0(z) \tag{4.31}$$

where α_{abs} is the pump absorption coefficient coefficient given by equation 4.31, $I_p(z) = \dfrac{P_p}{A_{core}}$ is the total pump intensity at any axial location z. Γ_p is the confinement factor, $n_0(z)$ is the population density of the ground state at any point z. Q_{PCQD} therefore has a similar distribution to the pump power distribution.

4.5.2 Inherent Relaxation Losses

Unlike quantum defects, inherent relaxation losses arise as a result of material properties linked to the vibrational energy and doping concentration of the host glass. These physically inherent losses are multiphonon relaxations, cross-relaxation on intermediate levels and up-conversion from the emitting levels.

   The amount of heat generated by multiphonon transitions is proportional to the energy difference converted to heat times the rate at which the transition occurs in a unit volume. The heat generated within a doped core section of length Δz per unit time is given by equation 4.32

$$Q_{nr}(z) = \left(\frac{n_i(z)}{\tau_{nrij}}\right) h\Delta v_{ij} \tag{4.32}$$

where n_i is the ion population of the energy level i with a multiphonon lifetime τ_{nri}.

Energy transfer between paired ions do not create heat by themselves but promote ions to energy-levels that are attractive to multiphonon relaxations. The heat generated by energy-transfer within a section of the core is given by equation 4.33. Cross relaxation processes results in cooling hence the negative sign [4.24].

$$Q_{ET}(z) = \rho_{UC}n_i(z)n_j(z)h\Delta v_{ij} - \rho_{CR}n_a(z)n_b(z)h\Delta v_{ab} \tag{4.33}$$

where ρ_{UC} and ρ_{CR} are the concentration dependent upconversion and cross relaxation rates. n_i and n_j are the axial ion population densities of energy levels i and j involved in the ion upconversion. $v_{ij} = \frac{c}{\lambda_{ij}}$ is the optical frequency of the upconversion transition. n_a and n_b are the axial ion population densities of energy level a and b involved in the cross relaxation process. $v_{ab} = \frac{c}{\lambda_{ab}}$ is the optical frequency difference of the cross relaxation process.

4.5.3 Heat model of a double-clad fibre laser

The steady-state heat equations for a double clad fibre in the radial(r) and axial(z) direction under air cooling are given by equation 4.34 [4.25]

$$\frac{1}{r}\frac{\partial}{\partial r}\left(r\frac{\partial T}{\partial r}\right) + \frac{\partial^2 T}{\partial z^2} = \begin{cases} -\frac{Q(r,z)}{K_c} & \text{core } 0 \leq r_{core} \leq r_1 \\ 0 & \text{clad } r_1 \leq r_{clad} \leq r_2 \end{cases} \tag{4.34}$$

where r_1 and r_2 are the core and cladding radius respectively. k_c is the thermal conductivity of the fibre. Q(r,z) is the thermal power density given by the sum of all heat sources generated within the core of the fibre. It is expressed by equation 4.35

$$Q(r,z) = Q_{PCQD} + Q_{nr} + Q_{ET} \tag{4.35}$$

In developing the boundary conditions, we reexamine the fibre geometry for continuities. The temperature and their derivaties at the boundary from the core to the clad are continous ($r_{core} = r_1$, $r_{clad} = r_1$) . This is expressed by equation 4.38

$$
\begin{aligned}
T_{core} &= T_{clad}, \quad r_{core} = r_{clad} = r_1 & (4.36) \\
\frac{\partial T_{core}}{\partial r} &= \frac{\partial T_{clad}}{\partial r} & (4.37)
\end{aligned}
$$

In addition, we expect that the temperature will be at its maximum at the centre of the fibre. Equation 4.38 expresses the zero gradient expected at the core centre.

$$
\frac{\partial T_{core}}{\partial r} = 0, \quad r = 0, z = 0 \rightarrow L \tag{4.38}
$$

At the boundary of the inner cladding where $r_{clad} = r_2$, we assume Newton's law of cooling which produces the final boundary condition in equation 4.39

$$
k\frac{\partial T_{clad}}{\partial r} = h\left[T_c - T(r,z)\right], \quad r = r_2 \tag{4.39}
$$

where h is the convective coefficient. T_c is the heat sink temperature.

The solution of the heat equation with the boundary conditions produces an analytic expression for the temperature distribution in the double clad fibre given by equation 4.41 [4.25]

$$
\begin{aligned}
T_{core}(r) &= T_c + \frac{Q_0 r_1^2}{2k}\left[ln\left(\frac{r_2}{r_1}\right) + \frac{k}{r_2 h} + \frac{1}{2} - \left(\frac{r^2}{2r_1^2}\right)\right](0 \le r \le r_1) & (4.40) \\
T_{clad}(r) &= T_c + \frac{Q_0 r_1^2}{2k}\left[\frac{k}{r_2 h} - ln\left(\frac{r}{r_2}\right)\right](r_1 \le r \le r_2) & (4.41)
\end{aligned}
$$

4.6 Summary and discussion

To summarise, this chapter has presented some of the most fundamental numerical techniques and underlying mathematical formulation for optical bulk and device modelling.

It presented the derivation of the rate equations based on the common interactions in a sample excited by pump photons. The solution techniques for the solution of rate equation based on the phenomenon of stiffness is also presented. A particle swarm algorithm is introduced to predict the magnitude of ion-ion interactions in samples with high concentrations. The rate equation technique was also modified for applications to gain medium and consequently fibre laser propagation. The chapter concludes with the derivation of a thermal model for double clad fibre. One of the main findings of the numerical techniques adopted is that the accuracy of the rate equation is important to understanding the evolution of light-matter interactions which underpins the applications we desire to study. The concepts presented are relevant to photoluminescence, gain and fibre laser and performance modelling considered in chapters 5, 6 and 7.

References

[4.1] C. R. Giles and E. Desurvire, "Modeling erbium-doped fiber amplifiers," *Lightwave Technology, Journal of*, vol. 9, no. 2, pp. 271–283, 1991.

[4.2] M. J. F. Digonnet, "Closed-form expressions for the gain in three- and four-level laser fibers," *IEEE Journal of Quantum Electronics*, vol. 26, pp. 1788–1796, 1990.

[4.3] C. Barnard, P. Myslinski, J. Chrostowski, and M. Kavehrad, "Analytical model for rare-earth-doped fiber amplifiers and lasers," *IEEE Journal of Quantum Electronics*, vol. 30, pp. 1817–1830, 1994.

[4.4] S. Jarabo and M. A. Rebolledo, "Analytic modeling of erbium-doped fiber amplifiers on the basis of intensity-dependent overlapping factors.," *Applied optics*, vol. 34, pp. 6158–6163, 1995.

[4.5] I. M. I. Habbab, A. A. M. Saleh, and P. K. Runge, "Erbium-doped fiber amplifiers: linear approximations," *Journal of Lightwave Technology*, vol. 13, pp. 33–36, 1995.

[4.6] T. Rasmussen, A. Bjarklev, J. H. Povlsen, O. Lumholt, and K. Rottwitt, "Numerical modeling of an integrated erbium-doped glass laser," *Fiber & Integrated Optics*, vol. 10, no. 3, pp. 239–243, 1991.

[4.7] O. Lumholt, A. Bjarklev, T. Rasmussen, and C. Lester, "Rare earth-doped integrated glass components: modeling and optimization," *Journal of Lightwave Technology*, vol. 13, pp. 275–282, 1995.

[4.8] P. Torres and A. M. Guzman, "Complex finite-element method applied to the analysis of optical waveguide amplifiers," *Journal of Lightwave Technology*, vol. 15, pp. 546–550, 1997.

[4.9] F. D. Pasquale and M. Zoboli, "Analysis of erbium-doped waveguide amplifiers by a full-vectorial finite-element method," *Journal of Lightwave Technology*, vol. 11, pp. 1565–1574, 1993.

[4.10] F. Di Pasquale, M. Zoboli, M. Federighi, and I. Massarek, "Finite-element modeling of silica waveguide amplifiers with high erbium concentration," *IEEE Journal of Quantum Electronics*, vol. 30, pp. 1277–1281, 1994.

[4.11] F. Schow, A. Riazi, O. Gandhi, and R. Grow, "Threshold technique for measuring parametric upconversion efficiency," *Quantum Electronics, IEEE Journal of*, vol. 19, pp. 491–492, Apr 1983.

[4.12] R. W. MacQueen, Y. Y. Cheng, A. N. Danos, K. Lips, and T. W. Schmidt, "Action spectrum experiment for the measurement of incoherent photon upconversion efficiency under sun-like excitation," *RSC Advances*, vol. 4, no. 95, pp. 52749–52756, 2014.

[4.13] J. Kennedy and R. Eberhart, "Particle swarm optimization," *Proceedings of ICNN'95 - International Conference on Neural Networks*, vol. 4, 1995.

[4.14] H. Wei, Z. Tong, and S. Jian, "Use of a genetic algorithm to optimize multistage erbium-doped fiber-amplifier systems with complex structures," *Optics express*, vol. 12, no. 4, pp. 531–544, 2004.

[4.15] C. Cheng, Z. Xu, and C. Sui, "A novel design method: A genetic algorithm applied to an erbium-doped fiber amplifier," *Optics communications*, vol. 227, no. 4, pp. 371–382, 2003.

[4.16] A. Mowla and N. Granpayeh, "A novel design approach for erbium-doped fiber amplifiers by particle swam optimization," *Progress In Electromagnetics Research M*, vol. 3, pp. 103–118, 2008.

[4.17] R. Quimby, *Photonics and Lasers: An Introduction*. Wiley, 2006.

[4.18] M. Digonnet, *Rare-Earth-Doped Fiber Lasers and Amplifiers, Revised and Expanded*. Optical Science and Engineering, Taylor & Francis, 2001.

[4.19] R. Quimby, L. Shaw, J. Sanghera, and I. Aggarwal, "Modeling of Cascade Lasing in Dy: Chalcogenide Glass Fiber Laser With Efficient Output at 4.5μm," *Photonics Technology Letters, IEEE*, vol. 20, pp. 123–125, Jan 2008.

[4.20] E. Desurvire, *Erbium-Doped Fiber Amplifiers: Principles and Applications*. Wiley Series in Telecommunications and Signal Processing, Wiley, 1994.

[4.21] S. Sujecki, "Stability of steady-state high-power semiconductor laser models," *JOSA B*, vol. 24, no. 5, pp. 1053–1060, 2007.

[4.22] S. Sujecki, "An Efficient Algorithm for Steady State Analysis of Fibre Lasers Operating under Cascade Pumping Scheme," *International Journal of Electronics and Telecommunications*, vol. 60, no. 2, pp. 143–149, 2014.

[4.23] P. C. Becker, J. R. Simpson, and N. Olsson, *Erbim-doped fiber amplifiers fundamentals and technology*. San Diego: Academic Press., 1999.

[4.24] M. Pollnau, "Analysis of heat generation and thermal lensing in erbium 3 μm lasers," *IEEE Journal of Quantum Electronics*, vol. 39, pp. 350–357, 2003.

[4.25] D. C. Brown and H. J. Hoffman, "Thermal, stress, and thermo-optic effects in high average power double-clad silica fiber lasers," *IEEE Journal of quantum electronics*, vol. 37, no. 2, pp. 207–217, 2001.

Chapter 5

Photoluminescence Modelling of Erbium doped sol-gel SiO$_2$

In the last chapter, an extensive discussion of the radiative properties of triply ionized rare earth ions derived from absorption measurements was presented. This was also followed by the formulation of the rate equation technique for the simulation of ion evolution in a bulk material or device. Therefore in this chapter the techniques presented are applied to an Erbium doped silica glass derived by the sol-gel technique. This starts with an experimental setup and then continue to the measurements used for the optical characterisation of the sample. Power dependence studies are implemented on the sample to guide in the selection of ion-ion interaction. Finally a numerical model is presented to reproduce the photoluminescence in high and low concentration samples with 488 nm and 800 nm pump excitation. Then an algorithm earlier described is implemented that searches the parameter space of the high concentration rate equation to optimize the associated second-order parameter based on a fit to experimental data. Beginning with an initial parameter set estimated randomly, the algorithm traces a path, minimising the error till a tolerance value is reached. The values obtained are compared to those published in literature and found to be comparable.

∽∞∞∞∞∽

104
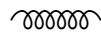
5.1 Experimental Setup and Results

The sol-gel method was used to synthesise the xerogel samples with 1, 4 and 10 mol % Er^{3+} ions (described in section 3.1.1) which upon processing at 1000 ^{o}C yielded flakes of irregular shapes. These flakes were crushed into powders by pestle and mortar for structural investigations and photoluminescence studies. The setup for photoluminescence and the measurements taken were described in section 3.2.2.1. The rest of this section focuses on the results from measurement for PXRD and then photoluminescence with continous wave excitation at 488nm and pulsed excitation at 800nm.

5.1.1 Structural investigations by PXRD

Figure 5.1 represents the powder X-ray Diffraction patterns for the sample B (4 mol % Er^{3+}) and sample C (10 mol % Er^{3+}) processed at 1000 ^{o}C. It is evident from the diffractograms that a crystalline phase for SiO$_2$ host is present in both samples. No match for the data was found for all the possible active crystalline phases of erbium compounds, but close matches to a combination of three major phases (cristobalite, tridymite, and quartz) of SiO$_2$ were identified. It is thus suggested that there is a passive crystalline phase present which was not identified with this software. In sample C, which is doped with 10 mol % Er^{3+} ions, the crystallisation of an Er$_2$O$_3$ phase is also observed in the diffraction pattern (Figure 5.1(b) marked with*).

5.1.2 Stokes Luminescence Spectroscopy - One-photon excitation (λ_{exc} = 488 nm)

Excitation of sample A, sample B and sample C with the 488 nm line of continuous wave Ar ion laser resulted in emission spectrum depicted in Figure 5.2, which shows characteristic highly structured Er^{3+} emission from several manifolds in the spectral range from 500 to 1100 nm. In the case of sample A and sample B, the spectra are dominated by the emission from $^4F_{9/2}$ manifold at 660 nm (red region of the spectrum), and from the $^4I_{11/2}$ level centered at 980 nm. In sample C, which has 10 % content of Er^{3+} ions, the emission
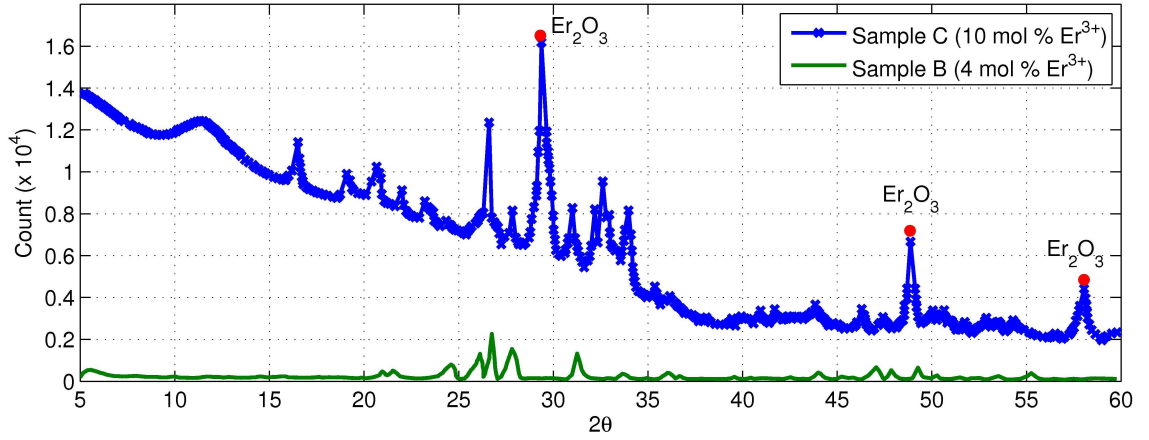
Figure 5.1: Powder X-ray diffraction patterns of sol-gel synthesised samples after annealing at 1000 $^o C$ and dwell for 2 hours. a) sample B (4 mol % Er^{3+} ions) and b) sample C (10 mol % Er^{3+} ions). In sample C, the peaks marked with (*) Er$_2$O$_3$ phase

emanating from the $^4I_{11/2}$ level is twice as intense as that from $^4F_{9/2}$, whilst emission from other manifolds remains comparatively weak.

Emission decay was studied using a 532 nm, 7 ns pulsed Nd:YAG laser as the excitation source. Representative kinetic traces for sample C, corresponding to the decay of $^4F_{9/2}$ excited state at 660 nm, is shown in Figure 5.3. The rise time of the emission obtained after deconvolution of the instrument response function is 37 ns. Emission decay is multiexponential. The unsatisfactory one-exponential fit to the data gives a lifetime of ca. 500 ns, which is significantly shorter than the lifetime of the $^4F_{9/2}$ in the isolated Er^{3+} ion. The multiexponential decay signifies either inhomogeniety of the local surrounding of the Er^{3+} ions, and/or a combination of different quenching mechanisms which may include quenching by OH oscillators [5.1,5.2] or quenching via energy transfer to another Er^{3+} centre [5.3].

5.1.3 Anti-stokes Luminescence Spectroscopy ($\lambda_{exc} = 800$ nm)

Up-conversion studies under 800 nm excitation were performed within the energy range 0 - 20 mJ, using the pulsed Ti:Sapph laser. Excitation with 800 nm pulse corresponds to a two-photon population of $^2G_{9/2}$ level (24100 - 25100 cm^{-1}), and to a one-photon population of $^4I_{9/2}$ level of Er^{3+}ion. Emission detection was performed in the range from
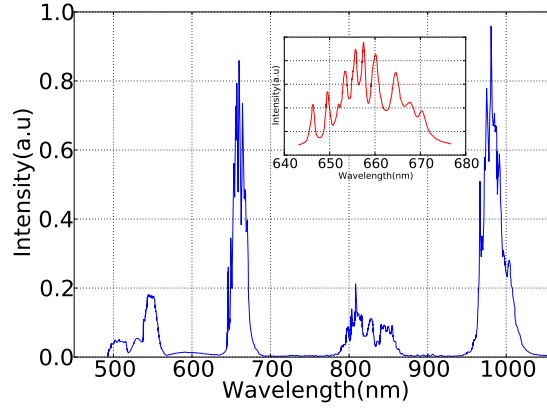
(a) sample A (1 mol% of Er^{3+} ions)
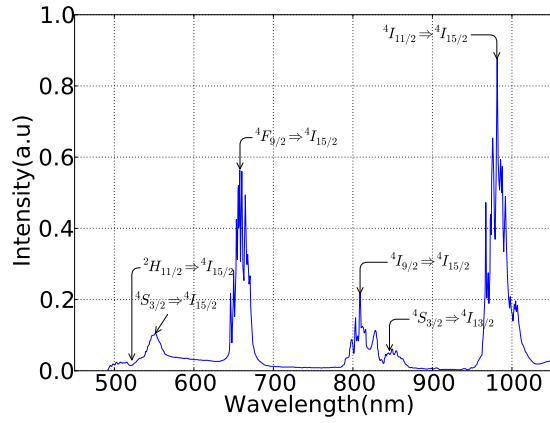
(b) sample B (4 mol% of Er^{3+} ions)
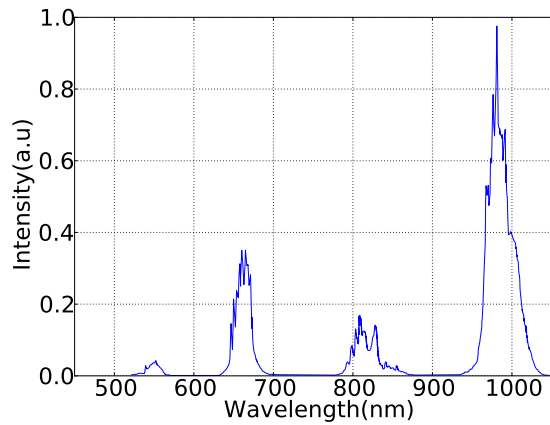
(c) sample C (10 mol% of Er^{3+} ions)

Figure 5.2: Emission Spectra of samples A, B and C, obtained under 488 nm, cw Ar ion laser excitation. The inset shows high resolution data for the emission from the $^4F_{9/2}$ manifold
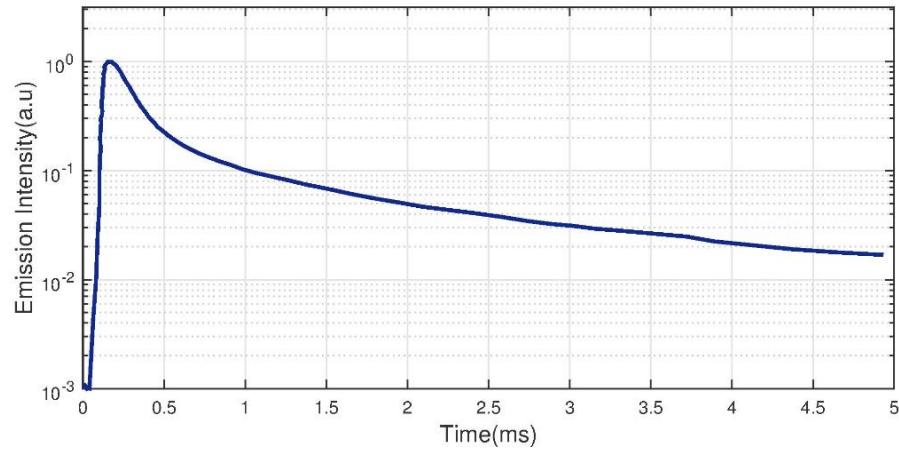
Figure 5.3: Emission decay of the $^4F_{9/2}$ excited state recorded at 660 nm following excitation of sample C (10 mol % Er^{3+} ions) with 7 ns, 532 nm laser pulse. Solid lines represent a multiexponential fit to the data with the following parameters: Rise time 37 ns (instrument response 32 ns), polyexponential decay with the lifetimes 103 ns (main component, 90 % of the decay), 420 ns, 1.39 μs, and 5.15 μs.

300 - 720 nm, the red-side detection limit was due to scattering of the 800 nm excitation pulse. Excitation of sample A, sample B and sample C with 800 nm, 25 ns pulses resulted in up-converted emission from 300 to 720 nm, which originated from a variety of excited states of the Er^{3+}ions (Figure 5.4). The emission spectra in all cases are dominated by the emission manifold at 650 - 660 nm due to the $^4F_{9/2} \rightarrow^4 I_{15/2}$ transition. The relative intensities of the emission emanating from different excited state manifolds is similar to that obtained under one-photon excitation described above.

Each emission manifold shows a well-pronounced progression characteristic of the Er^{3+}excited states (Figs. 5.4) . The inset in Figure 5.4(a) reveals the $^4F_{9/2}$ emission band with sharp sub-band structure due to Stark splitting, which indicates a crystalline host around the Er^{3+}ions, the presence of which is also proved by PXRD patterns shown in Figure 5.1 [5.4].

To investigate the mechanism of up-conversion, power dependence and kinetic studies were performed. The power dependence of the emission intensity for all transitions and for all samples is not linear. Figure 5.5 shows the power dependence of emission intensity for various transitions for sample C as a representative example, in Log (Intensity) vs. Log (Power) coordinates.
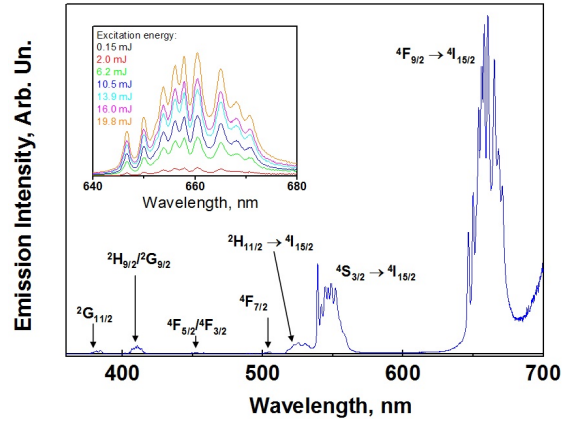
(a) sample A (1 mol% of Er^{3+}ions)
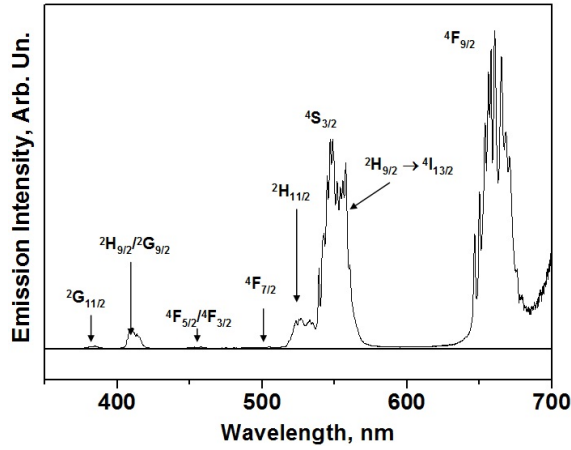
(b) sample B (4 mol% of Er^{3+}ions)
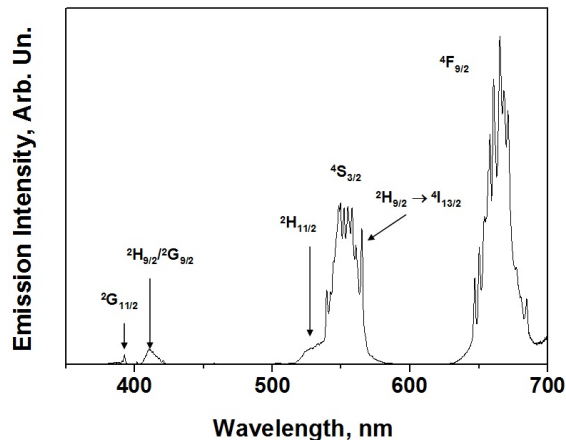
(c) sample C (10 mol% of Er^{3+}ions)

Figure 5.4: Emission spectrum of samples A, B and C obtained under excitation with 800 nm, 25 ns pulses. The inset shows the power dependence of the $^4F_{9/2} \rightarrow ^4 I_{15/2}$ transition. The transitions are from the excited states as labeled to the ground $^4I_{15/2}$ state unless specified otherwise.
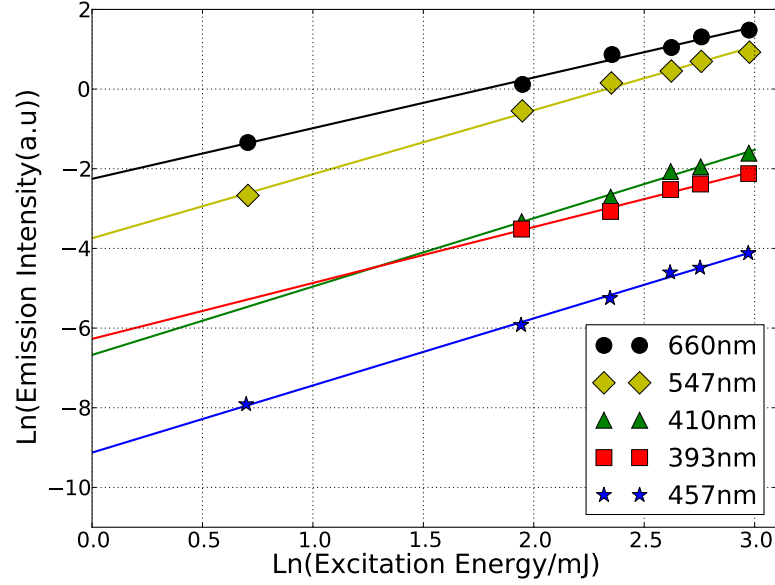
Figure 5.5: Power dependence of emission intensity for various transitions in sample C (10 mol % Er^{3+} ions) obtained under 800 nm, 25 ns pulsed excitation.

However, different transitions exhibit different power dependencies, indicating difference in the mechanism of the population of corresponding excited states in the up-conversion process (Table 5.1). The majority of the transitions exhibit approximately quadratic power dependence of the intensity of the up-converted emission (Table 5.1), indicating contribution of direct two photon absorption in the up-conversion process. The power dependence for 380 - 390 nm emission from $^4G_{11/2}$ state and for 410 nm emission from $^2G_{9/2}$ state is somewhat higher than 2. This is not surprising given that population of 390 nm level requires more energy than that of two photons of the excitation light of 800 nm, and hence the fact that this emission is observed implies involvement of higher order processes. At the same time, the power dependence of the emission intensity at 650 - 660 nm ($^4F_{9/2}$) is only 1.1, which rules out the direct two-photon nature of the process.

However, in our experiments thermal population may become possible due to the use of 10 Hz, 25 ns laser pulses with energies up to 20 mJ per pulse, which results in 0.8 MW peak power being deposited in the sample during 25 ns pulse. Another possible mechanism is population of $^4F_{9/2}$ via inefficient energy transfer from another Er^{3+} centre. Given the nearly quadratic power dependence for the majority of the transitions detected, at least

Table 5.1: Power dependence of the emission intensity (slopes of the in Log (Intensity) vs. Log (Power) plots) for sample A, sample B, and sample C under 800 nm, 25 ns excitation

Emission λ	Emitting state	A 1%	B 4%	C 10%
384 nm	$^4G_{11/2}$	1.7	2.2	1.5 (393 nm)
410 nm	$^2G_{9/2}$	2.2	2.2	1.8
452 nm	$^4F_{3/2}$	1.6	1.6	1.7 (457 nm)
548 nm	$^4S_{3/2}$	1.9	1.8	1.7
660 nm	$^4F_{9/2}$	1.1	1.6	1.3

two mechanisms can be envisaged for the population of higher lying excited states in the Er^{3+}ion. The first mechanism is two-photon excitation, in which the first photon of light is absorbed by the ground state, and, for the 800 nm, would populate $^4I_{9/2}$ level of Er^{3+}ion, which then would absorb a second photon of 800 nm populating the $^2G_{9/2}$ level within the duration of the laser pulse. The second mechanism implies energy transfer between several Er^{3+}centres after absorption of one photon of excitation light per centre. To distinguish between those two mechanisms, kinetic studies have been undertaken. Figure 5.6 shows emission kinetic traces for sample A, sample B and sample C obtained for up-converted emission from $^4S_{3/2}$ level at 550 nm.

According to the Er^{3+}ion energy level diagram (Figure 5.7), the $^4S_{3/2}$ level can be populated by photon absorption of the $^4I_{9/2}$ and $^4I_{13/2}$ states. In this process the absorption of an IR photon of 800 nm populates the $^4I_{9/2}$ level, the decay of which populates the $^4I_{13/2}$ level, which then absorbs another IR photon leading to population of the $^2H_{11/2}$, and $^4S_{3/2}$ is thermally populated from $^2H_{11/2}$. Alternatively, the $^4S_{3/2}$ level could be populated via two possible energy transfer up-conversion processes. One is $(^4I_{9/2}, ^4I_{9/2}) \rightarrow (^4I_{13/2}, ^4S_{3/2})$ (ETU 1 in Figure 5.7). Another possibility is an energy transfer process involving an erbium ion in the $^4I_{9/2}$ state that decays to the ground state concomitant with the energy transfer to another ion in the $^4I_{13/2}$ level, which is then promoted to the $^4S_{3/2}$ state (ETU 2 in Figure 5.7), although the $^4I_{9/2} \rightarrow ^4I_{13/2}$ relaxation would have to be quick enough in this case to occur within the time of the laser pulse. The other alternative, a transition from $^4I_{15/2} \rightarrow ^4I_{9/2}$ followed immediately by a $^4I_{9/2} \rightarrow ^2G_{9/2}$ transition will only give a radiative depopulation producing blue emission at 410 nm.
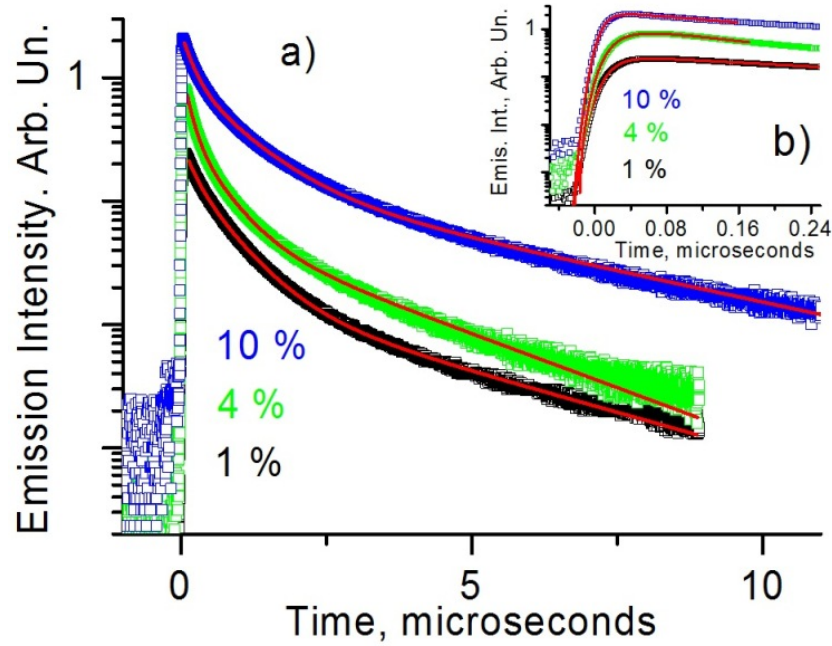
Figure 5.6: Emission kinetic traces for samples sample A (1 mol % Er^{3+}), sample B (4 mol %Er^{3+}) and sample C (10 mol % Er^{3+}) obtained for up-converted emission from $^4S_{3/2}$ level at 550 nm under 800 nm, 25 ns pulsed excitation. (a) normalized overall kinetic profile under ca. 15 mJ/pulse; b) initial part of the kinetic trace showing rise time of the emission obtained under 15 mJ/pulse.

Population of the $^4F_{9/2}$ level can also occur via at least two ETU processes. The first process involves energy transfer between two Er^{3+}ions, one in the $^4I_{9/2}$ state, and the other in the $^4S_{3/2}$ state (ETU 3 in Figure 5.7). Another possibility is an energy transfer via transition $(^4I_{9/2} \rightarrow {}^4I_{13/2})$ and $(^4I_{11/2} \rightarrow {}^4F_{9/2})$ (ETU 4 in Figure 5.7) and/or $(^4I_{11/2} \rightarrow {}^4I_{15/2})$ and $(^4I_{13/2} \rightarrow {}^4F_{9/2})$ (ETU 5 in Figure 5.7). These interpretations of green and red up-conversion mechanism have already been reported in the literature [5.5, 5.6]. Som and Karmaker [5.7] have reported an in-depth study on the $K_2OB_2O_3Sb_2O_3$ (KBS) glass system under excitation at 800 nm and proposed various mechanisms involved in the up-conversion bands originating from $^2H_{11/2} \rightarrow {}^4I_{15/2}$, $^4S_{3/2} \rightarrow {}^4I_{15/2}$ and $^4F_{9/2} \rightarrow {}^4I_{15/2}$ transitions with the strongest emission in the red region of the spectrum (645 nm). The possible up-conversion mechanisms proposed included excited state absorption (ESA), Energy transfers (ET), cooperative energy transfer (CET) and cross relaxation (CR) involving population of the metastable (storage) energy levels ($^2H_{11/2}$, $^4S_{3/2}$ and
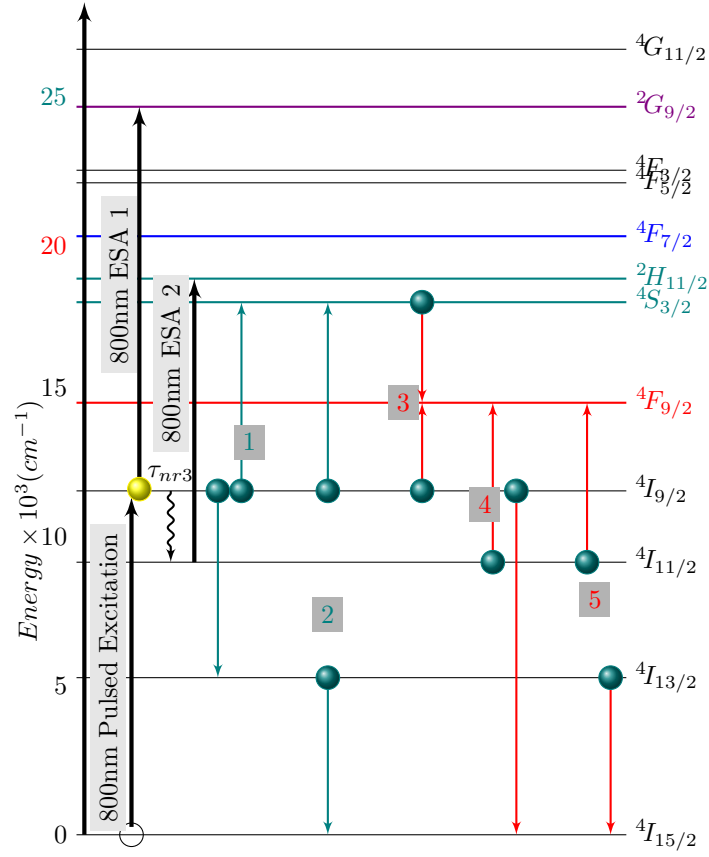
Figure 5.7: Possible up-conversion mechanisms for green up-conversion ($^4S_{3/2},^2H_{11/2} \to {}^4I_{15/2}$) and red up-conversion ($^4F_{9/2} \to {}^4I_{15/2}$) under pulsed excitation at 800 nm

$^4F_{9/2}$) by effects of multiphonon de-excitation and thermal population [5.7].

In the kinetic studies, deconvolution of the instrument response function from the emission data has shown that the emission rise time is 17 ± 5 ns for sample A at higher excitation energies, and 22 ± 5 ns for sample B at both low and high excitation energies. This fact rules out two-photon excitation process within single Er^{3+}centre since if this were the case, as explained above, population of the emitting state would have been achieved within the laser pulse. In case of sample C the rise time of the up-converted emission is faster than in sample A or sample B and is within the instrument response function. In this case kinetic data do not allow one to distinguish between a direct two-photon excitation and energy transfer between several Er^{3+}centres. However, given the power dependencies of emission intensities, it is proposed that up-conversion in sample C also

occurs via energy transfer, which is faster than in sample A or sample B due to shorter Er^{3+}- Er^{3+} distance in a more concentrated sample. Emission decay is multi-exponential in all cases. The multi-exponential decay cannot be satisfactorily modelled even by a three-exponential function; the "mean" lifetime obtained by a mono-exponential fit to the data constitutes approximately 700 ns in all cases which is significantly shorter than the lifetime of $^4S_{3/2}$ in an isolated Er^{3+} ion.

Power and lifetime studies of the up-converted emission in sample A, sample B and sample C can be rationalised as follows. The up-converted emission originates from energy transfer between several Er^{3+} centers, which populate higher energy level of one of the Er^{3+} centres acting as an energy acceptor; the efficiency of the process will be governed by selection rules and the distance between the centres.

Since the spectral profile and rise time of the up-converted emission is not significantly different in sample A vs. sample B, we propose that Er^{3+} ion has similar local environment in those two cases. This observation implies that there is a formation of clusters within the sample, the structure of which determines the population and decay of the various excited states in the Er^{3+} ion. Sample C, on the other hand, has a faster rise time, higher overall emission intensity, and somewhat different spectral profile to sample A and sample B, and more homogeneous emission behavior across the sample a difference which can be attributed to the "dilution" effect of Al$_2$O$_3$ [5.8]. It has been noted that co-doping with Al^{3+} is effective at dispersing rare-earths in silica based gel and glass matrices [5.9–5.11]

In the next section we will use a numerical model to further investigate the origin of the observed photoluminescence spectra.

5.2 Numerical Simulations

In this section we apply a numerical model to study in more detail the impact of the various up-conversion phenomena on the photoluminescence spectra. The underlying concepts of the model are well established in literature [5.12]. The model is based on the rate equation approach (section 4.1) which formulates the temporal change of the population density of

11 energy levels. This results in a generalised set of up to 11 coupled equations 5.1(in the absence of a pumping signal) that are complemented by the condition 5.2, which states that the populations of the levels not included in the model are negligibly small:

$$\frac{\mathrm{d}n_i}{\mathrm{d}t} = \frac{-n_i}{\tau_i} + \sum_{j=i}^{10} \frac{\beta_{ji} n_j}{\tau_{rj}} \pm W_{ab,cd} n_a n_b \pm C_{ab,cd} n_a n_b \qquad (5.1)$$

$$\sum_{i=0}^{10} n_i = N_d \qquad (5.2)$$

In the equation (5.1), n_i is the concentration of ions in a level i, τ_i is the total lifetime of level i, which is made up of both radiative τ_{ri} and non-radiative τ_{nri} lifetimes, β_{ji} is the branching ratio, N_d is the total ion concentration, $W_{ab,cd}$ and $C_{ab,cd}$ are the up-conversion and cross relaxation parameters that characterises uniquely ion-ion interaction for the material under consideration. The subscript a, b represents the originating level of the interaction while c, d represents the terminating level. Finally, we note the levels $^4S_{3/2}$ and $^2H_{11/2}$ are considered to be in thermal equilibrium, thus effectively forming one level (level 5 in Figure 5.7). Equation (5.2) is added for homogeneous solution to the differential equations.

The emission lifetimes needed for the rate equations (5.1) were obtained applying Judd-Ofelt analysis. [5.13,5.14] There is a large body of literature on the application of the Judd-Ofelt analysis to silica glass doped with erbium. Here we have used the parameters quoted by Rai et al. [5.15] for Al(NO$_3$)$_3$-SiO$_2$ prepared by the sol-gel method: $\Omega_2 = 4.038 \times 10^{-20}$ cm^2, $\Omega_4 = 2.073 \times 10^{-20}$ cm^2, $\Omega_6 = 1.855 \times 10^{-20}$ cm^2. Table 5.2 gives the calculated branching ratios and the radiative lifetimes for the first 7 levels. In calculating these values, we followed the standard procedures given in the literature. [5.16,5.17]

The electron-phonon coupling is weak in the case of rare earth ions and hence the multiphonon decay rate (if the energy gap is far greater than the phonon energy) can be expressed by the solution of the Dexter-Miyakawa equations: [5.18]

$$W_{mult}(T) = \beta e^{-\alpha \Delta E}[1 + n(T)]^p \qquad (5.3)$$

Table 5.2: Lifetimes and Branching ratios obtained from Judd-Ofelt analysis

Emission	$^4I_{13/2}$	$^4I_{11/2}$	$^4I_{9/2}$	$^4F_{9/2}$	$^4S_{3/2}$	$^4F_{7/2}$
lifetimes(ms)	6.169	5.109	4.527	0.575	0.192	0.222
$^4I_{15/2}$	1.0	0.851	0.709	0.907	0.668	0.787
$^4I_{13/2}$	-	0.149	0.282	0.043	0.274	0.119
$^4I_{11/2}$	-	-	0.009	0.048	0.022	0.058
$^4I_{9/2}$	-	-	-	0.003	0.035	0.034
$^4F_{9/2}$	-	-	-	-	0.000	0.001
$^4S_{3/2}$	-	-	-	-	-	0.000

$$n(T) = [e^{\hbar w/KT} - 1]^{-1} \tag{5.4}$$

where β, α are positive host-dependent material constants and are known to be almost unaffected by the type of the rare-earth dopant, n(T) is the phonon occupancy number (number of thermally generated phonons per mode at absolute temperature), T is the absolute temperature, $\hbar$w is the maximum energy of a phonon, which for silica glass host is 1100 cm^{-1} [5.19]. Following the values quoted in the literature we assumed that, β and α are 9.0×10^7 s^{-1} and 4.7×10^{-3} cm respectively [5.20]. Table 5.3 gives the values of the non-radiative lifetime which is then applied to the rate equation model (equation 5.1).

Table 5.3: Multiphonon Emission Rates for various multiplets

Emission	$^4I_{11/2}$	$^4I_{9/2}$	$^4F_{9/2}$	$^4S_{3/2}$	$^4F_{7/2}$
lifetimes	0.305 s	0.43 ms	5.87 ms	32.8 ms	5.86 μs

The parameters that describe the up-conversion processes are strongly dependent on the doping level, dopant distribution and the host material and are difficult to estimate. We therefore will use them as the fitting parameters in our model. The fitting procedure that we use here involves the application of a particle swarm algorithm [5.21] to fit the observed photoluminescence spectra using the rate equations model. In conformity with the assumptions of the Judd-Ofelt analysis we compare the integrated experimental photoluminescence intensity with the values of the photoluminescence intensity predicted by the rate equations model. In applying the PSO, technique, we attempt to minimise the function in equation 5.5. $PL_{exp}(\lambda)$ is the measured emission intensity of the bands and

PL_{sim} is the photoluminescence of each band calculated from rate equation analysis.

$$f(\lambda) = \sum_{i=1}^{5} \left(\int_{\lambda} PL_{exp}(\lambda)d\lambda - PL_{sim} \right) \tag{5.5}$$

The main problem here is a large number of the fitting parameters that needs to be considered. We therefore perform first an analysis of the photoluminescence obtained with the pump wavelength of CW 488 nm that is based on a linear model, i.e. a rate equations model that neglects the up-conversion phenomena. Then we use the conclusions from section 5.1 and the observations made applying the linear model to identify the dominant up-conversion processes. In the next step we use the particle swarm algorithm to reproduce the experimental photoluminescence spectra obtained with the CW 488 nm pump using the coefficients characterising the identified dominant up-conversion processes as the fitting parameters. This yields a set of constants that give the rates of the up-conversion processes. In order to verify the results we repeat the same procedure for the 800 nm pulsed excitation. We keep the same values of the up-conversion parameters and add the excited state absorption processes that were negligible when considering the 488 nm pumping with the expectation that the numerical results will reproduce the photoluminescence spectra observed when the pumping wavelength is equal to 800 nm. Once the coefficients characterising various up-conversion phenomena are estimated we can identify the dominant up-conversion processes. The initial vector n_i is of the form $n_i = [N_d, 0, 0, ...0]$. This indicates that prior to excitation, the erbium ions are initially at the ground state. All the excited states are empty.

5.2.1 Linear Model

In the linear model we neglect the up-conversion processes and consider levels up to the pump excited-level:

$$\frac{\mathrm{d}n_i}{\mathrm{d}t} = \frac{-n_i}{\tau_{ri}} - \frac{n_i}{\tau_{nri}} + \frac{n_{i+1}}{\tau_{nr(i+1)}} + \sum_{j=i}^{6} \frac{\beta_{ji}n_j}{\tau_{rj}} \Bigg|_{i \in (0...6)} \tag{5.6}$$

Table 5.4: 488 nm CW, Simulation parameters

Parameter	Value	Unit
Pump Power	70	mW
Pump Wavelength	488	nm
Absorption cross-section [5.22]	8×10^{-21}	cm^2
Erbium Concentration	1,4,10	mol %
Spot size	0.5×0.5	mm^2
Pump Photon Flux	2.1872×10^{23}	photons/m^{2}s
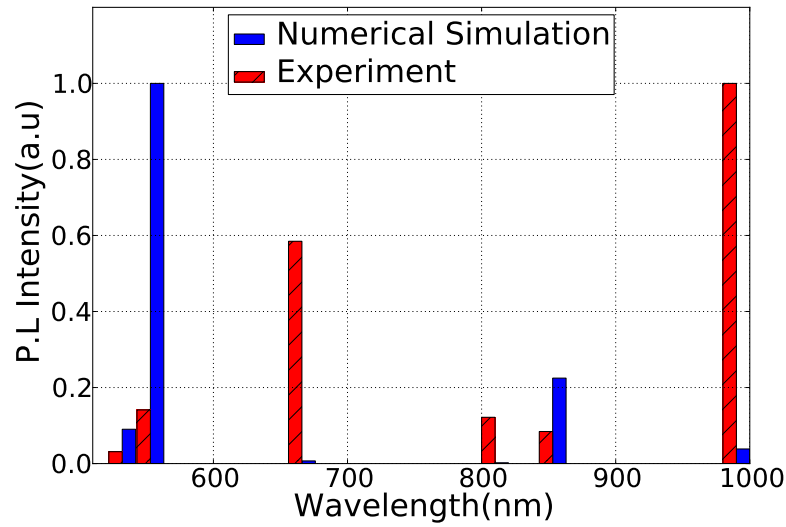
Figure 5.8: 488 nm CW Excitation, comparison between model and experiment for sample A

The simulation parameters describing the pump laser and the sample are listed in Table 5.4

Since the 488 nm pump was a continuous wave source, equations (5.6) were solved at steady state while the fluorescence intensity is calculated using the branching ratios and the radiative lifetimes listed in Table 5.2 from J-O analysis

Figure 5.8 shows the comparison of the experimental and calculated photoluminescence spectrum for the sample A. In the calculated spectrum the intensity of the green fluorescence (550 nm) is larger than that of the red one (656 nm) which is in clear contradiction with the experimental results. The red photoluminescence is weaker than the green one in the results predicted by the linear model because the 488 nm pump promotes ions to the highest considered level $^4F_{7/2}$, from which they fall very efficiently

to the level $^4S_{3/2}$ via multi-phonon relaxation. However, as there is a large energy gap (requiring about 5 phonons) between the levels $^4S_{3/2}$ and $^4F_{9/2}$ the feeding of the $^4F_{9/2}$ level via multiphonon relaxation is not as efficient as for the $^4S_{3/2}$ level. The second way of feeding the $^4F_{9/2}$ level is via the radiative transition from the $^4F_{7/2}$ level. This however, is not efficient either due to a very small branching ratio. As a result the population of the $^4F_{9/2}$ level is comparatively small, which results in a relatively weak luminescence. Further, Figure 5.8 shows that the 800 nm intensity peak that corresponds to the radiative transition from $^4I_{9/2}$ to the ground state is absent in the numerically obtained spectrum, which again is contrary to what was observed in the experiment. This is because the $^4I_{9/2}$ state is rapidly depleted of ions by fast multiphonon relaxation (at the rate of $\approx 2.3 \times 10^3$ s^{-1}) to $^4I_{11/2}$ while the multiphonon relaxation rate ($\approx 1.7 \times 10^2$ s^{-1}) from $^4F_{9/2}$ level and spontaneous emissions from higher levels are comparatively slow and hence unable to replenish the population of this level. Consequently, the population of the level $^4I_{9/2}$ is small, which combined with a fairly large radiative decay constant results in a negligibly small photoluminescence. Similar trends were observed for the samples B and C. This leads to the conclusion that the observed output spectra cannot be explained without an inclusion of the up-conversion processes. In the next section, we therefore consider a model that includes co-operative up-conversion and cross-relaxation processes.

5.2.2 Extended Model

The inability of the linear model to reproduce the experimental results makes it necessary to add the up-conversion processes to the model. Figure 5.9 shows ion-ion interactions represented by W$_{2,2,0,6}$, W$_{1,2,4,0}$, W$_{1,1,0,3}$ and C$_{0,5,1,3}$ that were identified on the basis of the power dependence studies presented in table 5.1. The interactions identified are in line with the ones predicted in a previous study using the same set of excitation wavelengths. [5.17] W$_{2,2,0,6}$ was selected because of the nearly quadratic power dependence of green emission in all samples considered. Addition of the relaxation process C$_{0,5,1,3}$ was based on the need to deplete the emission intensity of green fluorescence emanating from $^4S_{3/2}$ as observed in the linear model (Figure 5.8). It is also expected that C$_{0,5,1,3}$ would compete with the

multiphonon emission depleting $^4I_{9/2}$ energy level by recycling ions from lower ion-rich ground state $^4I_{13/2}$ to the 800 nm emission level. For this reason, we have ignored all second-order interactions originating from $^4I_{9/2}$, that are labeled 1,2,3,4 in Figure 5.7. Energy transfer up-conversion $W_{1,2,0,4}$ is a possible route for an efficient feed to the $^4F_{9/2}$ level. This is because levels $^4I_{11/2}$, and $^4I_{13/2}$ have long life times [5.18,5.23,5.24] attracting the accumulation of ions and consequently providing a large pool of ions as candidates for energy-transfer up-conversion to $^4F_{9/2}$ Inclusion of the up-conversion processes shown in
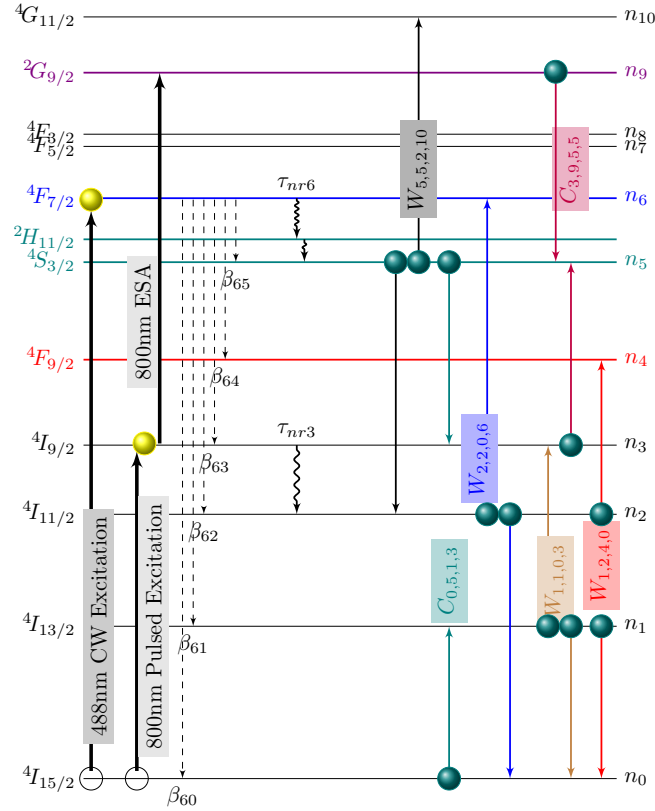
Figure 5.9: Energy level model of erbium pumped at 488 nm and 800 nm

Figure 5.9 leads to the following set of the coupled rate equations:

$$\frac{\mathrm{d}n_0}{\mathrm{d}t} = R_{p1}(n_3 - n_0) + R_{p2}(n_6 - n_0) + \frac{n_1}{\tau_{r1}} + n_1 n_2 W_{1,2,0,4} + n_1^2 W_{1,1,0,3} - n_0 n_5 C_{0,5,1,3} \quad (5.7)$$

$$+ \ n_2^2 W_{2,2,0,6} + \sum_{j=2}^{10} \frac{\beta_{j0} n_j}{\tau_{rj}} \quad (5.8)$$

$$\frac{\mathrm{d}n_1}{\mathrm{d}t} = \frac{-n_1}{\tau_1} + \frac{n_2}{\tau_{nr2}} - 2n_1^2 W_{1,1,0,3} - n_1 n_2 W_{1,2,0,4} + \sum_{j=2}^{10} \frac{\beta_{j1} n_j}{\tau_{rj}} + n_0 n_5 C_{0,5,1,3} \quad (5.9)$$

$$\frac{\mathrm{d}n_2}{\mathrm{d}t} = \frac{-n_2}{\tau_2} + \frac{n_3}{\tau_{nr3}} - 2n_2^2 W_{2,2,0,6} - n_1 n_2 W_{1,2,0,4} + \sum_{j=3}^{10} \frac{\beta_{j2} n_j}{\tau_{rj}} + n_5^2 W_{5,5,2,10} \quad (5.10)$$

$$\frac{\mathrm{d}n_9}{\mathrm{d}t} = R_{esa} n_3 - \frac{n_9}{\tau_9} + \frac{n_{10}}{\tau_{nr10}} + \frac{\beta_{109} n_{10}}{\tau_{r10}} - n_3 n_9 C_{3,9,5,5} \quad (5.11)$$

$$\frac{\mathrm{d}n_{10}}{\mathrm{d}t} = \frac{-n_{10}}{\tau_{10}} + n_5^2 W_{5,5,2,10} \quad (5.12)$$

R_{p1} and R_{p2} represent pump excitation at 800 nm and 488 nm respectively. For given values of the up-conversion parameters the solution to the set of equations (5.12) was obtained at a steady state using the Newton-Raphson method. [5.25] The optimal values of the up-conversion parameters were obtained by iteratively fitting the numerical results to the experimental spectra using the particle swarm method [5.21]. The details of the algorithm and the implementation are found in section 4.2 and Appendix D. The values of the coefficients obtained for the three samples using the particle swarm algorithm are given in the Table 5.5. The coefficients range between 0.01 - 100 $\times$ 10^{-17} cm^3/s which is in line with the values quoted in the available literature. [5.23,5.26,5.27]

Table 5.5: Table of up-conversion coefficients obtained by Particle Swarm Algorithm Optimisation

$\times$ 10^{-17}cm^{3}s^{-1}	$W_{2,2}$	$W_{1,1}$	$W_{1,2}$	$C_{0,5}$	$C_{3,9}$	$W_{5,5}$
A -1%	5.15	57.6	30.0	8.21	102	0.01
B - 4%	3.70	15.2	6.38	3.25	72	0.01
C -10%	4.59	7.1	1.27	4.37	42	0.01

Figure 5.10 shows the comparison between experimental and numerical results based on the coefficients provided in Table 5.5. Unlike the linear model the numerical results agree with the experimental ones. The intensity of the red photoluminescence increased because

of the energy transfer up-conversion between ions in level $^4I_{11/2}$ and $^4I_{13/2}$ promoting ions to the $^4I_{9/2}$ level at a faster rate than the combined effects of multiphonon and radiative decay. The 800 nm photoluminescence also becomes significant because of the cross relaxation C$_{0,5,1,3}$ process coupling ions from $^4S_{3/2}$ level and the ground state to the intermediate $^4I_{9/2}$ and $^4I_{13/2}$ levels, respectively. The energy transfer up-conversion term W$_{2,2,0,6}$) originating from the 980 nm ($^4I_{11/2}$) energy level accounts for the quadratic dependence of the green emission intensity on concentration. [5.27]

Table 5.6 shows the magnitude of the ion-ion coupling terms in equation 5.12 that were calculated using the values of the up-conversion coefficients listed in table 5.5. The magnitude of the coupling term n$_0$n$_5$C$_{0,5,1,3}$ increases at a higher rate with increase in concentration than those of the other terms. The cross relaxation process C$_{0,5,1,3}$ is therefore the dominant up-conversion process predicted by the model. The magnitude of the coupling terms n$_3$n$_9$C$_{3,9,5,5}$ and n$_5$n$_5$W$_{5,5,2,10}$ were not included in the table 5.6 because they are negligibly small.

Table 5.6: Magnitude of ion-ion coupling terms

$\times 10^{21}$cm^{-3}s^{-1}	$n_2^2 W_{2,2}$	$n_1^2 W_{1,1}$	$n_1 n_2 W_{1,2}$	$n_0 n_5 C_{0,5}$
A - 1%	0.0397	0.0865	0.1021	0.2875
B - 4%	0.3798	0.4713	0.3602	1.3954
C - 10%	0.6615	1.2984	0.6559	3.3867

Table 5.7 shows the simulation parameters. Equations (5.12) are solved in the time domain using LSODA(automatically selects between nonstiff (Adams) and stiff (BDF) methods) integration routines in python scipy library. [5.28]

Table 5.7: 800 nm Pulsed excitation, Simulation parameters

Parameter	Value	Unit
Pump Energy	0 - 20	mJ
Pump Wavelength	800	nm
Excitation spot size	1.5×1.5	mm
Absorption cross-section [5.29]	6.9×10^{-22}	cm^2
Excited state absorption cross-section [5.29]	1.07×10^{-21}	cm^2
Erbium Concentration	1,4,10	mol%
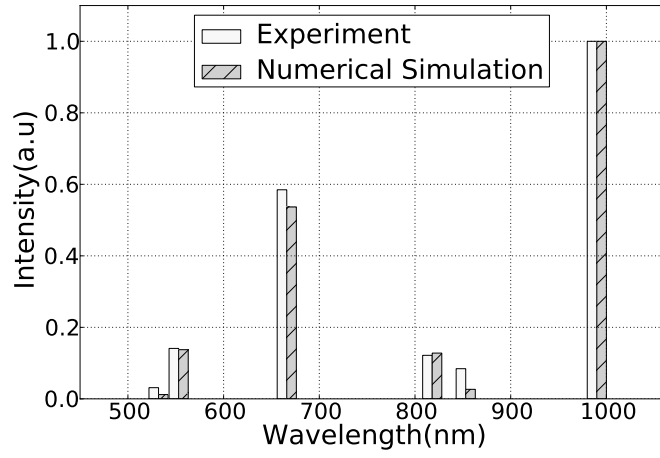
(a) sample A
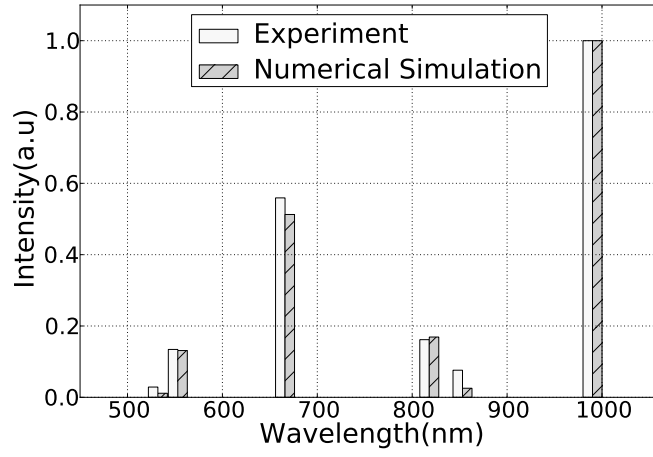
(b) sample B
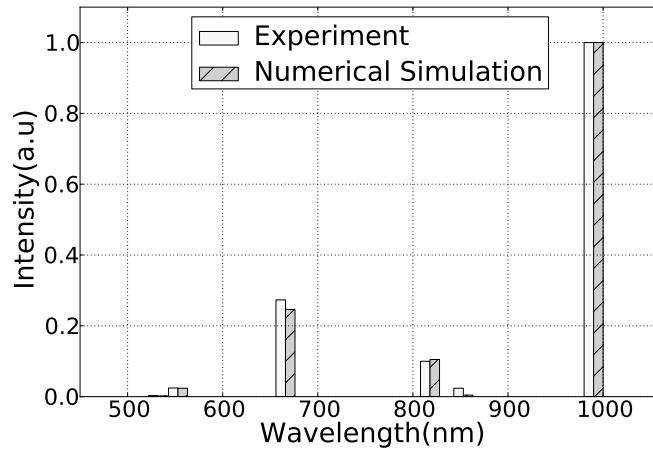
(c) sample C

Figure 5.10: Numerical and Experimental comparison of sample A, B and C based on extended model of 488 nm CW excitation
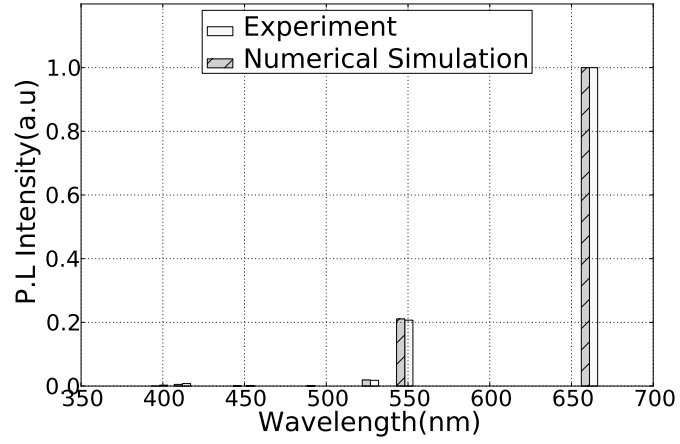
(a) sample A
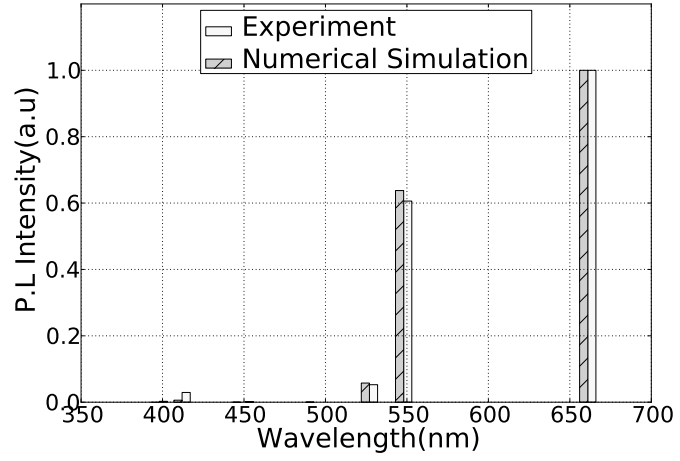
(b) sample B
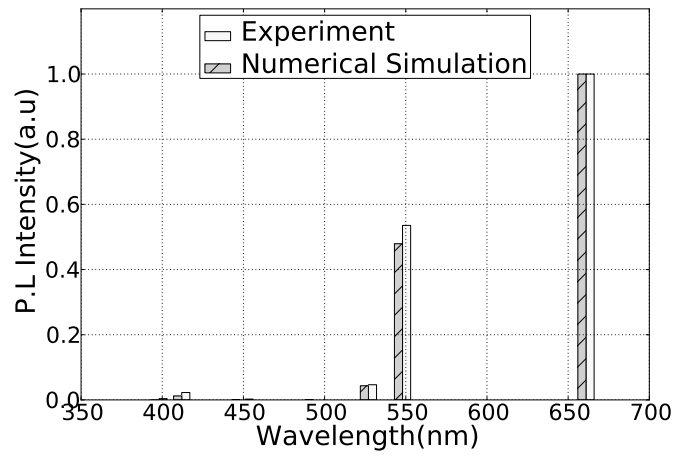
(c) sample C

Figure 5.11: Numerical and Experimental comparison of Samples A, B and C based on extended model of 800 nm, 25ns pulsed excitation

In order to cross-check the obtained up-conversion parameters we apply the rate equations model to reproduce the experimental results obtained with 800 nm pump. In these simulations we used the up-conversion parameters obtained at 488 nm pumping. The up-conversion term $W_{5,5,2,10}$ and excited state absorption which was insignificant in the 488 nm simulation allowed us to explain the emissions from 380 - 470 nm present in figs. 5.4.

The fluorescence magnitude was calculated by averaging the results over one complete cycle (10 Hz repetition rate, 25 ns pulse width), once a repeatable pulse train settles down. Figs. 5.11 shows the comparison between the numerical and experimental results obtained for the 800 nm pump. There is a fairly good agreement between both sets of results, which confirms that the values of the up-conversion parameters obtained by fitting the photoluminescence at 488 nm pumping allow for consistent predicting the photoluminescence spectrum with 800 nm pumping. Ion-ion coupling between the higher excited state ($^2G_{9/2}$, 407 nm) and the directly excited pump level ($^2I_{9/2}$, 800 nm) is responsible for the rapid accumulation of ions at the thermal levels ($^2H_{11/2}/^4S_{3/2}$) at the on-set of pump excitation.

The upconversion process has been observed at powers as low as 200 mW/cm^2. This estimate is based on 0.5 mJ as the lowest energy, 10 Hz repetition rate, focused into 1.5 mm $\times$ 1.5 mm (see Figure 5.5 for power dependence of the up-converted luminescence intensity under 800 nm excitation). This compares well with the values of 1 - 10^3 W/cm^2 for the up-converting nanoparticles. [5.30–5.32]

5.3   Summary and discussion

In summary, the excitation with CW 488 nm and pulsed 800 nm laser light of Er-doped SiO$_2$ powders with different concentrations of Er^{3+}, initiates up-conversion processes which lead to emission in the violet, green and red parts of the spectrum. The experimental results indicate that the mechanism of the up-conversion is due to energy transfer between several Er^{3+} centres present in close proximity within local clusters. We developed a

numerical model that includes the main up-conversion mechanisms indicated by the experimental results and calculated the values of the up-conversion coefficients. The values of up-conversion coefficients obtained from the numerical model agree with the ones found in the available literature. Further, using the numerical model, we identified that the cooperative up-conversion process W$_{5,5,2,10}$: $2(^4S_{3/2}) \rightarrow {}^4I_{11/2} + {}^4G_{11/2}$ and excited state absorption from $^4I_{9/2}$ are the key processes responsible for the violet emission observed with pulsed excitation with 800 nm source. The numerical results also show that the energy transfer process $W_{1,2,0,4}$: $^4I_{11/2} + {}^4 I_{13/2} \rightarrow {}^4I_{15/2} + {}^4 F_{9/2}$ is the dominant mechanism responsible for the strength of the red emission observed at 488 nm pumping. The up-conversion process was observed even at comparatively low powers 200 mW/cm^2, which make these materials promising candidates for up-conversion applications.

References

[5.1] F. Vetrone, J.-C. Boyer, J. A. Capobianco, A. Speghini, and M. Bettinelli, "Concentration-dependent near-infrared to visible upconversion in nanocrystalline and bulk Y$_2$O$_3$: Er^{3+}," *Chem. Mater.*, vol. 15, no. 14, pp. 2737–2743, 2003.

[5.2] D. Boye, A. Silversmith, J. Nolen, L. Rumney, D. Shaye, B. Smith, and K. Brewer, "Red-to-green up-conversion in Er-doped SiO_2 and $SiO_2 - TiO_2$ sol–gel silicate glasses," *J. Lumin.*, vol. 94, pp. 279–282, 2001.

[5.3] J. Castañeda, M. Meneses-Nava, O. Barbosa-Garcıa, E. De la Rosa-Cruz, and J. Mosiño, "The red emission in two and three steps up-conversion process in a doped erbium $SiO_2 - TiO_2$ sol–gel powder," *J. Lumin.*, vol. 102, pp. 504–509, 2003.

[5.4] Z. Pan, A. Ueda, R. Mu, and S. Morgan, "Upconversion luminescence in Er^{3+}-doped germanate-oxyfluoride and tellurium-germanate-oxyfluoride transparent glass-ceramics," *J. Lumin.*, vol. 126, no. 1, pp. 251–256, 2007.

[5.5] R. Balda, S. Garca-Revilla, J. Fernndez, V. Seznec, V. Nazabal, X. Zhang, J. Adam, M. Allix, and G. Matzen, "Upconversion luminescence of transparent Er^{3+}-doped chalcohalide glass–ceramics," *Opt. Mater.*, vol. 31, no. 5, pp. 760 – 764, 2009.

[5.6] H. Guo, "Green and red upconversion luminescence in CeO_2 : Er^{3+} powders produced by 785nm laser," *Journal of Solid State Chemistry*, vol. 180, no. 1, pp. 127–131, 2007.

[5.7] T. Som and B. Karmakar, "Efficient green and red fluorescence upconversion in erbium doped new low phonon antimony glasses," *Opt. Mater.*, vol. 31, no. 4, pp. 609–618, 2009.

[5.8] Y. Yu, Y. Wang, D. Chen, and F. Liu, "Efficient upconversion luminescence of Er^{3+} : $SrF_2-SiO_2-Al_2O_3$ sol–gel glass ceramics," *Ceram. Int.*, vol. 34, no. 8, pp. 2143–2146, 2008.

[5.9] S. Tanabe, "Optical transitions of rare earth ions for amplifiers: how the local structure works in glass," *Journal of Non-Crystalline Solids*, vol. 259, no. 1 - 3, pp. 1 – 9, 1999.

[5.10] Y. Zhou, Y. Lam, S. S. Wang, H. L. Liu, C. Kam, and Y. Chan, "Fluorescence enhancement of Er^{3+}-doped sol-gel glass by aluminum codoping," *Applied Physics Letters*, vol. 71, pp. 587–589, Aug 1997.

[5.11] A. Chiasera, M. Montagna, R. Rolli, S. Ronchin, S. Pelli, G. Righini, R. Gonalves, Y. Messaddeq, S. Ribeiro, C. Armellini, M. Ferrari, and L. Zampedri, "Er^{3+}/Yb^{3+}Co-Activated Silica-Alumina Monolithic Xerogels," *Journal of Sol-Gel Science and Technology*, vol. 26, no. 1-3, pp. 943–946, 2003.

[5.12] A. Jaboski, "Efficiency of anti-Stokes fluorescence in dyes," *Nature*, vol. 131, pp. 839–840, 1933.

[5.13] B. Judd, "Optical Absorption Intensities of Rare-Earth Ions," *Physical Review*, vol. 127, pp. 750 –, 1962.

[5.14] G. S. Ofelt, "Intensities of Crystal Spectra of Rare-Earth Ions," *The Journal of Chemical Physics*, vol. 37, no. 3, pp. 511–520, 1962.

[5.15] S. Rai and P. Dutta, "Structural and Optical Study Of Er in Sol-Gel Silicate Glass," in *AIP Conference Proceedings*, vol. 1147, p. 475, 2009.

[5.16] R. Caspary, *Applied Rare Earth Spectroscopy for Fiber Laser Optimization*. Berichte Aus der Lasertechnik Series, Shaker Verlag GmbH, 2002.

[5.17] A. Kanoun, N. Jaba, H. Mejri, H. Maaref, and A. Selmi, "Effects of Activator Ion Concentration on the Upconversion Processes in Er^{3+}-Doped $TeO_2 - -ZnO$ Glass," *physica status solidi (a)*, vol. 188, no. 3, pp. 1145–1151, 2001.

[5.18] C. Bouzidi, A. Moadhen, H. Elhouichet, and M. Oueslati, "Er^{3+}-doped sol-gel SnO_2 for optical laser and amplifier applications," *Applied Physics B*, vol. 90, no. 3-4, pp. 465–469, 2008.

[5.19] P. C. Becker, J. R. Simpson, and N. Olsson, *Erbim-doped fiber amplifiers fundamentals and technology*. San Diego: Academic Press., 1999.

[5.20] R. Quimby and B. Aitken, "Multiphonon energy gap law in rare-earth doped chalcogenide glass ," *J. Non-Cryst. Solids*, vol. 320, no. 1 - 3, pp. 100 – 112, 2003.

[5.21] J. Kennedy and R. Eberhart, "Particle swarm optimization," in *Neural Networks*, vol. 4, pp. 1942–1948, IEEE, 1995.

[5.22] L. Pavesia, "A review of the various efforts to a silicon laser," *in Proc. of SPIE*, vol. 4997, p. 207, 2003.

[5.23] W. Q. Shi, M. Bass, and M. Birnbaum, "Effects of energy transfer among Er^{3+}ions on the fluorescence decay and lasing properties of heavily doped Er: $Y_3AL_5O_{12}$," *J. Opt. Soc. Am. B*, vol. 7, pp. 1456–1462, Aug 1990.

[5.24] S. Georgescu, O. Toma, C. Florea, and C. Naud, "ESA processes responsible for infrared pumped, green and violet luminescence in low-concentrated Er: YAG," *J. Lumin.*, vol. 101, no. 1, pp. 87–99, 2003.

[5.25] C. Kelley, "Solving nonlinear equations with Newton's method," *SIAM*, pp. 1–103, 2003.

[5.26] G. Vossler, C. Brooks, and K. Winik, "Planar Er: Yb glass ion exchanged waveguide laser," *Electron. Lett.*, vol. 31, no. 14, pp. 1162–1163, 1995.

[5.27] V. Bogdanov, D. Booth, and W. Gibbs, "Energy transfer processes and the green fluorescence in heavily doped Er^{3+}: fluoride glasses," *J. Non-Cryst. Solids*, vol. 321, no. 1, pp. 20–28, 2003.

[5.28] E. Jones, T. Oliphant, and P. Peterson, "SciPy," 2001. Available online at `www.scipy.org` [Accessed: 11 March 2013].

[5.29] S. Zemon, B. Pedersen, G. Lambert, W. Miniscalco, L. J. Andrews, R. Davies, and T. Wei, "Excited-state absorption cross sections in the 800-nm band for Er-doped, Al/P-silica fibers: Measurements and amplifier modeling," *IEEE Photon. Technol. Lett*, vol. 3, no. 7, pp. 621–624, 1991.

[5.30] F. Wang and X. Liu, "Upconversion multicolor fine-tuning: visible to near-infrared emission from lanthanide-doped $NaYF_4$ nanoparticles," *J. Am. Chem. Soc.*, vol. 130, no. 17, pp. 5642–5643, 2008.

[5.31] H. H. Gorris and O. S. Wolfbeis, "Photon-Upconverting Nanoparticles for Optical Encoding and Multiplexing of Cells, Biomolecules, and Microspheres," *Chem Int. Ed.*, vol. 52, pp. 3584 – 3600, 2013.

[5.32] H. Dong, L.-D. Sun, and C.-H. Yan, "Basic understanding of the lanthanide related upconversion emissions," *Nanoscale*, vol. 5, pp. 5703–5714, 2013.

Chapter 6

Photoluminescence Modelling of Praseodymium Doped Chalcogenide Bulk and Fibre Glass

The experimentally obtained luminescence characteristics of Pr^{3+} doped chalcogenide bulk and glass fiber are studied numerically using a rate equation approach. The numerical model includes both the radiative and non-radiative transition paths whilst it neglects the up-conversion processes. Photoluminescence spectra at mid-infrared wavelengths ranging from 3.5 - 6 μm are obtained by using two pump wavelengths: 1.55 and 1.94 μm . Two similar material compositions 500 ppm and 1000 ppm of Pr^{3+} were compared: one with Galium as one of the Chalcogens and the other with Indium replacing Gallium. Numerical analysis provided a good fit for the dominant wavelengths at the mid-infrared region. A good agreement between the experiment and theory is obtained for the photoluminescence decay profiles. Conclusions are drawn based on the comparative efficiencies of measured and modelled photoluminescence for both sample types.

This study is arranged as follows. In Section 6.1, we re-examine photoluminescence reported in chalcogenide glass hosts. In Section 6.2, We briefly discuss the experimental techniques and highlight the justification

for replacing Gallium with Indium. In Section 6.3, we characterise all the samples using absorption spectroscopy which is used to reproduce the emission cross-sections in section 6.4 using the McCumber's analysis. The experimental measurement of photoluminescence in gallium and indium based samples is presented in Section 6.5. The rate-equation modelling of photoluminescence in bulk and fibre glasses (with reabsorption) is the subject of Section 6.6 through parameters obtained by Judd-Ofelt calculations. Section 6.7 summarises the results of this chapter and highlights the superior photoluminescence properties of Pr^{3+}in the novel indium chalcogenide when compared with the gallium analogues.

$\mathcal{CCCCCC}$
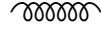
6.1 Photoluminescence in Chalcogenide Host

Materials such as chalcogenide glass with transparency beyond 10 μm can find application in mid-infrared lasers, fibre amplifiers and chemical sensors [6.1–6.3]. By choosing multicomponent glasses based on a suitable chalcogen, such as selenium with low phonon energy, high quantum efficiencies of radiative transitions can be engineered [6.3,6.4]. Along with the development of robust purification methods, stable compositions [6.5] and considering that there are numerous mid-infrared transitions available when doping with lanthanides, chalcogenide glasses are an attractive choice for realising robust photonic devices. In particular, Pr^{3+}doped chalcogenide glass with a Se-network former was found to provide highly efficient broadband mid-IR fluorescence [6.2,6.6].

Significant research effort has been put into studying the photoluminescence of lanthanide-doped chalcogenide glasses. Shaw *et al.* [6.7] identified the individual contributions of the overlapping transitions ${}^3H_6, {}^3F_2 \rightarrow {}^3H_5$ and ${}^3H_5 \rightarrow {}^3H_4$ in Pr^{3+}doped chalcogenide glass by appropriately adjusting the chopper operating frequency in the photoluminescence measurement setup. It was found that knowledge of the actual

population distribution between energy levels is necessary for an accurate calculation of the lifetime and consequently also for the evaluation of the quantum efficiency of an energy level. Kasap *et al.* [6.8] have predicted the steady-state photoluminescence of $(Ge_{23.5}Ga_{11.8}Se(S)_{64.7})_{98}Er_2$ using a Monte-Carlo model. Although the results presented [6.8] clearly demonstrated that an accurate prediction can be made, the study was limited to the 1450 nm - 1650 nm wavelength region. Park *et al.* [6.6] identified several emission bands in the mid-IR range of Pr^{3+}singly doped $Ge_{30}Ga_2Sb_8Se_{60}$ glasses with varying Pr^{3+}concentration. A spectra deconvolution technique quantified level populations and revealed interactions like cross-relaxations and excited state absorption processes [6.6]. However, the intensities identified seemed to originate from several Stark levels that could not be clearly assigned to specific energy levels of the Pr^{3+}ion.

Here, we focus on the mid-infrared wavelength range. We use a rate equations based model to explain the experimentally observed photoluminescence spectra and photoluminescence decay profiles. First we extract spectroscopic parameters that characterises the sample from FTIR measurements. We also seek to produce phenomenological parameters of multiphonon transitions in both Indium and Gallium Samples. Finally, the study establishes the superior photoluminescence property of Indium over Gallium.

6.2 Glass Fabrication

The samples were prepared by the same melt and quench method described in Section 3.1.2 and in other publications [6.5,6.9]. The introduction of Gallium is known to improve the rare-earth solubility and luminescence behaviour. Furthermore, it binds the ion to selenium centres. Gallium and Indium belong to the same group in the periodic table and therefore, they have the same solubility characteristics. With a larger atomic mass, Indium is projected to produce lower phonon energies and improved photoluminescence over gallium. The next section examines the spectroscopic properties of both types of glasses with 500 and 1000 ppm doping concentrations.

6.3 Absorption Spectroscopy

Absorption measurements for the Pr^{3+} doped chalcogenide fibre samples were made using Fourier Transform Infra Reflectometry (FTIR) Spectrometry (described earlier in Section 3.2.1). Figure 6.1 shows the dependence of the absorption cross-section on the wavelength for the 500 ppm and 1000ppm Pr^{3+} doped chalcogenide glass fibre samples measured by FTIR. In order to obtain absorption cross-section from the absorption coefficient [6.10], the results were scaled using the doping concentration of Pr^{3+} ions and the thickness of the sample. The absorption bands presented in Figure 6.1 corresponds to transitions from the ground state ($^3H_4$) to the $^1G_4$, $^3F_4$, $^3F_3$, $^3F_2$, $^3H_6$ and, $^3H_5$ states. The skew due to background spectra has been removed through baseline correction (see Section 3.2.1) to show only the Pr^{3+} ion contribution to the absorption. These transitions are used to construct a low-resolution energy level diagram for the Pr^{3+} in the chalcogenide glass (see Figure 6.16). The strong overlap of the $^3F_4$, $^3F_3$ absorption bands and the $^3F_2$, $^3H_6$ absorption band is due to the small gap between these levels (450 cm^{-1} and 600 cm^{-1} respectively). Comparing the Gallium and Indium-based absorption bands at $^3F_4/^3F_3$ and $^3F_2/^3H_6$, it was observed that the shape of the spectrum only differ slightly for each of the 500 ppm and 1000 ppm pairs. At the mid-IR (3.5 - 5.5 μm) wavelengths however, there is clear distinction in the absorption measurements for comparative concentrations of Gallium and Indium.
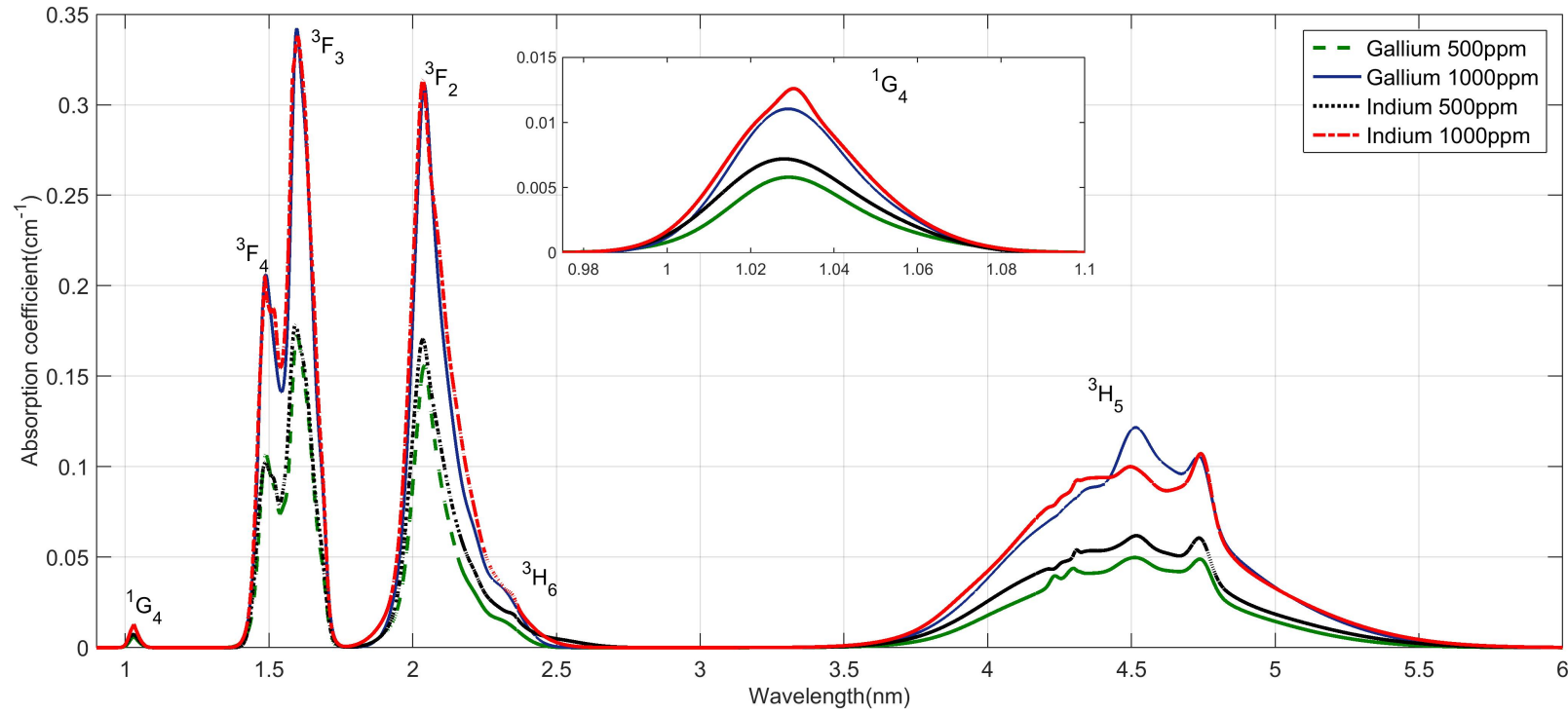
Figure 6.1: Absorption coefficient versus wavelength for different concentrations of Indium (Pr^{3+}:GeAsInSe) and Gallium (Pr^{3+}:GeAsGaSe) based chalcogenide glass samples measured in this research work after baseline correction with least square approximation. The inset is the $^1G_4$ absorption coefficient.

For all the bands, the ratio of absorption in Gallium to Indium based glass samples is 0.86±0.16 for the 500 ppm samples and 0.87±0.18 for the 1000 ppm Pr^{3+}concentration. This calculation will reveal later how subtle changes in composition by substituting Indium for Gallium influences spectroscopic properties especially in the Mid-IR. Table 6.1 shows the peak wavelengths(with a spectra resolution of 1nm) of each transition extracted from the absorption data. This wavelength was obtained by selecting the value of λ that produced the maximum σ_{abs} in each band. Two peaks were assigned to the $^3H_5$ transition because the absorption peak of a few gaseous impurity coincides with this absorption band. The overlapping transitions $^3F_4/^3F_3$ and $^3F_2/^3H_6$ have been deconvolved with a linear combination of Gaussian functions using the Equation 6.1.

Table 6.1: Wavelengths of Energy levels determined by Absorption measurement of Pr^{3+}:GeAs(Ga/In)Se glass

Transition Band	Gallium - λ_{peak}(nm)		Indium - λ_{peak}(nm)	
	500 ppm	1000 ppm	500 ppm	1000 ppm
$^1G_4$	1029	1029	1028	1030
$^3F_4$	1489	1489	1488	1486
$^3F_3$	1598	1597	1592	1600
$^3F_2$	2041	2040	2035	2035
$^3H_6$	2299	2296	2312	2251
$^3H_5$	4515	4515	4515	4501
	4737	4733	4734	4740

$$\sigma_{abs}(\lambda) = \sum_{i=0}^{j} a_i e^{\left(log_e 2\left(-\frac{\lambda-\lambda_i}{d\lambda_i}\right)^2\right)} \tag{6.1}$$

where a_i is the peak value of the absorption, λ_i is the central wavelength, $d\lambda_i$ is the half width at half maximum and i is the number of Gaussians used in the fit. Appendix A.1 lists the values of a_i , λ_i, and $d\lambda_i$ for all transitions in the measured absorption.

6.4 Calculation of Emission Cross Sections

In this section we apply the McCumber's theory of reciprocity discussed in Section 3.5 to calculate the emission cross sections of all the transition bands from the absorption measurement. Calculated emission cross-sections have been previously used to successfully

predict photoluminescence in erbium and vice-versa [6.11]. Therefore, by comparing with similar glasses from literature coupled with the McCumber's theory, emission cross-section can be resolved for all the bands. The following subsections discusses how the emission cross sections were obtained for 6 bands of Pr^{3+}:GeAsGaSe and Pr^{3+}:GeAsInSe.

6.4.1 Band Emission $0.8 - 1.2$ μm, $^1G_4$

The absorption spectrum of the $^1G_4$ energy level is often lost in the instrument noise because of the magnitude of the absorption cross section compared to other transitions. A fit after baseline correction produces a nearly Gaussian absorption spectrum. Figure 6.2 shows the emission cross section calculated using the McCumber's relations. The shape of the emission is similar to the photoluminescence published in literature for the $^1G_4 \rightarrow$ $^3F_4$, 3400nm transition [6.7].
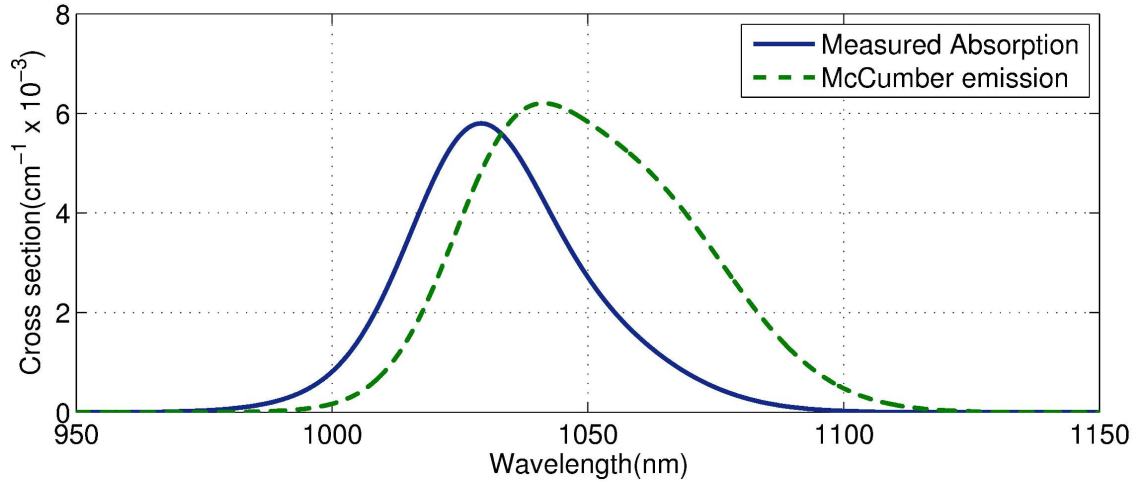
Figure 6.2: Cross sections of the $^1G_4$ band

6.4.2 Band Emission $1.4 - 1.8$ μm, $^3F_4/^3F_3$

The absorption spectrum of the $1.4 - 1.8$ μm band is made up of two distinct peaks which are assigned to $^3F_4$ and $^3F_3$, respectively. The spectra overlap between the two makes the two energy levels difficult to distinguish. The shape of the peaks makes it possible to separate the spectra by deconvolution using Gaussian curves. McCumber's theory of

reciprocity predicts the spectra dependence of emission cross section and, consequently, provides a good estimate of the photoluminescence from the excited level. In this work, we use the photoluminescence measurement ($^3F_4$/ $^3F_3 \rightarrow$ $^3H_4$) from literature [6.2,6.12–6.14] as reference in producing the emission cross sections. The FWHM from the reference photoluminescence is 130±13 nm which can be attributed to the difference in measurement setups used by the authors [6.2,6.12–6.14]. Figure 6.3 shows the stark levels and Figure 6.4 shows the photoluminescence measured in similar glasses published in the literature. The intensities of the photoluminescence are normalised to arbitrary units for the purpose of comparison.
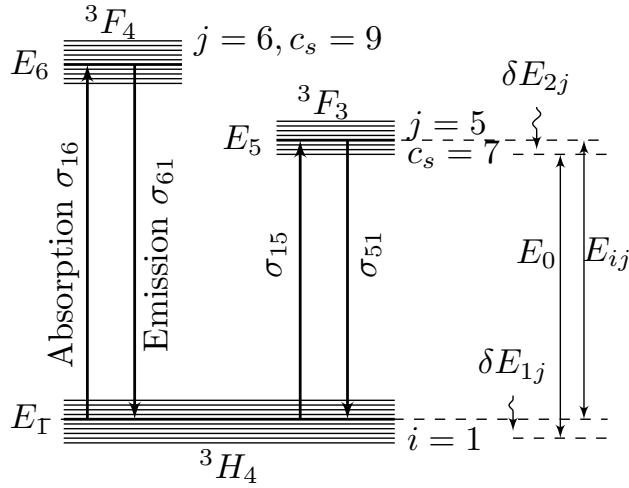
Figure 6.3: Stark Levels of the $^3F_4$/ $^3F_3$ transition

The number of stark levels are 9, 7 and 9 corresponding to $^3F_4$, $^3F_3$ and $^3H_4$ multiplets. Assuming the positions of all the stark components are known, Equation 3.18 can be applied to the energy-levels $^3F_4$ and $^3F_3$ by Equation 6.2 and Equation 6.3 respectively:

$$\frac{N_1}{N_6} = \frac{1 + \sum_{j=2}^{9} e^{-\frac{E_{1j}}{kT}}}{e^{\frac{-E_0}{kT}} \left[1 + \sum_{j=2}^{9} e^{-\frac{E_{6j}}{kT}}\right]} \tag{6.2}$$

$$\frac{N_1}{N_6} = \frac{1 + \sum_{j=2}^{9} e^{-\frac{E_{1j}}{kT}}}{e^{\frac{-E_0}{kT}} \left[1 + \sum_{j=2}^{7} e^{-\frac{E_{5j}}{kT}}\right]} \tag{6.3}$$
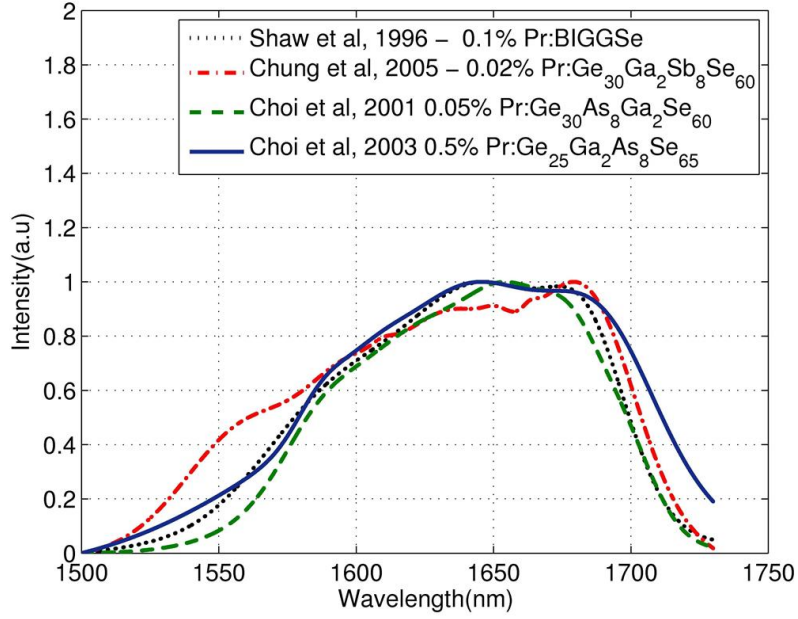
Figure 6.4: Measured photoluminescence of the $^3F_4/\ ^3F_3$ transition in different Pr^{3+}: Chalcogenide glasses [6.2,6.12–6.14]

E_0 is the separation between the lowest component of each manifold (see Figure 6.3) and E_{ij} is the energy difference between the jth and the lowest component of level. Figure 6.5 shows the absorption cross sections from measurement, the emission cross sections of the Pr^{3+}:GeAsGaSe glass as predicted by McCumber's reciprocity theorem and the average emission spectra measured by other authors [6.2,6.12–6.14].

6.4.3 Band Emission $1.8 - 2.5\ \mu m$, $^3F_2/^3H_6$

The photoluminescence measured by Shaw *et al.* [6.2] was based on a 1064 nm pump wavelength and the transition measured in the band of interest is predicted to contain overlapping photoluminescence from the dominant $^1G_4 \rightarrow\ ^3H_6$ (1850nm), $^3F_2/\ ^3H_6 \rightarrow ^3H_4 (\approx$ 2150 nm) and $^3F_3/\ ^3F_4 \rightarrow\ ^3H_5 (\approx 2400$nm). With three possible overlapping transitions, it is difficult to isolate the band of interest $(^3F_2/\ ^3H_6 \rightarrow ^3H_4)$. However, through Gaussian decompositions, the contributions of the overlapping transitions can be seen. Han *et al.* [6.15] measured photoluminescence with 1480nm pump wavelength and the photoluminescence is predicted to contain only two transitions $^3F_2/\ ^3H_6 \rightarrow\ ^3H_4$ and $^3F_3/$
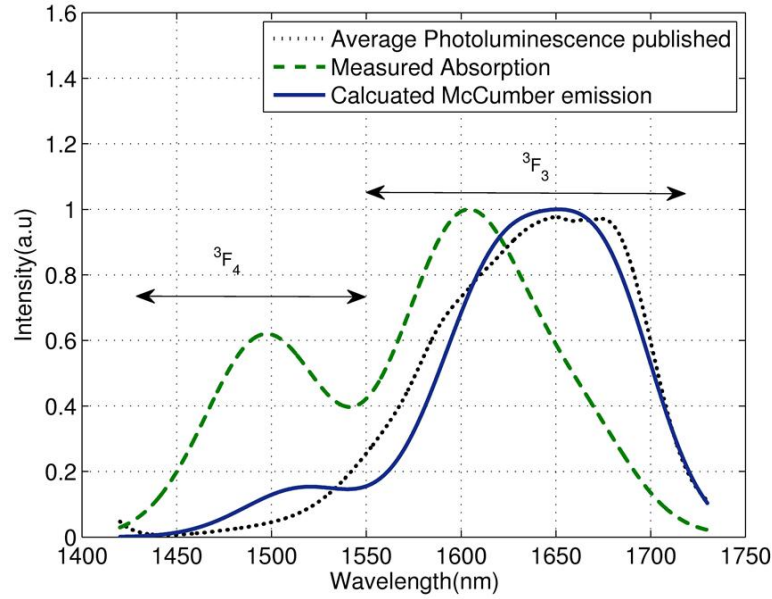
Figure 6.5: Calculated emission cross section of $^3F_4/^3F_3$ transition compared with average measurement published in literature

$^3F_4 \rightarrow {}^3H_5$. Emission from the transition $^3F_3/\ ^3F_4 \rightarrow {}^3H_5$(2400nm) is predicted to be stronger because the emitting level is directly pumped. The measurement made by Yong *et al.* [6.15] had features that are slightly different based on spectral shift from those of other authors [6.2,6.16], an effect attributable to the experimental setup at very low temperatures. In Figure 6.6, the extracted photoluminescence obtained by Gaussian fits (greyed out) for the transition $^3F_3/\ ^3F_4 \rightarrow {}^3H_5$ measured by Shaw *et al.* [6.2] is comparable to those measured by kim *et al.* [6.16] for the same transition. We therefore conclude that the peak at 2124 nm [6.2] and 2200 nm [6.16] are contributions from the transition of interest; $^3F_2/^3H_6 \rightarrow {}^3H_4$. The peak of the emission from the isolated band highlights that photoluminescence from $^3H_6$ dominates the band's emission and the contributions from $^3F_2$ is small in line with the 97% predicted by Boltzmann's statistics. Figure 6.7 shows the calculated emission cross section by McCumber's reciprocity theorem compared with the one extracted from literature. It is important to emphasize that the glass we compared with is not of exact composition as those used in this research and as such the emissions from both glasses are bound to have a few differences. However, the basic feature are still similar.
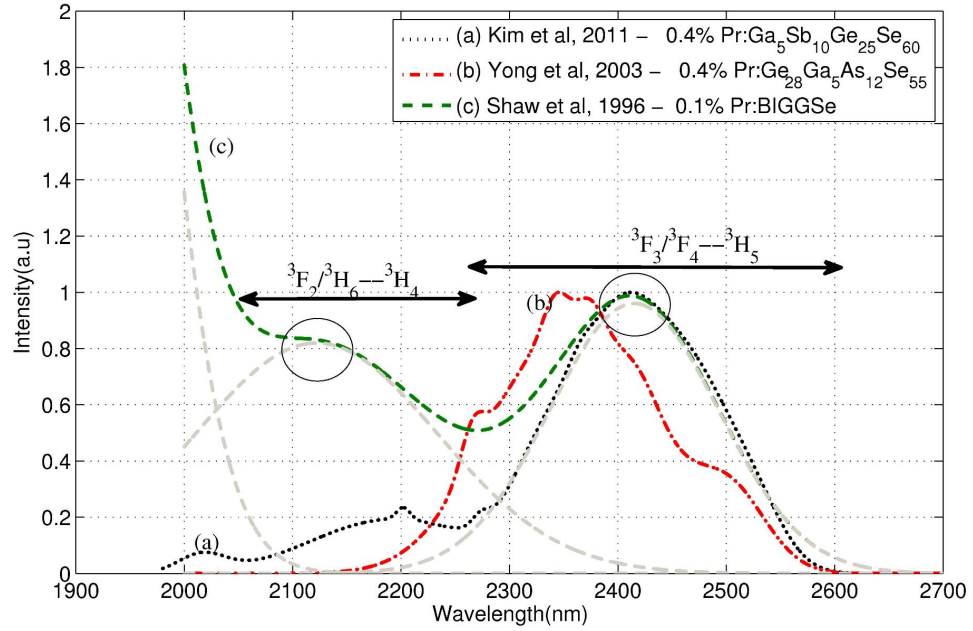
Figure 6.6: Photoluminescence $1.8 - 2.5$ μm band from other chalcogenide glasses in literature [6.2, 6.15,6.16]
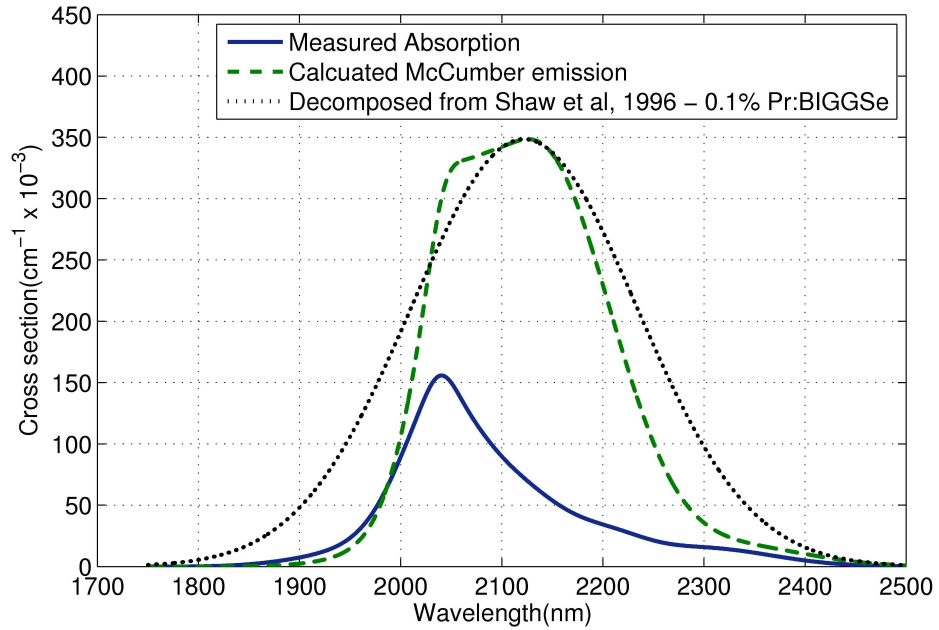
Figure 6.7: Calculated Emission cross section in the $^3F_2/$ $^3H_6$band compared with literature

6.4.4   Band Emission $3.5 - 6.0$ μm, $^3H_5$

There are varied views in literature about the exact assignment of the $^3H_5$ peak wavelength in Pr^{3+}:Chalcogenide. This disparity is traceable to the mid-IR broadband emission

which coincides with the absorption fingerprint of a few gases (HSe, HGe [6.2]). Figure 6.8 shows the mid-IR photoluminescence measurement of Pr:Chalcogenide found in the literature [6.2,6.6,6.17]. In the measurement, an inter-band transition contributes to the spectrum and therefore the actual emission for the $^3H_5 \rightarrow\ ^3H_4$ transition is different from the one measured in Figure 6.8.
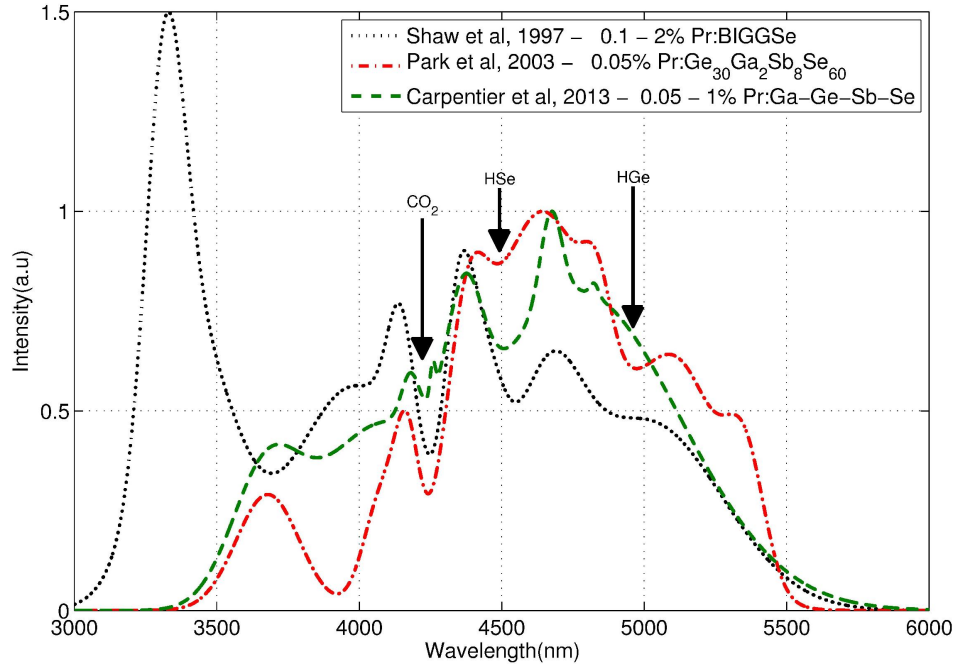
Figure 6.8: Mid-IR Photoluminescence of Pr^{3+}:chalcogenide glasses from literature [6.2,6.6,6.17]

The absorption measurement in undoped Gallium and indium glasses (Section 3.3) was used to correct the influence of gaseous impurities on the absorption measurement (doped Ga and Indium) before emission calculations. The spectrum coinciding with the absorption wavelength of a few gaseous impurities at 4.2 μm (CO_2) and 4.5 μm (HSe) was used as a guide to estimate the magnitude of the correction required for the measurement. Figure 6.9 shows the McCumber emission cross-section which is an indication of the true photoluminescence for the $^3H_5 \rightarrow\ ^3H_4$ transition. The difference between the calculated emission cross section and the measured photoluminescence reveals the contribution of the inter-band transitions to the broad-band emission. By using the McCumber reciprocity, the equivalent absorption cross-section for the $^3H_6 \rightarrow\ ^3H_5$ inter-band transition can be

calculated if the exact magnitude of the gaseous impurities 4.2 μm (CO_2) and 4.5 μm (HSe) in the photoluminescence measurement are known.
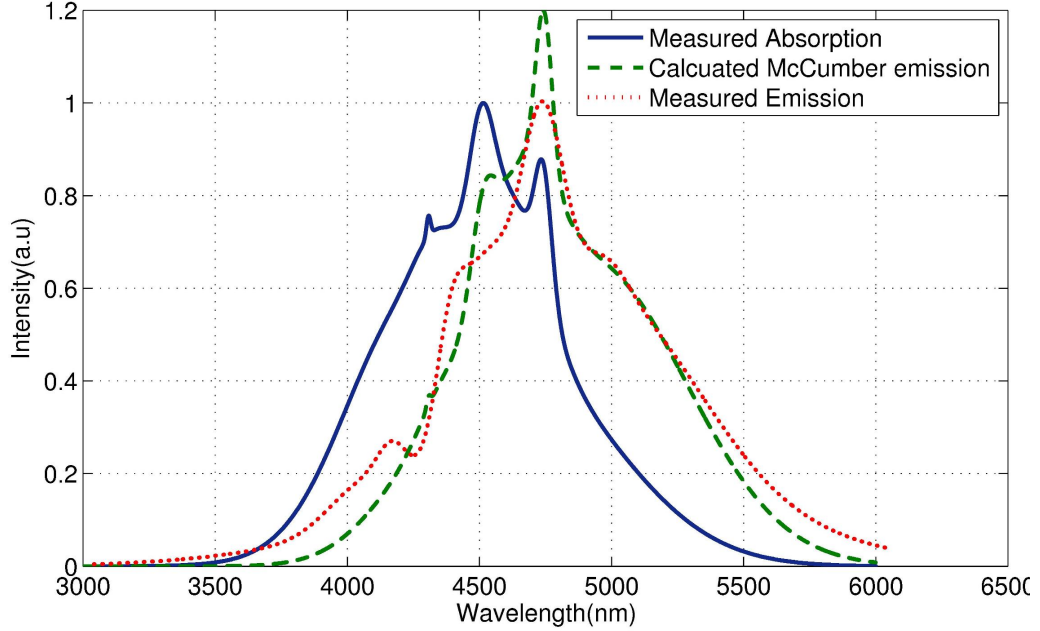
Figure 6.9: Normalised absorption/emission coefficients and measured luminescence for $^{3}H_{5} \rightarrow$ $^{3}H_{4}$ transition

6.4.5 Cumulative Emission

This section summarises all the results of all the emission bands calculated in sections 6.4.1, 6.4.2, 6.4.3 and 6.4.4. The modified McCumber relationship was used to produce the emission cross-sections and by comparing with photoluminescence from available literature [6.2,6.6,6.12–6.17], the results were within acceptable accuracy. Figure 6.10 shows the emission cross sections for all six transitions of 500 ppm and 1000 ppm of Gallium and Indium glasses. The results of this Section and those of Section 6.3 are essential to assess the potential of the glasses as candidates for photoluminescence, amplification and lasing. In the next section, we analyse photoluminescence measured in the chalcogenide glasses and estimate lifetimes from emission decay measurements.
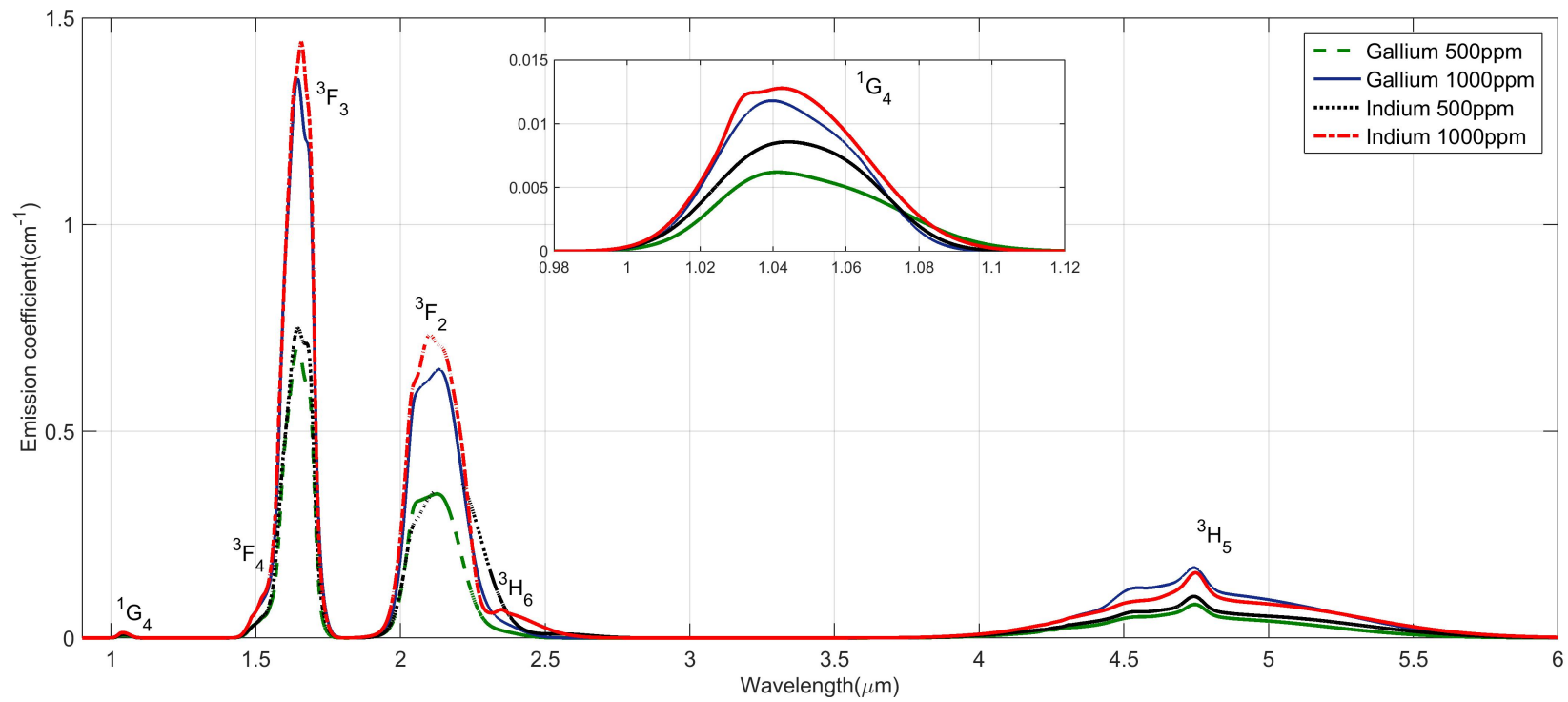
Figure 6.10: Calculated emission coefficient versus wavelength for different concentrations of Indium (Pr^{3+}:GeAsInSe) and Gallium (Pr^{3+}:GeAsGaSe) based chalcogenide glass samples measured in this research work after baseline correction with least square approximation. The inset is the $^1G_4$ emission coefficient.

6.5 Photoluminescence Results

In this section, we present the photoluminescence spectra measured for the Pr^{3+}doped chalcogenide fibre sample. The sample was pumped by a 1.55 μm and 1.94 μm laser diode operating in continuous wave (CW) mode.

6.5.1 Comparison of PL GeAsGa/InSe bulk glasses

Two similar setups as described in section 3.2.2.2 were used to measure the photoluminescence in 500 ppm Pr^{3+}:GeAs**Ga/In**Se bulk glasses. Incident pump was 0.5 mm from the corner with 2 mm orthogonal collection to reduce the effect of self-absorption. Figure 6.11 shows the Mid-IR photoluminescence spectra of 493 ppw Pr^{3+}:GeAs**Ga/In**Se bulk glass pumped at 1550 nm (50.2 mW) with normalized peak emission of 1. The actual emission intensity in the Indium sample is twice that of the Gallium sample with the same concentration of Pr^{3+}. The same setup was repeated for samples with doping concentration of 1000 ppm and the measured intensities were found to be double approximately with increased doping concentration [6.18].
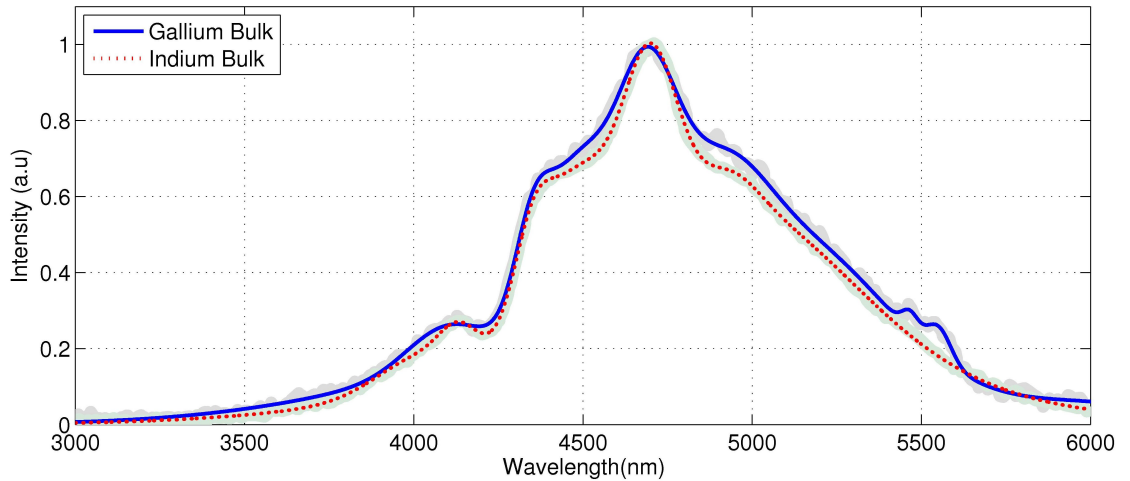
Figure 6.11: Normalised photoluminescence intensities of Indium (Pr^{3+}:GeAsInSe) and Gallium (Pr^{3+}:GeAsGaSe) based chalcogenide glass samples [6.18]

The shape of the photoluminescence is similar to those measured in a previous experimental setup with 1.94 μm pump diode. This suggests that the contributions

to mid-IR luminescence from higher excited states $^3F_4/\ ^3F_3$ were negligible [6.9].

6.5.2 Lifetime Decay Measurement

The Photoluminescence intensity decay of the $^3H_5 \rightarrow\ ^3H_4(4.7\ \mu\text{m})$ transition as a function of time for the 500 ppm and 1000 ppm Pr:GeAs(Ga/In)Se is measured as a function of time. The same setup is also used to measure the decay intensity of 500 ppm Indium based sample at 3.6 μm . Figures 6.12 and 6.13 shows the decay measurements. The decay curves are fitted with a single exponential function [6.19] corresponding to the first e-folding times of the PL Intensity to allow comparison.
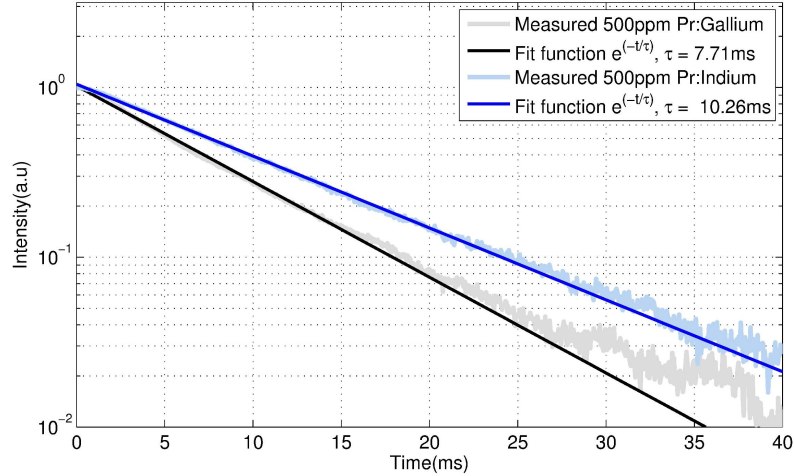
Figure 6.12: PL decay at $^3H_5 \rightarrow\ ^3H_4$ for pumping at 1550 nm, 500 ppm Pr:GeAs(Ga/In)Se bulk glass [6.18]

6.6 Numerical Simulation

The previous sections provided the measurements for the Pr^{3+} doped glasses. In this section, we develop numerical models to describe the phenomenon observed from the experiment. First we extract quantitative values of spectroscopic properties to produce the required parameters for numerical simulations. Subsequently, produce rate equation models of photoluminescence in bulk and fibre glass.
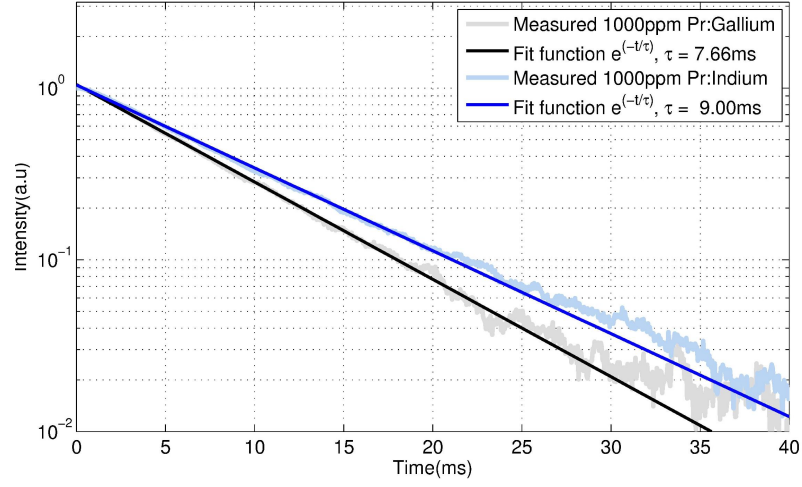
Figure 6.13: PL decay at $^3H_5 \to {}^3H_4$ for pumping at 1550 nm, 1000 ppm Pr:GeAs(Ga/In)Se bulk glass [6.18]

6.6.1 Judd-Ofelt Calculations

Lifetime measurements are difficult to obtain experimentally, as a few components of the multiphonon transitions present themselves in the measurements. Judd-Ofelt (J-O) analysis provides an alternative approach to extract emission lifetime values by calculating phenomenological parameters known as the Judd-Ofelt parameters from fits of line strengths to absorption data. The Judd-Ofelt procedure described in Section 3.4 is applied here to Pr^{3+}:Chalcogenide with Gallium and Indium network formers. Six absorption bands are used for each of the measurements (see Table 6.1, on page 135). Table 6.2 shows the calculated J-O parameters and standard deviation for the Pr^{3+} doped bulk samples, which are in good agreement for Ga bulk glass. All values stated are quoted as $\times 10^{20} \ cm^2$.

Table 6.2: Calculated Judd-Ofelt parameters for bulk glass Pr^{3+}:GeAs(**Ga/In**)Se

Glass (Pr^{3+}:GeAs(Ga/In)Se)	Ω_2	Ω_4	Ω_6	δ_{rms}
Gallium - 500ppm	15.8244	3.9083	11.2214	0.21118
Gallium - 1000ppm	14.2342	6.472	10.895	0.46024
Indium - 500ppm	9.3236	5.5026	6.0375	0.58627
Indium - 1000ppm	8.3681	3.8255	5.8774	0.21064

There are few publications to compare with indium-based selenide-chalcogenide glass

and in particular its J-O parameters in bulk glass. The Judd-Ofelt parameters were observed to be sensitive to the selection of the integrated absorption cross-sections, especially for the overlapping transitions $^3F_4/$ $^3F_3$ and $^3F_2/$ $^3H_6$. Boltmann's statistics was used to reassign the individual components of the overlapping transitions for consistent integrated absorptions across all glass samples. Table 6.3 and 6.4 shows the calculated radiative lifetimes and the oscillator line strengths for a few transitions using the average values from Table 6.2 for the respective glasses. The full listing of all the other transitions can be found in Appendix B.1

Table 6.3: Spontaneous emission lifetime for Pr^{3+}:GeAsGaSe

Transition to $^3H_4$	$K_{calc}(cm^{-1})$	$\lambda(nm)$	f_{meas}	f_{calc}	A_{ed}	$\tau(ms)$
$^3H_5$	2110.9	4737	10.1271	9.5246	122.31	8.1759
$^3H_6$	4350.7	2299	1.5814	1.7340	168.24	3.353
$^3F_2$	4900.7	2041	11.0531	11.1459	4051.5	0.21572
$^3F_3$	6258.4	1598	10.6349	10.7946	5872.1	0.12807
$^3F_4$	6714	1489	5.4526	5.9081	3210.2	0.20722
$^1G_4$	9716.9	1029	0.1993	0.2864	501.69	0.1401

Table 6.4: Spontaneous emission lifetime for Pr^{3+}:GeAsInSe

Transition to $^3H_4$	$K_{calc}(cm^{-1})$	$\lambda(nm)$	f_{meas}	f_{calc}	A_{ed}	$\tau(ms)$
$^3H_5$	2110.9	4737	0.1173	0.1575	89.039	11.231
$^3H_6$	4350.7	2299	3.0005	3.2166	128.1	4.2342
$^3F_2$	4900.7	2041	5.9021	5.9844	3262.1	0.26981
$^3F_3$	6258.4	1598	6.4637	6.4983	4404.6	0.16925
$^3F_4$	6714	1489	1.0751	0.9464	2244.6	0.28685
$^1G_4$	9716.9	1029	5.5266	5.2811	363.7	0.19403

The experimental lifetime τ_{exp} measured for $^3H_5$ is 10.1 ms (527 ppm, GeAsInSe) and 7.8 ms (493 ppm, GeAsGaSe) respectively. The calculated quantum efficiency of the transition defined as $\frac{\tau_{exp}}{\tau_{rad}}$ is close to 100%, given that the Judd-Ofelt calculation is accurate within $\pm 20\%$. This suggests a good incorporation of Pr in the low phonon selenide chalcogenide glass host matrix.

6.6.2 Multiphonon Lifetimes

The multiphonon lifetimes depend on the maximum phonon energy of the host glass and the energy gap between the energy-levels. In Figure 6.14, we compare from literature, the measured Raman spectra of praseodymium doped chalcogenide glass hosts containing Germanium and Gallium. The inclusion of Arsenic and Selenium($Ge_{25}Ga_2\mathbf{As_8Se_{65}}$) [6.12] produced Raman peaks at $\approx$190 cm^{-1} and 220 - 300 cm^{-1}. While the addition of Arsenic and Sulphur $Ge_{30}Ga_2\mathbf{As_6S_{62}}$ [6.15] introduced Raman peaks at $\approx$ 230 cm^{-1} and $\approx$ 330 cm^{-1}. Including Selenium alone ($Ge_{30}Ga_5\mathbf{Se_{65}}$, $Ge_{25}Ga_5\mathbf{Se_{70}}$) [6.20] produced two distinct peaks at $\approx$210 cm^{-1} and $\approx$270 cm^{-1}. From the measurements of Choi *et al.* [6.12] and Nemec *et al.* [6.20], it is observed that the inclusion of Arsenic is responsible for the peaks in the range 220 - 250 cm^{-1}. This is further confirmed by comparing the measurements of Choi *et al.* [6.12] with those of Yong *et al.* [6.15] in which Sulphur was substituted for Selenide with both samples retaining almost equal number of Arsenic atoms. With reference to the two samples containing Arsenic, Sulphur is observed to increase the highest phonon energy to $\approx$ 330 cm^{-1} [6.15,6.21]. Another measurement by Zolyomi *et al.* [6.22] in Indium based samples also confirmed that sulphur raised the highest phonon energy to $\approx$ 293 cm^{-1}, an increase of $\approx$ 29% over the selenide counterpart. This difference can be traced to a heavier atomic mass of Selenium (78.96 amu) compared to Sulphur (32.065 amu) [6.23].

It is estimated that based on all the glasses compared, the maximum phonon energy in our chalcogenide glass material (GeGaAsSe, [6.24]) will be close to those of the Arsenic and Selenium based glass [6.12]. We predict that the maximum phonon energy is $\approx$ 245$\pm$ 10 cm^{-1}in the gallium based sample. The maximum phonon energy of the Indium based sample is taken as $\approx$ 230 cm^{-1} after the work of Zolyomi *et al.* [6.22]

The multiphonon lifetimes were extracted by considering the quantum efficiency of the luminescence levels presented in Table 6.3 and 6.4. Values less than 99% is an indication of the presence of multiphonon decay from that excited level. Here an analysis of the non-radiative transition lifetimes is presented. A Pr^{3+} ion can relax non-radiatively to
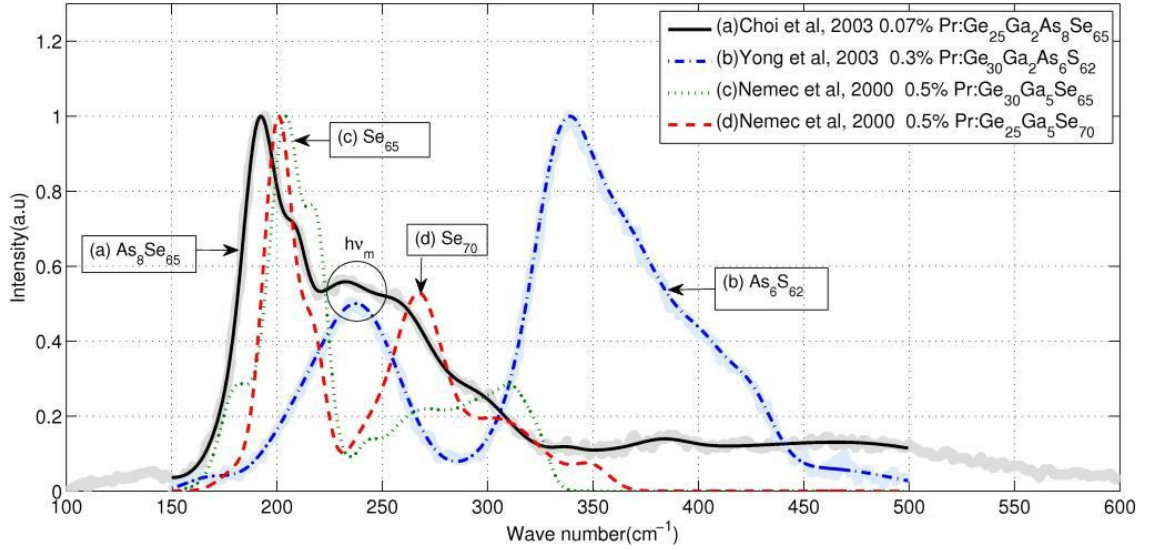
Figure 6.14: Raman Spectroscopy of Pr^{3+}:Chalcogenide Glass with varying combinations of network formers [6.12,6.15,6.20]

the next lower lying manifold by releasing the number of phonons required to bridge the gap between the two energy levels involved. The rate multiphonon relaxation was introduced in Section 2.5 and restated in equation 6.4 for completeness.

$$W_{nr} = Ce^{-\alpha \Delta E} \left[n(T) + 1 \right]^p \tag{6.4}$$

where α and β are host-dependent phenomenological parameters used as a fit to the experimental data[11] while n(T) is the number of thermally generated phonons per mode:

$$n(T) = \left(e^{\frac{h\nu}{KT}} - 1 \right)^{-1} \tag{6.5}$$

T is the absolute temperature and $h\nu$ is the maximum energy of a phonon.

There are many glass compositions that are generally referred to as chalcogenide glass. Typically, α and β parameters in equation 6.4 and consequently the rates of the multiphonon decay vary with the glass composition (Figure 6.15). In a previous study, Choi *et al.* [6.12] reported fairly high values of multiphonon decay rate for chalcogenide glass (see Figure 6.15). We tried to use these results in the next section but could not reproduce the experimentally observed results. This led us to the conclusion that the

Table 6.5: Table of multiphonon lifetimes

Transition	Energy gap(ΔE)	$n_{phonons}$	τ_{nr}(s)
$^3H_5 \to {}^3H_4$	2110.9	8	0.172 (Ga) , 0.123(In)
$^3H_6 \to {}^3H_5$	2239.8	9	0.291(In)
$^3F_2 \to {}^3H_6$	550	2	Interpolated
$^3F_3 \to {}^3F_2$	1357.7	6	1.8125×10^{-3} [6.7]
$^3F_4 \to {}^3F_3$	455.6	2	Interpolated
$^1G_4 \to {}^3F_4$	3002.9	13	Interpolated

multiphonon transition rates reported by Choi *et al.* [6.12] might be overestimated, most likely due to a low purity of the chalcogenide glass. This conclusion is further supported by the results of Shaw *et al.* [6.7] whereby an average decay rate of $83 s^{-1}$ ($\eta = 80\%$) was measured for the $^3H_5$ energy level in a purified, low Pr^{3+} concentration (1000 ppm) chalcogenide glass. Following the results of Shaw *et al.* [6.7] we made an alternative estimation of the multiphonon transition rate in a chalcogenide glass (Figure 6.15). By combining the lifetime measurements in Section 6.5.2 with the calculated lifetimes in Tables 6.3 and 6.4, the multiphonon lifetimes can be determined. A fit to equation 6.4 produced values of $\alpha = 8.07 \times 10^3$ cm and $\beta = 7.28 \times 10^6 s^{-1}$, which we use in the simulations presented in the next section. Table 6.5 presents the multiphonon lifetimes obtained consequently from equation 6.4. The first two rows presents the multiphonon lifetimes obtained from quantum efficiencies while the others were obtained by interpolation based on the parameter fit to equation. The values quoted for $^3F_3 \to {}^3F_2$ were taken from another glass with similar composition previously published by another research group [6.7]. The results demonstrate that multiphonon decay is not significant in the Gallium and Indium glass for energy gaps greater than 1500 cm^{-1}.

6.6.3 Photoluminescence Models of bulk glasses

In order to predict the stationary populations of the electronic energy levels shown in figure 6.16, we propose a generalised numerical model restricted to a linear set of processes expected in low concentration samples. This assumption is supported by our experiment [6.9,6.18] and in published literature [6.25], where concentration quenching
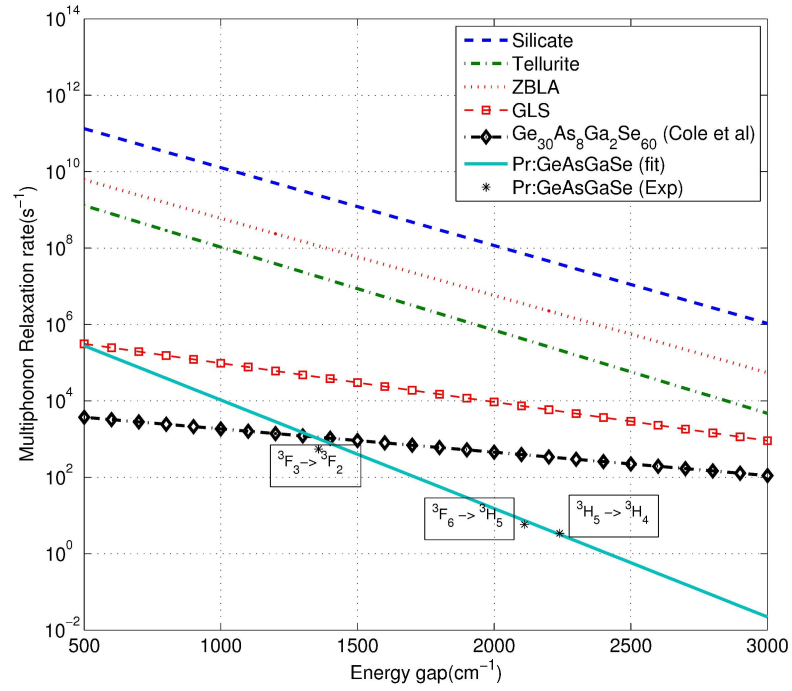
Figure 6.15: Multiphonon Rate of Pr^{3+}:GeAsGaSe compared with other glasses
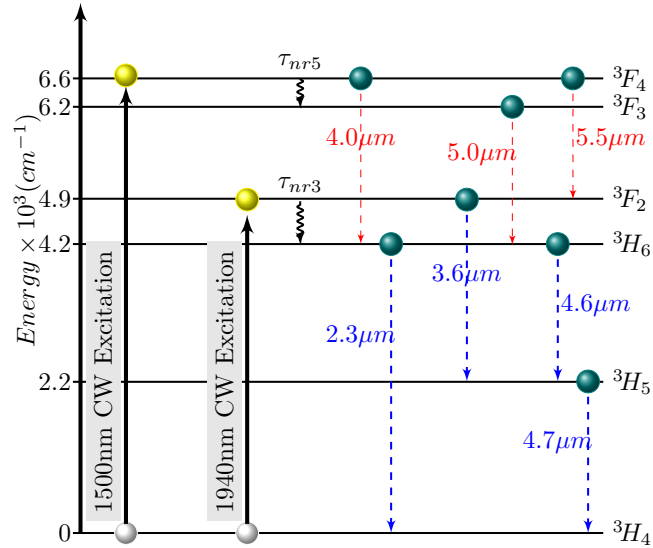
was not detected below 1500 ppm.

Figure 6.16: Energy level diagram of Pr^{3+}ion

The Pr^{3+} system is characterised by low phonon energies and hence the energy levels are considered as successively connected by spontaneous emissions, except for energy gaps

below (550 cm^{-1}; $^3F_2 \rightarrow ^3H_6$, $^3F_4 \rightarrow ^3F_3$) where multiphonon transitions are considered. Following the rate equation approach we formulate equations that relate the temporal change of energy level populations: n_0, n_1, n_2 , n_3 , n_4 and n_5 of Pr^{3+}corresponding to the energy levels $^3H_4$, $^3H_5$, $^3H_6$, $^3F_2$, $^3F_3$ and $^3F_4$ respectively, with the rates of the radiative and non-radiative transitions. Equation 6.7 is the combined rate equations for 1940 nm and 1500 nm pump excitation.

$$
\begin{aligned}
\frac{dn_0}{dt} &= -n_0 R_{pa,1500} + n_5 R_{pe,1500} - n_0 R_{pa,1940} + n_3 R_{pe,1940} + \frac{n_1}{\tau_{r1}} + \frac{n_1}{\tau_{nr1}} \\
&\quad + \sum_{i=2}^{j=5} \frac{\beta_{i0} n_i}{\tau_{ri}} \\
\frac{dn_1}{dt} &= -\frac{n_1}{\tau_{r1}} - \frac{n_1}{\tau_{nr1}} + \frac{n_2}{\tau_{nr2}} + \sum_{i=2}^{j=5} \frac{\beta_{i1} n_i}{\tau_{ri}} \\
\frac{dn_2}{dt} &= -\frac{n_2}{\tau_{r2}} - \frac{n_2}{\tau_{nr2}} + \frac{n_3}{\tau_{nr3}} + \sum_{i=3}^{j=5} \frac{\beta_{i2} n_i}{\tau_{ri}} \\
\frac{dn_3}{dt} &= n_0 R_{pa,1940} - n_3 R_{pe,1940} - \frac{n_3}{\tau_{r3}} - \frac{n_3}{\tau_{nr3}} + \frac{n_4}{\tau_{nr3}} + \sum_{i=4}^{j=5} \frac{\beta_{i2} n_i}{\tau_{ri}} \\
\frac{dn_4}{dt} &= -\frac{n_4}{\tau_{r4}} - \frac{n_4}{\tau_{nr4}} + \frac{n_5}{\tau_{nr5}} + \frac{\beta_{54} n_5}{\tau_{r5}} \\
\frac{dn_5}{dt} &= n_0 R_{pa,1500} - n_5 R_{pe,1500} - \frac{n_5}{\tau_{r5}} - \frac{n_5}{\tau_{nr5}}
\end{aligned}
\tag{6.6}
$$

Where $R_{pa,\lambda} = \frac{\sigma_{\lambda,abs} I_\lambda}{h\upsilon_\lambda}$ is the pump absorption rate at the pump wavelength λ given a pump photon flux I_λ and $R_{pe,\lambda} = \frac{\sigma_{\lambda,ems} I_\lambda}{h\upsilon_\lambda}$ is the pump spontaneous emission rate at the pump wavelength λ at the excited level. $\sigma_{\lambda,abs}$ and $\sigma_{\lambda,ems}$ are the absorption and emission cross-sections respectively (see section 6.3, figure 6.1 and section 6.4.5, figure 6.10). We complement the equations 6.7 by the following

$$
n_{Pr} = n_0 + n_1 + n_2 + n_3 + n_4 \tag{6.7}
$$

Which implies that the population of the higher lying energy states is negligible because of very fast non-radiative decay, in agreement with the experimentally observed inferred

Table 6.6: Simulation parameters Pr^{3+}:GeAs(Ga/In)Se bulk glass

Parameter	Gallium		Indium		Unit
Pump Wavelength	1550	1940	1550	1940	mW
Pump power	17 - 105	59 - 200	17 - 105	59 - 200	nm
Absorption cross-section	-	-	-	-	cm^2
Doping Concentration	493, 994	493, 994	493, 994	493, 994	ppm
Spot size	-	-	-	-	cm^2

absence of up-conversion photoluminescence. The total Pr^{3+}ion concentration in the chalcogenide sample - n_{Pr} was estimated from density and molar mass from available literature [6.26]. 500ppm of Pr^{3+} ion is approximately 6.53×10^{18} ions/cm^3 and 1.16×10^{19} ions/cm^3 in Gallium and Indium respectively. Table 6.6 lists the simulation parameters of our model. The life times for the relevant transitions are presented in Appendix A.

In the experiment, the pump laser was modulated at 8 Hz and 10 Hz. The low frequency pump modulation excites the energy levels of Pr^{3+} for a period, long enough to attain a steady state. We therefore solved equation 3 at steady state ($n_i = 0$) and compared the solution with the experimentally observed photoluminescence spectra. In Figures 6.17, 6.18, 6.19 and 6.20, the calculated photoluminescence spectrum obtained from the rate equation model is presented for 1.55 μm and 1.94 μm pumping, respectively. When compared with pumping at 1.55 μm , fewer transitions are observed with 1.94 μm pumping because only 4 energy levels are involved in the excitation: ${}^3H_4$, ${}^3H_5$, ${}^3H_6$and ${}^3F_2$. Further, the distribution of light intensity between various contributing processes varies at both pumping wavelengths. This explains the differences between the experimentally obtained photoluminescence spectra at 1.55 μm and 1.94 μm pumping. The photoluminescence figures for Gallium and Indium pumped with 1550nm looks similar because the calculated photoluminescence has been scaled to maximum peak of unity. The same observation can be made with 1940nm excitation. To differentiate the photoluminescence calculated for Indium and Gallium at the mid-IR, we have used Gaussian approximations whose areas are scaled to the calculated PL. Figure 6.21 the results for mid-IR PL simulation for both indium and gallium pumped at 1550nm.

For the time-resolved luminescence, equation 6.7 is solved in the time domain using an
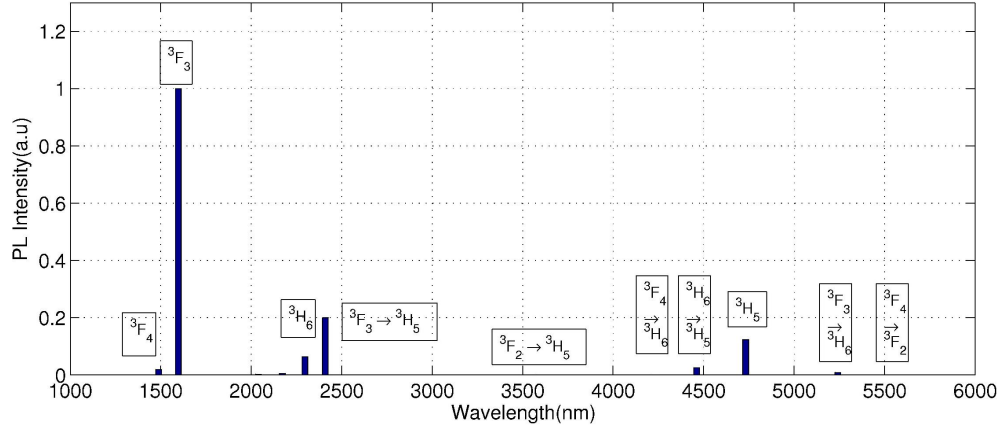
Figure 6.17: Simulation result of Pr^{3+}:GeAsGaSe photoluminescence (pump wavelength of 1.55 μm).
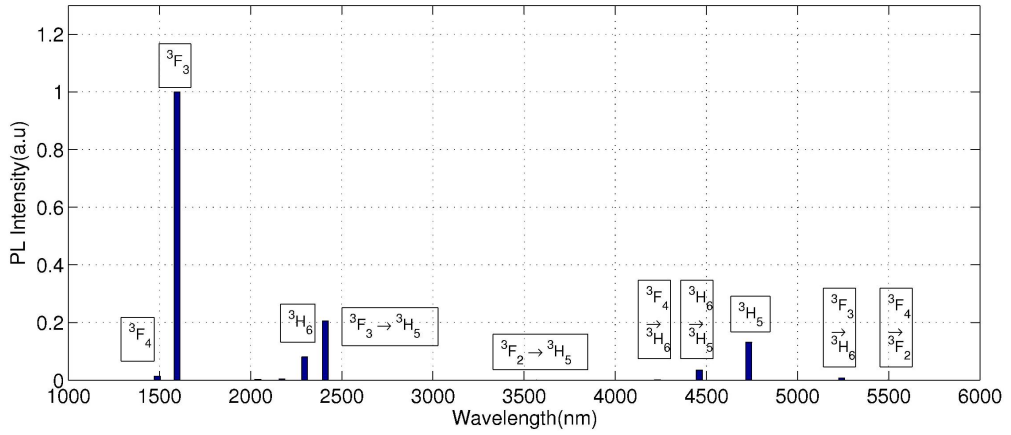
Figure 6.18: Simulation result of Pr^{3+}:GeAsInSe photoluminescence (pump wavelength of 1.55 μm).

adaptive Runge-Kutta integration routine [6.27]. The numerical (scaled and normalised) results and approximate fit obtained for the decay profiles at $^3F_4$, $^3F_3$ and $^3H_5$ are presented in Figures. 6.22. The decay lifetime of the $^3F_4$, $^3F_3$ is found to be 212 μs while 230 μs (Judd-Ofelt),and 272 μs (experiment) were reported [6.9]. Likewise, the fit function to $^3H_5$ decay profile produced a decay lifetime of 10.05 ms for which 10.2 ms (Judd-Ofelt),and 11.5 ms (experiment) were reported [6.9]. There is therefore a good agreement between both sets of results and the ones obtained from experiment.
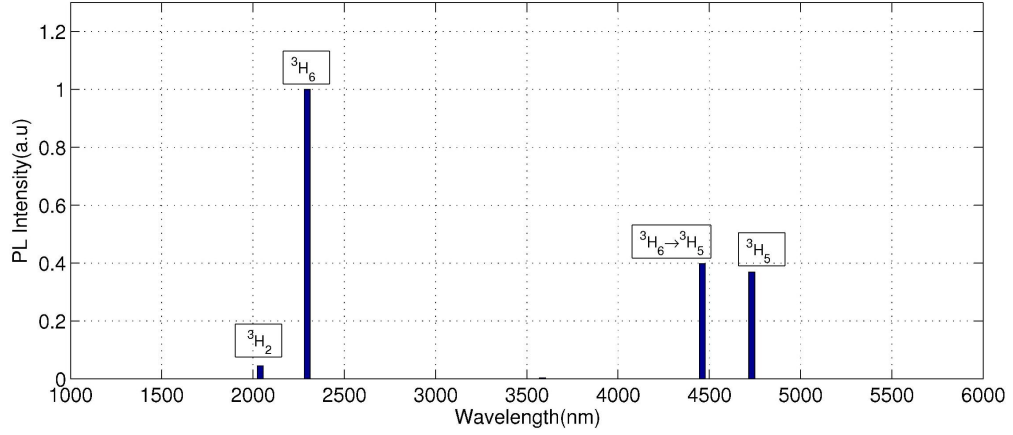
Figure 6.19: Simulation result of Pr^{3+}:GeAsGaSe photoluminescence (pump wavelength of 1.94 μm).
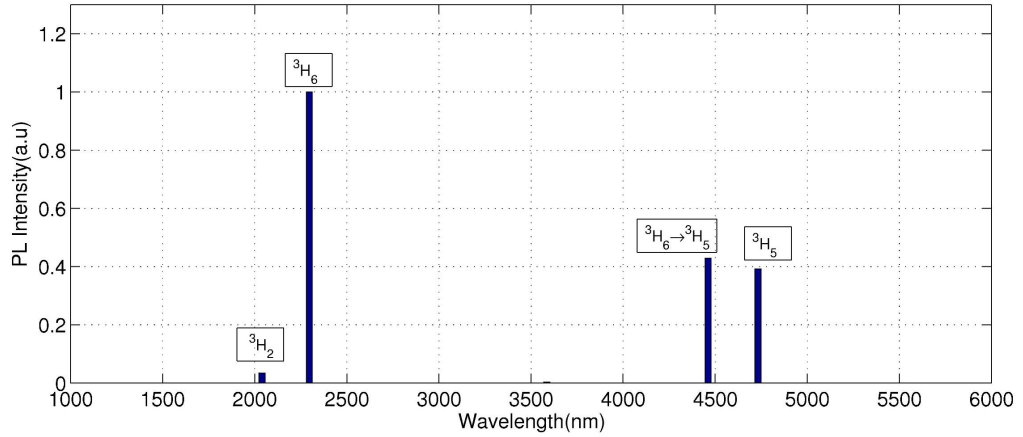
Figure 6.20: Simulation result of Pr^{3+}:GeAsInSe photoluminescence (pump wavelength of 1.94 μm).

6.6.4 Photoluminescence Models of Fibre glasses

The $^3H_5 \to {}^3H_4$ transition shows a large spectral overlap between the absorption and emission spectra shown in figure 6.9, therefore reabsorption at other wavelengths cannot be ruled out. The high number of stark levels in the ground state $(^3H_4, 2J_0 + 1 = 9)$ and the first excited state $(^3H_5, 2J+1 = 11)$ also presents numerous starting points for possible absorption transitions. The long interaction length of an optical fibre compared to a bulk sample causes some photons emitted from the $^3H_5 \to {}^3H_4$ transition to be easily reabsorbed by Pr^{3+} ions in the ground state. The reabsorbed photons behave like secondary pump

155
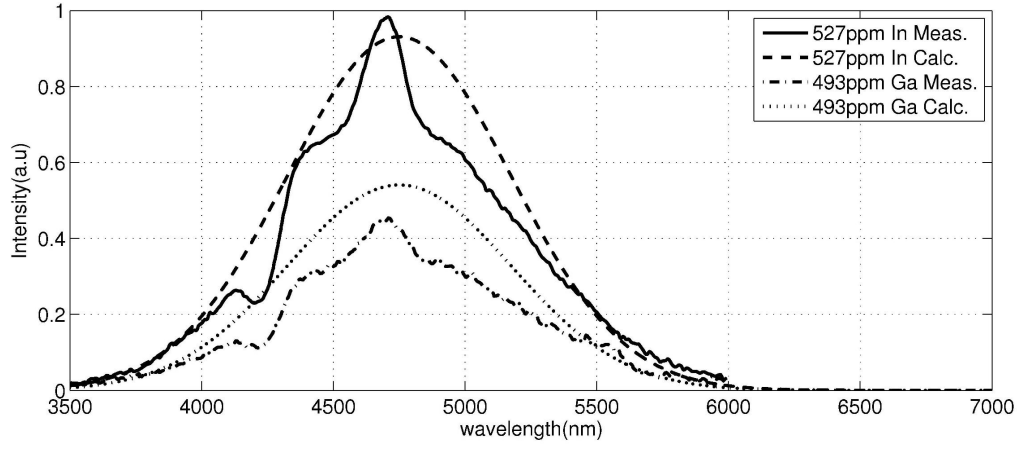
Figure 6.21: Comparison between simulation and experiment of Pr^{3+}:GeAs(Ga/In)Se at MIR photoluminescence (pump wavelength of 1.55 μm).
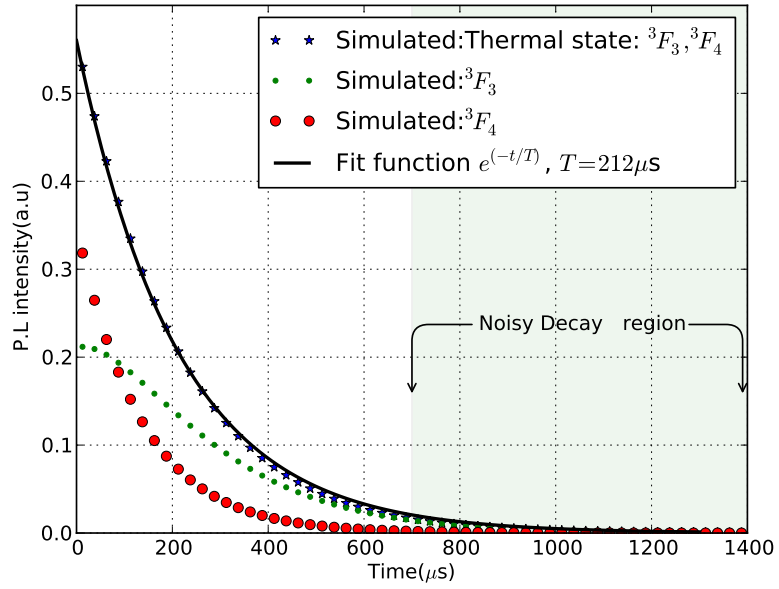
Figure 6.22: Modelled decay curve of the $\left(^3F_4,\ ^3F_3\right) \rightarrow \ ^3H_4$ lifetime in 500 ppm doped Pr^{3+}:GeAsGaSe glass with 1.55 μm pump wavelength

excitations and promote ions to the edge of the stark levels, which are then re-emitted at longer wavelengths. Figure 6.23 shows the influence of reabsorption on photoluminescence measured in the mid-IR for step-index Indium and Gallium based fibres.

To investigate the reabsorption process at 1550nm pumping, we modify equation 6.7 as follows
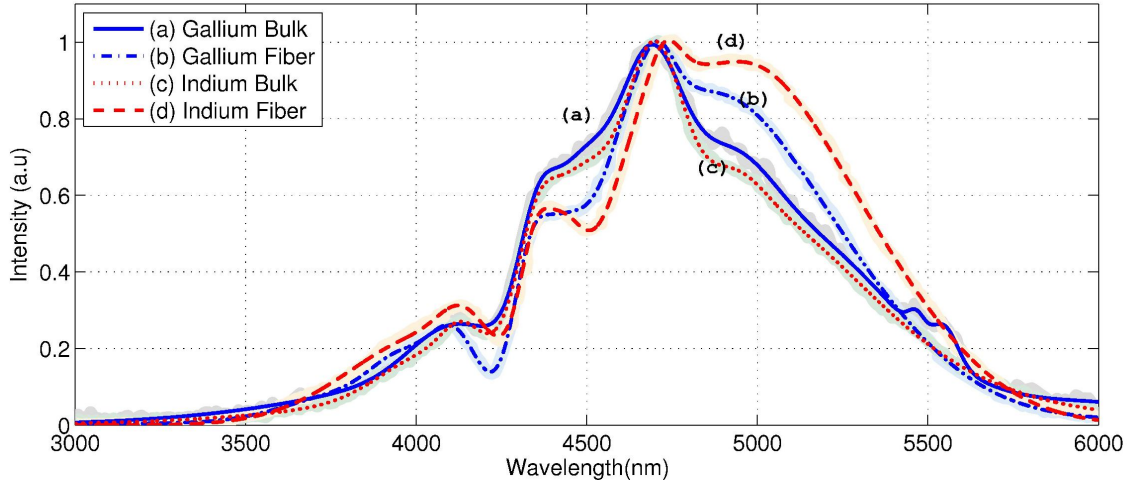
Figure 6.23: Normalized PL spectra of 493 ppmw Pr^{3+}-GeAsGaSe / GeAsGaSe SIF and 498 ppmw Pr^{3+}-GeAsInSe / GeAsInSe SIF Pr^{3+}-GeAsInSe / GeAsInSe SIF, each pumped at 1550 nm

$$
\begin{aligned}
\frac{dn_0}{dt} &= -n_0 R_{pa,1500} + n_5 R_{pe,1500} - n_0 R_{reabs,4700} + \frac{n_1}{\tau_{r1}} + \frac{n_1}{\tau_{nr1}} \\
&\quad + \sum_{i=2}^{j=5} \frac{\beta_{i0} n_i}{\tau_{ri}} \\
\frac{dn_1}{dt} &= n_0 R_{reabs,4700} - \frac{n_1}{\tau_{r1}} - \frac{n_1}{\tau_{nr1}} + \frac{n_2}{\tau_{nr2}} + \sum_{i=2}^{j=5} \frac{\beta_{i1} n_i}{\tau_{ri}} \\
\frac{dn_2}{dt} &= -\frac{n_2}{\tau_{r2}} - \frac{n_2}{\tau_{nr2}} + \frac{n_3}{\tau_{nr3}} + \sum_{i=3}^{j=5} \frac{\beta_{i2} n_i}{\tau_{ri}} \\
\frac{dn_3}{dt} &= -\frac{n_3}{\tau_{r3}} - \frac{n_3}{\tau_{nr3}} + \frac{n_4}{\tau_{nr3}} + \sum_{i=4}^{j=5} \frac{\beta_{i2} n_i}{\tau_{ri}} \\
\frac{dn_4}{dt} &= -\frac{n_4}{\tau_{r4}} - \frac{n_4}{\tau_{nr4}} + \frac{n_5}{\tau_{nr5}} + \frac{\beta_{54} n_5}{\tau_{r5}} \\
\frac{dn_5}{dt} &= n_0 R_{pa,1500} - n_5 R_{pe,1500} - \frac{n_5}{\tau_{r5}} - \frac{n_5}{\tau_{nr5}}
\end{aligned}
\tag{6.8}
$$

Where all parameters retain their usual assignments. The parameter $R_{reabs,4700}$ represents the emitted photon flux at 4700nm which serves as an excitation source for

Table 6.7: Simulation Parameters for GeAs(Ga/In)Se fibre optically-clad

Parameter	Gallium	Indium	Unit
Pump Wavelength	1550	1550	nm
Pump power	24.5	24.5	mW
Fiber Length	0.115	0.110	m
Doping Concentration	493, 994	493, 994	ppm

ions in the ground state along the length of the fibre.

$$R_{reabs,4.7um} = \frac{\sigma_{\lambda,abs} I_\lambda}{h\upsilon_\lambda} \tag{6.9}$$

The reemitted photoluminescence (5 μm) originates from the lower multiplets of the 11 stark levels in $^3H_5$. Therefore the population of the ions in level 1 (n_1) is reassigned by Boltzmann's distribution to consist of contributions n_1^a (4.7 μm) and n_2^b (5.0 μm). The relationship between the long and short wavelength contributions are give by equation 6.10 where $n_1^a + n_1^b = n_1$

$$\frac{n_1^a}{n_1^b} = e^{\frac{-h\upsilon}{K_B T}} \tag{6.10}$$

The energy difference of the two stark levels is taken to be hv ≈ 247 cm^{-1}, therefore at room temperature, Boltzmann statistics predicts an occupation number of about 22% for the upper level $\lambda_{4.7}$. This percentage is used to assign values to n_1^a and n_1^b after steady-state calculation of n_1.

Equation 6.9 is complemented with a fibre propagation equation (see section 4.3) for a pump at 1550nm and photoluminescence signal at 4700nm.

We solve the fibre propagation equation for photoluminescence through the fibre in a single pass, ignoring residual end reflectivities. We note that based on the original calculation in bulk materials, the mid-IR transition is made up of the following transitions: $^3F_2 \rightarrow {}^3H_5$(3.5 μm), $^3F_4 \rightarrow {}^3H_6$(4.2 μm), $^3H_6 \rightarrow {}^3H_5$(4.4 μm), $^3H_5 \rightarrow {}^3H_4$(4.7 μm), $^3F_3 \rightarrow {}^3H_6$(5.2 μm), $^3F_4 \rightarrow {}^3F_2$(5.5 μm) (see appendix for all transitions). Therefore to reproduce the fiber photoluminescence therefore, we use gaussian representations, with FWHM taken from the absorption cross-sections of the originating levels, and absolute area is proportional to the calculated intensities. The re-emission at 5.0 μm is represented

by a guassian curve with the same FWHM as the absorption cross-section of $^3H_4 \rightarrow {}^3H_5$.

6.6.5 Praseodymium doped fibre amplifier

In this section, a 1D steady state model is used to investigate the potential of the Indium and Gallium based glass samples as amplifiers for mid-IR signal. The co-propagating pump configuration is adopted, in which the pump wavelength of 1530 nm propagates in the same direction as the signal wavelength 4730 nm. Table 6.8 shows the simulation parameters used to study the glasses as potential candidates for PDFA in the mid-IR

Table 6.8: Simulation parameters of PDFA based on 1000ppm Pr:GeAs(Ga/In)Se glass

Parameter	Gallium	Indium	
R	5 μm	5 μm	Doping radius
L	1.45 m	1.45 m	Fibre Length
σ_p	1.15 $\times 10^{-20}$ cm^2	7.47 $\times 10^{-21}$ cm^2	Pump absorption cross section
σ_s	1.28 $\times 10^{-20}$ cm^2	7.96 $\times 10^{-21}$ cm^2	Signal emission cross section
N_d	1000 ppm	1000 ppm	Praseodymium ion concentration
Γ_s	0.9	0.9	Confinement factor for signal
Γ_p	0.9	0.9	Confinement factor for pump
τ_{r1}	7.66 ms	9.0 ms	$^3H_5 \rightarrow {}^3H_4$ lifetime
λ_p	1530 nm	1530 nm	Pump wavelength
λ_s	4730 nm	4730 nm	Signal wavelength

Figure 6.24 shows the dependence of the amplifier gain on the pump power in co-propagating configuration assuming the signal power is -40 dBm and the pump power is varied between 1 dBm and 20 dBm. At 20 dBm, the Indium based fibre experienced a signal gain of $\approx$ 2 dB over the Gallium based counterpart.

Figure 6.25 shows the dependence of the amplifier gain on the signal power in co-propagating configuration assuming the pump power is 20 dBm and the signal power is varied between -40 dBm and 0 dBm. A gain value of 49.51 dB ($\approx$ 2 dB greater than the Gallium based counterpart) was calculated with -40 dBm signal power in the Indium based fibre.

Figure 6.26 shows the dependence of the amplifier gain on wavelength with a pump power of 20 dBm at 1530 nm and signal power of -40 dBm operating between 4400 - 5200
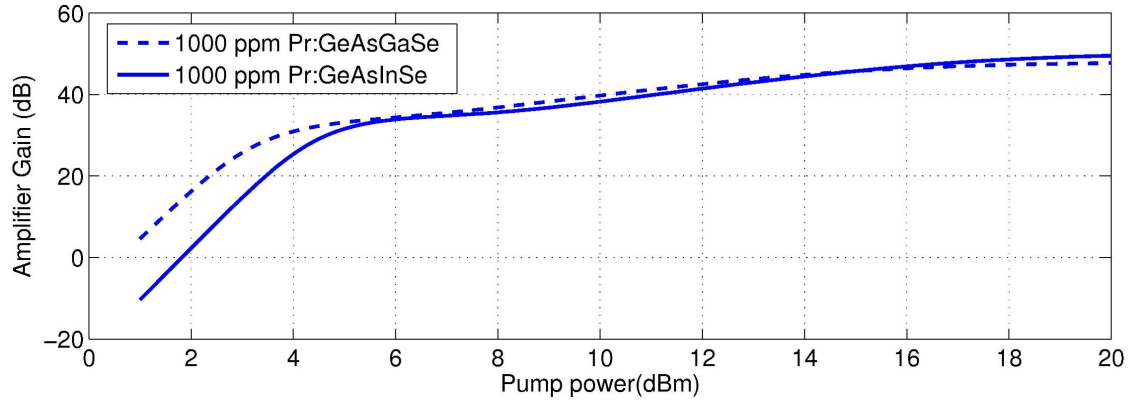
Figure 6.24: Dependence of the amplifier gain on the pump power in co-propagating pump configuration

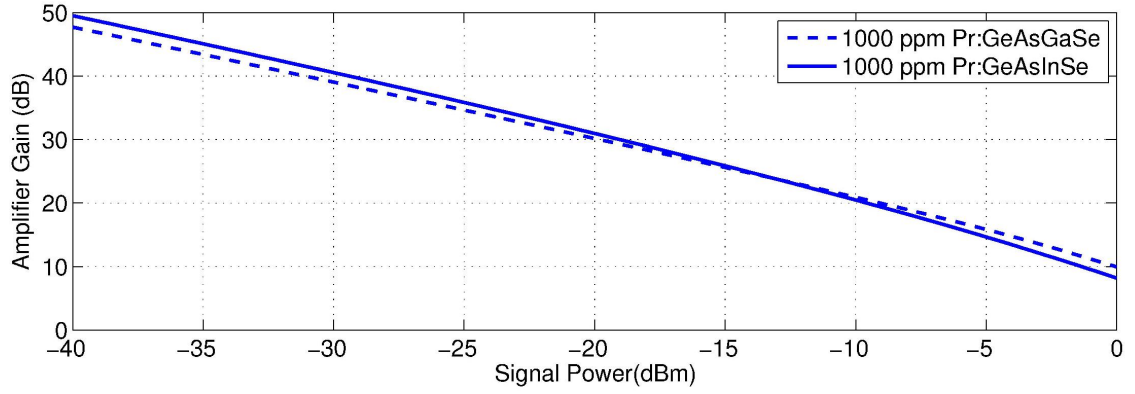**Figure 6.25:** Dependence of the amplifier gain on the signal power in co-propagating pump configuration

nm. Like the other configurations in figures 6.24 and 6.25, a gain difference of ≈ 2 dB was achieved at the peak wavelength in the Indium fibre compared to Gallium fibre
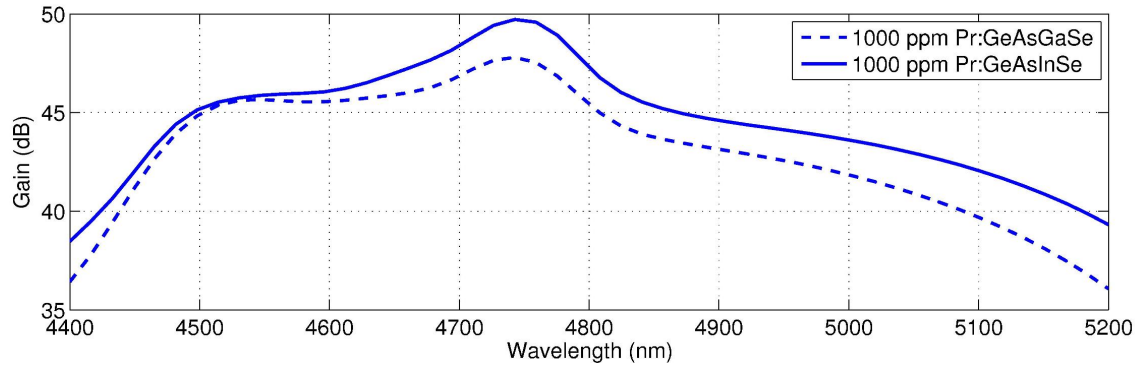
Figure 6.26: Dependence of the amplifier gain on the signal wavelength in co-propagating pump configuration

6.7 Summary and discussion

In this work, 500 and 1000 ppm Pr^{3+} doped chalcogenide bulk glass and fibre have been prepared by the melt and quench method. It has been established that at this low dopant concentration the bulk/fibre glass was capable of generating intense broadband mid-infrared emission without energy up-conversion. The numerical model was able to show the specific contributions of the levels $^3F_3$, $^3F_4$ to the decay profile observed in experiment. We also established that the long decay tail observed with the $^3H_5 \rightarrow {}^3H_4$ emission is a result of linear contributions from upper lying states. The lifetime ratio between $^3H_5 \rightarrow {}^3H_4$ and $^3H_6 \rightarrow {}^3H_4$ transitions coupled with the strong emission when pumped with CW laser makes this fibre a potential source for a realisation of a laser operating at 4.6 μm . We presented an investigation into the photoluminescence properties of praseodymium doped selenide chalcogenide glasses by comparing a mathematical model with experimental data. Judd-Ofelt analysis has been performed on Pr^{3+}:GeAs(Ga/In)Se glass with compositions described elsewhere [6.18,6.24]. The Judd-Ofelt intensity parameters produced all the relevant radiative transition rates and branching ratios. The multiphonon rates associated with the glass were also presented and compared with existing literature. Higher intensities of mid-IR photoluminescence in GeAsInSe compared to GeAsGaSe is an evidence of lower phonon energy in the former than the latter and this is possibly just very local to the Pr^{3+} ion as the indium and gallium are generally thought to complex the Pr^{3+} ion in chalcogenide glasses. The model presented was able to produce photoluminescence intensities which showed similar trends to the calculated emission intensities.

Also, a numerical model was developed to validate the presence of photon reabsorption in a chalcogenide glass fibre leading to emission at longer wavelengths in the mid-IR with a 1550 nm pump diode. The spectroscopic data from fibre samples strongly suggests that due to the magnitude of the reabsorption, a high pump power will be required to realise a laser in Pr^{3+} doped gain media.

References

[6.1] J. Nishii, S. Morimoto, I. Inagawa, R. Iizuka, T. Yamashita, and T. Yamagishi, "Recent advances and trends in chalcogenide glass fiber technology: a review," *Journal of non-crystalline solids*, vol. 140, pp. 199–208, 1992.

[6.2] L. Shaw, B. Harbison, B. Cole, J. Sanghera, and I. Aggarwal, "Spectroscopy of the IR transitions in Pr^{3+}doped heavy metal selenide glasses.," *Optics express*, vol. 1, pp. 87–96, Aug. 1997.

[6.3] A. Zakery and S. R. Elliott, "Optical properties and applications of chalcogenide glasses: a review," *Journal of Non-Crystalline Solids*, vol. 330, no. 1, pp. 1–12, 2003.

[6.4] J. Sanghera and I. Aggarwal, "Active and passive chalcogenide glass optical fibers for IR applications: a review," *Journal of non-crystalline solids*, vol. 256, pp. 6–16, 1999.

[6.5] Z. Tang, N. C. Neate, D. Furniss, S. Sujecki, T. M. Benson, and A. B. Seddon, "Crystallization behavior of Dy^{3+}-doped selenide glasses," in *Journal of Non-Crystalline Solids*, vol. 357, pp. 2453–2462, 2011.

[6.6] B. J. Park, H. S. Seo, J. T. Ahn, Y. G. Choi, D. Y. Jeon, and W. J. Chung, "Mid-infrared ($3.5 - 5.5$ μm) spectroscopic properties of Pr^{3+}-doped Ge–Ga–Sb–Se glasses and optical fibers," *Journal of Luminescence*, vol. 128, pp. 1617–1622, Oct. 2008.

[6.7] L. Shaw, B. Cole, P. Thielen, J. Sanghera, and I. Aggarwal, "Mid-wave IR and long-wave IR laser potential of rare-earth doped chalcogenide glass fiber," *IEEE Journal of Quantum Electronics*, vol. 37, no. 9, pp. 1127–1137, 2001.

[6.8] S. Kasap, K. Koughia, M. Munzar, D. Tonchev, D. Saitou, and T. Aoki, "Recent photoluminescence research on chalcogenide glasses for photonics applications," *Journal of Non-Crystalline Solids*, vol. 353, pp. 1364–1371, May 2007.

[6.9] L. Sójka, Z. Tang, D. Furniss, H. Sakr, A. Oladeji, E. Bereś-Pawlik, H. Dantanarayana, E. Faber, A. Seddon, T. Benson, and S. Sujecki, "Broadband, mid-infrared emission from Pr^{3+} doped GeAsGaSe chalcogenide fiber, optically clad," *Optical Materials*, vol. 36, pp. 1076–1082, Apr. 2014.

[6.10] M. Munzar, C. Koughia, D. Tonchev, K. Maeda, T. Ikari, C. Haugen, R. Decorby, J. N. McMullin, and S. O. Kasap, "Optical properties of Er-doped $Ga_x(Ge_{0.3}Se_{0.7})_{100-x}$ glasses," *Opt. Mater.*, vol. 28, no. 3, pp. 225–230, 2006.

[6.11] P. C. Becker, J. R. Simpson, and N. Olsson, *Erbim-doped fiber amplifiers fundamentals and technology.* San Diego: Academic Press., 1999.

[6.12] Y. G. Choi, Y. B. Seo, and J. Heo, "Enhancement in lifetimes of the Pr^{3+}: 1.6 μm emission in Ge–Ga–As–Se glasses with CsBr addition," *Journal of materials science letters*, vol. 22, no. 11, pp. 795–798, 2003.

[6.13] Y. G. Choi, K. H. Kim, B. J. Park, and J. Heo, "1.6 μm emission from $Pr^{3+}:(^3F_3,^3F_4)\to {}^3H_4$ transition in $Pr^{3+}-$ and $Pr^{3+}/\ Er^{3+}$-doped selenide glasses," *Applied Physics Letters*, vol. 78, no. 9, p. 1249, 2001.

[6.14] W. J. Chung, H. S. Seo, B. J. Park, J. T. Ahn, and Y. G. Choi, "Selenide Glass Optical Fiber Doped with Pr^{3+} for U-Band Optical Amplifier," *ETRI journal*, vol. 27, no. 4, pp. 411–417, 2005.

[6.15] Y. S. Han and J. Heo, "Midinfrared emission properties of Pr^{3+}-doped chalcogenide glasses at cryogenic temperature," *Journal of Applied Physics*, vol. 93, no. 11, pp. 8970–8974, 2003.

[6.16] J. K. Kim, B. Kyou Jin, W. J. Chung, B. J. Park, J. Heo, and Y. G. Choi, "Influence of the Ga addition on optical properties of Pr in Ge–Sb–Se glasses," *Journal of Physics and Chemistry of Solids*, vol. 72, no. 11, pp. 1386–1389, 2011.

[6.17] F. Charpentier, F. Starecki, J.-L. Doualan, P. Jovari, P. Camy, J. Troles, S. Belin, B. Bureau, and V. Nazabal, "Mid-IR luminescence of Dy^{3+} and Pr^{3+} doped

$Ga_5Ge_{20}Sb_{10}S(Se)_{65}$ bulk glasses and fibers," *Materials Letters*, vol. 101, pp. 21–24, 2013.

[6.18] H. Sakr, D. Furniss, Z. Tang, L. Sojka, N. A. Moneim, E. Barney, S. Sujecki, T. M. Benson, and A. B. Seddon, "Superior photoluminescence (PL) of Pr^{3+}-In, compared to Pr^{3+}-Ga, selenide-chalcogenide bulk glasses and PL of optically-clad fiber," *Opt. Express*, vol. 22, pp. 21236–21252, Sep 2014.

[6.19] Zunzun.com, "Online Curve Fitting and Surface Fitting at ZunZun.com," 2014. Available online at www.zunzun.com [Accessed: 11 March 2013].

[6.20] P. Němec, B. Frumarová, and M. Frumar, "Structure and properties of the pure and Pr^{3+}-doped $Ge_{25}Ga_5Se_{70}$ and $Ge_{30}Ga_5Se_{65}$ glasses," *Journal of Non-Crystalline Solids*, vol. 270, no. 1, pp. 137–146, 2000.

[6.21] D. Lezal, J. Pedlikova, and J. Zavadil, "Chalcogenide glasses for optical and photonics applications," *J. Optoelectron. Adv. Mater*, vol. 6, pp. 133–137, 2004.

[6.22] V. Zólyomi, N. Drummond, and V. Fal'ko, "Electrons and phonons in single layers of hexagonal indium chalcogenides from ab initio calculations," *Physical Review B*, vol. 89, no. 20, p. 205416, 2014.

[6.23] D. Atwood, *The Rare Earth Elements: Fundamentals and Applications*. EIC Books, Wiley, 2013.

[6.24] T. Zhuoqi, *Rare earth ion doped selenide-based chalcogenide glasses and fibres towards mid-infrared fibre lasers*. Phd thesis, University of Nottingham, 2012.

[6.25] D. W. Hewak, J. M. Neto, B. N. Samson, J. Wang, H. Tate, A. Pearson, W. S. Brocklesby, G. Wylangowski, R. I. Laming, D. N. Payne, *et al.*, "Spectroscopy of Pr^{3+}-doped low-phonon-energy glasses based on halides and sulfides," in *Optical Tools for Manufacturing and Advanced Automation*, pp. 102–117, International Society for Optics and Photonics, 1994.

[6.26] M. Bilkova, P. Nemec, and M. Frumar, "Spectroscopic properties of Pr^{3+} ions in Ge-In-S chalcogenide glasses," *Journal of optoelectronics and advanced materials*, vol. 7, no. 5, pp. 2247–2253, 2005.

[6.27] E. Jones, T. Oliphant, and P. Peterson, "SciPy," 2001. Available online at `www.scipy.org` [Accessed: 11 March 2013].

Chapter 7

Design of an Erbium-Doped Double Clad ZBLAN Fiber Laser

A high powered octagonal double clad Er:ZBLAN (33 /330 μm , NA=0.13) glass fibre diode pumped at 976 nm for mid-infrared light generation is studied using a one dimensional rate equation model. The fibre laser design employs the concept of cascade lasing. The results obtained demonstrate that efficient cascade lasing may be achieved in practice without the need for complex fibre grating fabrication as previously adopted in fibre lasers, as a sufficient level of feedback for laser action is provided by Fresnel light reflection at ZBLAN glass fibre air interfaces. Further enhancement of the laser efficiency is achieved by terminating one of the fibre ends with a mirror to observe laser operation in one direction. A numerical analysis of the effect of the Er^{3+} doping concentration and fibre loss on the laser operation shows that with 60 W of pump power at 0.98 μm wavelength, high lasing efficiency at 2.73 μm wavelength can be achieved with Er^{3+} ion concentrations of 60,000 ppm which is commercially available. Nonlinear interactions are identified with the aid of an experimental setup and their effect on the laser efficiency is discussed. We have also introduced reabsorption as a limiting factor in double-clad fiber laser. A comprehensive model of an Erbium doped ZBLAN laser with thermal optimisation is presented which accounts for heating sources

due to homogenous up-conversion, cross relaxation, multiphonon emission, pump and laser signal propagation.

〰〰〰
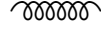
7.1 Introduction

Fibre lasers are the subject of considerable research interest. Erbium-doped silica fibre lasers with output power levels around 500W [7.1] have been demonstrated under continuous wave (CW) operation. The natural minimum loss at 1.5 μm possesses significant challenge in extending the emission wavelengths of silica-based fibre lasers. At longer wavelengths, the emission efficiency of erbium in silica is limited by the high phonon energy of the glass matrix which introduces competing multi-phonon relaxation paths. ZBLAN on the other hand, is a heavy metal fluoride glass with a wide transmission window of $0.3 - 5$ μm and a good rare earth ion solubility. Compared with silicate glasses, ZBLAN glass has a lower maximum phonon energy (of ≈ 565 cm^{-1} [7.2]) because the bond strength is weaker while atoms forming the glass are heavier [7.3].

Double clad fibre provides opportunities for realisation of high power lasers with improved confinement when compared with the traditional step index single clad Fibres. In this work, we focus on two geometries of the double-clad Fibre with different doping levels of the erbium ions. In the model employed we include up-conversion processes that produce the green photoluminescence in ZBLAN fibre laser. Under a continuous wave (CW) pump an investigation of the influence of the fibre length, input pump power and facet reflectivity on the laser operating characteristics are studied. Finally, the modelling results are compared with experimental ones.

7.2 Fibre Laser Modelling

The measured absorption cross section spectra used in this study is obtained from the literature [7.4], fitted using a linear combination of Gaussian functions and then

extrapolating for all desired wavelengths using the Equation 7.1

$$\sigma_{abs}(\lambda) = \sum_{i=0}^{j} a_i e^{\left(-ln(2)\left(\frac{\lambda-\lambda_i}{d\lambda}\right)^2\right)} \tag{7.1}$$

where a_i is the peak value of the absorption, λ is the central wavelength, $d\lambda_i$ is the half width at half maximum and i is the number of Gaussians used in the fit. Appendix A.3 lists the values of a_i, λ_i, and $d\lambda_i$ for the transitions whose spectral dependence are important to the laser modelling. The emission spectrum of the signal is available from intensity measurement while the corresponding absorption cross-section is resolved from the reciprocity theorem described by McCumber [7.5]. The corresponding emission cross-sections of the pump and idler were calculated using McCumber [7.5] and Judd-Ofelt [7.6,7.7] analysis. Figures 7.1, 7.2, and 7.3 show cross-sections for the pump (≈ 0.98 μm), idler (≈ 1.55 μm and signal (≈ 2.7 μm) waves that are used in the calculations.
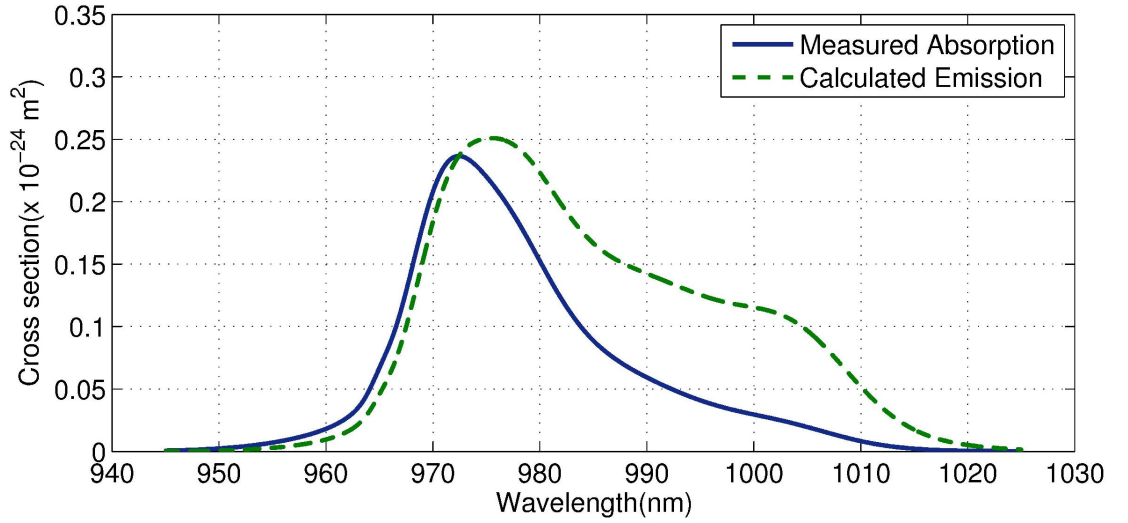
Figure 7.1: Emission and absorption cross sections for pump (980nm)

Two double-clad fibre geometries that are referred to as 'Fibre 1' and 'Fibre 2' are investigated in this work. Fibre 1 is a 5000 ppm erbium doped ZBLAN fibre with 4.7 μm core diameter and 124 μm circular inner cladding diameter. Fibre 2 is a 60000 ppm erbium doped ZBLAN fibre with a 33 μm core diameter and a 330 μm octagonal inner-cladding diameter. We note that both fibres are commercially available. Their schematic diagrams
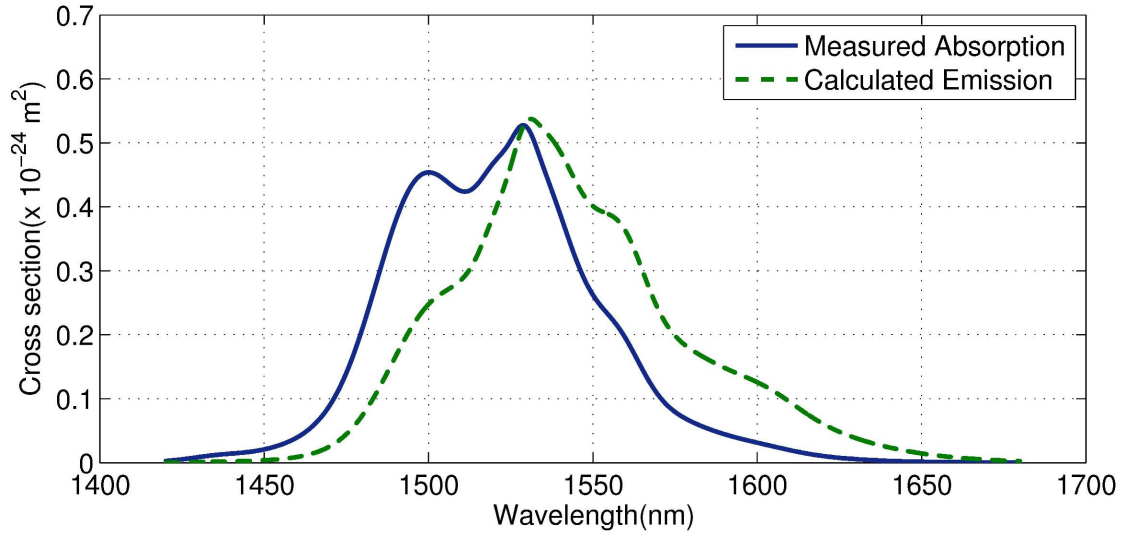
Figure 7.2: Emission and absorption cross sections for signal (1550nm)
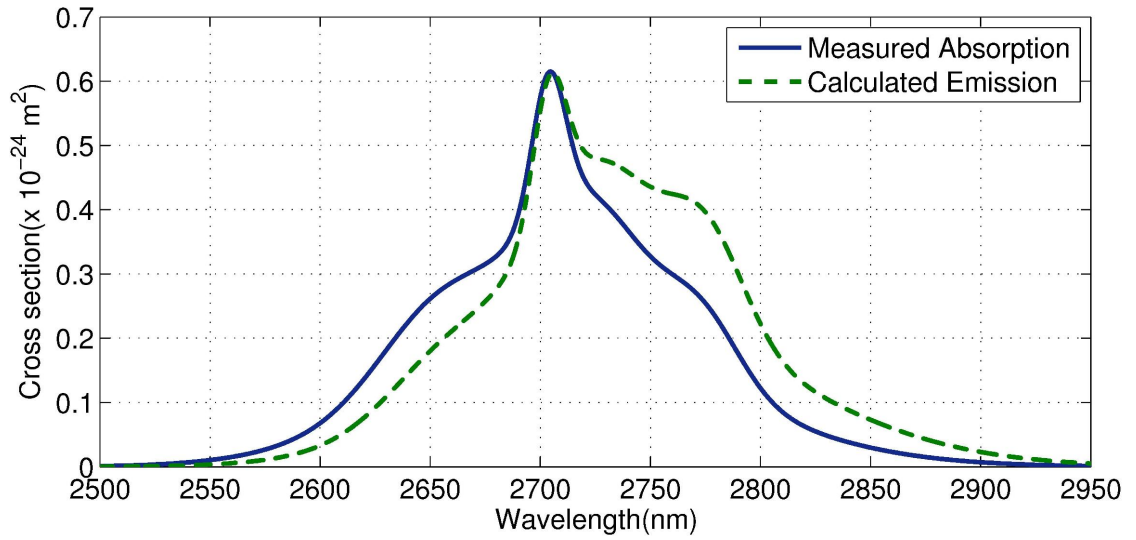
Figure 7.3: Emission and absorption cross sections for idler (2700nm)

of cross sectional refractive index distributions are presented in Figure 7.4.

Using the linearity of Beer-Lambert law and the erbium concentrations of the fibres, the absorption coefficients are scaled from the original measurements obtained from the literature [7.4] given that 1000 ppm of erbium is equivalent to $1.6 \times 10^{19} ions/cm^3$ [7.8].

The properties of the two erbium doped ZBLAN fibres are investigated theoretically using the rate equations which are subsequently described. Figure 7.5 shows the

(a) 'Fibre 1', Circular double clad fibre doped with erbium ions at 5,000ppm

(b) 'Fibre 2', Octagonal double clad fibre - doped with erbium ions at 60,000ppm
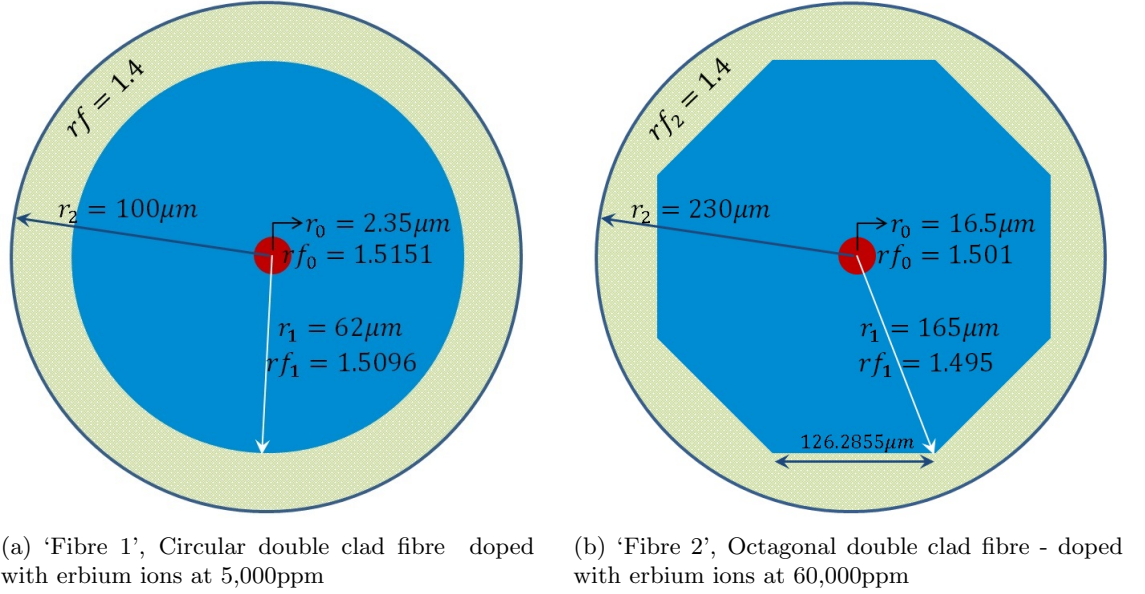
Figure 7.4: Cross section and refractive index distribution for Er^{3+}:ZBLAN double clad fibre

corresponding energy-level diagram for the erbium ion doped ZBLAN glass. Fibre 2 is highly doped which makes ion-ion interactions highly probable. In our experimental setup, we observe a visible green-glow when using this fibre. This confirms an emission from the thermally coupled levels $^{2}H_{11/2}$/ $^{4}S_{3/2}$ which can only be populated by energy transfer from lower lying energy states. Therefore interactions of ion-ion energy transfer up-conversions are labelled as W_{2206}, W_{1103}. The cross relaxation is labelled as C_{0513}. They are included in the energy-level diagram of Figure 7.5. Ion-ion interactions are excluded from the analysis of 'Fibre 1' given the relatively low level of erbium doping.

Excited ions at the $^{4}F_{7/2}$ levels are rapidly depleted by multi-phonon transition to the thermal levels $^{2}H_{11/2}$/ $^{4}S_{3/2}$ as the energy gap can be bridged by 2 phonons. This effectively makes the 3 levels $^{4}F_{7/2}$, $^{2}H_{11/2}$ and $^{4}S_{3/2}$ to act as a single band. The energy level $^{4}F_{9/2}$ is not directly populated by any of the energy transfer processes or indirectly by multi-phonon relaxations. This is because of the relatively large energy gap that separates level $^{4}F_{9/2}$ from the upper lying level $^{4}S_{3/2}$. As a result of this, the contribution of $^{4}F_{9/2}$ to the system at equilibrium is negligible. The energy diagram is therefore represented by 5 levels: $^{4}I_{15/2}$, $^{4}I_{13/2}$, $^{4}I_{11/2}$, $^{4}I_{9/2}$ and $^{4}S_{3/2}$/ $^{2}H_{11/2}$/ $^{4}F_{7/2}$. In our simulations the

coefficients for energy transfer up-conversion and cross relaxation processes are taken from the available literature [7.9–7.11].
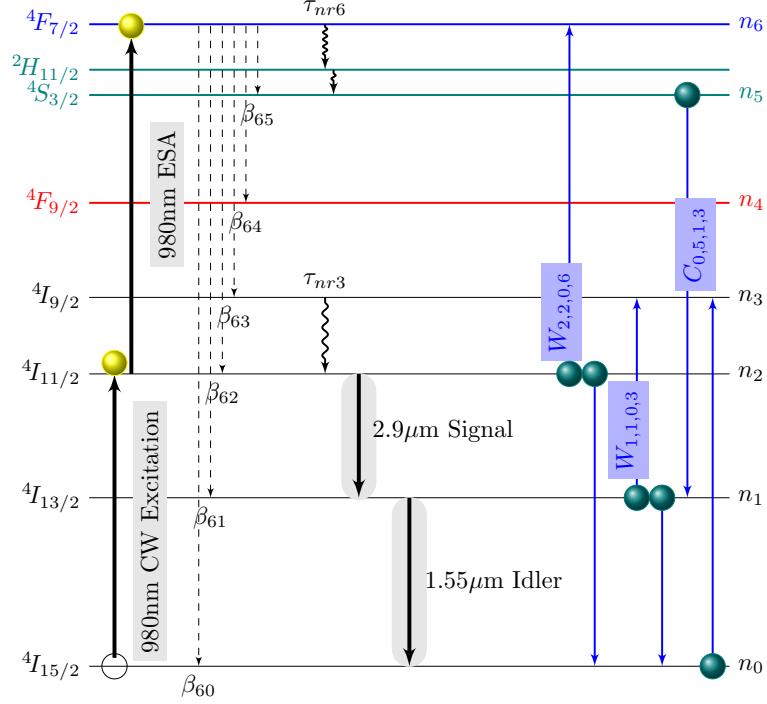
Figure 7.5: Energy level diagram of Er:ZBLAN showing pump, signal and idler transitions.

We therefore obtain the rate equations 7.2 which are complemented by the conservation law, equation 7.4, where $R_w = \frac{P_w}{h\upsilon_w A_{core}}$ is the photon flux rate and the subscript 'w' is 'p' for the pump, 'id' for the idler and 's' for signal while P_w denotes the power, h is the Planck's constant, Acore is the area of the fibre core. σ_{ap}, σ_{ad} and σ_{as} are the pump, idler and signal absorption cross sections while σ_{ep}, σ_{ed} and σ_{es} are the pump, idler and signal emission cross sections. τ_i is the total lifetime which includes both radiative (τ_r)

and non-radiative (τ_{nr}) processes. β_{ij} is the branching ratio from level i to j.

$$
\begin{aligned}
\dot{N_0}(z) &= (-N_0\sigma_{ap} + N_2\sigma_{ep})R_p + \frac{N_1}{\tau_1} + (N_1\sigma_{ed} - N_0\sigma_{ad})R_{id} + \sum_{i=2}^{6} \frac{\beta_{i0}N_i}{\tau_i} \quad (7.2) \\
&+ W_{2206}N_2^2 - C_{0513}N_5N_0 + W_{1103}N_1^2 \\
\dot{N_1}(z) &= -(N_1\sigma_{ed} - N_0\sigma_{ad})R_{id} + (N_1\sigma_{es} - N_0\sigma_{as})R_s + \sum_{i=2}^{6} \frac{\beta_{i1}N_i}{\tau_i} - \frac{N_1}{\tau_1} \\
&+ \frac{N_2}{\tau_{nr2}} + C_{0513}N_5N_0 - 2W_{1103}N_1^2 \\
\dot{N_2}(z) &= -(N_1\sigma_{es} - N_0\sigma_{as})R_s + \sum_{i=3}^{6} \frac{\beta_{i2}N_i}{\tau_i} - \frac{N_2}{\tau_2} + \frac{N_3}{\tau_{nr3}} - 2W_{2206}N_2^2 \\
\dot{N_3}(z) &= \sum_{i=4}^{6} \frac{\beta_{i3}N_i}{\tau_i} - \frac{N_3}{\tau_3} + \frac{N_4}{\tau_{nr4}} + W_{1103}N_1^2 + C_{0513}N_5N_0 \\
\dot{N_4}(z) &= \sum_{i=5}^{6} \frac{\beta_{i4}N_i}{\tau_i} - \frac{N_4}{\tau_4} + \frac{N_5}{\tau_{nr5}} \quad\quad (7.3) \\
\dot{N_5}(z) &= \sum_{i=6}^{6} \frac{\beta_{i5}N_i}{\tau_i} - \frac{N_5}{\tau_5} + \frac{N_6}{\tau_{nr6}} - C_{0513}N_5N_0 \\
\dot{N_6}(z) &= -\frac{N_6}{\tau_6} + \frac{N_6}{\tau_{nr6}} + W_{2206}N_2^2
\end{aligned}
$$

$$
N_{Er} = N_1 + N_2 + N_3 + N_4 + N_5 + N_6 \quad\quad (7.4)
$$

The branching ratios β_{ij} and lifetimes were taken from Caspary [7.4]. The multiphonon transition rates are calculated from the energy gap law (see Section 2.5, page 28), using the phenomenological parameters $\alpha = 5.19 \times 10^{-3}$ cm and B $= 10^8$ s^{-1} [7.12]. The full listing of branching ratios, radiative and non-radiative lifetimes is in Appendix B.2. The simulation parameters are summarised in Table 7.1.

To investigate the ion-ion interactions presented as candidates influencing the green emission in the doped fibre, a photoluminescence model is first explored in bulk glass. In the photoluminescence model, equation is integrated relative to time, taking $R_s = R_{id} = 0$. Figure 7.6 shows the photoluminescence model of the erbium ion in time domain.

The evolution of erbium ions reached steady state at $\approx$ 1 ms. The number of ions

Table 7.1: Er^{3+} doped ZBLAN glass fibre laser modelling parameters for the fibres

Parameter	Value	Unit
Er^{3+} ion concentration	5000, 60000	ppm
Core radius	Fibre1 - 2.35, Fibre2 - 16.5	μm
Cladding radius	Fibre1 - 62, Fibre2 - 165	μm
Fibre length	1 - 20	m
Fibre loss at 3 μm	0.5	dB/m
Overlap factor for pump	0.14, 1.11	%
Radiative lifetimes	$\tau_{r1} = 8.52$, $\tau_{r2} = 7.87$,	ms [7.4]
Multiphonon lifetimes	$\tau_{nr4} = 1.67$, $\tau_{nr5} = 8.75$	ms [7.9] [7.13]
Pump power	60	W
Energy transfer parameters	$W_{2204} = 1.0 \times 10^{-17}$,	cm^3/s [7.11]
	$W_{1103} = 2.8 \times 10^{-17}$,	
	$C_{0413} = 2.4 \times 10^{-17}$	
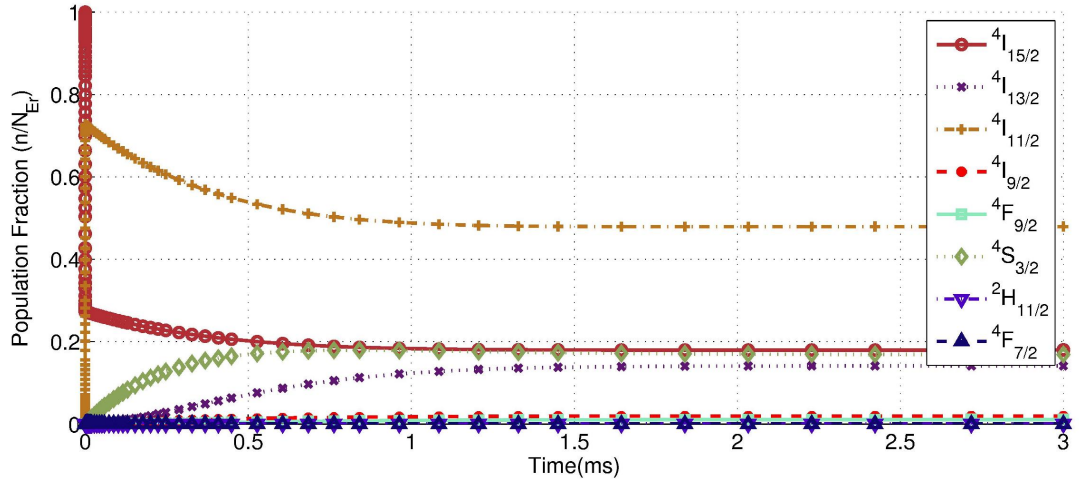
Figure 7.6: Time evolution of erbium ions in ZBLAN glass

in the $^4I_{11/2}$ energy level is ≈ 3 times the population in the $^4I_{13/2}$. The result indicates that population inversion can be achieved easily between $^4I_{11/2}$ and $^4I_{13/2}$. Therefore the lasing signal originating from the transition $^4I_{11/2} \rightarrow {}^4I_{13/2}$ (2.73 μm) can be realised in the present setup given the stated material properties.

Figure 7.7 shows the steady state photoluminescence intensities of the energy-levels. The relative magnitude of the green(532 nm) to red (656 nm) photoluminescence from the simulation is comparable to the ones presented in the measurement by Schutz *et al.* [7.14] in erbium doped ZBLAN glass. Since photoluminescence is a precursor to lasing, this preliminary investigation of photoluminescence shows that the right parameters of

multiphonon transition, radiative lifetimes and ion-ion interactions have been included.
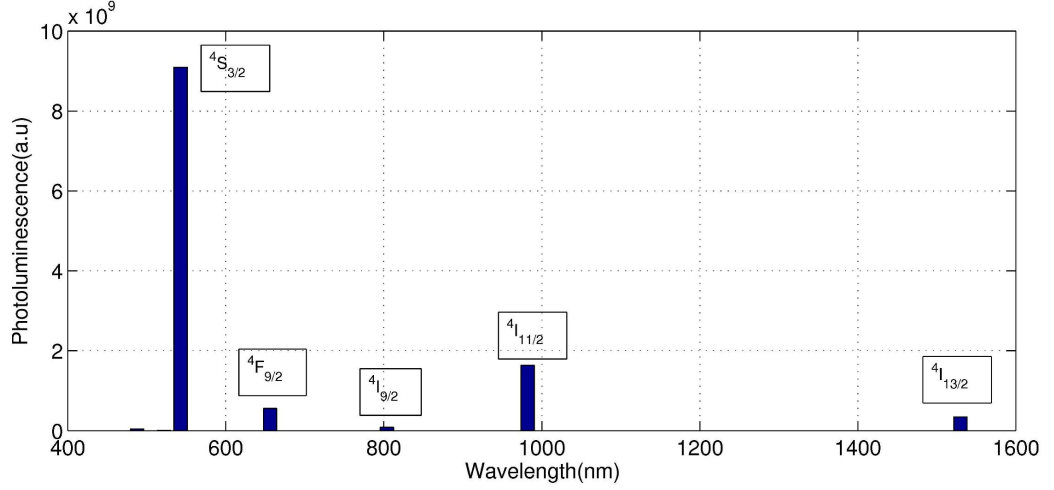
Figure 7.7: Steady state photoluminescence of erbium ions in ZBLAN glass

Therefore, the evolution of the pump, signal and idler powers can be calculated by solving the following set of ordinary differential equations:

$$
\begin{aligned}
\frac{dP_p^\pm\left(\lambda_p\right)}{dz} &= \pm\Gamma_p\left(\lambda_p\right)P_p^\pm\left(\lambda_p\right)\left(\sigma_{02}N_0 - \sigma_{20}N_2\right) \pm \alpha(\lambda_p)P_p^\pm(\lambda_p) \\
\frac{dP_{s1}^\pm\left(\lambda_{s1}\right)}{dz} &= \pm\Gamma_{s1}\left(\lambda_{s1}\right)P_{s1}^\pm\left(\lambda_{s1}\right)\left(\sigma_{12}N_1 - \sigma_{21}N_2\right) \pm \alpha(\lambda_{s1})P_{s1}^\pm(\lambda_{s1}) \qquad (7.5) \\
\frac{dP_{s2}^\pm\left(\lambda_{s2}\right)}{dz} &= \pm\Gamma_{s2}\left(\lambda_{s2}\right)P_{s2}^\pm\left(\lambda_{s2}\right)\left(\sigma_{01}N_0 - \sigma_{10}N_1\right) \pm \alpha(\lambda_{s2})P_{s2}^\pm(\lambda_{s2})
\end{aligned}
$$

The symbol '$\pm$' represents the direction of the travelling waves, where '$+$' is the forward travelling wave and '$-$' is the backward travelling wave. Where $P_p = P_p^+ + P_p^-$, $P_{s1}(\lambda_{s1}) = P_{s1}^+(\lambda_{s1}) + P_{s1}^-(\lambda_{s1})$ and $P_{s2}(\lambda_{s2}) = P_{s2}^+(\lambda_{s2}) + P_{s2}^-(\lambda_{s2})$.

σ_{ij} and σ_{ji} are the absorption and emission cross sections respectively. $\alpha(\lambda)$ is the intrinsic absorption and loss in the fibre. Γ_p, Γ_s is the overlap factor between the pump, signal and the fiber doped core.

At both fiber ends, i.e. z = 0 or z = L, the mirrors reflects the co- and counter-propagating photon fluxes into each other. If we denote the reflectivity of input and output mirror by $R_{in}(v)$ and $R_{out}(v)$ respectively, we get the following boundary

conditions:

$$
\begin{aligned}
\phi^+(v,0) &= R_{in}(v)\phi^-(v,0) + T_{in}(v)\phi_p(v) \\
\phi^-(v,l) &= R_{out}(v)\phi^+(v,l) \\
\phi^+(\varphi,0) &= R_{in}(\varphi)\phi^-(\varphi,0) \qquad\qquad (7.6) \\
\phi^-(\varphi,l) &= R_{out}(\varphi)\phi^+(\varphi,l) \qquad\qquad (7.7) \\
\phi^+(\psi,0) &= R_{in}(\psi)\phi^-(\psi,0) \\
\phi^-(\psi,l) &= R_{out}(\psi)\phi^+(\psi,l)
\end{aligned}
$$

The fibre ends were either terminated by air-glass interface or a mirror. The equations 7.2, 7.6, and 7.8 are solved using coupled solution method [7.15,7.16]. The procedure for the algorithm is described earlier in Section 4.3.2. In the simulation, the step size is 0.01m and the given tolerance condition is 1×10^{-8}.

7.3   Results of Numerical simulations

In the simulations, we assume that the pump laser module delivers 60 W at 980 nm. In figures 7.8 and 7.9 we show the dependence of the signal and idler power on the fibre length for the pump power equal 60 W. These results show that the optimal length of the fibre for 'Fibre 1' is 17.3 m for the laser configuration that relies on Fresnel reflections only while for the configuration that uses a mirror, it is 13.2 m. 'Fibre 2' has an optimum length of 2.8 m for the laser configurations that relies on Fresnel reflections only and 1.8m for the configuration that uses a mirror.

In fibre 2, it is evident that a larger cross section produces a larger absorption per unit length and therefore a shorter length to absorb the same pump power when compared with fibre 1. Also with a higher concentration of ions per unit volume in fibre 2, the absorption region of the input photon flux will be shorter than those of fibre 1.

Figures 7.10 and 7.11 show the dependence of the idler and signal powers on the pump power. In these calculations we use the optimal fibre length extracted from figures 7.8 and

(a) Fresnel

(b) Mirror
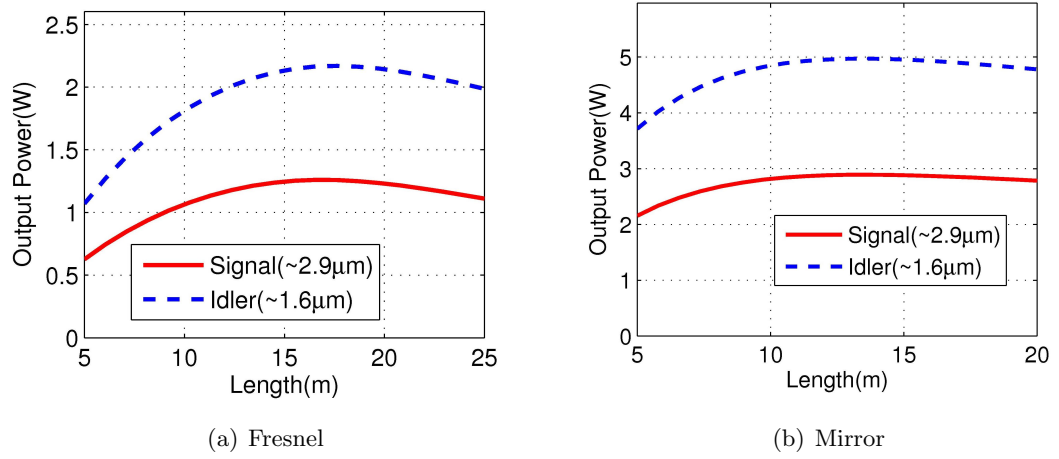
Figure 7.8: Fibre 1: Calculated dependence of idler and output signal powers on the fibre length

(a) Fresnel

(b) Mirror
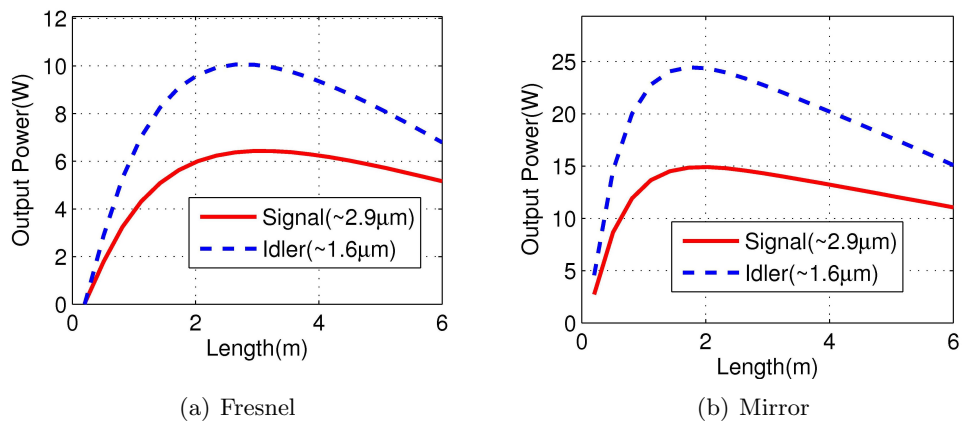
Figure 7.9: Fibre 2: Calculated dependence of idler and output signal powers on the fibre length

7.9. 'Fibre 1' produced a slope efficiency of 2.1% (Signal) and 3.7% (Idler) for the laser configuration that relies on Fresnel reflections only while the one that uses mirror has slope efficiencies of 4.9% (Signal) and 8.4% (Idler). 'Fibre 2' produced a slope efficiency of 13.0% (Signal) and 22.8% (Idler) for the laser configuration that relies on Fresnel reflections only while the one that uses mirror produced slope efficiencies of 27.8% (Signal) and 48.2% (Idler).

(a) Fresnel　　　　　　　　　　　　　　(b) Mirror
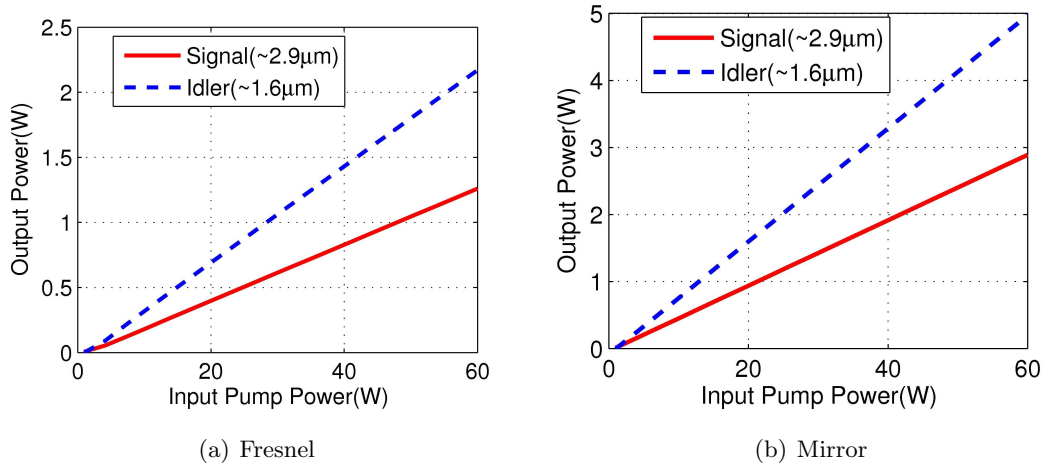
Figure 7.10: Fibre 1: Calculated dependence of idler and output signal on input pump power

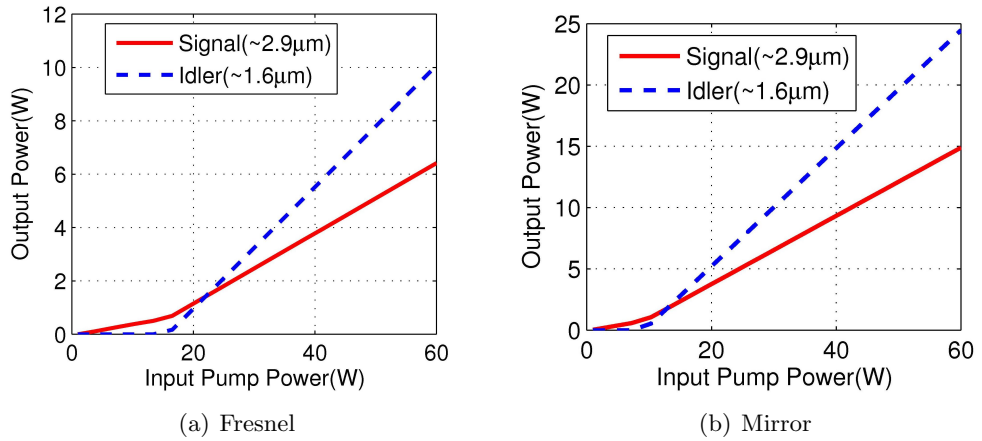(a) Fresnel　　　　　　　　　　　　　　(b) Mirror

Figure 7.11: Fibre 2: Calculated dependence of idler and output signal on input pump power

The results indicates that Fibre 2 is a more efficient fibre when compared to fibre 1 in terms of length, ion-concentrations and slope efficiencies. The next sections discusses

the properties of Fibre 2 for a more optimum configuration that closely reproduces the experiment and practicable in a realistic device.

7.3.1 Reabsorption of green luminescence

In the numerical model we demonstrated that the presence of upconversion in 'Fibre 2' produces photoluminescence from the thermal levels $^2H_{11/2}$/ $^4S_{3/2}$. Within the long section of the fibre, the green luminescence behaves like a secondary pump excitation and is therefore reabsorbed within the fibre. We therefore modify the numerical model described earlier to account for reabsorption. Equation 7.8 shows the equations relevant to the reabsorption process.

$$
\begin{aligned}
\dot{N}_0(z) &= (-N_0\sigma_{ap} + N_2\sigma_{ep})R_p + (N_1\sigma_{ed} - N_0\sigma_{ad})R_{id} + \sum_{i=2}^{6}\frac{\beta_{i0}N_i}{\tau_i} \\
&+ W_{2206}N_2^2 - C_{0513}N_5N_0 + W_{1103}N_1^2 - N_0\sigma_{542nm}R_{reabs} + \frac{N_1}{\tau_1} \\
\dot{N}_6(z) &= -\frac{N_6}{\tau_6} + \frac{N_6}{\tau_{nr6}} + W_{2206}N_2^2 + N_0\sigma_{542nm}R_{reabs}
\end{aligned}
\tag{7.8}
$$

Where σ_{542nm} is the absorption cross-section of the green luminescence wavelength and R_{reabs} is the photon flux generation rate of the green emission. This can be calculated from the formular for photoluminescence in equation 4.3.

7.3.2 Thermal optimisation

High-power scaling is very desirable, however, it is limited by heat generation inherent within the fiber device. This leads to fiber core melting, fracture and instability of the laser operation. This section examines the heat produced by the non-radiative (multiphonon) transitions in the double-clad fibre during the optical pumping, using a numerical model. The fiber laser model presented earlier included two energy transfer processes (up-conversion from $^4I_{13/2}$ and $^4I_{11/2}$) and a cross-relaxation process from $^4S_{3/2}$ in the rate equation. These processes lead to the exchange of energy and therefore generation of heat. The approximate analytical thermal model developed here was extended from

previous works [7.17,7.18] .

For the laser system, the heat generated by non-radiative transitions originates from energy levels separated by less than 2300 cm^{-1}, which can be bridged by 4 phonons based on the highest phonon energy of ZBLAN. The most prominent non-radiative transitions are $^4I_{9/2} \to {}^4I_{11/2}$ and $^4F_{7/2} \to {}^2H_{11/2}/^4S_{3/2}$. The amount of heat generated by these transitions is proportional to the energy difference converted to heat times the rate at which the transition occurs in a unit volume. The heat generated within a doped core section of length Δz per unit time is given by Equation 7.9

$$Q_{nr} = h\Delta z A_c \left(\frac{\Delta v_{65} N_6(z)}{\tau_{nr6}} + \frac{\Delta v_{32} N_3(z)}{\tau_{nr3}} \right) \qquad (7.9)$$

Where N_6, τ_{nr3}, τ_{nr6} are the population density, lifetime of excited level $^4I_{9/2}$ and lifetime of the terminal excited level $^4F_{7/2}$, respectively. h is the Planck's constant, v_{ij} ($v_{65} = c(1/\lambda_6 - 1/\lambda_5)$ and $v_{32} = c(1/\lambda_3 - 1/\lambda_2)$) is the optical frequency difference of the transitions. A_c is the core area. In 'Fibre 1', the absence of upconversion to $^4F_{7/2}(N_6 = 0)$ reduces Equation 7.9 to the second term which is ($\frac{\Delta v_{32} N_3(z)}{\tau_{nr3}}$)in the equation.

Further contributions to heating comes from energy transfer of paired ions by processes of upconversion and cross-relaxations. These processes do not create heat by themselves but promote ions to energy-levels ($^4F_{7/2}$and $^4I_{11/2}$) that are attractive to multiphonon relaxations. The heat generated by energy-transfer within a section of the core is given by equation 7.10.

$$Q_{ET}(z) = (N_2^2 W_{2206}^2 + N_1^2 W_{1103}^2 - N_0 N_5 C_{0513})h\Delta v_s \Delta z A_c \qquad (7.10)$$

Heat is also generated by the absorption component of the fiber loss due to pump, signal and idler. The heat generated along a short length of the fibre Δz is given by Equation 7.11

$$Q_z = \alpha_l oss \left[Pp(z) + Ps(z) + Pid(z) \right] \Delta z. \qquad (7.11)$$

where α_{loss} is the absorption loss coefficient. For simplicity α_{loss} is assumed uniform

in the core of the fibre and $P_p(z)$ is the total pump laser power at z for comprising both the forward and signal propagating power.

The temperature distribution in the fibre laser can be found by solving the steady-state heat diffusion equation whose analytical expression is presented in Section 4.5.3 (Equation 4.41).

Figures 7.13 and 7.12 show the thermal variation in the core of the fibre with length. Figure 7.14 shows the temperature variation in the core of the fibre at the left end (z=0) of the fibre laser. Figure 7.15 shows the temperature variation in the core of the fibre at the end of the gain medium. For the configuration with fresnel reflection, the results of the thermal investigation show a maximum temperature of 430.8 K at the end of the fibre while the minimum temperature of 346.5 K is recorded at the 11.8 m into the gain medium.

Figure 7.12: Thermal distribution showing the variation along the fibre with the core and clad sections, Fresnel Reflection(Colour code: blue is coldest, red is the hottest and white is the point that coincides with the minimum temperature)
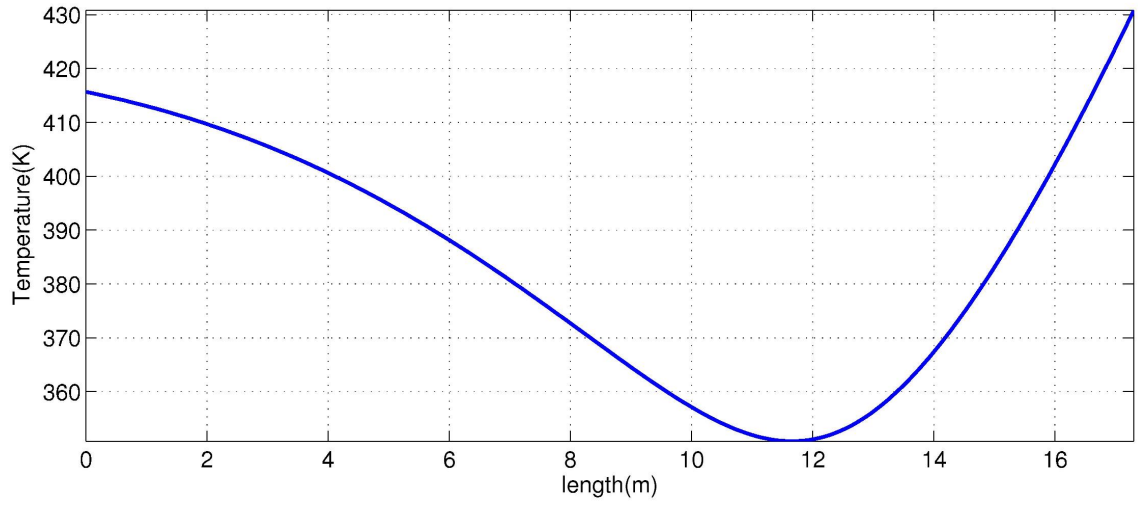
Figure 7.13: Fibre 1 - Thermal distribution along the gain medium, Fresnel Reflection
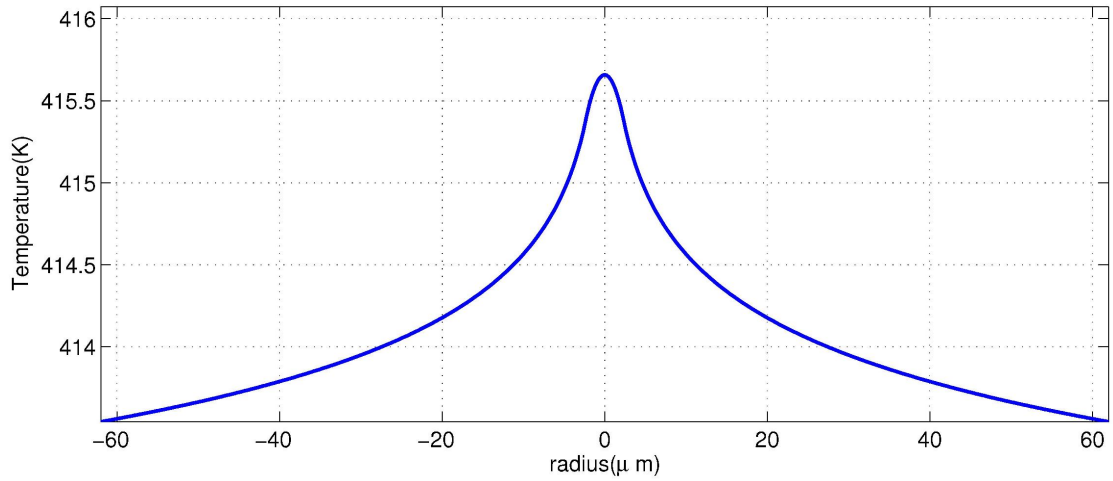
Figure 7.14: Fibre 1 - Thermal variation in the core and clad at z = 0, Fresnel Reflection

The simulation is repeated with 'Fibre 1' terminated by fully reflective mirrors at the left end of the fibre. Figures 7.17 and 7.16 show the thermal variation in the core of the fibre with length. Figure 7.18 shows the temperature variation in the core of the fibre at the left end (z=0) of the fibre laser. Figure 7.19 shows the temperature variation in the core of the fibre at the end of the gain medium. For the configuration with Fresnel reflection, the results of the thermal investigation show a maximum temperature of 585 K at the end of the fibre, while the minimum temperature of 410.5 K is recorded at the pump input of the gain medium. With a glass transition temperature of 533 K in ZBLAN, the
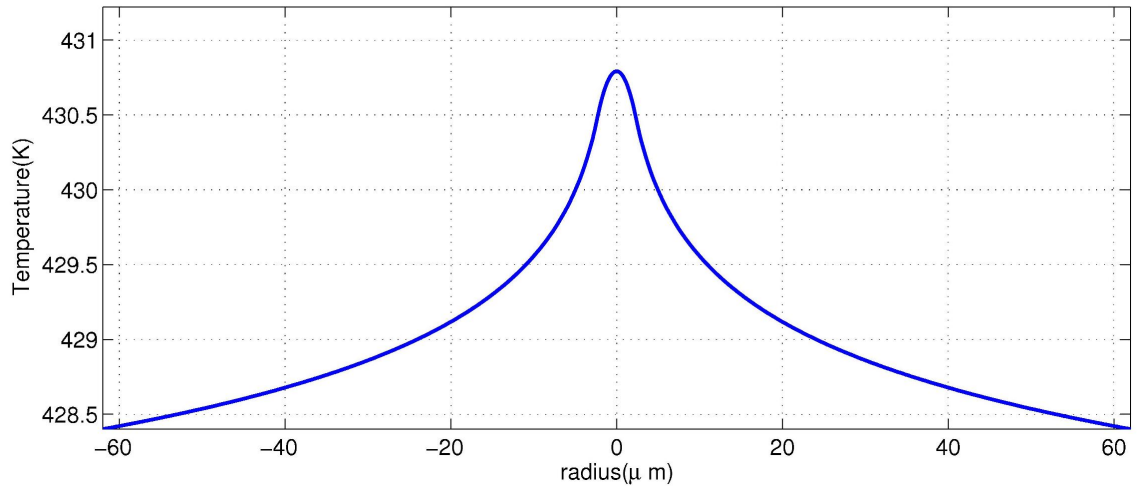
Figure 7.15: Fibre 1 - Thermal variation in the core and clad at z = L, Fresnel Reflection

results of mirror reflection configuration suggest that the system can not be safely operated beyond 10 m without damaging the fibre.

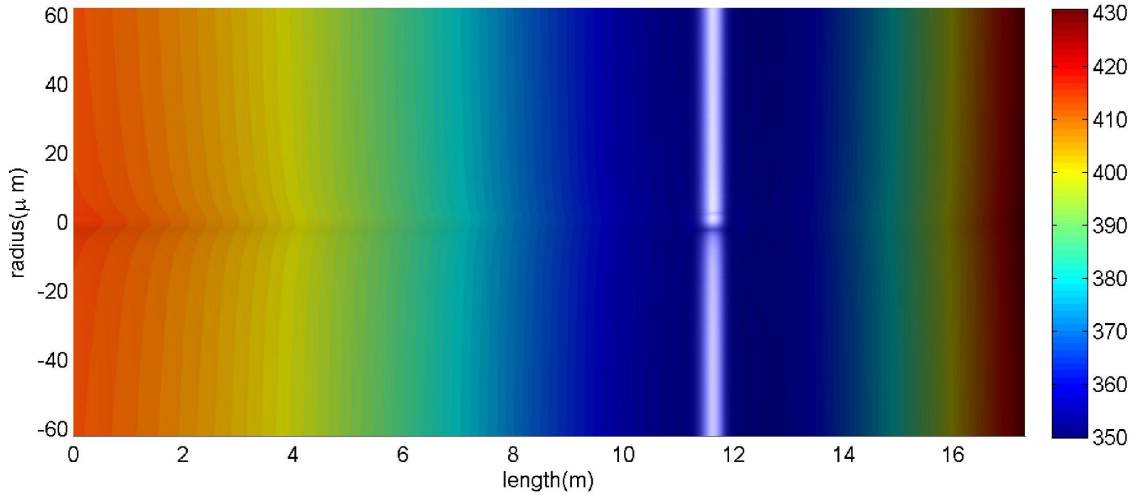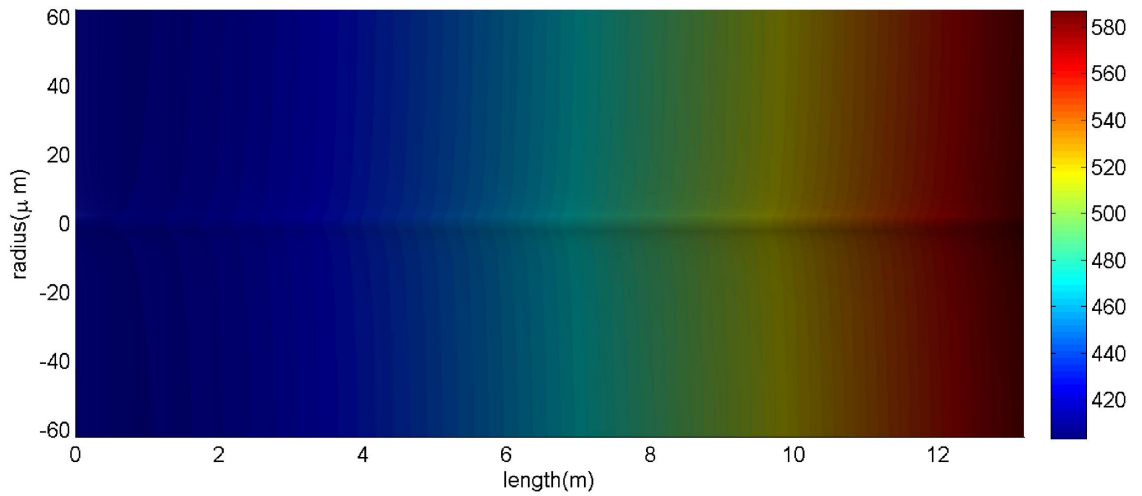**Figure 7.16:** Thermal distribution showing the variation along the fibre with the core and clad sections, Mirror Reflection
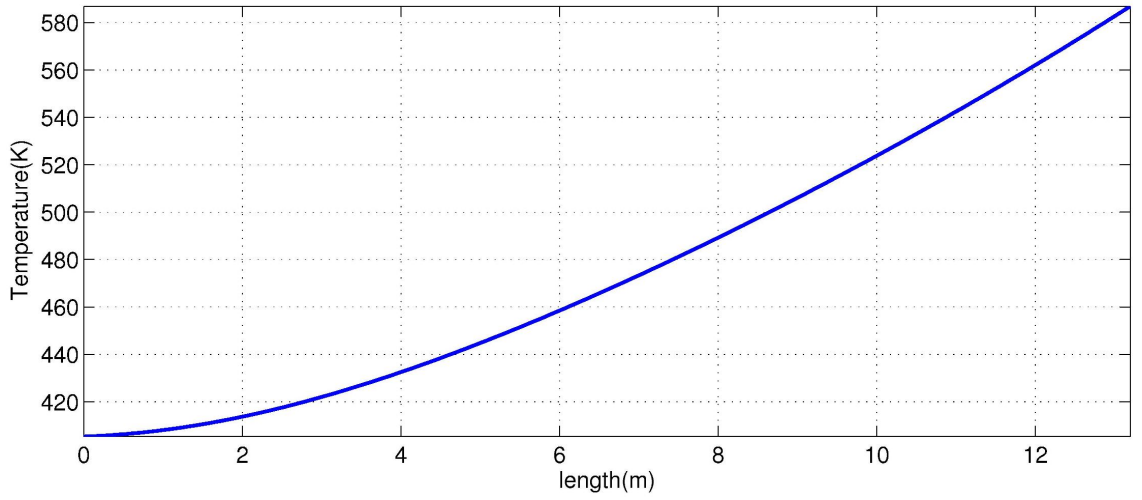
Figure 7.17: Fibre 1 - Thermal distribution along the gain medium, Mirror Reflection
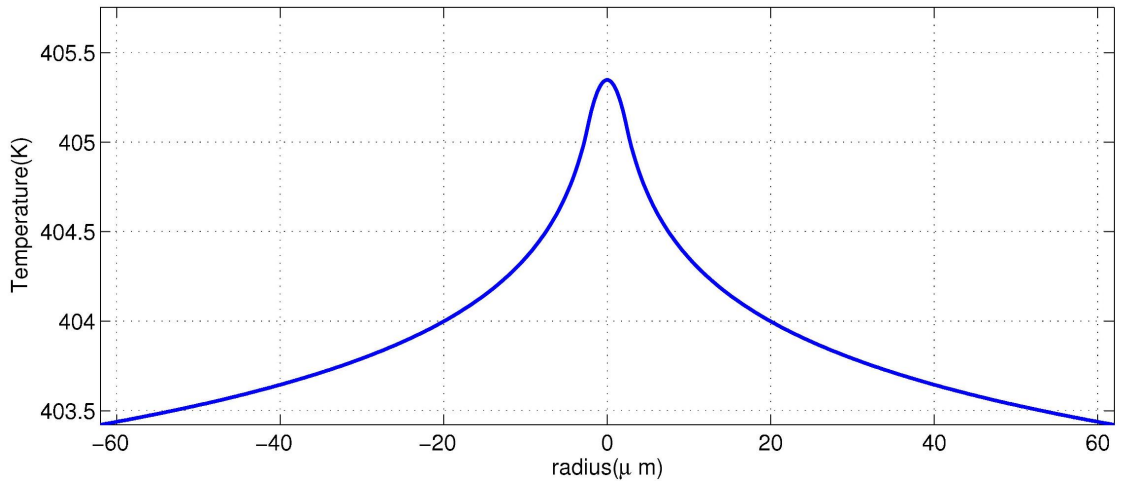
Figure 7.18: Fibre 1 - Thermal variation in the core and clad at z = 0, Mirror Reflection

7.4 Experimental Verification of the Numerical Simulation

In order to verify the numerical model earlier presented, an experiment set-up is developed. The fibre is pumped by a laser diode delivering 60 W of CW power at the wavelength of 980 nm. The 2 m long fiber is obtained from Fiberlabs with a core diameter of 33 μm and an inner clad diameter of 330 μm (octagonal-shape) and a a core diameter of 4.7 μm and an inner clad diameter of 33 μm (circular-shape). The 60,000 ppm Er-doped fibre had a NA of 0.124, which supported multi-mode transmission at the signal wavelength. Mode
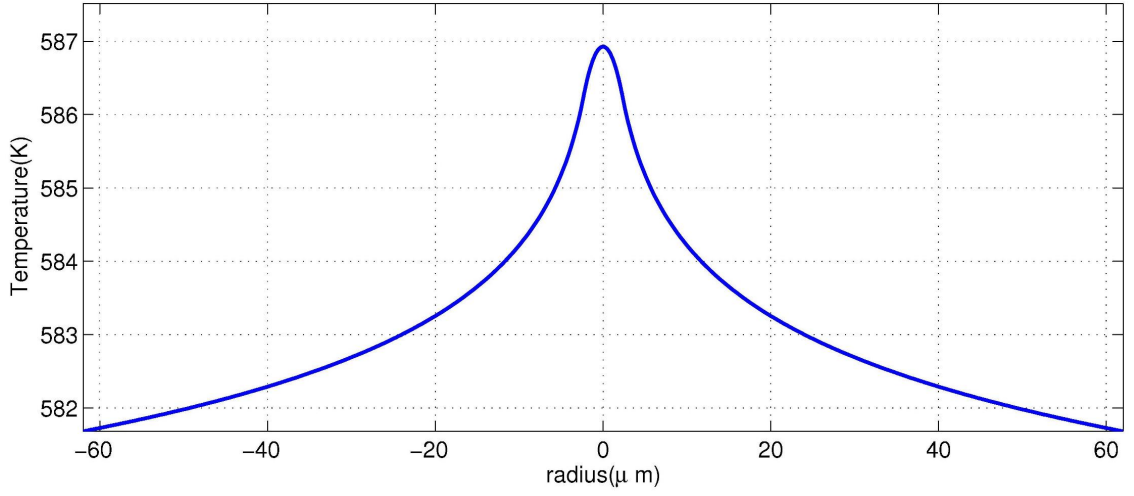
Figure 7.19: Fibre 1 - Thermal variation in the core and clad at z = L, Mirror Reflection

mixing was achieved by bending the fibre to a figure of eight/kidney shape to enhance the fundamental mode. Figure 7.20 shows the pump coupling results. A maximum absorption of ≈75% is measured.

Two different fibre lengths were tested, one cooled (5.5m) and the other without cooling (8 m). Increase in length is expected to compensate the thermal distribution within the core. A maximum output power of 7.8 W and slope efficiency of 13% is measured in the uncooled fibre. While a maximum output power of 11.9 W and a slope efficiency of 17% is measured in the cooled fibre. Figure 7.21 shows the change in output power with absorbed pump power.

Following the results reported from the numerical models, this work was extended to report on the acousto-optically Q-switched laser performance of a 976 nm diode-pumped Er:ZBLAN fibre laser operating at room temperature. The experiment setup and measurements were carried out by LISA laser products, Gooch and Gousego LTd, and Vivid Components Ltd. The 2.5 m long multimode fibre had a 6 mol.% Er-doped core diameter of 33 μm and a cladding diameter of 330 μm (NAcore = 0.12, NAclad = 0.5, FiberLabs Inc.) with an absorption of ≈ 5 dB/m at 980 nm. The fibre was conductively cooled to T = 20° by placing it on an aluminium plate. The ends of the fibre were sandwiched in cooled fibre chuck holders to avoid damage. The laser resonator was set up
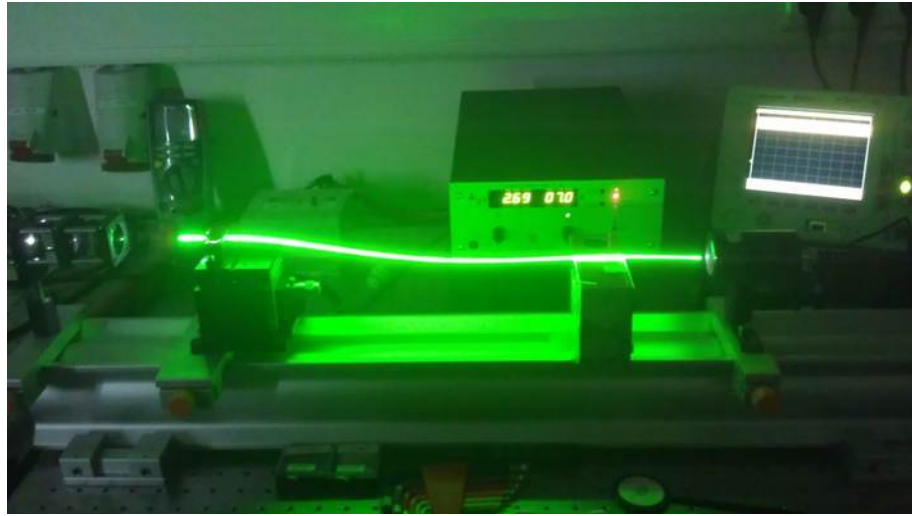
(a) Fibre luminescence
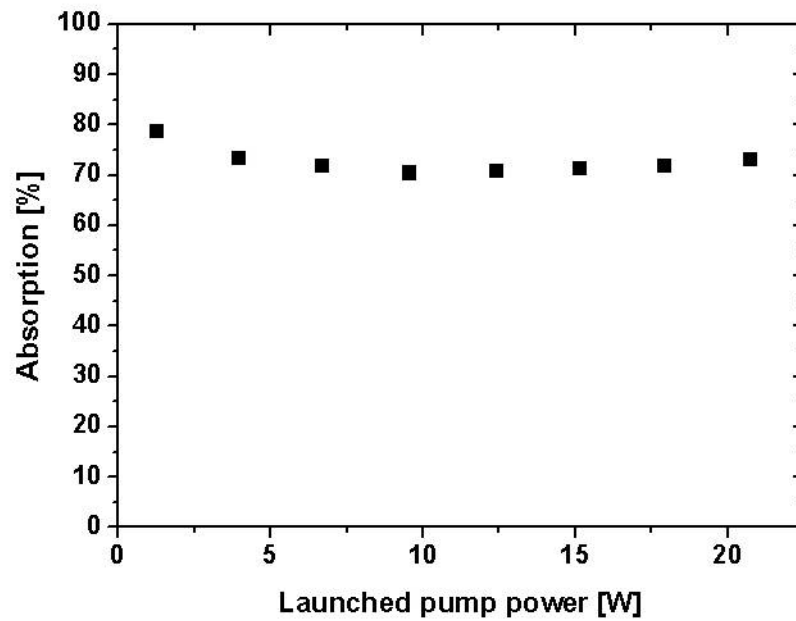
(b) Pump Absorption

Figure 7.20: Pump light coupling results of active fibre

by an external highly reflective mirror at 3 m and the Fresnel reflection at the opposite
fibre end. A novel TeO_2-based acousto-optical modulator (AOM) fabricated by Gooch
and Housego was used for Q-switching the cavity at 1 kHz pulse repetition rate. Both
facets of the AOM were anti-reflective coated at 2.7 - 3 μm and the active aperture was
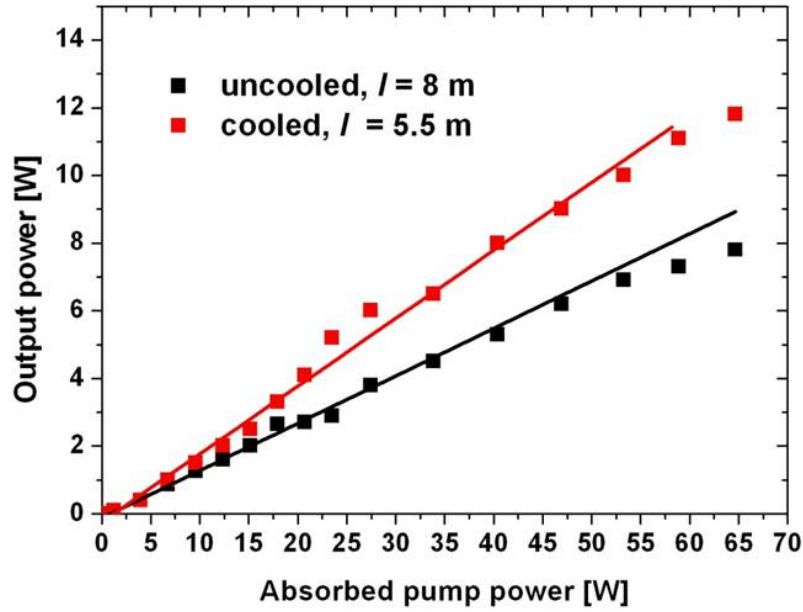
Figure 7.21: Fibre 2 experiment- Pump power versus output power

1.5 mm.

Figure 7.22(a) shows the pulse energy and the pulse duration of the Q-switched Er:ZBLAN fibre laser. The laser threshold was reached at 5 W of pump power. Stable Q-switching could be observed for pump power levels higher than 5.5 W. As can be seen the maximum pulse energy was 560 μJ at a pulse repetition rate of 1 kHz limited by prelasing. The corresponding minimum pulse duration was 53 ns leading to a maximum pulse peak power of 10.6 kW. This value exceeds already published work by an order of magnitude [7.19] and clearly demonstrates the potential for the practical use. The energy fluence at the output fibre end was calculated to be ≈ 70 J/cm^2 at the maximum pulse energy level and no damage was observed. The pulse-to-pulse amplitude fluctuation was measured to be less than 12 %. Figure 7.22(b) shows the spectrum at 2.79 μm in Q-switched laser operation and the shape of the laser pulses at the highest pulse energy level. In the near future further experiments with different pulse repetition rates will be carried out. Regarding power scaling AOM drivers with higher RF power to suppress prelasing will be used and bulk glass substrates will be spliced to the fibre ends to decrease the thermal stress of the fibre ends and prevent damage.
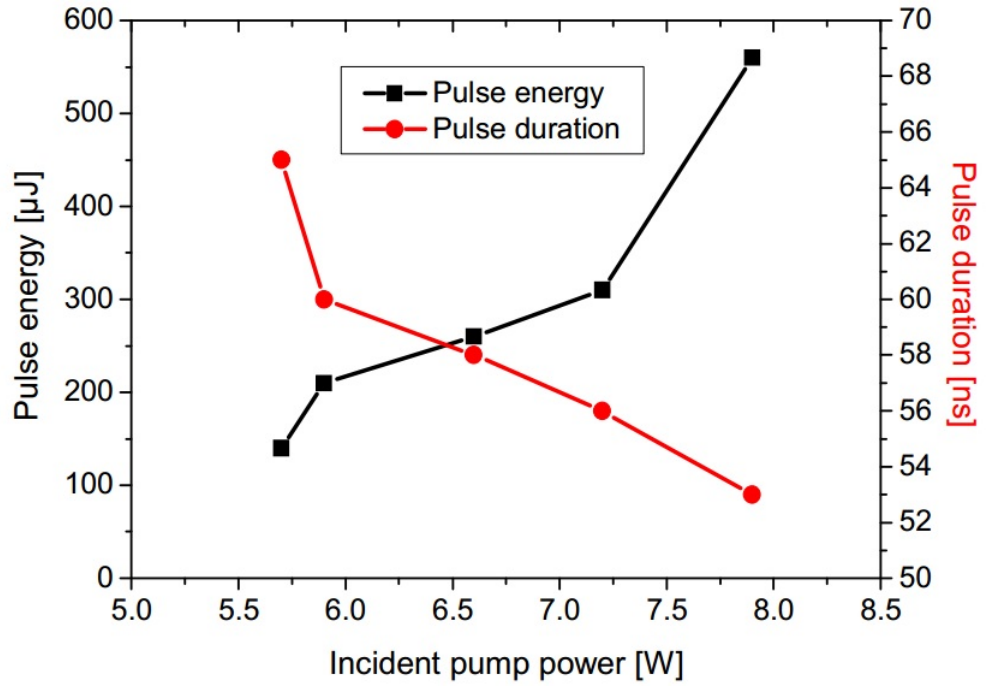
(a) Pulse energy and pulse duration at 1 kHz pulse repetition rate
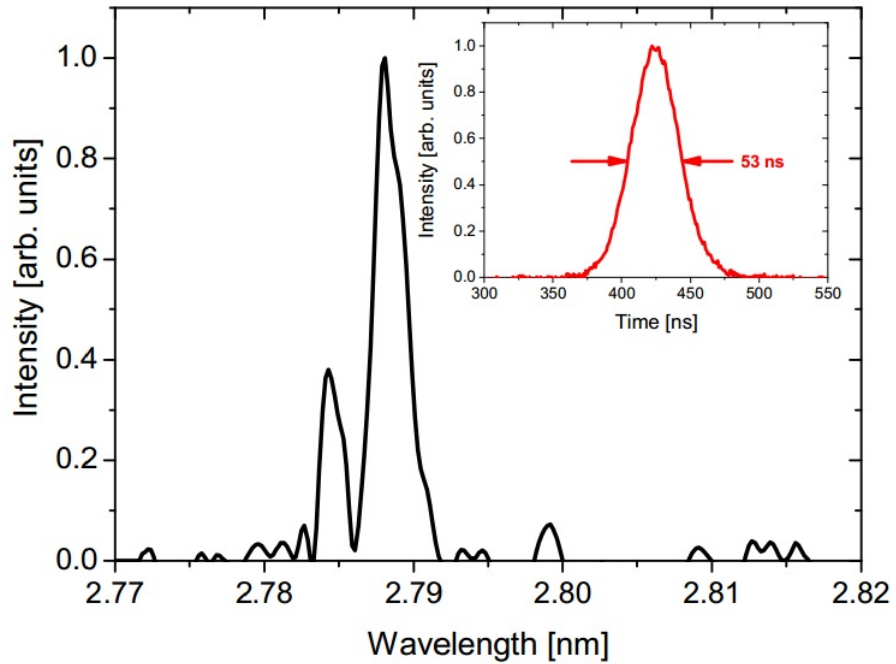
(b) Spectrum in Q-switched operation mode. The inset shows the recorded laser pulse at the highest energy level

Figure 7.22: High-Energy Q-switched Er:ZBLAN Fibre Laser at 2.79 μm

7.5   Summary and Discussion

The CW-laser characteristics and the evolution of a double-clad fiber laser were described. Starting with a theoretical model, a propagation characteristic was built and an optimum length was proposed for the lasing operation. By solving the phonon energy-dependent temperature model, an optimum operating temperature was proposed, which matched the temperature roll-over observed in the experiment. An experimental setup was used to validate the numerical model and the results presented are a clear documentation of the design of an erbium doped ZBLAN fiber laser

Two double-clad fibres have been considered for the realisation of a mid-infrared fibre laser. The proposed device uses either Fresnel reflections at both ZBLAN glass-air interfaces or the Fresnel reflection on one side and a fully reflective mirror on the other one. The results obtained showed that the device that uses a mirror is more efficient with cooling or operation around the optimum length. Further, the highly-doped, double-clad octagonal geometry with the larger core allows us to achieve higher optical efficiency when compared to the circular clad fibre with a comparatively lower concentration of erbium. An extension of the application of this work was also discussed in application to a high-energy Q-switched Er:ZBLAN Fibre Laser at 2.79 μm.

References

[7.1] J. Limpert, A. Liem, H. Zellmer, and A. Tünnermann, "500 w continuous-wave fibre laser with excellent beam quality," *Electronics Letters*, vol. 39, no. 8, pp. 645–647, 2003.

[7.2] R. M. Almeida and J. D. Mackenzie, "Vibrational spectra and structure of fluorozirconate glasses," *The Journal of Chemical Physics*, vol. 74, no. 11, pp. 5954–5961, 1981.

[7.3] S. D. Jackson, "Towards high-power mid-infrared emission from a fibre laser," *Nature photonics*, vol. 6, no. 7, pp. 423–431, 2012.

[7.4] R. Caspary, *Applied Rare Earth Spectroscopy for Fiber Laser Optimization.* Berichte Aus der Lasertechnik Series, Shaker Verlag GmbH, 2002.

[7.5] D. McCumber, "Einstein relations connecting broadband emission and absorption spectra," *Physical Review*, vol. 136, no. 4A, p. A954, 1964.

[7.6] B. Judd, "Optical Absorption Intensities of Rare-Earth Ions," *Physical Review*, vol. 127, pp. 750 –, 1962.

[7.7] G. S. Ofelt, "Intensities of Crystal Spectra of Rare-Earth Ions," *The Journal of Chemical Physics*, vol. 37, no. 3, pp. 511–520, 1962.

[7.8] M. Pollnau, C. Ghisler, W. Lüthy, and H. P. Weber, "Cross sections of excited-state absorption at 800 nm in erbium-doped ZBLAN fiber," *Applied Physics B*, vol. 67, no. 1, pp. 23–28, 1998.

[7.9] M. Pollnau and S. D. Jackson, "Erbium 3 μm fiber lasers," *IEEE Journal of Selected Topics in Quantum Electronics*, vol. 7, no. 1, pp. 30–40, 2001.

[7.10] M. Pollnau and S. D. Jackson, "Energy recycling versus lifetime quenching in erbium-doped 3-μm fiber lasers," *Quantum Electronics, IEEE Journal of*, vol. 38, no. 2, pp. 162–169, 2002.

[7.11] P. S. Golding, S. D. Jackson, T. A. King, and M. Pollnau, "Energy transfer processes in Er^{3+}-doped and Er^{3+}, Pr^{3+}-codoped ZBLAN glasses," *Phys. Rev. B*, vol. 62, pp. 856–864, Jul 2000.

[7.12] R. Reisfeld and C. K. Jrgensen, "Chapter 58 Excited state phenomena in vitreous materials ," in *Handbook on the Physics and Chemistry of Rare Earths* (J. Karl A. Gschneidner and L. Eyring, eds.), vol. 9 of *Handbook on the Physics and Chemistry of Rare Earths*, pp. 1 – 90, Elsevier, 1987.

[7.13] H. W. Moos, "Spectroscopic relaxation processes of rare earth ions in crystals," *Journal of Luminescence*, vol. 1, pp. 106–121, 1970.

[7.14] S. S., W. M., C. R., and K. W., "Erbium-Doped Fluoride Glass Waveguides for Laser Applications," *Transparent Optical Networks (ICTON), 2010 12th International Conference on*, 2010.

[7.15] S. Sujecki, "Stability of steady-state high-power semiconductor laser models," *JOSA B*, vol. 24, no. 5, pp. 1053–1060, 2007.

[7.16] S. Sujecki, "An Efficient Algorithm for Steady State Analysis of Fibre Lasers Operating under Cascade Pumping Scheme," *International Journal of Electronics and Telecommunications*, vol. 60, no. 2, pp. 143–149, 2014.

[7.17] O. Hadeler, *Distributed feedback fibre laser strain and temperature sensors.* PhD thesis, University of Southampton, 2002.

[7.18] M. Pollnau, "Analysis of heat generation and thermal lensing in erbium 3 μm lasers," *IEEE Journal of Quantum Electronics*, vol. 39, pp. 350–357, 2003.

[7.19] S. Tokita, M. Murakami, S. Shimizu, M. Hashida, and S. Sakabe, "12 W Q-switched Er^{3+}: ZBLAN fiber laser at 2.8 μm," *Optics letters*, vol. 36, no. 15, pp. 2812–2814, 2011.

Chapter 8

Conclusions and Future Work

This Chapter reiterates our research questions, contributions and findings. The aim of this project was to investigate the suitability of silica, ZBLAN and chalcogenide glasses as host materials for rare-earth (RE) doped applications in the NIR and Mid-IR wavelengths. Three main questions to be addressed were:

1. Can we accurately identify and predict the values of ion-ion interactions in RE ions from a spectroscopic point of view and verify it in experiment?

2. Can the ion-ion interactions impact the performance of a laser and to what extent does it affect the design based on thermal considerations?

3. Can we extract the spectroscopic and phenomenological parameters of selenide-chalcogenide glasses for use in modelling the superior photoluminescence property of Indium over Gallium based analogues?

4. Can we produce a suite of numerical techniques to optimise the properties of lanthanide doped materials for bulk materials, fibres and lasers.

The work presented in this thesis concentrated mainly on addressing the first question in Er^{3+} doped silica, the second question in Er^{3+} doped ZBLAN, third question in Pr^{3+} doped Chalcogenide glass while the fourth question was addressed in all the glasses considered. In Section 8.1, we recall some of the findings of this research and state the important results. Section 8.2 describes the contributions of the study, the limitations encountered and what

could have been done. Finally Section 8.3 presents some of the future outlook and research that can be carried forward given the insights produced by this research work.

<center>∿∿∿∿∿∿</center>
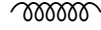
8.1 Main results of this study

This section presents the results laid out in the context of the initial goals and objectives of this research. The section proceeds as follows: description of the results in erbium doped bulk glass, erbium doped ZBLAN glass and praseodymium doped bulk/fibre glass.

8.1.1 Erbium doped sol-gel SiO_2

The suitability of silica glass as a host material for RE ion-ion investigation is confirmed by the mature technology and the availability of the sol-gel technique which is capable of incorporating a wide variety of dopants. Therefore, this study examined three samples of erbium doped sol-gel SiO_2 with different doping levels. With the foundation of the physics of rare-earth ions laid, a rate-equation technique was developed to produce the photoluminescence emissions in the samples. With the aid of power dependence studies and the kinetic properties of the energy-levels, the author identified the five dominant processes of upconversion that are responsible for the observed photoluminescence. A particle swarm optimisation was applied to predict the values of the chosen parameters under 488 nm excitation. The result was applied to a rate-equation model under 800 nm excitation and a good agreement was found when compared to experiment. The results showed that the important processes of energy-transfer and cross-relaxations can be correctly identified by combining power dependence studies with a particle swarm algorithm.

8.1.2 Praseodymium doped Chalcogenide bulk and fibre glasses

Due to their potential low phonon energy, chalcogenide glasses are considered as suitable hosts for wavelength applications greater than those for which silica is known (> 2 μm). In the $3 - 5$ μm wavelength range, praseodymium doped fibre lasers and amplifiers are still in active development. In this study, the objective is to develop a praseodymium doped fibre amplifier with improved photoluminescence based on gallium and indium host glasses for mid-IR applications. Furthermore the objective is to assess the performance (gain, and NF characteristics) of PDFAs by means of modelling and measurements. To develop such fibres, the spectroscopic properties of the host glasses is of major importance in determining the efficiency of the final device. Here the determination of optical properties of the candidate (Gallium and Indium) selenide based chalcogenide glasses have been investigated with a numerical model which was also validated by experiment.

Using pure chemical elements as starting materials, selenide based chalcogenide glasses incorporating Indium/Gallium were prepared for the author by the Novel Glasses Photonics Group of the University Of Nottingham by melting in vitreous silica ampoules, followed by quenching. The purification of the raw materials is essential to produce glasses of desired optical characteristics. This is still the focus of on-going research in the group. One of the major requirements for the glass for the mid-IR application is low effective phonon energy. This determines multiphonon energy transfer from the $^3F_2$/ $^3H_6$ excited state to the next lower level $^3H_5$ and those of $^3H_5$ to the ground state $^3H_4$ by lattice vibrations of the host glass. This study predicts that the effective phonon energy of the Gallium based glasses is approximately 250 cm^{-1} and those of Indium based glasses is approximately 230 cm^{-1} and is comparatively lower than those of chalcogenide glasses with Sulphur network formers ($330 - 350$ cm^{-1} [8.1]). By virtue of the (up to $\times$ 1.25) longer emission lifetime of praseodymium in the Indium hosts compared to the gallium hosts, the luminescence measured in the Indium Sample shows superior intensity (up to two times) to those of gallium in the mid-IR. This was reproduced with the aid of a numerical model. Using the spectroscopic parameters of radiative and non-radiative lifetimes, a

rate equation model was used to produce all the interband photoluminescence transitions spanning the wavelength $1.5 - 6.0$ μm . Fibre reabsorption at longer wavelengths was also modelled by reducing the stark multiplet of $^3H_5$ to a simplified 2-level rate equation. The source of the excitation was the photoluminescence produced by the $^3H_5 \to$ $^3H_4$ transition.

8.1.3 Erbium doped ZBLAN Fibre laser

The $^4I_{11/2} \to$ $^4I_{13/2}$ transition wavelength of erbium coincides with the absorption wavelength of water and therefore a potential wavelength for tissue surgery. In silica glass hosts however, this transition is rapidly quenched by multiphonon transition because of the high phonon energy of silica. The lower phonon energy in ZBLAN hosts compared to silica glass hosts makes it suitable to excite the $^4I_{11/2} \to$ $^4I_{13/2}$ transition wavelength efficiently for laser operations. Er:ZBLAN has been reviewed in literature [8.2] and a number of research have produced the spectroscopic parameters of erbium in ZBLAN glass hosts [8.3–8.5].

Therefore, this study examined two commercially available double clad fibre samples of Er:ZBLAN with different concentrations and geometry. This study found that the fibre with higher concentration required a shorter length compared to the fibre with lower concentration for efficient lasing operation. This is in-line with the theory of absorption per unit volume. The study then proceeded to produce the optimum operating length for the fibres by considering thermal operations in cascade lasing operation. It was found that with a glass transition temperature of 533 K, the actual optimum length is less than 10 m.

8.2 Contributions and Limitations of the research

A major contribution of this work is that it provided for the first time, an understanding of the population dynamics in Pr^{3+} doped selenium based chalcogenide with indium and gallium network formers. It also resulted in the extraction of non-radiative phenomenological parameters for the indium and gallium based samples.

The validity of the McCumber theory has been experimentally validated by applying it to ground state transitions in chalcogenide glasses. The theory was tested by comparing cross sections calculated using the McCumber's relation with a range of photoluminescence measurements found in available literature. For meaningful comparison, the fluorescence data has been taken from a range of glasses with similar/close compositions. The absorption spectra of Pr^{3+} is characterised by a number of overlapping transitions and therefore Boltzmann's statistics was employed to separate such transitions for consistent results in Judd-Ofelt calculations. This technique avoided the need for more measurements or additional computation compared to previous studies [8.6–8.8].

The Pr^{3+} doped GeAs(Ga/In)Se fibre rod analysed in this study was found to have excellent photoluminescence capability in both Indium and Gallium based samples. They were however not suitable for amplification and laser operation because of the large core (≈ 200 μm diameter) and short length (100 - 150 mm). A model was however developed using the spectroscopic properties of the bulk materials. The model revealed that with a smaller core and increased length of the orders of 1 m, a mid-IR (4.7 μm) fibre amplifier with a gain as high as 40 dB can be realised in co-propagating pump configuration. This is based on the assumption that the fabrication process is able to produce a fibre with minimum loss at the pump and signal wavelengths.

8.3   Future Outlook

With the extraction of phenomelogical parameters to describe the multiphonon transitions, accurate predictions can be made by introducing short excitation pulses and measuring the decay profile, first at cryogenic temperatures, then at increasing temperature. Following this up with a Raman spectroscopy and fitting to the energy-gap equation in the praseodymium doped samples would yield very accurate results for the non-radiative phenomenological parameters

As the development of low-loss chalcogenide glass is a new area of research, the performed experiments only gave a glimpse into the potential of the novel glasses. The

method would benefit greatly from the elimination of glass impurities (HSe, HGe) and atmospheric impurities (CO_2) especially as it directly overlays the mid-IR spectrum of interest. The production and accompanying simulation of a single-mode core chalcogenide glass with distinct core-clad refractive index will open up several different areas where further work can extend this research

It is important to note that in the thermal model of the ZBLAN fibre considered, the influence of thermal lensing on refractive index has not been considered in both experiment and simulation. Research into this would form tbe basis of future interesting research.

References

[8.1] Y. S. Han and J. Heo, "Midinfrared emission properties of Pr^{3+}-doped chalcogenide glasses at cryogenic temperature," *Journal of Applied Physics*, vol. 93, no. 11, pp. 8970–8974, 2003.

[8.2] X. Zhu and N. Peyghambarian, "High-power ZBLAN glass fiber lasers: review and prospect," *Advances in OptoElectronics*, vol. 2010, 2010.

[8.3] R. Caspary, *Applied Rare Earth Spectroscopy for Fiber Laser Optimization*. Berichte Aus der Lasertechnik Series, Shaker Verlag GmbH, 2002.

[8.4] P. S. Golding, S. D. Jackson, T. A. King, and M. Pollnau, "Energy transfer processes in Er^{3+}-doped and Er^{3+}, Pr^{3+}-codoped ZBLAN glasses," *Phys. Rev. B*, vol. 62, pp. 856–864, Jul 2000.

[8.5] M. Pollnau, C. Ghisler, W. Lüthy, and H. P. Weber, "Cross sections of excited-state absorption at 800 nm in erbium-doped ZBLAN fiber," *Applied Physics B*, vol. 67, no. 1, pp. 23–28, 1998.

[8.6] A. A. Kornienko, E. B. Dunina, and A. A. Kaminskii, "Dependence of the line strength of ff transitions on the manifold energy," *physica status solidi (b)*, vol. 157, no. 1, pp. 261–266, 1990.

[8.7] R. S. Quimby and W. J. Miniscalco, "Modified Judd–Ofelt technique and application to optical transitions in Pr^{3+}–doped glass," *Journal of Applied Physics*, vol. 75, no. 1, pp. 613–615, 1994.

[8.8] P. Goldner and F. Auzel, "Application of standard and modified Judd–Ofelt theories to a praseodymium–doped fluorozirconate glass," *Journal of Applied Physics*, vol. 79, no. 10, pp. 7972–7977, 1996.

Appendix A

Fit Coefficients

A.1 Pr:GeAsGa/InSe Absorption Cross-section fits

Table A.1: 500 and 1000 ppm Pr^{3+}:GeAsGaSe

Transition	index	500 ppm			1000 ppm		
		α	$\lambda(\ \mu\text{m}\ )$	$d\lambda(\ \mu\text{m}\ )$	α	$\lambda(\ \mu\text{m}\ )$	$d\lambda(\ \mu\text{m}\ )$
$^1G_4$	0	0.0033	1.0273	0.0139	0.0109	1.0285	0.0159
	1	0.0027	1.0365	0.0246	0.0019	1.0551	0.0137
$^3F_4$	0	0.0894	1.4888	0.0247	0.0572	1.4806	0.017
	1	0.0172	1.4731	0.0436	0.1664	1.5013	0.0397
	2	0.0449	1.5232	0.0151			
	3	0.0429	1.549	0.015			
$^3F_3$	0	0.0659	1.5884	0.0195	0.0765	1.5907	0.0148
	1	0.1406	1.6205	0.0434	0.2975	1.6142	0.0477
	2	0.0173	1.688	0.0156	0.0306	1.6871	0.015
$^3F_2$	0	0.0031	1.9082	0.0505	0.0256	2.0383	0.0148
	1	0.017	2.039	0.0168	0.1400	2.0339	0.0389
	2	0.0671	2.0337	0.0403	0.1692	2.0781	0.0880
	3	0.0832	2.0777	0.0859			
$^3H_6$	0	0.0148	2.2985	0.0807	0.0326	2.2964	0.0846
	1	0.0093	2.2124	0.0377	0.0164	2.2138	0.0345
$^3H_5$	0	0.0123	4.1181	0.1986	0.0545	4.2395	0.2822
	1	0.0282	4.5771	0.4305	0.0377	4.505	0.0587
	2	0.0129	4.3471	0.1254	0.0288	4.7438	0.0393
	3	0.0163	4.5104	0.0616	0.0427	4.7139	0.4094
	4	0.014	4.7464	0.037	0.0416	4.6257	0.1232
	5	0.0152	4.6536	0.1153	0.0069	4.8196	0.1532
	6	0.0052	4.2323	0.0171	0.0131	0.0131	0.073
	7	0.0052	4.2966	0.0232			

Table A.2: 500 and 1000 ppm Pr^{3+}:GeAsInSe

		500 ppm			1000 ppm		
Transition	index	α	$\lambda(\,\mu\text{m}\,)$	$d\lambda(\,\mu\text{m}\,)$	α	$\lambda(\,\mu\text{m}\,)$	$d\lambda(\,\mu\text{m}\,)$
$^1G_4$	0	0.0015	1.054	0.0156	0.0067	1.0253	0.0154
	1	0.007	1.027	0.0176	0.0014	1.0308	0.0036
	2				0.0054	1.0375	0.0213
$^3F_4$	0	0.1009	1.4863	0.0321	0.0152	1.4851	0.004
	1	0.0324	1.5218	0.014	0.0664	1.4739	0.0211
	2				0.1531	1.515	0.0472
	3				0.0222	1.4936	0.019
	4				0.0206	1.5194	0.0096
$^3F_3$	0	0.1565	1.6146	0.0476	0.3157	1.5999	0.0319
	1	0.0314	1.5478	0.0145	0.0338	1.6276	0.0117
	2	0.0536	1.5829	0.0177	0.0383	1.689	0.014
	3	0.0189	1.685	0.0166	0.1391	1.6532	0.024
	4				0.024	1.5808	0.0053
	5				0.0229	1.6772	0.0336
$^3F_2$	0	0.0192	2.0341	0.0172	0.0366	2.0342	0.015
	1	0.0592	2.0147	0.0385	0.2415	2.0336	0.0485
	2	0.0509	2.0596	0.0495	0.0678	2.0918	0.029
	3	0.0748	2.0987	0.1107	0.0264	1.9813	0.089;
	4				0.0863	2.1371	0.0387
	5				0.0295	2.199	0.0382
$^3H_6$	0	0.0022	2.217	0.0198	0.0199	2.2003	0.1196
	1	0.002	2.351	0.0178	0.0266	2.2505	0.1371
	2	0.0048	2.467	0.126	0.0034	2.3477	0.0157
	3	0.0136	2.3124	0.0806			
$^3H_5$	0	0.0235	4.6135	0.1479	0.0035	3.9179	0.0996
	1	0.0242	4.182	0.2567	0.0229	4.7011	0.0852
	2	0.0085	4.3351	0.0935	0.0289	4.7486	0.0337
	3	0.0033	4.3074	0.0093	0.0454	4.677	0.4506
	4	0.0187	4.7419	0.0372	0.0622	4.3236	0.3201
	5	0.0324	4.6243	0.4505	0.0109	4.4865	0.0359
	6	0.0177	4.5075	0.054	0.0029	4.3066	0.0111
					0.0012	4.3251	0.0293
					0.0155	4.5391	0.0522

A.2 Separating Gaussian fits to absorption bands in Judd-Ofelt calculations

Of the 6 absorption peaks identified from FTIR measurements of Pr^{3+}:GeAs(Ga/In)Se (see figure 6.1), each of the band pairs $^3H_6$/ $^3F_2$ and $^3F_3$/ $^3F_4$ overlap. Integrating the cross section measurements is straight-forward but separating the contribution of the

individual components of the pairs for Judd-Ofelt calculation is difficult and will most likely be inconsistent. In these cases, the absorption lines have to be split by employing the Boltzmann's statistics.

A.3 ZBLAN Absorption Cross-section

Table A.3: Coefficient of Gaussian fits to absorption cross-section of Er^{3+}:ZBLAN

i	Transition:	Pump ($^4I_{15/2} \rightarrow ^4I_{11/2}$)	Signal($^4I_{11/2} \rightarrow ^4I_{13/2}$)	Idler($^4I_{13/2} \rightarrow ^4I_{15/2}$)
1	α ($\times 10^{-24} m^2$)	0.0769	0.2089	0.0428
	λ(cm^{-1})	10304.6445	3697.9436	6539.7244
	$d\lambda$ (cm^{-1})	34.8922	12.0847	16.3947
2	α ($\times 10^{-24} m^2$)	0.0796	0.0895	0.3104
	λ(cm^{-1})	10199.5603	3759.2423	6678.2601
	$d\lambda$ (cm^{-1})	145.3985	46.2109	69.7741
3	α ($\times 10^{-24} m^2$)	0.1281	0.1518	0.2901
	λ(cm^{-1})	10258.588	3602.4024	6530.8988
	$d\lambda$ (cm^{-1})	60.2524	26.5206	60.3718
4	α ($\times 10^{-24} m^2$)	0.0063	0.2204	0.0636
	λ(cm^{-1})	10361.8763	3649.3286	6418.7236
	$d\lambda$ (cm^{-1})	12.0478	111.3487	34.3172
5	α ($\times 10^{-24} m^2$)	0.0098	0.2518	0.0036
	λ(cm^{-1})	9968.2803	3668.6058	6240.8248
	$d\lambda$ (cm^{-1})	59.1574	42.2105	41.9992
6	α ($\times 10^{-24} m^2$)	-	-	0.1758
	λ(cm^{-1})	-	-	6559.1249
	$d\lambda$ (cm^{-1})-	-	-	189.5
7	α ($\times 10^{-24} m^2$)	-	-	0.005
	λ(cm^{-1})	-	-	6967.5833
	$d\lambda$ (cm^{-1})	-	-	45.7945
8	α ($\times 10^{-24} m^2$)	-	-	0.0318
	λ(cm^{-1})	-	-	6580.7527
	$d\lambda$ (cm^{-1})	-	-	23.5654

B

Lifetimes and Concentration

B.1 Lifetimes of Praseodymium doped Chalcogenide glasses

Table B.1: Spectroscopic parameters of 1000 ppm Pr:GeAs(Ga/In)Se calculated by Judd-Ofelt analysis

		Gallium 1000 ppm		Indium 1000 ppm	
Transition	λ(nm)	β	τ_r(ms)	β	τ_r(ms)
$^3H_5 \rightarrow\ ^3H_4$	4740.4	1.0	7.7246	1.0	11.807
$^3H_6 \rightarrow\ ^3H_4$	2250.5	0.5642	3.1572	0.5454	4.4316
$\rightarrow\ ^3H_5$	4284.6	0.4358		0.4546	
$^3F_2 \rightarrow\ ^3H_4$	2035.3	0.8716	0.2030	0.8771	0.2933
$\rightarrow\ ^3H_5$	3566.6	0.1281		0.1227	
$\rightarrow\ ^3H_6$	21285	0.0000		0.0002	
$^3F_3 \rightarrow\ ^3H_4$	1599.8	0.7573	0.1196	0.7497	0.1810
$\rightarrow\ ^3H_5$	2414.7	0.2211		0.2322	
$\rightarrow\ ^3H_6$	5533.1	0.0212		0.0177	
$\rightarrow\ ^3F_2$	7476.6	0.0000		0.0004	
$^3F_4 \rightarrow\ ^3H_4$	1485.7	0.6565	0.1955	0.6544	0.2998
$\rightarrow\ ^3H_5$	2163.9	0.2614		0.2677	
$\rightarrow\ ^3H_6$	4371.8	0.0800		0.0758	
$\rightarrow\ ^3F_2$	5501.9	0.0021		0.0021	
$\rightarrow\ ^3F_3$	20831	0.0000		0.0000	
$^1G_4 \rightarrow\ ^3H_4$	1030.3	0.0706	0.1323	0.0710	0.2044
$\rightarrow\ ^3H_5$	1316.4	0.6042		0.6067	
$\rightarrow\ ^3H_6$	1900.3	0.2790		0.2762	
$\rightarrow\ ^3F_2$	2086.6	0.0043		0.0045	
$\rightarrow\ ^3F_3$	2894.3	0.0061		0.0061	
$\rightarrow\ ^3F_4$	3361.3	0.0357		0.0355	

B.2   Lifetimes of Erbium doped ZBLAN

Table B.2: Spectroscopic parameters calculated by Judd-Ofelt analysis and Energy gap law

Transition	$\lambda(nm)$	β	τ_r(ms)	τ_{nr}(s)
$^4I_{13/2} \rightarrow {}^4I_{15/2}$	1529.30	1.0	8.52	-
$^4I_{11/2} \rightarrow {}^4I_{15/2}$	972.77	0.8358	7.87	-
$\rightarrow {}^4I_{13/2}$	2673.09	0.1642	-	0.1118 s
$^4I_{9/2} \rightarrow {}^4I_{15/2}$	800.40	0.7267	6.78	-
$\rightarrow {}^4I_{13/2}$	1679.31	0.2627	-	-
$\rightarrow {}^4I_{11/2}$	4517.06	0.0106	-	89.4 μs
$^4F_{9/2} \rightarrow {}^4I_{15/2}$	650.66	0.9064	0.86	-
$\rightarrow {}^4I_{13/2}$	1132.49	0.0436	-	-
$\rightarrow {}^4I_{11/2}$	1964.99	0.0466	-	-
$\rightarrow {}^4I_{9/2}$	3477.95	0.0034	-	1.67ms
$^4S_{3/2} \rightarrow {}^4I_{15/2}$	540.15	0.6681	0.73	-
$\rightarrow {}^4I_{13/2}$	835.11	0.2734	-	-
$\rightarrow {}^4I_{11/2}$	1214.56	0.0226	-	-
$\rightarrow {}^4I_{9/2}$	1661.23	0.0356	-	-
$\rightarrow {}^4F_{9/2}$	3180.29	3.9224e-04	-	8.75ms
$^2H_{11/2} \rightarrow {}^4I_{15/2}$	521.62	0.9193	0.26	-
$\rightarrow {}^4I_{13/2}$	791.63	0.0328	-	-
$\rightarrow {}^4I_{11/2}$	1124.72	0.0301	-	-
$\rightarrow {}^4I_{9/2}$	1497.61	0.0146	-	-
$\rightarrow {}^4F_{9/2}$	2630.17	0.0032	-	-
$\rightarrow {}^4S_{3/2}$	15205.24	5.8207e-06	-	0.045 μs
$^2F_{7/2} \rightarrow {}^4I_{15/2}$	486.30	0.7772	0.34	-
$\rightarrow {}^4I_{13/2}$	713.04	0.1269	-	-
$\rightarrow {}^4I_{11/2}$	972.43	0.0600	-	-
$\rightarrow {}^4I_{9/2}$	1239.21	0.0343	-	-
$\rightarrow {}^4F_{9/2}$	1925.14	0.0014	-	-
$\rightarrow {}^4S_{3/2}$	4877.90	6.6593e-06	-	-
$\rightarrow {}^2H_{11/2}$	7181.87	1.9212e-04	-	0.85 μs

.